TKK Radio Science and Engineering Publications

Espoo, November 2010 **REPORT R18**

ACTIVE AND PASSIVE DIELECTRIC ROD WAVEGUIDE COMPONENTS FOR MILLIMETRE WAVELENGTHS

Thesis for the degree of Doctor of Science in Technology

Patrik Pousi

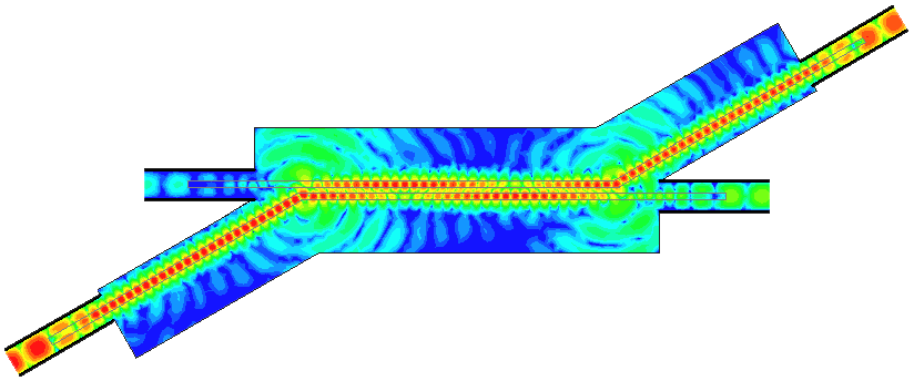

Aalto University

School of Science and Technology

Faculty of Electronics, Communications, and Automation

Department of Radio Science and Engineering

TKK Radio Science and Engineering Publications

Espoo, November 2010 **REPORT R18**

ACTIVE AND PASSIVE DIELECTRIC ROD WAVEGUIDE COMPONENTS FOR MILLIMETRE WAVELENGTHS

Thesis for the degree of Doctor of Science in Technology

Patrik Pousi

Dissertation for the degree of Doctor of Science in Technology to be presented with due permission of the Faculty of Electronics, Communications and Automation, for public examination and debate in Auditorium S4 at Aalto University School of Science and Technology (Espoo, Finland) on the 26th of November, 2010, at 12 noon.

Aalto University
School of Science and Technology
Faculty of Electronics, Communications, and Automation
Department of Radio Science and Engineering

Distribution:
Aalto University School of Science and Technology
Department of Radio Science and Engineering
P.O. Box 13000
FI-00076 AALTO
Tel. +358 9 470 22261
Fax +358 9 470 22267
E-mail ari.sihvola@tkk.fi

ISBN 978-952-60-3462-1 (paper)
ISBN 978-952-60-3463-8 (electronic)
ISSN 1797-4364 (paper)
ISSN 1797-8467 (electronic)

Picaset Oy
Helsinki 2010

Aalto University
School of Science and Technology

ABSTRACT OF DOCTORAL DISSERTATION	AALTO UNIVERSITY SCHOOL OF SCIENCE AND TECHNOLOGY P.O. BOX 13000, FI-00076 AALTO http://www.aalto.fi

Author Juho Patrik Pousi

Name of the dissertation
Active and passive dielectric rod waveguide components for millimetre wavelengths

Manuscript submitted 18.6.2010	Manuscript revised 27.10.2010

Date of the defense 26.11.2010

☒ Monograph ☐ Article dissertation (summary + original articles)

Faculty	Electronics, Communications and Automation
Department	Radio Science and Engineering
Field of research	Radio Engineering
Opponent	Prof. Dr.-Ing. Lorenz-Peter Schmidt
Supervisor	Professor Antti Räisänen
Instructor	Docent Dmitri Lioubtchenko

Abstract

In this thesis, active and passive dielectric rod waveguide (DRW) components have been studied and developed for millimetre wavelengths. DRW antennas made of relatively high permittivity materials like silicon and sapphire are designed and simulated with HFSS (a commercial electromagnetic structure simulator based on Finite Element Method) at frequencies up to 325 GHz. A prototype antenna for D band (110-170 GHz) has been fabricated and measured. The location of the phase centre of an antenna is an important parameter in many applications, especially when the antenna is used as a feed for a reflector. This location of the phase centre for the DRW antenna has been studied with different methods from measurement results obtained with a planar scanner at W band.

A high-permittivity DRW antenna is an interesting candidate for an antenna array element. According to W-band simulations and measurements the mutual coupling between the elements is relatively low even with the distance of ~λ/2 as the element spacing. This makes the DRW an appealing alternative as an element for densely packed arrays.

However, mutual coupling studies for antenna arrays revealed a very strong coupling phenomenon when the distance between the elements is small. At some point the power is transferred completely from the excited waveguide to the neighbouring waveguide. This phenomenon is similar to cross-talk in optical fibres. In that regime cross-talk has been utilised in many applications, e.g. in directional couplers. In this thesis a frequency selective coupler based on that strong coupling has been developed. Frequency selectivity is based on the fact, that the waveguide length required for complete power transfer depends on the frequency. The length that is required for the power to transfer from one waveguide to the other and back is also called as the beat length. A prototype coupler has been simulated, manufactured and measured at W band. The results are very promising for this type of components made of DRWs for millimetre wavelengths.

Different types of DRW junctions for power division have also been studied. Such junctions can be used also for monitoring the propagating power in a DRW. Junctions can be designed for both E and H planes depending on the application. Symmetric and asymmetric Y-type junctions have been designed and studied with simulations in both planes.

Active components studied in this thesis include a travelling-wave amplifier based on GaAs/AlGaAs heterostructure and a DRW phase shifter designed for ferroelectric varactors fed through Au strips, both designed for W band. A DRW travelling-wave amplifier is based on the interaction between an electron drift and an electromagnetic wave travelling in a periodic structure. Electronic gain of 10 dB/cm at 150 V/cm has been measured at 70-80 GHz. The proposed novel prototype of millimetre-wave phase shifter includes a dielectric rod waveguide with a periodic printed array of electrically small dipoles loaded with ferroelectric varactors. Measurement results of a non-tunable phase shifter prototype show that optimally a phase shift of 60 deg/dB can be obtained at W band.

Keywords dielectric rod waveguide, millimetre wave, antenna, mutual coupling, travelling-wave amplifier

ISBN (printed) 978-952-60-3462-1	ISBN (printed) 1797-4364
ISBN (pdf) 978-952-60-3463-8	ISBN (pdf) 1797-8467
Language English	Number of pages 204

Publisher Aalto University, Department of Radio Science and Engineering

Print distribution Aalto University, Department of Radio Science and Engineering

☒ The dissertation can be read at http://lib.tkk.fi/Diss/2010/isbn9789526034638/

Aalto-yliopisto
Teknillinen korkeakoulu

VÄITÖSKIRJAN TIIVISTELMÄ	AALTO-YLIOPISTO PL 13000, 00076 AALTO http://www.aalto.fi

Tekijä Juho Patrik Pousi

Väitöskirjan nimi
Aktiivisia ja passiivisia dielektriseen aaltoputkeen perustuvia komponentteja millimetriaaltoalueelle

Käsikirjoituksen päivämäärä 18.6.2010	Korjatun käsikirjoituksen päivämäärä 27.10.2010
Väitöstilaisuuden ajankohta 26.11.2010	
☒ Monografia	☐ Yhdistelmäväitöskirja (yhteenveto + erillisartikkelit)

Tiedekunta	Elektroniikka, tietoliikenne ja automaatio
Laitos	Radiotiede ja -tekniikka
Tutkimusala	Radiotekniikka
Vastaväittäjä	Prof. Dr.-Ing. Lorenz-Peter Schmidt
Työn valvoja	Professori Antti Räisänen
Työn ohjaaja	Dosentti Dmitri Lioubtchenko

Tiivistelmä

Tässä väitöskirjassa on kehitetty aktiivisia ja passiivisia dielektriseen aaltoputkeen perustuvia komponentteja millimetriaaltoalueelle. Korkean permittiviisyyden omaavista materiaaleista, kuten safiirista tai piistä, valmistetusta dielektrisesti aaltoputkesta on suunniteltu ja simuloitu sauva-antenneja aina 325 GHz:n taajuuteen asti. Prototyyppiantenni on rakennettu taajuusalueelle 110-170 GHz, jolla sen toimivuus on todettu myös mittauksin. Vaihekeskipisteen tarkka sijainti on tärkeä tietää monissa sovelluksissa, erityisesti kun antennia käytetään syöttöantennina. Vaihekeskipisteen paikka on määritetty kolmella eri analyysimenetelmällä perustuen tasoskannerilla tehtyihin mittauksiin.

Korkeapermittiiviset dielektriset sauva-antennit ovat myös mielenkiintoinen vaihtoehto käytettäväksi antenniryhmissä. Taajuusalueen 75-110 GHz (W- alue) simulointien ja mittausten mukaan elementtien välinen keskinäiskytkentä on vähäistä aina etäisyydelle $\lambda/2$ asti. Tämä tekee dielektrisistä sauva-antenneista hyvän vaihtoehdon tiheää pakkausta vaativiin antenniryhmäsovelluksiin.

Väitöskirjassa keskinäiskytkennän on havaittu kuitenkin olevan erittäin voimakasta lyhyillä etäisyyksillä. Tietyllä etäisyydellä aaltoputkessa jopa kaikki sähkömagneettinen teho siirtyy viereiseen aaltoputkeen. Tämä ilmiö tunnetaan optisissa kuiduissa ja niissä ilmiötä on käytetty hyväksi esimerkiksi suuntakytkimissä. Tässä työssä ilmiön pohjalta on kehitetty taajuusriippuva kytkin W-alueelle. Tehon siirtymiseen kokonaan viereiseen aaltoputkeen tarvittava matka riippuu taajuudesta ja kytkimessä käytetään tätä hyväksi. Simulointien pohjalta on valmistettu prototyyppikytkin, jonka toiminta on todettu hyväksi mittauksin. Tulokset ovat lupaavia tämän tyyppisille komponenteille käytettäväksi millimetriaaltotaajuksilla.

Tehonjakoa varten työssä on suunniteltu myös erilaisia W-alueen aaltoputkiliitoksia. Liitoksia voi käyttää myös esimerkiksi aaltoputkessa kulkevan tehon seurantaan. Työssä on suunniteltu sekä symmetriset että epäsymmetriset Y-liitokset niin pysty- kuin vaakasuorassa tasossa.

Työssä kehitettyjä aktiivisia komponentteja ovat dielektriseen aaltoputkeen suunnitellut kulkuaaltovahvistin ja säädettävä vaiheensiirrin, molemmat W-alueelle. Kulkuaaltovahvistin pohjautuu GaAs/AlGaAs-heteroliitokseen, jossa elektronivirta vahvistaa jaksollisessa rakenteessa kulkevaa sähkömagneettista aaltoa. 10 dB/cm:n elektroninen vahvistus on mitattu 150 V/cm:n sähkökentällä taajudella 80 GHz. Vaiheensiirtimen säädettävyys perustuu säädettäviin ferroelektrisiin varaktoreihin, jotka on kiinnitetty aaltoputken sivulle metalliliuskoihin. Prototyypin, jossa varaktorit on korvattu kiinteillä kapasitansseilla, mittaukset osoittavat, että ~60 °/dB:n vaiheensiirto voidaan toteuttaa W-alueella.

Asiasanat dielektriset aaltoputket, millimetriaallot, antenni, keskinäiskytkeytyminen, kulkuaaltovahvistin

ISBN (painettu) 978-952-60-3462-1	ISSN (painettu) 1797-4364
ISBN (pdf) 978-952-60-3463-8	ISSN (pdf) 1797-8467
Kieli englanti	Sivumäärä 204

Julkaisija Aalto-yliopisto, Radiotieteen ja -tekniikan laitos

Painetun väitöskirjan jakelu Aalto-yliopisto, Radiotieteen ja -tekniikan laitos

☒ Luettavissa verkossa osoitteessa http://lib.tkk.fi/Diss/2010/isbn9789526034638/

PREFACE

Studies leading to this Doctoral thesis were carried out in the Department of Radio Science and Engineering in Aalto University School of Science and Technology.

I am grateful for my supervisor Professor Antti Räisänen for the possibility to work in an inspiring and international atmosphere of radio science. I highly appreciate his guidance and support throughout this work. Special thanks go to Dr. Sergey Dudorov and Docent Dmitri Lioubtchenko, who acted also as my instructor. Both of them were great help in creating and developing ideas for this thesis. I am thankful also to all other members of millimetre-wave research group, especially Juha Mallat, Juha Ala-Laurinaho and Aleksi Tamminen for their co-operation and help. I thank Dr. Pablo Padilla who helped us in DRW antenna phase centre measurements during his three month visit in the department.

I thank also our technicians Lauri Laakso and Eino Kahra who have always been ready to help in constructing the prototypes and measurement setups. Laboratory engineer Viktor Sibakov and laboratory technician Lorenz Schmuckli have both been a great help in many practical things. I thank also other members of the personnel of the department for creating a joyful working environment.

I would like also to thank our partners at MC2 Microtechnology and Nanoscience Laboratory of Chalmers University of Technology, Gothenburg, Sweden. I am especially grateful to Dr. Mats Hagberg, Dr. Ulf Södervall, Mr. Mahdad Sadeghi and Dr. Anatoli Deleniv who were all of great help in manufacturing prototypes for this thesis in the clean room facilities of Chalmers.

I would like to thank the pre-examinators Professor Andrea Neto and Dr. Alexander Schuchinsky for their careful reading and commentary of the first version of the thesis.

I highly appreciate the financial support from the Finnish Cultural Foundation, the Foundation of Emil Aaltonen and the Finnish Society of Electronics Engineers.

Finally, I would like to thank all of my dear friends and family, especially my wife and son, Annika and Paulus, for their continuous support and company.

In Espoo 27.10.2010,

Patrik Pousi

TABLE OF CONTENTS

LIST OF SYMBOLS

α	Phase constant
α_p	Propagation loss
β	Phase constant
δ_s	Converge criterion for S parameters in HFSS
ε	Dielectric constant, permittivity
η	Wave impedance in free space
λ	Wavelength
tan δ	Loss tangent, $=\frac{\varepsilon''}{\varepsilon'}$
E	Electric field
H	Magnetic field
k	Propagation constant, $k=2\pi/\lambda$
S_{11}	Reflection coefficient
S_{21}	Transmission coefficient

LIST OF ABBREVIATIONS

BCB	Benzocyclobutene
D band	Frequency band 110-170 GHz
DC	Direct current
DRA	Dielectric resonator antenna
DRW	Dielectric rod waveguide
EM	Electromagnetic
FOM	Figure of merit
FSW	Ferrite strip waveguide
HFSS	High frequency structure simulator
IR	Infra red
MVNA	Millimetre-wave vector network analyzer
PAA	Phased array antenna
PEC	Perfect electric conductor
P-i-n	p-type - intrinsic - n-type semiconductor junction (diode)
PMC	Perfect magnetic conductor
RAM	Radar absorbing material
SEM	Scanning electron microscope
SIS	Superconductor-insulator-superconductor
TWA	Travelling-wave amplifier
UWB	Ultra wide band
W band	IEEE radar band designation for 75-110 GHz band

1 INTRODUCTION

Technology in the millimetre and terahertz range is a growing field of research and applications. The terahertz range is normally meant to cover the frequency band 300 GHz - 3 THz in the electromagnetic spectrum, corresponding to submillimetre wavelengths between 1 mm and 100 μm. Until lately, this has been also a largely unexplored part of the electromagnetic spectrum. The growing interest is mostly due to emerging new applications and the need of new frequencies as the lower frequencies are reaching their limits, e.g. in accuracy, capacity or capability. Since 1960's the radio astronomy has had a major interest in millimetre waves, but the recent advances in millimetre and terahertz technologies have made it possible to imagine many other interesting applications in the near future. However, one problem of moving to the submillimetre wavelengths and terahertz range is the difficulty in implementing many critical components in these frequencies.

Millimetre and terahertz waves are very interesting as they possess characteristics of both of their neighbours in electromagnetic spectrum, i.e., microwaves and infrared. These waves can pass easily through fog, smoke and some solid materials, like thin walls and clothes, yet can be focused as light to create images of objects. This makes the terahertz range very interesting in several imaging applications for example in safety, navigation, medicine and biology. Compared to microwaves, the terahertz range offers also a large relative bandwidth which will be required in the future short range wireless communications applications. However, for larger terrestrial distances the atmospheric attenuation is too large.

The major problem is that the fundamental hardware for building commercial systems for millimetre and terahertz applications is very expensive or does not exist at all today. Currently, the researchers are still far from having room-temperature emitters and receivers in terahertz range that would also be cost effective and small in size. Operating temperatures are normally very low and the implementation costs are very

high. To obtain cost effective, room-temperature millimetre and terahertz devices long term research and many technological breakthroughs are required.

Components based on dielectric rod waveguides are an interesting field of research that could partly answer to some of the open questions. They often offer cost effective and low loss solutions. In nature dielectric rods can be found for example in human eye, where the retina includes over 100 million dielectric antennas (both rods and cones) for receiving visible light.

Dielectric materials are increasingly used at frequencies above 100 GHz. In general, dielectric material is an insulator that can be polarized by an electric field. In practical applications, most dielectric materials are solid but also some liquids and gases can serve as good dielectric materials, e.g., distilled water is a fair dielectric. Also dry air is an excellent dielectric, and it is used in variable capacitors and some types of transmission lines. An important property of a dielectric is its ability to support an electromagnetic field while dissipating minimal energy in the form of heat. The lower the dielectric loss, the more effective is the dielectric material. Dielectric materials are used in making for example waveguides, directional couplers and phase shifters.

In this thesis work some of the active and passive components based on dielectric rod waveguides, made of silicon, sapphire and gallium arsenide, have been studied and developed. Especially silicon and gallium arsenide are interesting as they are widely used in industry, thus offering many well developed and cost effective techniques to use.

1.1 Objectives and scope of the thesis

This work is a Doctoral thesis for the Department of Radio Science and Engineering of Aalto University School of Science and Technology. The main objective is to study and design active and passive millimetre wave components based on dielectric rod

waveguides (DRW), mostly made of low loss and relatively high-permittivity materials like silicon, sapphire and gallium arsenide, for millimetre-wave frequencies. All the proposed components can be operated at W band and many of them can be also scaled to higher frequencies.

This thesis work is a continuation for the research work already done in this field in the Department of Radio Science and Engineering, namely DRWs and DRW antennas at W band. In the first stage, dielectric rod waveguides are further developed and studied to be used as antennas for 110-170 GHz and 220-325 GHz frequency bands. Nowadays these frequencies are often denoted also to belong to low terahertz frequency range. In this thesis the terahertz band is considered to start from 100 GHz and to end in the infra red region (~10 THz).

Dielectric rod waveguide antennas studied in this thesis work have a rectangular cross-section and they are excited with a metal waveguide. Different structures have been simulated to find the appropriate DRW dimensions, prototypes have been constructed and measured and some support structures for the DRW have been proposed. The suitability of the DRW elements for antenna arrays has also been studied at W band. Other passive components designed in this thesis are power dividers and a frequency selective coupler that is based on cross-talk between two identical dielectric waveguides, both designed for W band.

Active components include a prototype of a travelling-wave amplifier that uses an AlGaAs/GaAs heterostructure to create an effective electron drift to amplify the electromagnetic wave propagating in a DRW. The other active component studied is a tunable DRW phase shifter. These are also designed for W band. All the components designed and studied in this thesis can also be scaled to higher frequencies with some restrictions.

1.2 Scientific contribution

The main scientific contributions of this doctoral thesis are the following:

I Further development and analysis of dielectric rod waveguide antennas with rectangular cross-section for 110-170 GHz and 220-325 GHz frequency ranges have been made. Prototype silicon and sapphire antennas for 110-170 GHz have been fabricated and measured. A study of the phase centre position in such an antenna with different analysis methods based on planar scanner measurements at W band has been performed [1]-[3].

II A study of the suitability of the DRWs to be used as an antenna array element has been carried out. Results showing low mutual coupling between the elements with separation over ~λ/2 have been obtained. A metal waveguide power splitter for the feed of the antenna elements at 90 GHz has been developed, fabricated and tested. A two-element prototype antenna has been fabricated and measured [4],[5].

III Power dividers based on DRW junctions have been developed. Different types of junctions have been proposed for W band.

IV Cross-talk phenomenon in rectangular DRWs at millimetre-wave frequencies has been studied. A frequency selective directional coupler for W band based on cross-talk between two identical DRWs has been developed. A prototype has been fabricated and successfully tested [6],[7].

V Experimental study of the travelling-wave amplifier principle to be used in DRWs by using an AlGaAs/GaAs heterostructure has been carried out. A prototype amplifier has been developed with promising results of ~10 dB/cm electronic gain with 150 V/cm electric field at 70-80 GHz. However, true insertion gain has not yet been achieved [8],[9].

VI A tunable DRW phase shifter concept for W band based on ferroelectric varactors has been developed. Measurement results of the non-tunable phase shifter prototype have shown that optimally a phase shift of ~60 deg/dB can be obtained [10].

As indicated above, the main results of this thesis have been published in international scientific journals and conferences [1]-[10].

This thesis describes the research done mostly by the author, but in collaboration with the members of the millimetre wave research group in the Department of Radio Science and Engineering. Dr. Pablo Padilla participated in the DRW antenna phase centre studies during his three month visit from the Technical University of Madrid.

The development of a tunable DRW phase shifter has been done in collaboration with the Physical Electronics Laboratory in Department of Microtechnology and Nanoscience, MC2, Chalmers University of Technology. Their research group has helped with the simulations and thin ferroelectric film technology.

Processing work for travelling-wave amplifier has been done at MC2 Nanofabrication Laboratory, Chalmers University of Technology, Göteborg, Sweden. It has been financed by the FP6-Research Infrastructures program MC2ACCESS through Contract No: 026029.

1.3 Contents of the thesis

The first part of the thesis covers the background and context of the work. In Chapter 2, millimetre-wave waveguides and antennas are briefly reviewed in general. Chapter 3 contains a literature review of the dielectric rod waveguide antennas.

The second part consists of Chapters 4 to 7. Chapters 4 and 5 describe the novel DRW antennas using silicon and sapphire rod waveguides for 110-170 GHz and 295-325 GHz frequency bands. In Chapter 6 the position of the phase centre in such antennas is studied. Chapter 7 contains the analysis of a DRW as an antenna array element. A 90-GHz metal waveguide power divider was developed for the prototype measurements.

The third part contains the study of cross-talk and power transfer between DRWs (Chapter 8). This phenomenon is used in frequency-selective coupler design for W band in Chapter 9. DRW power dividers are studied in Chapter 10.

In the last part active DRW devices are studied. These include a travelling-wave amplifier based on AlGaAs/GaAs heterostructure (Chapter 11) and a tunable phase shifter (Chapter 12). Chapter 13 provides the conclusion.

2 OVERVIEW OF MILLIMETRE-WAVE WAVEGUIDES AND ANTENNAS

As the frequency increases in the electromagnetic spectrum to the THz range the techniques that are used at the microwave frequencies cannot be applied anymore. For example metal parts have increasing losses and the component dimensions get so small that they become difficult to manufacture. For these reasons in the millimetre-wave range quasi-optical techniques based on free-space propagation are more suitable. However, dielectric components offer also lower losses combined with good waveguiding properties. Dielectrics can be also used in antennas. In this chapter millimetre-wave waveguides and antennas are briefly reviewed.

2.1 Millimetre-wave waveguides

A rectangular metal waveguide can be used in the whole millimetre-wave frequency band, whereas the regular coaxial lines are available only up to 60 GHz. One problem of these regular waveguides is the difficulty in integration, and the other is the metallic losses. In the lower end of the millimetre-wave band, microstrip lines or finlines are often used in integrated circuits. Other waveguide types suitable for millimetre wavelengths are, e.g., coplanar waveguides, dielectric waveguides and the combinations of microstrip and rectangular metallic waveguides.

The conducting losses of a rectangular metal waveguide for the fundamental TE_{10} mode can be calculated with the following formula [11]

$$\alpha_{cTE10} = \frac{R_s}{\eta\sqrt{1-(\lambda/2a)^2}}\left(\frac{1}{b}+\frac{\lambda^2}{2a^3}\right), \tag{2.2}$$

where a is the waveguide cross-section length in x-axis, b the length in y-axis, $R_s = \sqrt{\pi \cdot f \cdot \mu / \sigma}$ is the surface resistance (μ is the permeability, δ is the conductivity) and η = 376,7 Ω the free space wave impedance. It can be seen that in theory the losses per wavelength increase with the frequency with the factor of $f^{3/2}$, if the dimensions decrease inversely proportionally to the frequency. In practise the losses are higher due to the surface roughness that becomes more and more significant at millimetre wavelengths.

In millimetre-wave frequencies rectangular waveguiding structures are more attractive than circular structures because of their better compatibility with integrated circuits and easier manufacturing processes. The ground metal plane in the image and insulated image waveguide makes them also easily applicable in active circuits. One interesting waveguiding structure is also a non-radiative waveguide (dielectric waveguide between two metal plates) [12]. Figure 2.1 presents the main types of rectangular dielectric waveguides. The insulated image waveguide differs from the image waveguide by an additional layer with the permittivity less than that of the top dielectric. This helps to reduce the metal losses in the ground plane.

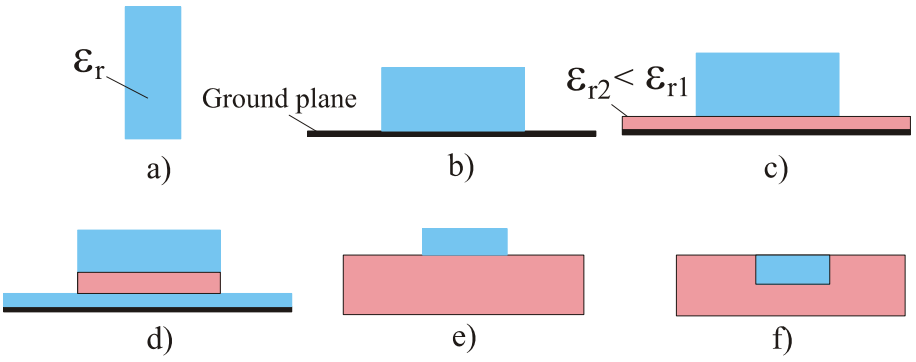

Figure 2.1. Main types of rectangular dielectric waveguiding structures: a) dielectric rod waveguide, b) image waveguide, c) insulated image waveguide, d) layered ribbon waveguide, e) and f) possible other solutions.

2.2 Antennas with high directivity

In quasi-optical systems the power propagates ideally in the form of a Gaussian beam. For example a corrugated horn antenna is a good source for a Gaussian beam and 98% of the radiated power is at the basic waveform of the Gaussian beam [11]. Another suitable horn antenna for launching the Gaussian beam is Potter's horn, but also diagonal horns, conical horns and pyramidal horns are used for this purpose. Also a dielectric rod antenna and a corner cube antenna are good Gaussian beam launchers. Figure 2.2 presents examples of corrugated horn and Potter's horn antennas.

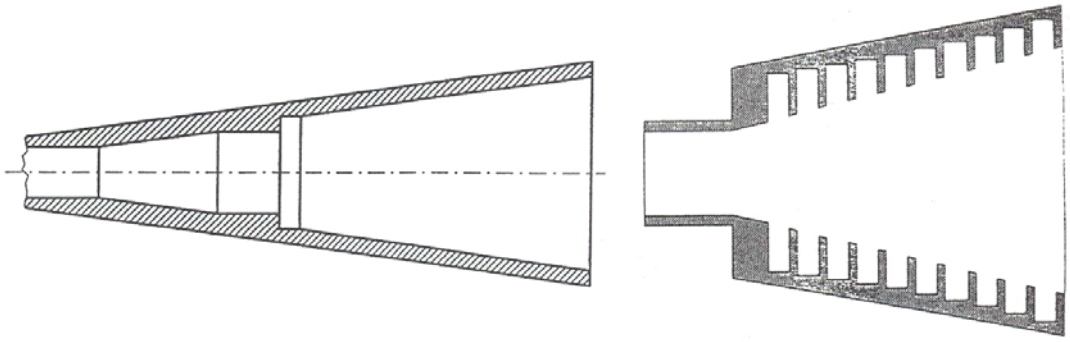

Figure 2.2. Potter's horn (left), corrugated horn antenna (right) [11],[13].

In many millimetre-wave applications high directivity is desired and that can be achieved with reflectors. Reflector antennas are normally fed from the primary focus, or they are of Cassegrain type fed from the secondary focus via a subreflector. A reflector antenna may be also off-set fed either from the primary or secondary focus. These basic types are presented in Figure 2.3.

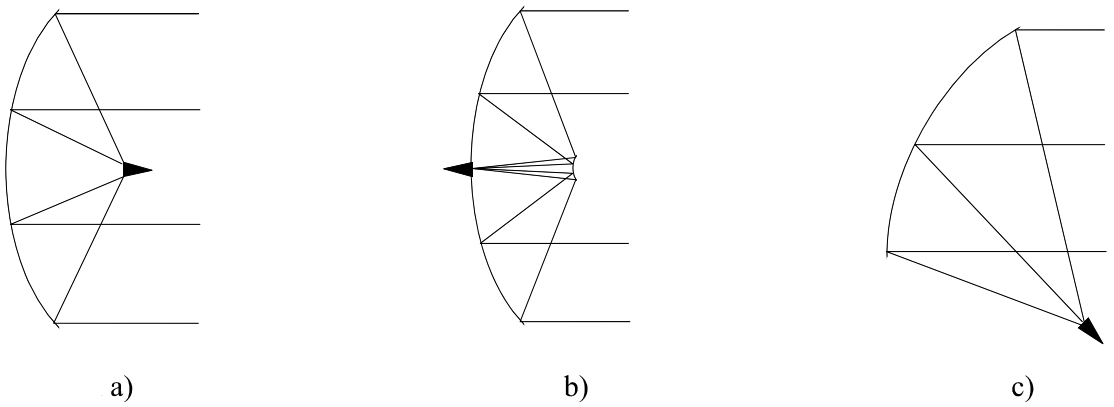

Figure 2.3. Basic reflector antenna types: a) feed in the primary focus, b) Cassegrain-antenna, c) off-set fed.

Also a lens antenna can be used instead of a reflector antenna. A lens antenna is a phase shifter that transforms a spherical phase front to a planar phase front. A simple convex lens is presented in Figure 2.4 (a). Lenses are often used in quasi-optical systems to match the beams or to correct the phase errors of horn antennas. Lens antennas are not as popular in the microwave range as they are in the millimetre-wave range, because the weight of the antenna increases with the wavelength. A wave can be focused also with a Fresnel zone plate (Figure 2.4 (b)). The plate consists of Fresnel's zones that are situated on the plate depending on the desired focal point and the wavelength that is used. There is a phase difference of 180˚ between the zones and it is corrected by making every second zone thinner. Compared to a normal lens such a plate is light-weight, but is has a rather poor aperture efficiency [11],[13].

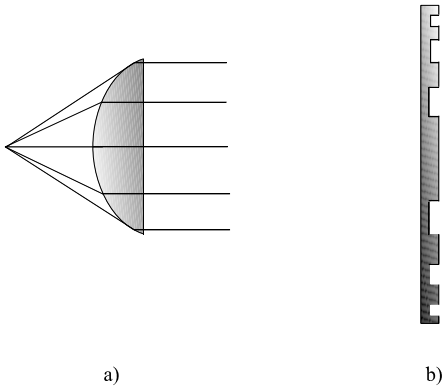

Figure 2.4. a) Lens antenna, b) Fresnel zone plate.

One antenna type that can be used up to 100 GHz is the leaky-waveguide antenna. A hole in the waveguide radiates if it interferes the surface currents. A linear array can be formed by adding several holes one wavelength apart. A planar array can be made by combining several parallel leaky waveguides. Such antennas have good efficiency, but they are expensive to manufacture.

2.3 Integrated millimetre-wave antennas

The heart of an integrated THz receiver is an antenna and a matching network between the mixer and the antenna. The coupling loss between the antenna and the incoming radiation is the first loss encountered in the receiver and it contributes directly to the noise figure. Integrated millimetre-wave antennas are usually physically small and have a small effective aperture for collecting the incoming radiation. Earlier one limitation for millimetre-wave receivers was the unavailability of planar detectors compatible with the integrated antennas. Advances in planar Schottky diodes and SIS detector technologies had a significant effect to overcome these problems. Also antenna-coupled microbolometers have provided good results in non-coherent receivers in cooled passive submillimetre-wave imaging systems [14].

Microstrip patch antennas are very popular in the microwave range and they can be used also in the millimetre wave region up to 100 GHz. The ohmic losses become large above 100 GHz. The benefits of the patch antennas are the planar structure, small manufacturing costs and integrability. The weaknesses of microstrip antennas are the bad efficiency and a narrow bandwidth. Also the feeding network becomes complex in large antenna arrays and that increases the losses. In the millimetre-wave range the manufacturing tolerances become a limiting factor, because the feeding strips are normally only 0.1 to 0.2 mm wide.

Other antenna types in millimetre-wave range that also have good integrability are dipole and slot antennas and broadband bowtie, spiral and log-periodic antennas. These last three types are presented in Figure 2.5. Such antennas can be very wideband, but often they suffer from low radiation efficiency. End-fire and etched monolithic horn antennas are also used in integrated systems. For example a mixer diode and the matching circuit can be integrated with these almost planar antennas. Such integrated SIS- and Schottky-mixer front-ends are used up to 800 GHz [11].

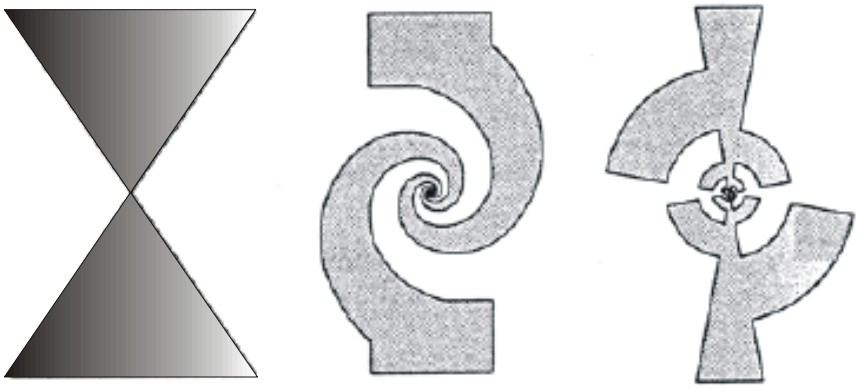

Figure 2.5. a) Bowtie antenna, b) spiral antenna, c) log-periodic antenna.

Elementary antennas, such as electrically short dipoles and small loops, on dielectric substrates suffer from power loss to substrate modes. As the thickness of the substrate increases these elementary antennas couple power to substrate modes, in some cases

more than 90%. This translates into a requirement of impractically thin substrates for low loss dipole antennas at millimetre wavelengths. The substrate thickness should be less than 0.01 λ_0 for a dipole antenna and less than 0.04 λ_0 for a slot antenna. However, the slot antennas are relatively insensitive for substrate thickness compared to the dipole antennas and several millimetre-wave receivers using a slot antenna have been designed, e.g., on GaAs substrate [15]. If the substrate is infinitely thick, no surface waves are created. Then the radiation is concentrated towards the dielectric. The relation between the radiation towards the air and towards the dielectric is $\varepsilon_r^{3/2}$ [11]. A dielectric lens in the hemispherical form is equivalent to the infinite substrate.

Recently such integrated lens antennas have gathered a lot of interest to be used at submillimetre and terahertz frequencies. In regular configuration, a feed antenna is placed directly next to the lens or very close to it with a matching layer, as in the antenna configuration in Figure 2.6. The most common lens types are elliptical and extended hemispherical lenses.

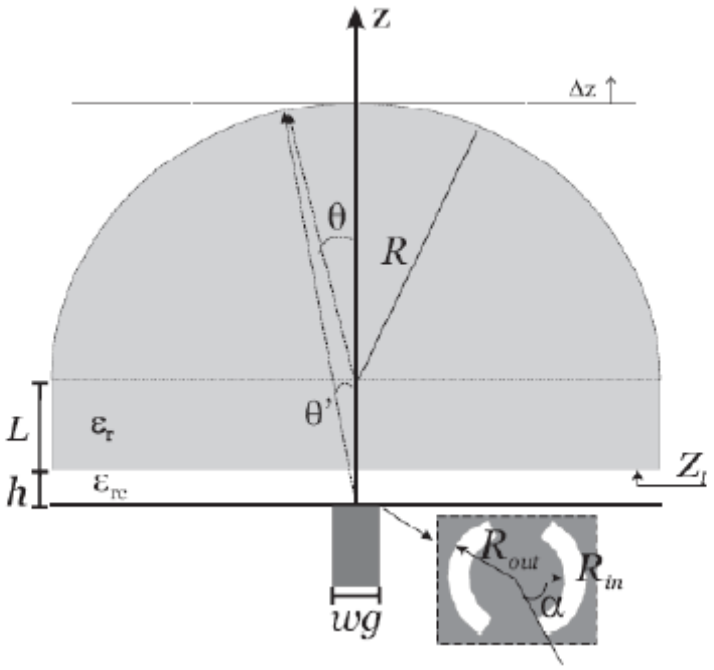

Figure 2.6. Extended hemispherical lens antenna excited with leaky wave waveguide feed [16].

Dielectric resonator antennas (DRA) have also gathered a lot of interest and this type of antennas are also a good alternative for millimetre wavelengths. DRA antennas were first proposed in [17] and analysed, e.g., in [18]. The radiation efficiency in such dielectric resonator antennas is usually very good due to low losses. Choosing a high permittivity material also the size of the antenna can be significantly reduced, although the lower permittivity materials offer better operating bandwidths [19].

Dielectric rod waveguide antennas are an interesting alternative to be used in millimetre wavelengths. As they are travelling-wave type of antennas, they offer a wide operating frequency band and especially in rectangular form also a good integrability. There are a lot of studies made about them by numerous authors and many articles are published about dielectric rod waveguides [20]-[32]. In Chapter 3 DRW antennas are presented in more detail.

3 DIELECTRIC ROD WAVEGUIDE ANTENNAS

Dielectric rod waveguide antennas have been studied for a long time, already since the World War II. They are also an interesting alternative for future Ultra Wide Band (UWB) applications operating in the microwave region. Such an antenna has been developed for example for antipersonnel mine detection [21]. Dielectric rod waveguides (DRW) have lower losses, wider tolerances and lower costs than standard metal waveguides in the millimetre wave region. As the dielectric material can be any semi-insulating semiconductor, different semiconductor devices can be designed directly in the waveguide by means of ion implantation and multilayer epitaxy. DRWs are light-weight and they have also a much broader operating frequency bandwidth. The discovery of millimetre-wave dielectric integrated circuits and communications systems has generated an interest in developing also antennas from dielectric materials and that way make the integration to the rest of the system easier [22]. Such antennas are interesting as they can provide a good performance combined with cost efficiency.

One great benefit of the dielectric rod waveguide antennas is that they can be designed to have radiation patterns that change only little over a large frequency band. Another interesting feature of DRW antennas is that they can have a flat region in radiation pattern around the boresight. DRWs, especially with rectangular cross-section, also offer interesting possibilities to use them in integrated circuits. In a simple antenna a dielectric rod is placed at the end of the waveguide and the electromagnetic power fed to the waveguide is transferred to the dielectric and finally radiated to free space [23],[24].

Earlier, materials with a low dielectric constant were widely and successfully used as antennas. However, the excitation of such dielectric rods is problematic as the propagating electromagnetic field is mostly outside of the rod. For this reason, often a horn-like structure was used in the transition with a tapering section in the rod to improve matching. This problem can be overcome by using materials with relatively

high permittivity, $\varepsilon_r \approx$ 10-15. The EM power is more concentrated to the rod and the unwanted radiation at the feed end is reduced, even without a horn structure, and there will be more power available in a controlled distribution. The dimensions of materials with high dielectric permittivity can also be made very small without losing waveguiding properties [25]. In [26] a dielectric rod antenna for 600 GHz for an imaging system has been fabricated from MgO by laser ablation.

3.1 Propagation and radiation in dielectric rods

The dielectric waveguide is an open transmission line, therefore the field distribution both inside and outside the dielectric core has to be considered. For a circular cross-section waveguide the field solution can be found relatively easily in terms of Bessel functions, but for a rectangular cross-section, which is often more practical, no closed-form solution exists [27]. Many numerical methods have been developed for the complex electromagnetic problems such as the finite element method, the finite difference method, and the moment method. However, the main disadvantages of these numerical methods are the required, usually heavy, computation resources and the impossibility for an analytical analysis of the solution. Especially in a case of a rectangular dielectric waveguide it is difficult to obtain accurate results [27],[28].

3.1.1 Propagation in rectangular dielectric waveguides

In a standard rectangular or circular metal waveguides the field solution can be found in terms of TE and TM modes. However, in the case of an open rectangular dielectric waveguide, these solutions become impossible. In general, the boundary conditions couple the electric and magnetic fields and the solutions are referred to as hybrid modes. The propagating modes are often denoted as E^x_{mn} or E^y_{mn} depending on which direction the strongest electrical field is pointing. Indices *m* and *n* denote how many extremes the distribution has in the horizontal (*x*) and vertical (*y*) directions respectively [27]. If two different polarizations can propagate, it means also a possibility to transform from one polarization to another. Additionally, the propagation in dielectric waveguides is

dispersive in its nature. This means that waves with different frequencies propagate with different velocities. An example of the cross-sectional field distribution, for mode E_{12}^{y}, in a dielectric waveguide with a rectangular cross-section is shown in Figure 3.1.

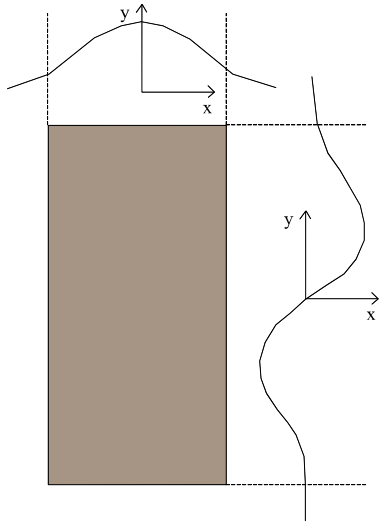

Figure 3.1. Field distribution H_x of propagating mode E_{12}^{y} in the rectangular dielectric rod waveguide.

One simple numerical method that can be applied also for rectangular dielectric waveguides is called Marcatili's method [29]. In this method, the cross-section area and its perpendicular surroundings are divided into five regions with homogeneous but possibly different refractive indices (Figure 3.2). The fields in the shadowed region are not considered, as they are much less important for the waveguide properties than the other regions.

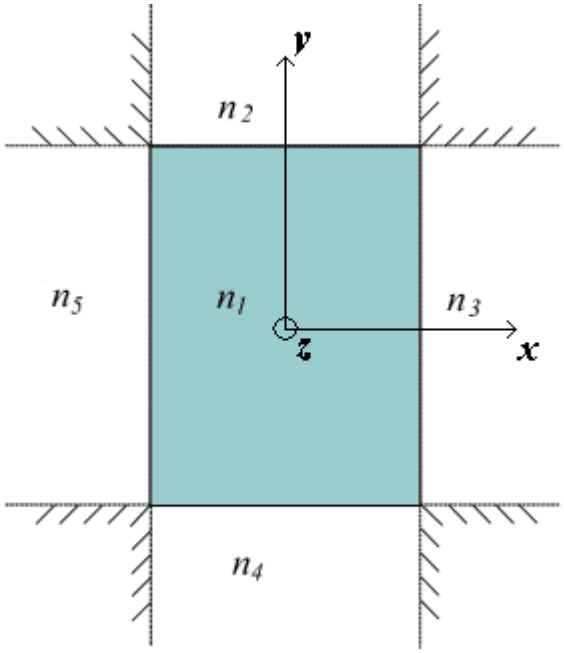

Figure 3.2. The geometry of a rectangular dielectric waveguide in Marcatili's method.

The fields are assumed to be approximately sinusoidally distributed inside the waveguide and exponentially decaying outside regions. For example the field component H_x can be expressed in the following way [27]:

$$H_{xv} = \exp(-jk_z z + j\omega t)\begin{cases} M_1 \cos(k_x x + \alpha)\cos(k_y y + \beta) \\ M_2 \cos(k_x x + \alpha)\exp(-k_{y2} y) \\ M_3 \cos(k_y y + \beta)\exp(-k_{x3} x) \\ M_4 \cos(k_x x + \alpha)\exp(k_{y4} y) \\ M_5 \cos(k_y y + \beta)\exp(-k_{x5} x) \end{cases} \quad (3.1)$$

for each region v=1-5, respectively. $M_{1\ldots5}$ are unknown amplitude coefficients, k_x and k_y are the propagation constants in the waveguide in the horizontal and vertical directions, k_{x3} and k_{y2} are the decay factors in the outer regions, and α and β are additional phase constants. In the symmetric system, the field distributions are given by cosine or sine functions with a null or a maximum at the rod centre, and in this case phase constants α and β equal either 0 or $\pm\pi/2$. The other field components are written as

$$H_{y\upsilon} = 0 \tag{3.2}$$

$$H_{z\upsilon} = -\frac{j}{k_z}\frac{\partial H_{x\upsilon}}{\partial x} \tag{3.3}$$

$$E_{x\upsilon} = -\frac{1}{\omega\varepsilon_0 n_\upsilon^2 k_z}\frac{\partial^2 H_{x\upsilon}}{\partial x \partial y} \tag{3.4}$$

$$E_{y\upsilon} = \frac{k_0^2 n_\upsilon^2 - k_{y\upsilon}^2}{\omega\varepsilon_0 n_\upsilon^2 k_z} H_{x\upsilon} \tag{3.5}$$

$$E_{z\upsilon} = \frac{j}{\omega\varepsilon_0 n_\upsilon^2}\frac{\partial H_{x\upsilon}}{\partial y} \tag{3.6}$$

where k_0 is the wave number in vacuum.

Figures 3.3 and 3.4 present the typical propagation and loss characteristics of rectangular dielectric waveguides [27]. It can be observed that the dielectric waveguide has two fundamental modes without a cut-off frequency. In Figure 3.4 figure α_{p0} is the propagation loss of a plane wave in the infinite medium filled with the same material as the dielectric waveguide core. It can be seen that at very high frequencies the loss factor gets very close to α_{p0}, because of the strong field concentration in the rod. At low frequencies the fields are only little concentrated in the rod and that makes also the losses small.

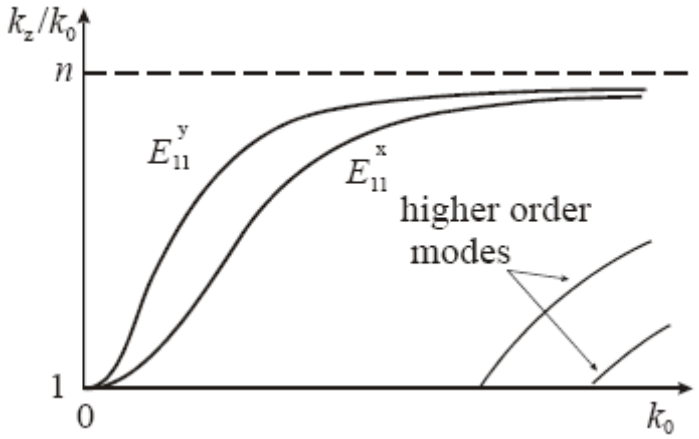

Figure 3.3. Typical dependence of propagating modes on the propagation factor k_z/k_0.

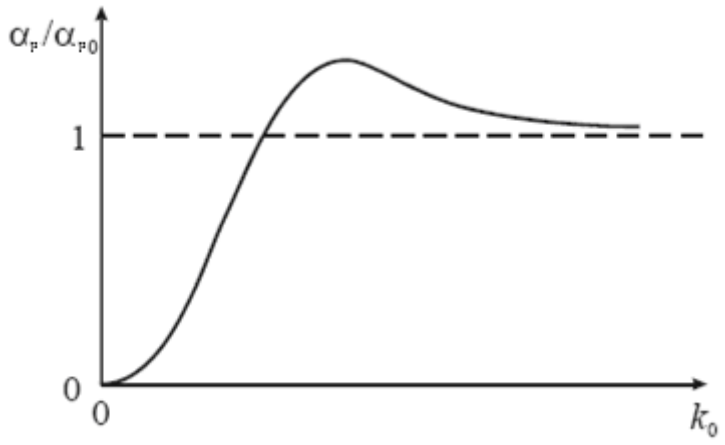

Figure 3.4. Loss factor α/α_0 for the fundamental mode as a function of the wave number in vacuum k_0 .

As was mentioned, Marcatili's method is a very simplified way to analyze the fields and some other methods are also proposed by several authors. In [30] Goell presented a more accurate numerical method almost at the same time as Marcatili. In [31] Marcatili's method was modified to be applicable also for uniaxial anisotropic crystals. Anisotropy in this case means that the dielectric permittivity has different values depending on the direction the material is observed. Such a method was very much needed as many high-quality dielectric materials available for fabrication of millimetre wave waveguides are uniaxial anisotropic crystals, like sapphire.

3.1.2 Radiation

The most used dielectric waveguide antennas are travelling-wave antennas. They can be further divided in two distinct classes: surface wave and leaky-wave antennas [22]. These basic antenna types are presented in Figure 3.5.

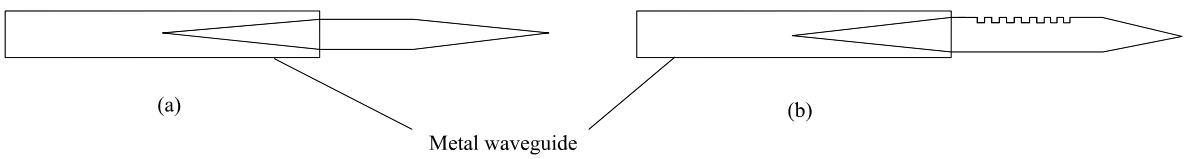

Figure 3.5. Surface-wave antenna (a), leaky-wave antenna (b).

Surface-wave antennas have a smooth dielectric surface. In general, the radiation from such a structure takes place primarily from the feed region and the rod termination. A longitudinal taper in the rod improves the radiation characteristics and it causes the radiation to occur from the entire length of the taper. The gain of the antenna increases with the taper length, but often at the expense of higher side lobes.

A leaky-wave antenna contains periodic discontinuities in the rod and it produces a relatively narrow and frequency-scannable beam. This means that the angular direction of the beam is a function of frequency. If the radiation in the end-fire direction is wanted to be as small as possible, the radiation taper should not be used at all. However, leaky-wave antennas are less practical to manufacture as the frequency increases, because the dimensions become smaller and smaller [22].

In general, radiation from dielectric rod antennas occurs only at discontinuities. Such discontinuities can be at the feed, at the termination of the rod and along any taper in the rod. A rod without a taper radiates only from the feed and terminal ends. Typically, this type of antenna is characterised by high side lobes and low gain [23],[32]. To improve the matching from the metal waveguide to the dielectric different kinds of tapering sections of the dielectric in the feed end can be designed.

By applying Snell's law at the interface between the dielectric rod and air, the radiating parts of the rod can be found theoretically. Snell's law at the interface can be written in the following form:

$$\frac{\sin\theta_2}{\sin\theta_1} = \sqrt{\frac{\varepsilon_{r1}}{\varepsilon_{r2}}}, \tag{3.7}$$

where θ_1 is the angle of the incoming ray in respect to the normal of the interface and θ_2 the angle of the transmitted ray. In the case when the rod is made of gallium arsenide (ε_r = 13), the critical incoming angle that still keeps the wave inside the rod is 16.1˚. This angle increases as the permittivity of a rod material gets smaller, thus making more power radiating along the rod. In Figure 3.6 a simplified ray model of a rectangular dielectric rod with and without taper sections is presented. The benefits of the taper to reduce the radiation along the rod and the reflections from the terminal end can be seen.

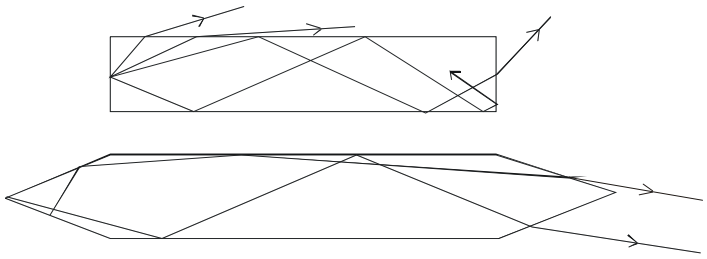

Figure 3.6. Simplified ray-model of the dielectric rods showing the effect of a taper.

It is clear that a significant reduction of reflection loss can be achieved by tapering the rod, and according to several articles a very good matching can be achieved with different tapering methods. Dielectrics of low permittivity are more difficult to match and their matching can be improved with horn structures [33],[34]. By tapering also the terminal end of the rod reflections are significantly decreased and also radiation characteristics can be modified. One very interesting property of the DRW antennas that is achieved by tapering the radiating part is that the beamwidth remains the same for a large bandwidth [24]. Low sidelobe level is a feature of a relatively short tapered rod. If the radiation taper length of the antenna is increased the gain will increase, but also the sidelobe level will often increase [34].

It has been shown that rectangular dielectric waveguides with high dielectric constant ($\varepsilon_r > 9$) can be well matched with a standard metal waveguide to achieve losses less than 0.1 dB per transition without any horn structure at the feed [35],[36].

3.2 Excitation methods of DRW antennas

An important consideration in the design of dielectric rod antennas is the efficient excitation. High excitation efficiency enables high gain and broadband operation [37]. Several excitation methods have been proposed during the years, e.g., dipoles, slots and waveguides have been proposed [38]-[40]. One interesting excitation method is to use a magnetic ring current source outside the dielectric rod [41]. Recently this idea was developed further and the ring was located inside the rod exciting the HE_{11} mode in the cylindrical rod [42].

3.3 Losses of DRWs

If a dielectric material has the loss tangent of about 10^{-4} and a relative permittivity of 10-15, the waveguide losses can be expected to be in the order 5 dB/m at 150 GHz. At this frequency attenuation of 10-12 dB/m is typical for the standard metal waveguide. There are some differences in reported values, because all the parameters depend on the material growth conditions and methods.

Diamond is well known for its negligible absorption value from microwave to infrared region. For example single crystal silicon has a crystal structure similar to diamond. This means that lattice vibration arises only at mid-infrared region. The only other absorption process in the terahertz range is the free carrier absorption. One traditional way to improve the dielectric properties of silicon is to compensate the conductivity by doping of acceptors. The free carrier concentration in any semiconductors can be avoided either by making the material extremely pure or including holes during the manufacture. The resistivity increases in both cases and thus it can be concluded that the higher the resistivity, the lower is the absorption loss in millimetre wavelength region [43],[44]. Table 3.1 presents the permittivity and loss tangent values of some dielectrics.

Table 3.1. Parameters of some dielectrics [13],[25].

Materials	Permittivity (ε_r), f=10 GHz	Permittivity (ε_r), f=140 GHz	tan δ, f=140 GHz
Si (doped)	11.9	11.6-11.8	$>0.03 \cdot 10^{-4}$
GaAs	13.0	10.9-13.03	$3 \cdot 10^{-4}$
Sapphire	$\varepsilon_{r,\rho}$=9.39 $\varepsilon_{r,z}$=11.56	$\varepsilon_{r,\rho}$=9.39 $\varepsilon_{r,z}$=11.56	$1.1\text{-}2.1 \cdot 10^{-4}$
Fused quartz	3.8	~3.8	$\sim 1 \cdot 10^{-4}$
Teflon	2.06	1.96-2.0	$3\text{-}4 \cdot 10^{-4}$
Al_2O_3	9.7	10.5	$2.7\text{-}3.2 \cdot 10^{-4}$

3.4 Tapers of the dielectric rods

Many different types of matching and radiating tapers can be imagined and designed for DRWs. Often the limiting factor is the manufacturing process and the fragility of the dielectric material. Some of the possible taper geometries are presented in Figure 3.7. A rod which has a pyramidal taper (tapered both in the E and H plane) is difficult to machine and it is also mechanically weak. These problems are exacerbated when the frequency increases and the antenna dimensions get smaller. Experimentally it has been found that the antenna characteristics of a rod tapered only in the E plane are not degraded compared to a pyramidal taper. Sometimes characteristics are even improved [34]. Rods tapered only in the H plane are never as good as those tapered in both planes [23].

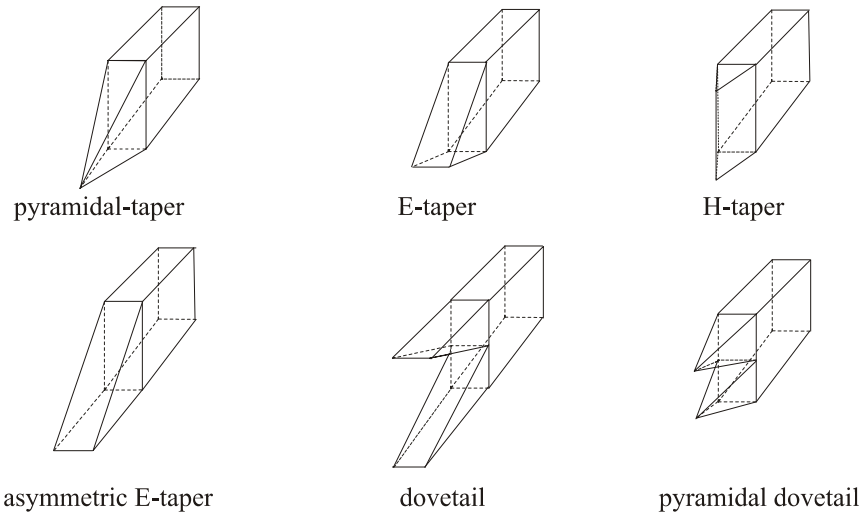

Figure 3.7. Different taper geometries.

The benefit of the dovetail tapers is the better broadband characteristics, but their manufacturing is complicated [45].

As said, one important feature of the taper is the possibility to modify the radiation pattern with the taper design. F. J. Zucker developed design principles to obtain maximum gain for dielectric rod antennas [20], and they were also implemented with DRW antennas with rectangular cross-section. However, these design principles often lead to very thin structures and, thus, they are often not practical at short wavelengths.

It has been shown that for a material with $\varepsilon_r = 2.33$ and with an E-plane taper that the longer taper section increases the gain and the main beam becomes narrower. Eventually as the length is increased more, distortion of the main beam occurs, which results in high sidelobes [34].

3.5 Phase centre of a dielectric rod antenna

Phase centre is an important parameter in many antenna applications. It is defined to be the reference point which results in the minimum phase difference between the measured wave front and a spherical wave front around the main beam. Its accurate location is needed for example when using antenna as a feed for a reflector antenna. In that case it is important that the phase centre of the feed antenna is located as accurately as possible in the focal point of the reflector [46].

For a DRW antenna the phase centre is determined by a combination of radiations from the metal waveguide end and dielectric rod. In [32] it is estimated that in the ideal case where there are two radiation sources, the phase centre would be about one quarter of the rod length from the terminal end. It is also estimated that the phase centre will move towards the rod termination with increasing dielectric constant of the rod. In [47] and [48] a simple method to measure the phase centre of the rectangular dielectric rod waveguides was developed.

4 DRW ANTENNA DESIGNS AND THEIR SIMULATIONS

In this chapter, the antenna design process for 110-170 GHz and 295-325 GHz frequency bands is presented. Dielectric materials used for antennas are monocrystalline sapphire ($\varepsilon_r\parallel$= 11.56, $\varepsilon_r\perp$ = 9.39, $tan\ \delta \approx 10^{-4}$) cut along the optical axis and silicon (ε_r = 11.9, $tan\ \delta \approx 10^{-4}\ldots10^{-3}$).

4.1 Antenna for 110-170 GHz and its simulations

A standard rectangular metal waveguide (WR-6, cross-sectional area of 1.65 x 0.83 mm^2) is used as a feed element. In the simplest design the dielectric rod is inserted in the middle of the waveguide opening. It is difficult to fix the rod exactly in the middle of the metal waveguide; one possible solution is to use thin porous Teflon films around the rod to fit it between the walls of the metal waveguide. However, this is not a very durable solution for real applications, but it can be used in demonstration prototypes. In Figure 4.1 this solution with a 42-mm silicon antenna connected to a metal waveguide without a flange is presented. The taper length in both ends of the rod is 4 mm.

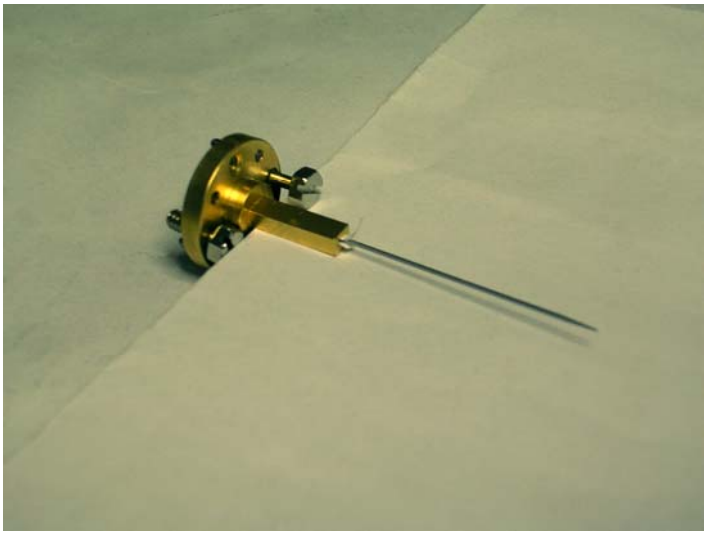

Figure 4.1. Silicon antenna for D band with Teflon film holder.

As two polarizations can propagate in a DRW, there is a possibility of field transformation from one polarization to another, i.e. cross-polarization may occur. One way to decrease this effect is to design the waveguide so that different polarizations have different propagation constants. Choosing a rectangular cross-section other than a square is one possibility to solve this problem. The cross-section area has been chosen from the condition a/b = 0.5, where a is the horizontal length and b the vertical length. Also $k_0 b$ = 1.7-1.9, where $k_0 = 2\pi/\lambda_0$ and λ_0 is the wavelength of the central frequency of the desired frequency band. This condition has been earlier successfully used for ferrite strip waveguides (FSW) in the frequency range of 30-150 GHz [49] and found to be suitable for DRW antennas at W band [24]. From this condition it can be calculated that b=0.58-0.65 mm and a=0.29-0.32 mm when the centre frequency is 140 GHz.

Finite element method (FEM) based Ansoft HFSS^{TM} 9.2 software is used to simulate and study DRW antenna structures. Different simulations are performed to obtain a better comprehension of DRW antennas in 110-170 GHz frequency range. In the first stage rectangular cross-sections of different sizes and different taper lengths are studied to find the optimum dimensions. Simulations with different kinds of radiation tapers are performed to study the effect to the radiation patterns. Finally the effect of the parasitic radiation absorber is studied. Figure 4.2 presents the basic simulation setup (quarter of the structure is needed).

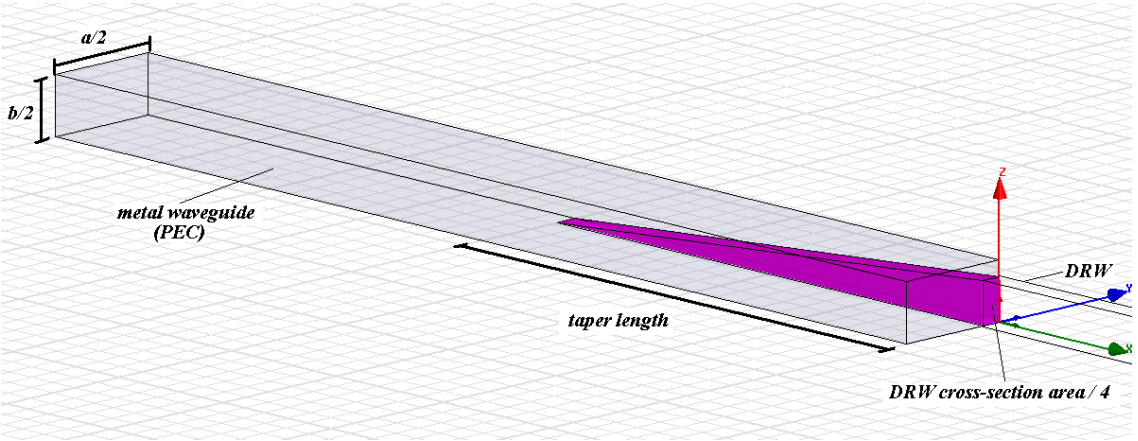

Figure 4.2. Basic simulation setup for metal waveguide – DRW simulations.

4.1.1 Feed taper of the sapphire rod

A transition from a standard rectangular waveguide (1.65 x 0.83 mm^2) to another one through a sapphire rod is simulated with different cross-section dimensions and tapers to find the optimal structure.

As discussed in Section 3.2, an E-plane taper is found to have a very good performance combined with relatively simple manufacturing process. H plane is horizontal plane and E plane the vertical plane. As the dimensions are very small in D band, this work is concentrated only in E-plane tapers.

In the structures that are large compared to the wavelength the electromagnetic simulations require a lot of computational resources. For this reason it is always useful if the simulation time can be reduced. HFSS allows the use of symmetry planes for symmetric structures, which reduces the computation time significantly. As our structure is symmetric in both the E and H planes, it is sufficient to simulate only one quarter of the structure. As in this case the electromagnetic fields propagate partially outside of the rod, there must be enough free space around the rod to get reliable simulation results. It is important also to note that in HFSS this air box and its radiation boundary should be set far enough from the rod. Recommendation in HFSS is that the radiation boundary should be set at least $\lambda/4$ away from any radiation source, otherwise the results will be distorted. Other recommendation is that the radiation boundary should usually also be at a distance greater than the maximum dimension of the source. In practice it has been found that beyond the distance over 3λ (~ 8 mm at 110 GHz) the results do not change anymore in the case of DRW antennas [25]. The simulation setup with symmetry planes is presented in Figure 4.3. The external walls of the airbox are set as radiation boundaries in HFSS. Metal waveguide is simulated as an infinitely thin rectangular box with a perfect electric conductor (PEC) boundary.

It has to be noticed that this simulation setup does not take into account the currents on the metal waveguide external surfaces. These currents would probably cause extra

radiation to the system. However, the accurate modeling of the waveguides would increase significantly the required calculation capacity.

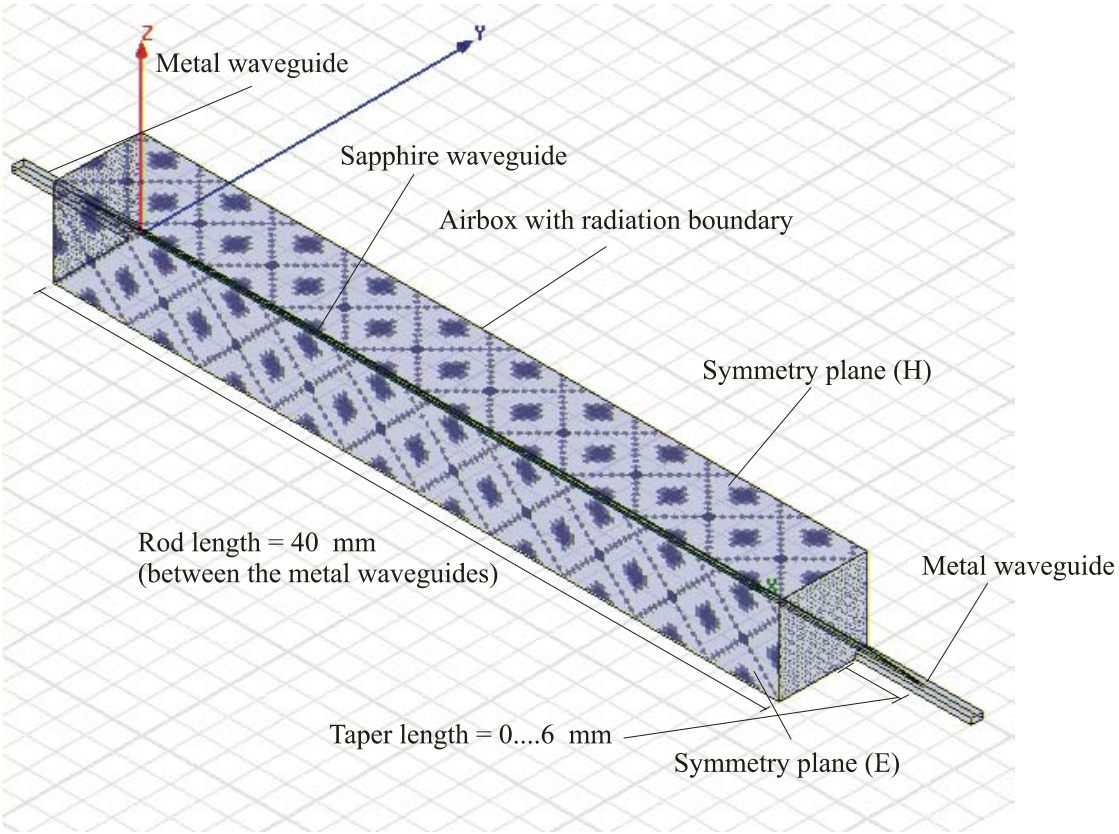

Figure 4.3. Simulation setup for DRW transition in 110-170 GHz.

First different feed taper lengths are studied with an anisotropic sapphire rod with 0.30 x 0.60 mm^2 cross-section. This cross-section is in the middle of the design rules set in [49]. An accurate analysis of the cross-section is presented later in this chapter. Simulations are performed with the taper length from 0 to 6 mm. Anisotropy in this case means that the permittivity of the material depends on the axis. For fused monocrystalline sapphire in the longitudinal axis (x-axis in the simulation) ε_r = 11.56 and for other axis ε_r = 9.39 (y- and z-axis) [35]. Both ends of the rod have the same taper length. The rod length between the metal waveguides is 40 mm. The simulated transmission and reflection coefficients are presented in Figures 4.4 and 4.5.

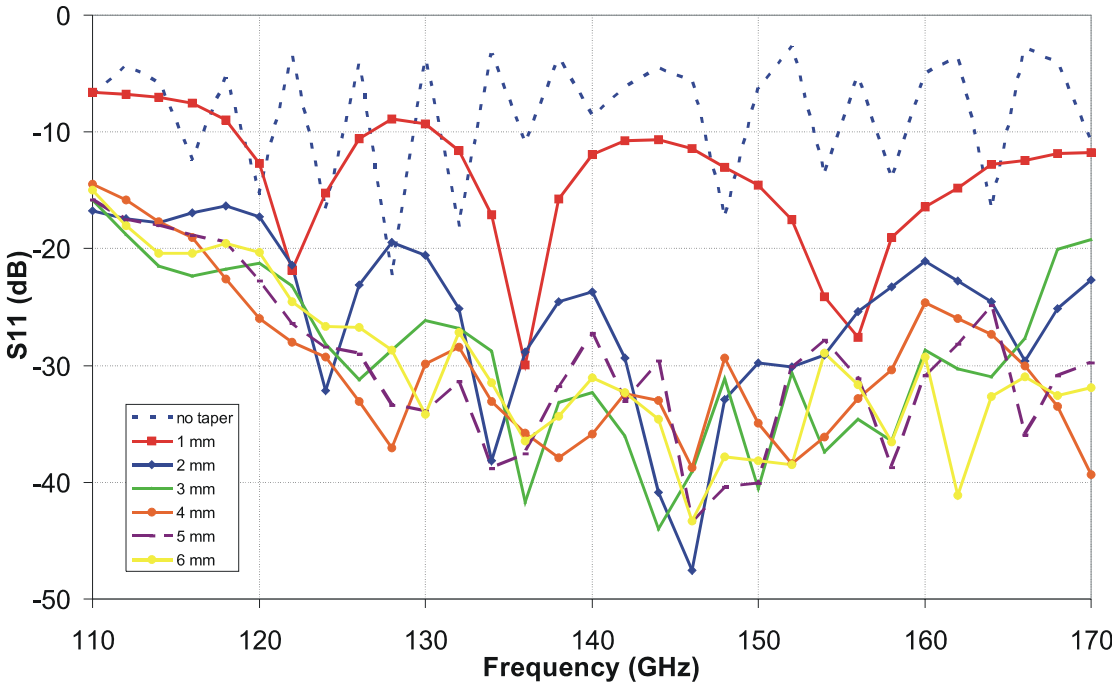

Figure 4.4. Simulated S_{11} with different feed taper length of a sapphire rod.

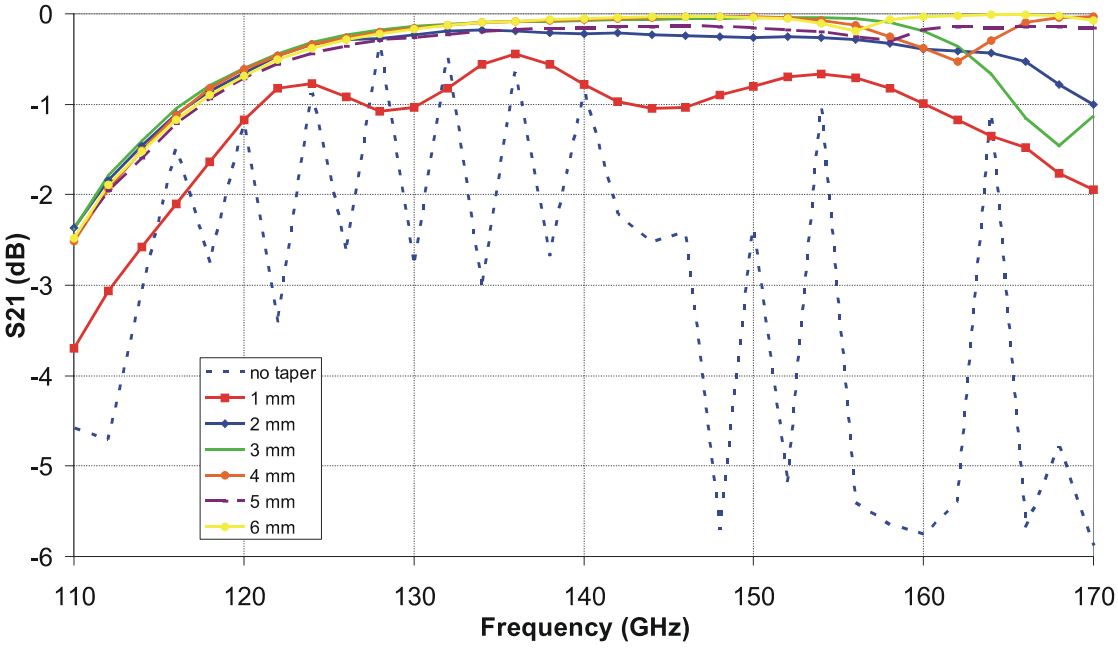

Figure 4.5. Simulated S_{21} with different feed taper length of a sapphire rod.

As expected the benefit of the taper section is clearly seen in both figures when using longer taper section. However, only a slight improvement is seen for tapers longer than 3 mm. The benefit of the longer tapers seems to be the shallower dips in the higher frequency end in S_{21}. A 6-mm taper has already an almost flat S_{21} in the higher frequency range. It can be also seen that in lower frequencies the matching is not very good and even a longer taper does not improve it. One reason might be that the cross-section area of the rod is not optimal for the whole frequency range. This will be studied with simulations in the next section. Figure 4.6 presents the simulated E field in sapphire rod waveguide transition between two metal waveguides at 140 GHz. Taper length in this case is 3 mm. Field propagating partially outside the sapphire rod can be observed.

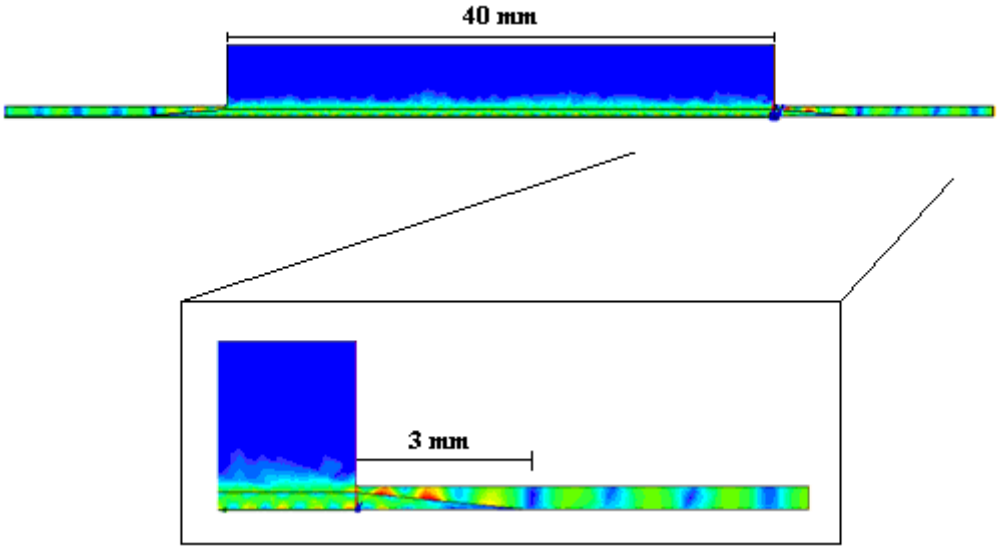

Figure 4.6. Simulated E field in the sapphire rod waveguide transition (quarter in the setup) between two metal waveguides at 140 GHz.

4.1.2 Cross-section of the sapphire rod

In the next stage, propagation characteristics with different cross-section sizes are studied. As calculated earlier the optimum cross-section dimensions are b = 0.58-0.65 mm and a = 0.29-0.32 mm. As the metal waveguide dimensions are 1.65 x 0.83 mm^2, b can not be larger than 0.83 mm. The cross-section size in the simulation is varied from 0.50 x 0.25 mm^2 to 0.82 x 0.41 mm^2. The rod length between the metal waveguides also in this simulation setup is 40 mm. The feed taper is 3 mm in both ends. Simulated reflection and transmission coefficients are presented in Figures 4.7 and 4.8.

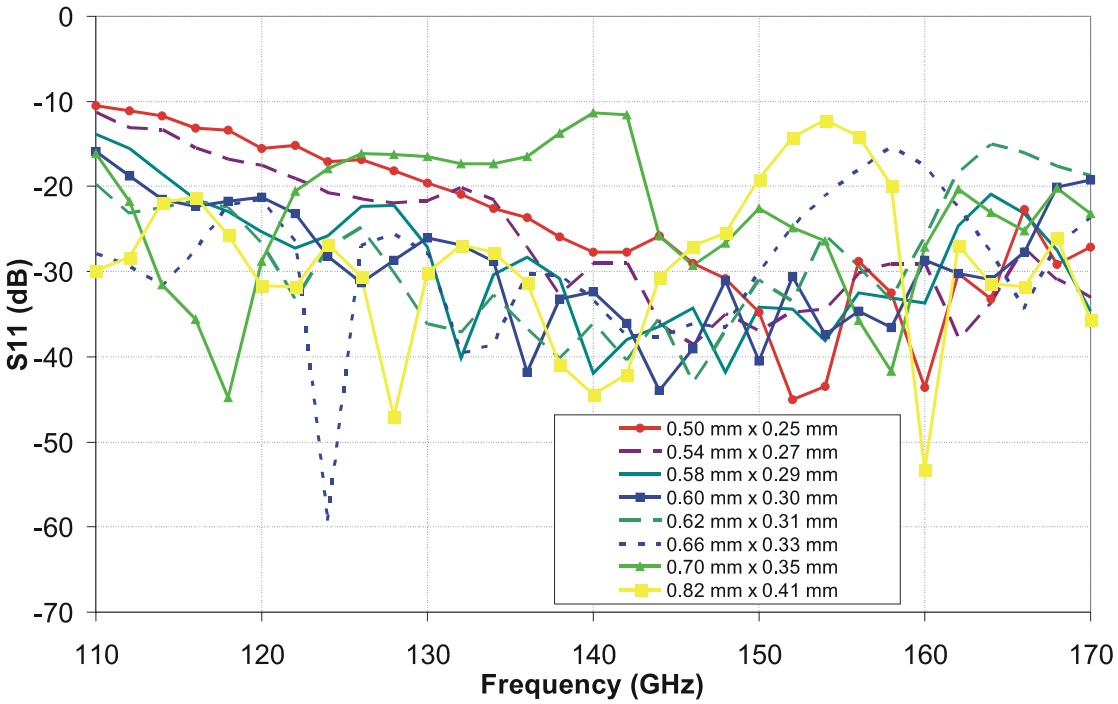

Figure 4.7. Simulated S_{11} for different cross-section sizes of a sapphire rod.

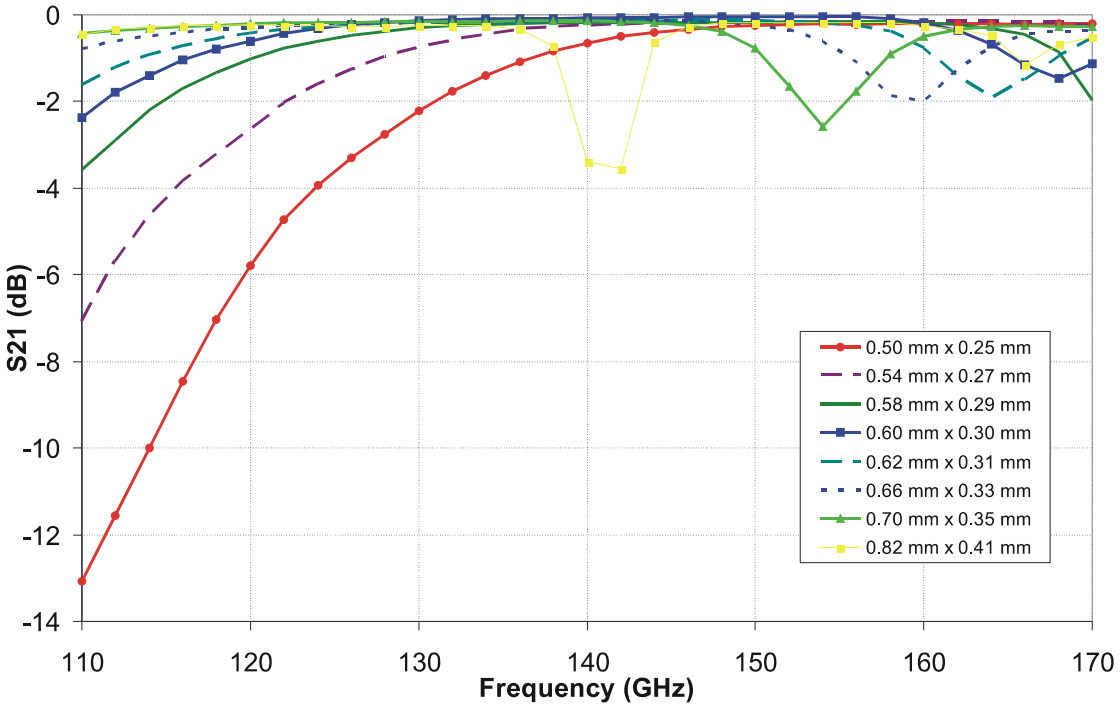

Figure 4.8. Simulated S_{21} for different cross-section sizes of a sapphire rod.

According to the simulation results it is clear that the matching is improved at lower frequencies when the cross-section area is larger. On the other hand matching becomes unstable at higher frequencies as the cross-section area is increased. Dips can be seen in S_{21}. As the height of the rod is increased almost to equal to the height of the metal waveguide the dip becomes deeper and it is also shifted to a lower frequency. Such dips are due to the increased radiation from the feed because of the phase mismatch between the wave inside the taper and the wave in the metal waveguide [25]. Longer tapers would make the dips smaller as it is found out in the taper length simulations. The cross-section of 0.60 x 0.30 mm^2 seems to offer a good compromise with the overall matching over a wide frequency range with a relatively low mismatch at the higher frequency end.

4.1.3 Feed taper and cross-section for the silicon rod

The same simulations have been done also with silicon rods to see if the observed dips depend on the material anisotropy. The results can be seen in Figures 4.9-4.12. As can be seen in the simulations with different taper lengths (Figures 4.9 and 4.10), the matching is better in lower frequencies with silicon rods than with sapphire. In cross-section simulations the dips seem to behave rather similarly also with silicon waveguides, although they are little smaller (from 1 to 2 dB) and they are slightly shifted to lower frequencies (from 2 to 4 GHz). Also in the higher frequency end new and deeper dips can be observed for the largest cross-section areas. Thus the dips can not be avoided either in materials that are not anisotropic.

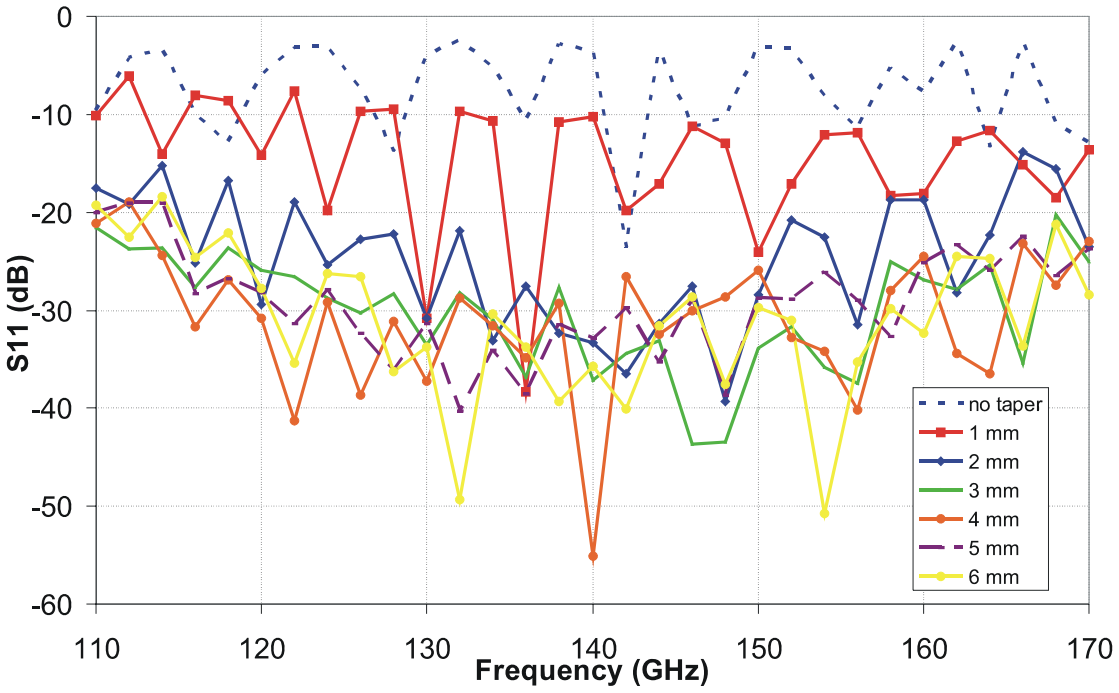

Figure 4.9. Simulated S_{11} for different feed taper length of a silicon rod.

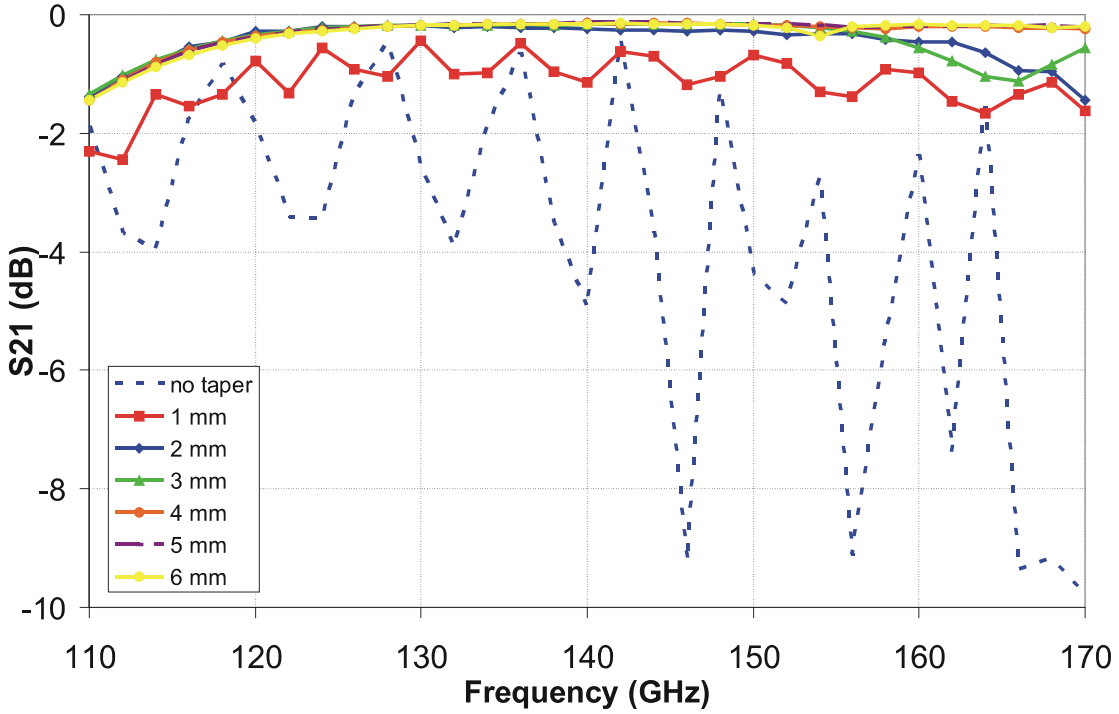

Figure 4.10. Simulated S_{21} for different feed taper length of a silicon rod.

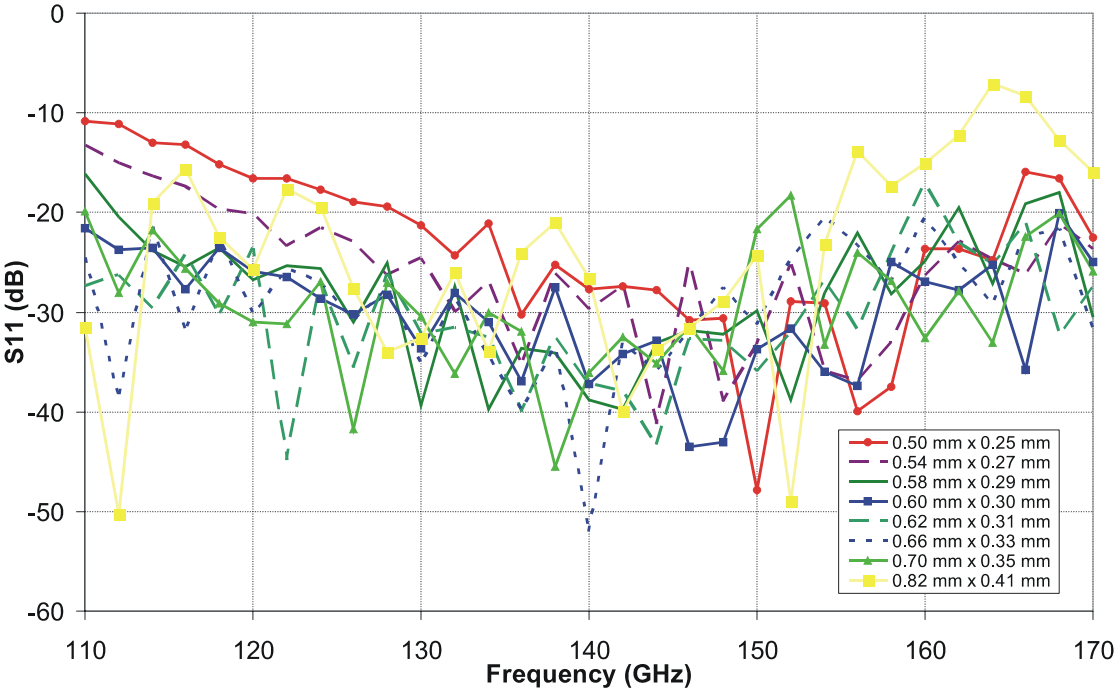

Figure 4.11. Simulated S_{11} for different cross-section size of a silicon rod.

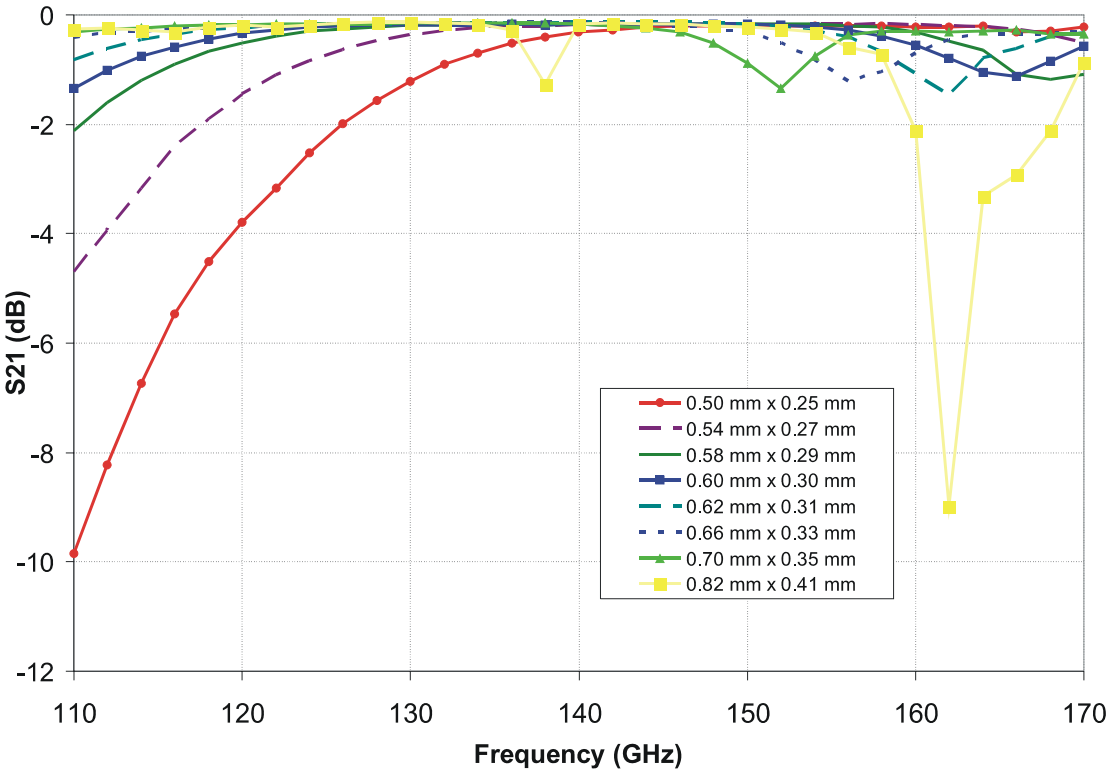

Figure 4.12. Simulated S_{21} for different cross-section size of a silicon rod.

4.1.4 Radiation taper

In this section sapphire rod is studied as an antenna. The other end of the dielectric rod is now left free and by defining the air box as a radiation boundary the radiation characteristics of the DRW antennas can be evaluated. The simulation setup is presented in Figure 4.13.

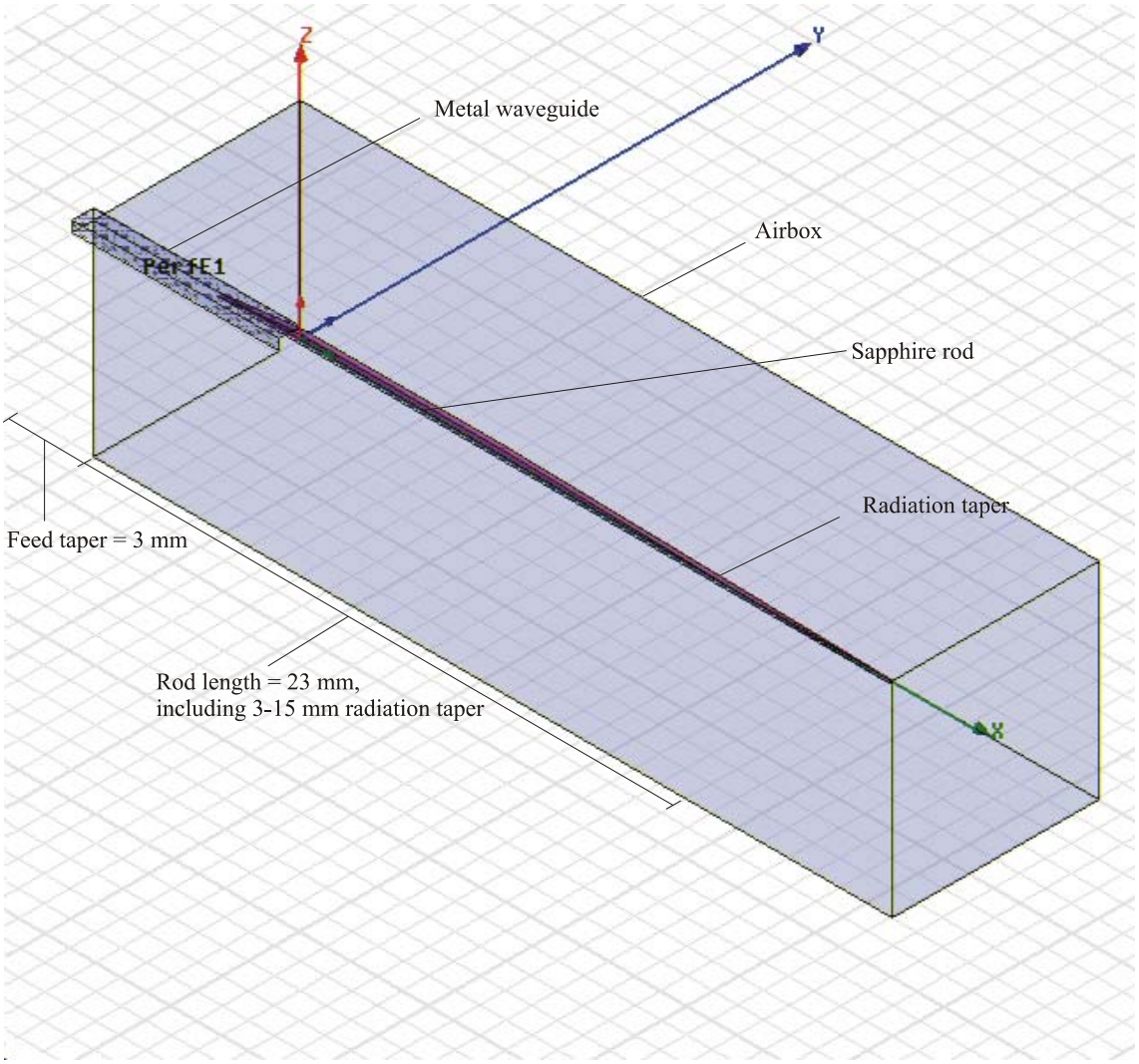

Figure 4.13. Setup for the radiation taper simulations.

Radiation taper length is varied from 3 mm to 15 mm. Total rod length is 26 mm. Simulated S_{11} with five radiation tapers of different length is presented in Figure 4.14. The cross-section area is chosen for 0.30 x 0.60 mm^2 as it was found to be a good compromise in Sections 4.1.2 and 4.1.3.

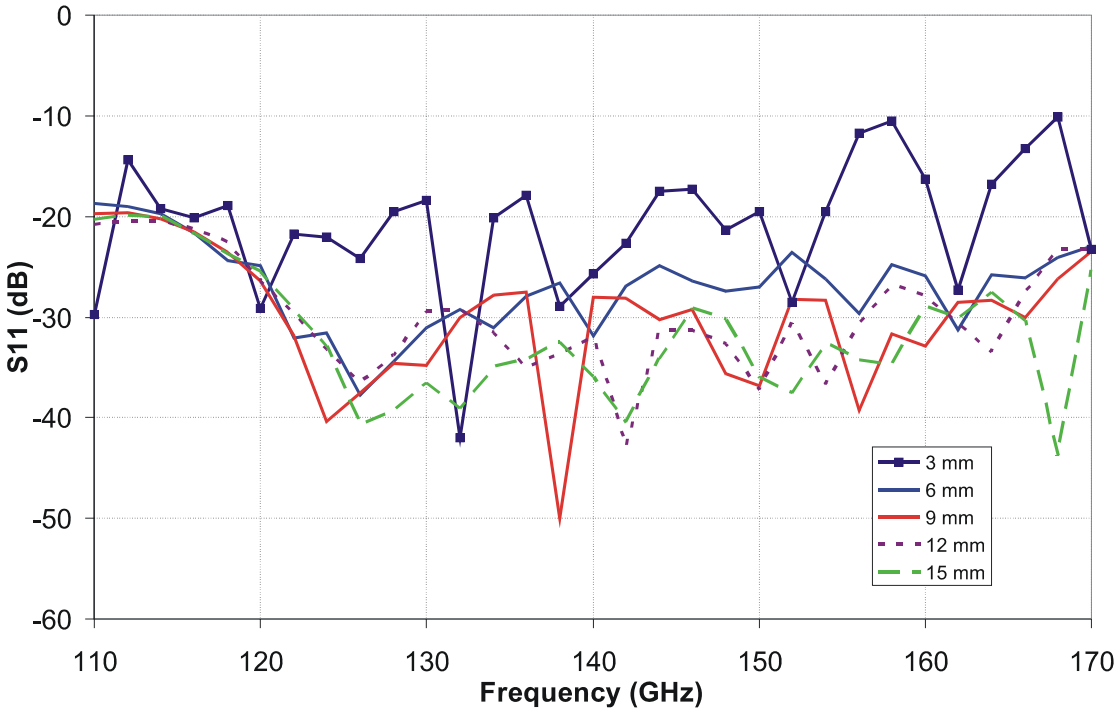

Figure 4.14. Simulated S_{11} of sapphire rod antenna with different radiation taper lengths.

A significant improvement in the reflection level can be seen between the taper lengths of 3 mm and 6 mm. Longer tapers do not improve much S_{11}, but the radiated beam is more directive as expected. This can be seen from the radiation patterns. Simulated H- and E-plane (horizontal and vertical) radiation patterns at 140 GHz can be seen in Figures 4.15 and 4.16. Beamwidths at -10-dB level are listed in Table 4.1.

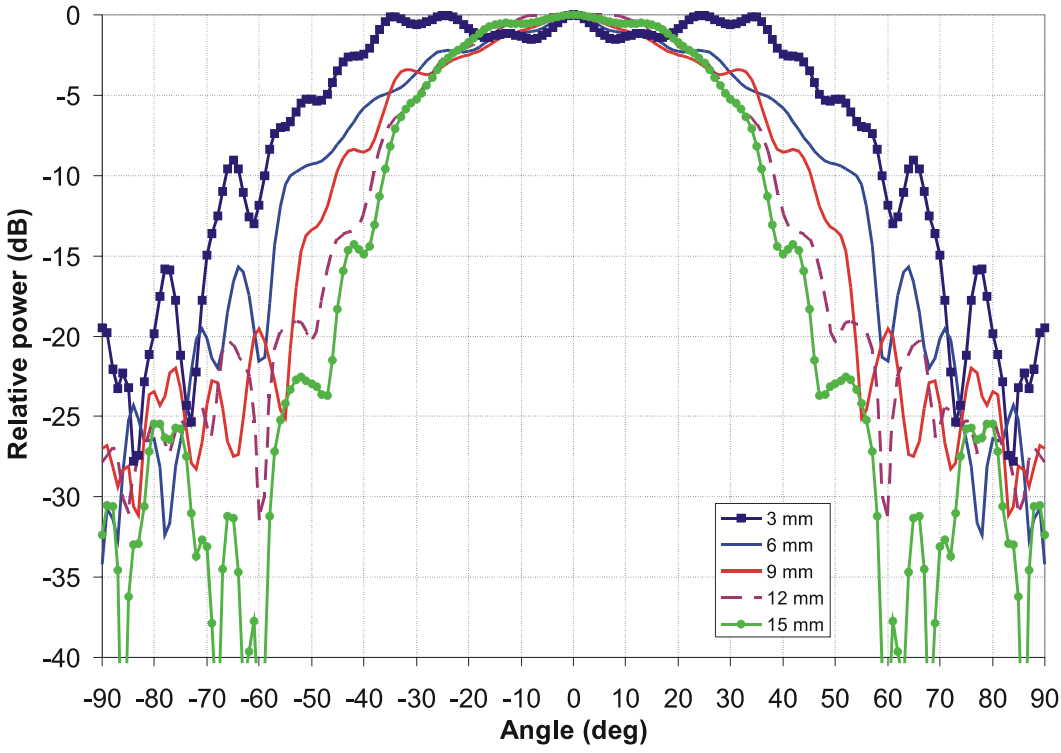

Figure 4.15. Simulated H-plane radiation pattern with different radiation taper length.

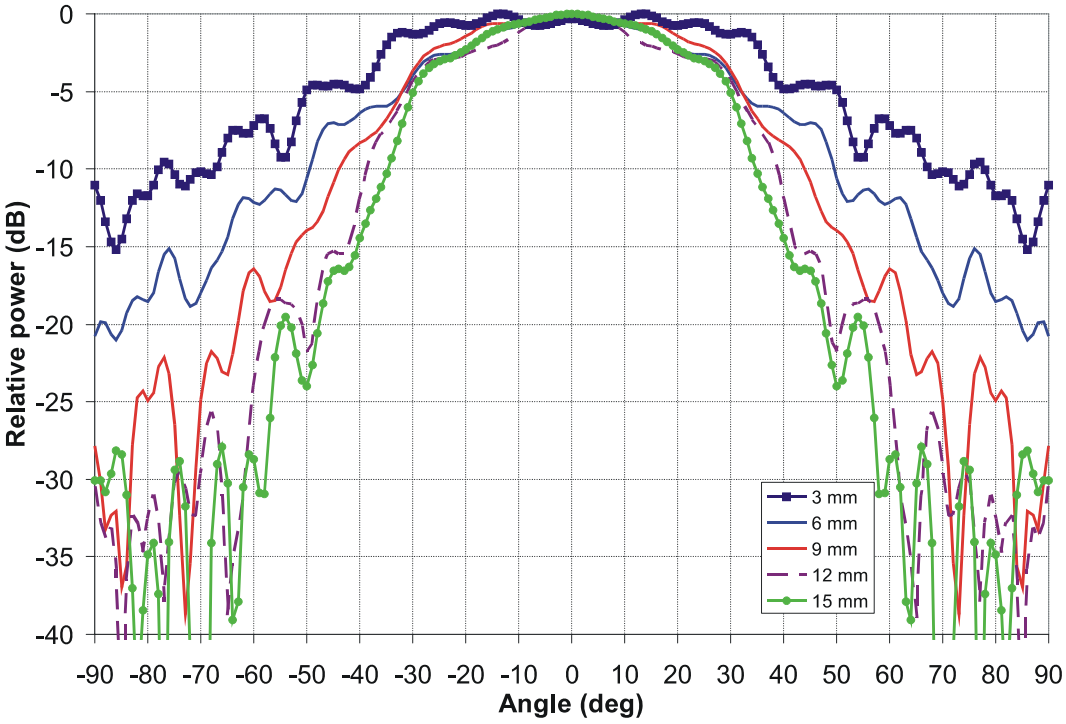

Figure 4.16. Simulated E-plane radiation pattern with different radiation taper length.

The antennas with a longer radiation taper are more directive and also the ripple in pattern is diminished. The problem with a long taper, especially in the case of silicon, is the fragility both in manufacturing and in use. Sapphire is better material for long radiation tapers due to its better durability.

Table 4.1. -10-dB beamwidth with different radiation tapers at 140 GHz.

Radiation taper length	***H-plane beamwidth (-10 dB)***	***E-plane beamwidth (-10 dB)***
3 mm	118˚	134˚
6 mm	106˚	98˚
9 mm	90˚	88˚
12 mm	76˚	78˚
15 mm	72˚	70˚

Figure 4.17 shows the radiated electric fields with 3-mm and 15-mm tapers. The directive effect of the longer taper is clearly visible.

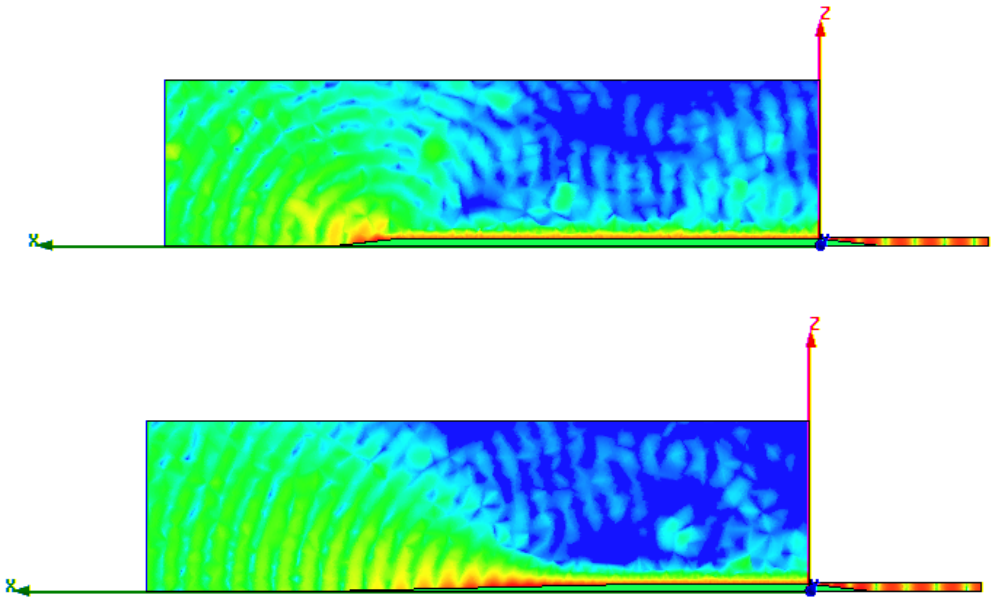

Figure 4.17. Electric fields in sapphire antennas at 140 GHz with 3 mm and 15 mm tapers.

It is interesting to see how a tapered dielectric rod radiates at different frequencies. Figure 4.18 shows the E field in the sapphire antenna with 15 mm taper at 110, 140 and 170 GHz. It is clearly visible that the shorter the wavelength the more the field is concentrated closer to the dielectric core. The field is also propagating closer to the tip of the rod at higher frequencies.

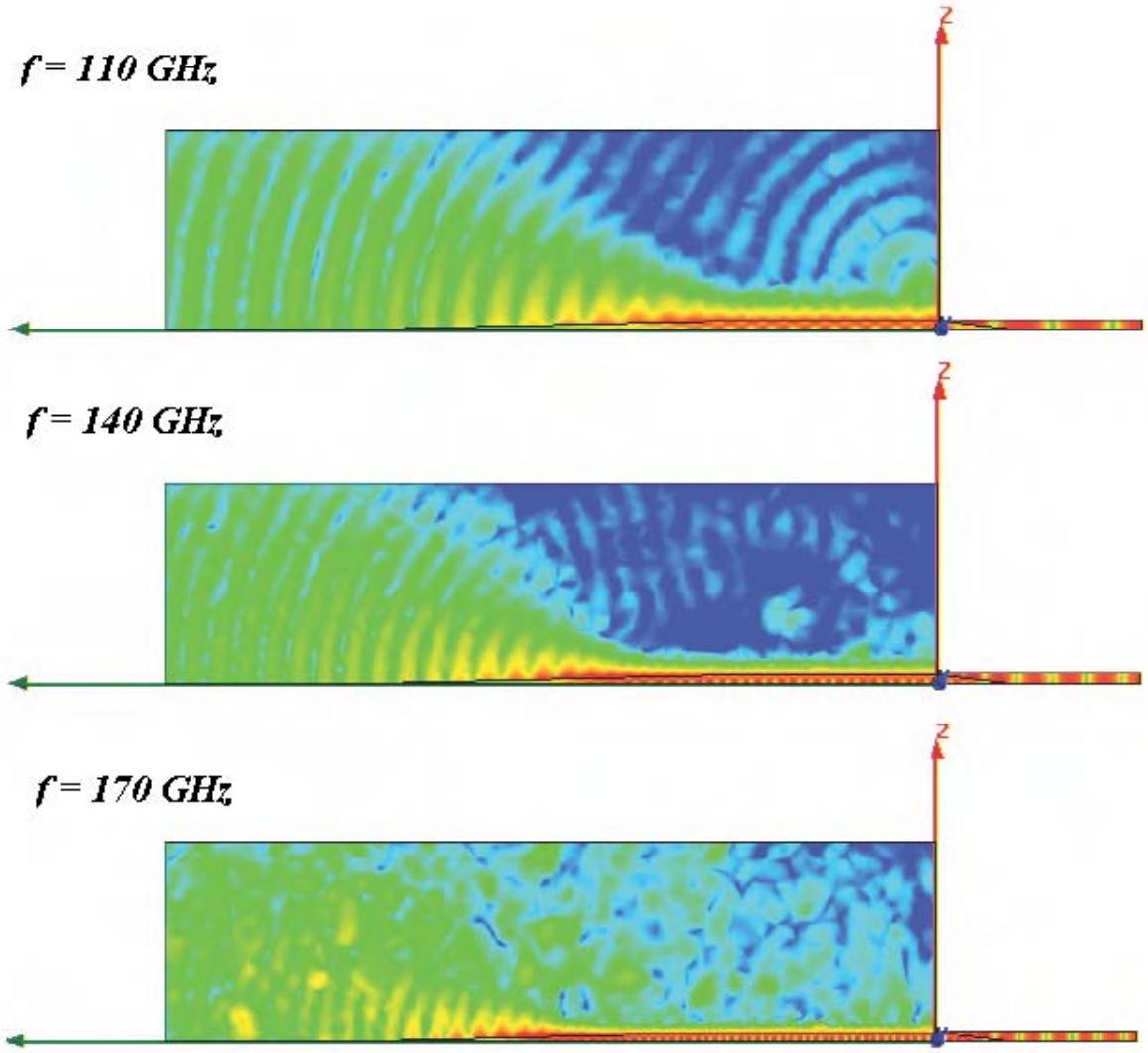

Figure 4.18. E field in a sapphire antenna at 110, 140 and 170 GHz.

4.1.5 Truncated radiation taper

As very long radiation tapers are not very practical, and certainly not very durable, it is interesting to know how a truncated radiation taper would behave. If the antenna characteristics are not much degraded, such tapers would be easier to manufacture. Different cut lengths are simulated in HFSS for a sapphire antenna with a 9-mm radiation taper (Figure 4.19).

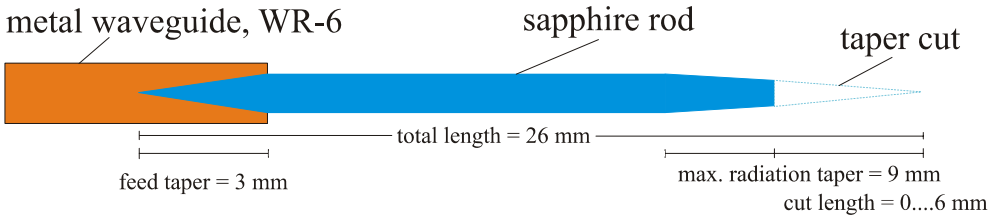

Figure 4.19. Geometry of the sapphire rod antenna with a cut in radiation taper.

Simulated S_{11} can be seen in Figure 4.20. The results are interesting as the cuts smaller than 4 mm do not seem to have much effect for the matching.

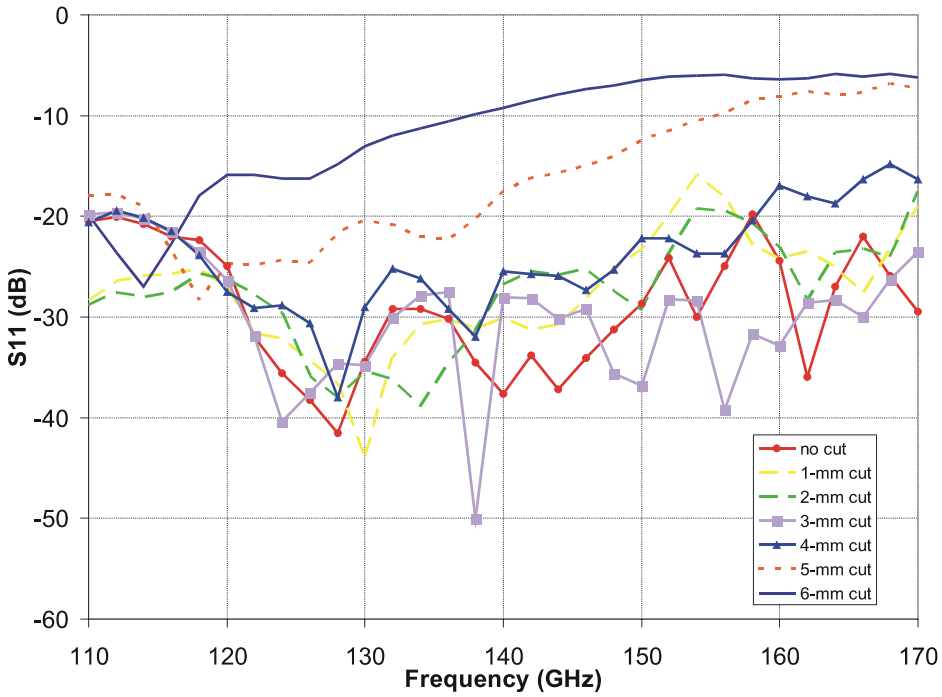

Figure 4.20. Simulated S_{11} with different cuts of the 9-mm radiation taper.

H- and E-plane radiation patterns at 140 GHz are shown in Figures 4.21 and 4.22. An increased sidelobe level can be observed when the cut is more than 4 mm. The radiation pattern is slightly wider already with the smallest cuts. The reason for a very little difference between the cuts until 3 mm is that nearly all the power has radiated along the taper until this point. For higher frequencies the cut distance gets shorter if the same characteristics are desired as the field propagates closer to the core.

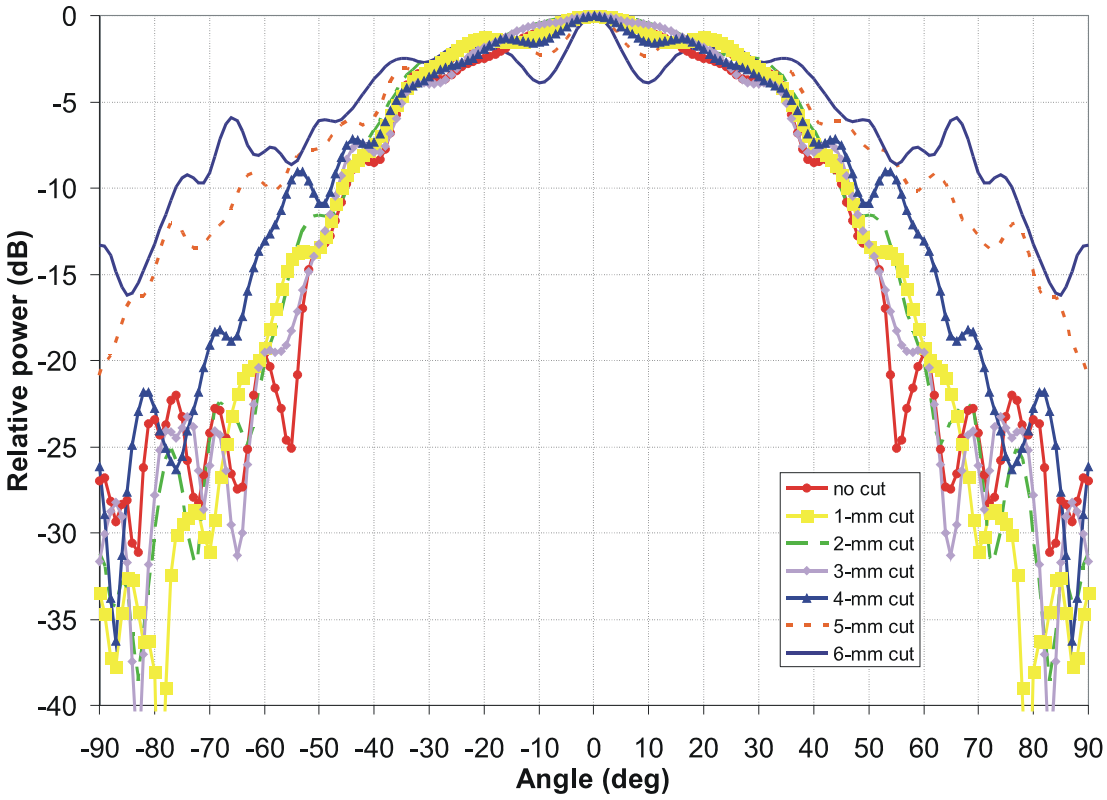

Figure 4.21. Simulated H-plane radiation pattern with different cuts of the 9-mm radiation taper.

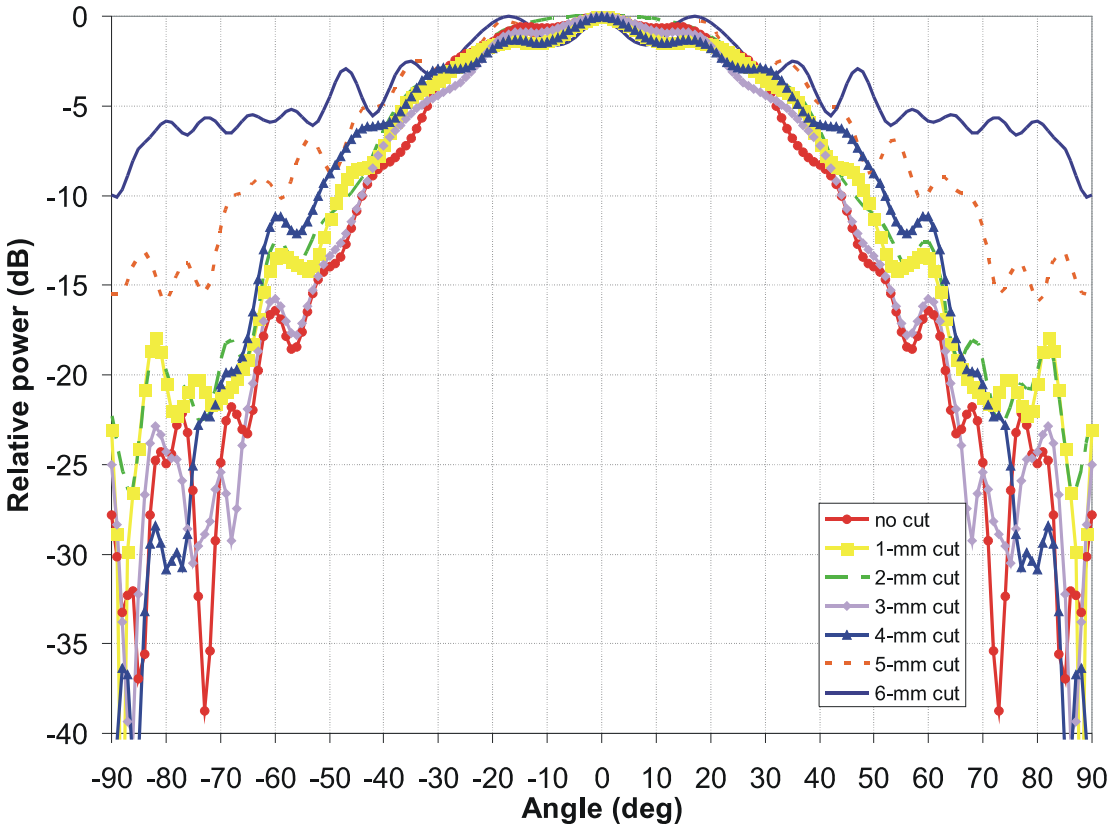

Figure 4.22. Simulated E-plane radiation pattern with different cuts of the 9-mm radiation taper.

4.2 Absorption of the radiation from the transition region

Radiation from the transition region of a DRW and a metal waveguide end in many cases causes unwanted features to the radiation pattern. Especially if a metal waveguide with a flange is used, the flange often radiates strongly. In order to suppress this parasitic radiation some kind of absorber has to be put around the dielectric rod without disturbing the waveguiding properties too much.

One possible solution is to use TK THz RAM tile around the rod. The tile surface is composed of small pyramids with the base and height both 1 mm. In this case it is more a scatterer than an absorber. Symmetrical nature of the surface also permits the

operation on both vertical and horizontal polarizations without adjusting the tiles. The pyramidically patterned tile works as an incoherent scatterer and has very wide angular scattering spectrum. Above 100 GHz the reflection is always less than -30 dB. One tile has the surface area of 25 x 25 mm^2 and several tiles can be connected to each other to form arbitrary absorbing surfaces. Tiles are fabricated from plastic based on polypropylene [50] and these tiles have been found to be suitable absorbing material for millimetre and submillimetre wavelengths [51]. In Figure 4.23 an absorber composed of 4x4 tiles is presented. At 9.4 GHz polypropylene has been measured to have the relative permittivity $\varepsilon_r = 2.27$ and the loss tangent $tan\delta = 8 \cdot 10^{-5}$ [52].

Figure 4.23. An absorber composition of 16 TK THz RAM tiles.

4.2.1 Simulations with TK THz RAM absorber around the DRW

Unfortunately due to insufficient calculation capacity a complete 25 x 25 mm^2 tile could not be simulated even if the symmetry planes were in use. Thus the simulated results are for a tile of the size 16 x 16 mm^2. The simulated structure is presented in Figure 4.24.

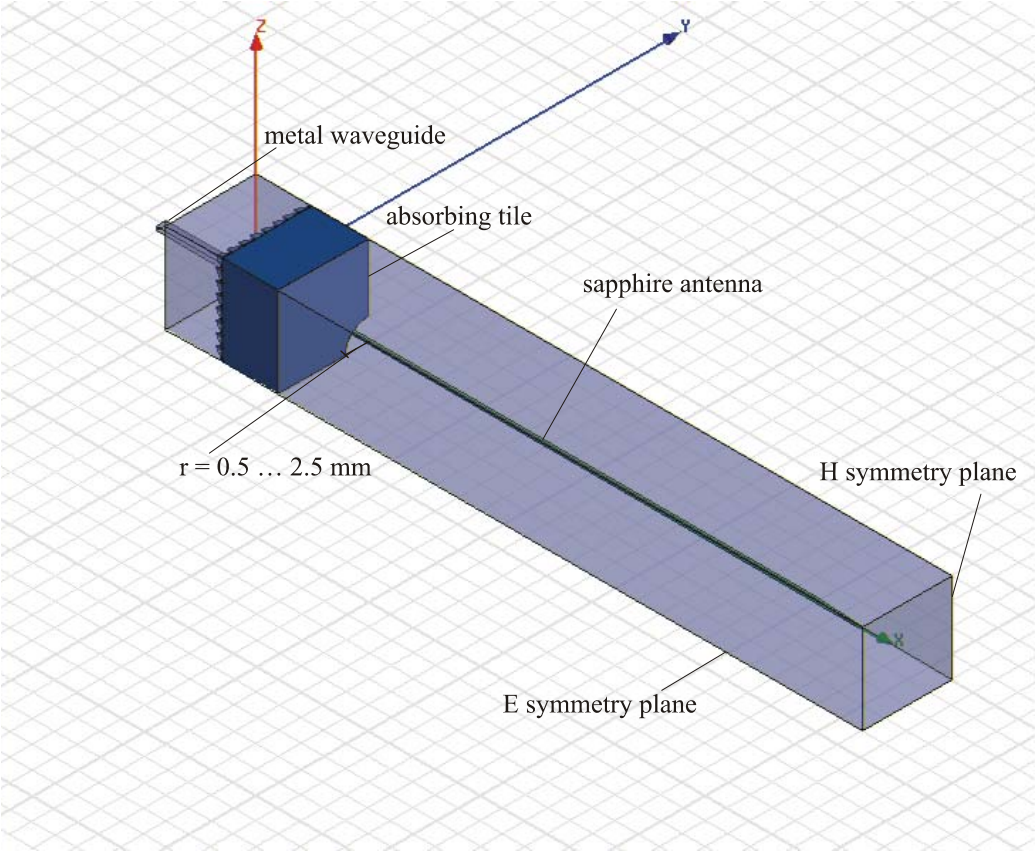

Figure 4.24. Simulation setup with an absorbing tile.

As the electromagnetic field propagates partially outside the rod, a too small hole in the tile may distort the propagating field and also cause unwanted radiation. On the other hand, a too large hole does not block enough radiation from the transition region, and, thus it is important to find the optimal radius for the hole. The structure was simulated with five different diameters. Figure 4.25 shows the simulated electric field in four different cases: with the hole diameter of $2r$ = 1…5 mm.

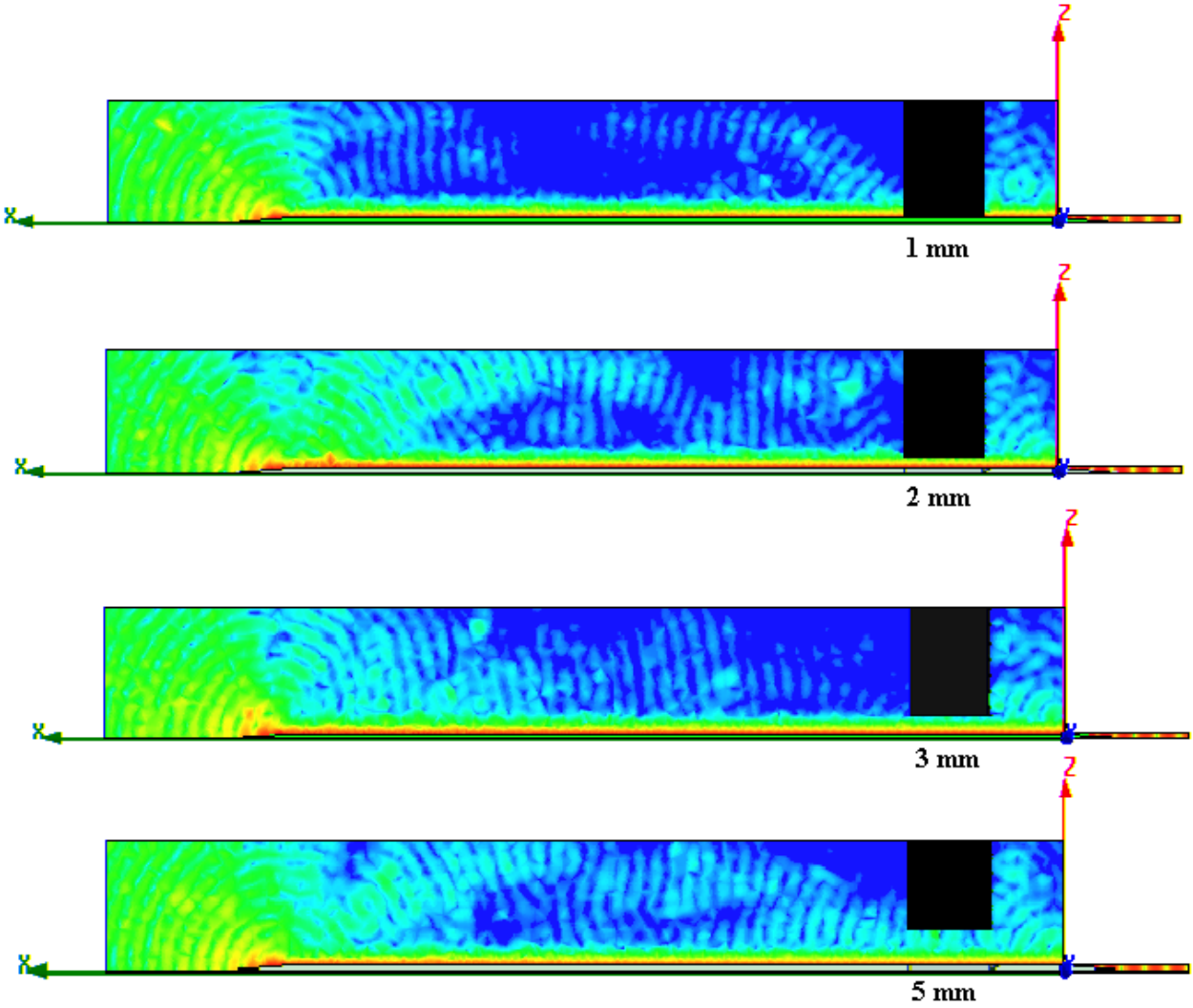

Figure 4.25. Simulated electric field at 140 GHz when the hole diameter in the tile is 2r=1, 2, 3 and 5 mm.

Figure shows clearly how a 1-mm hole blocks completely the propagating field outside of the rod causing at the same time additional radiation at the lower tile edge. A diameter of 3 mm at 140 GHz seems to be quite optimal as the propagating field is not disturbed. A larger hole already lets quite much of transition radiation through. Radiation patterns in H and E plane are shown in Figures 4.26 and 4.27. On the other hand, at lower frequencies the field is stronger outside the rod and this has to be taken into account when designing the absorber for a specific application. It is also clear that the antenna efficiency and gain are diminished as part of the radiating power is blocked.

Typically a high-permittivity DRW antenna without any absorber has efficiency over 90%. Depending on the matching ~5-10 % of the power is radiated from the transition.

As in the real prototype the tile would be connected to the metal waveguide with a 0.5 mm thick piece of Styrofoam, the tile does not block completely the parasitic radiation. Thus, at the angles above 56˚ the radiated power level is larger compared to the situation where the parasitic radiation is completely blocked. According to these radiation patterns, the benefit of the absorber does not seem to be significant at this frequency. But it has to be remembered that the metal waveguide is modelled as an infinitely small perfect electric conductor (PEC) boundary. This kind of simplified structure probably causes less unwanted radiation than a real metal waveguide. Unfortunately such a real structure that is large compared to the wavelength requires more memory and calculation capacity than is available.

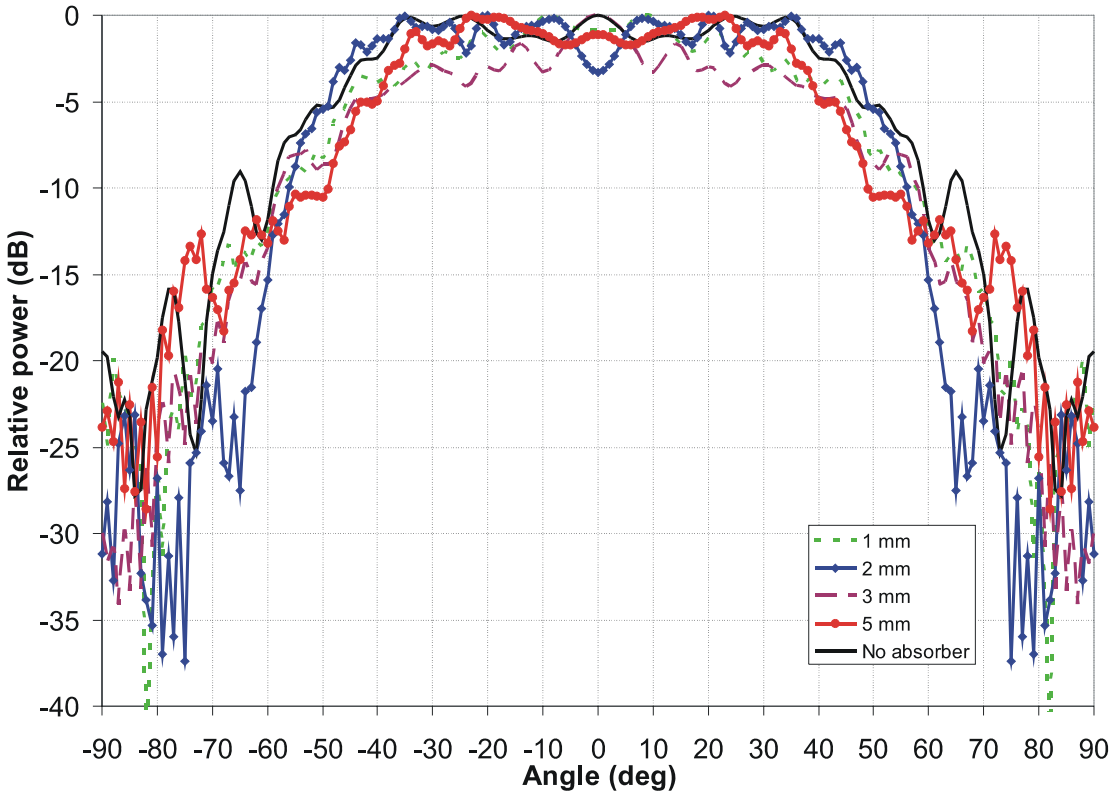

Figure 4.26. Simulated H-plane radiation pattern at 140 GHz with different absorber tile hole sizes.

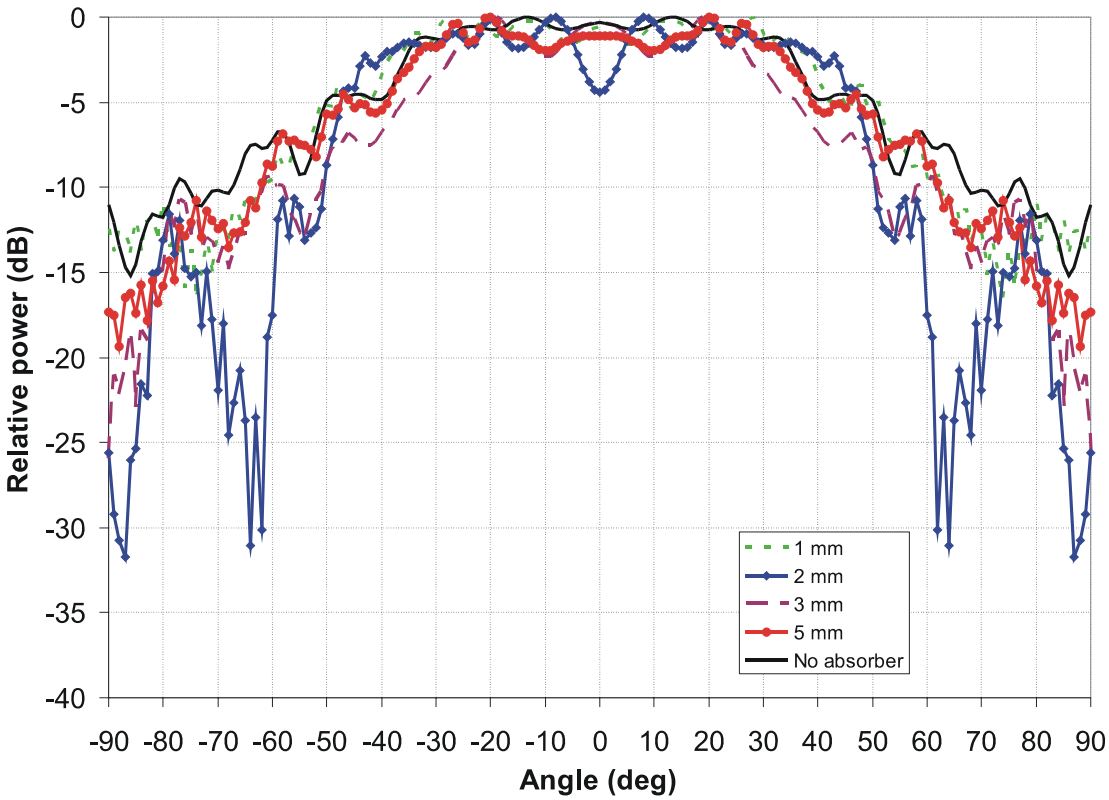

Figure 4.27. Simulated E-plane radiation pattern at 140 GHz with different absorber tile hole sizes.

4.3 Antenna for 295-325 GHz and its simulations

Cross-section of the rod is defined in similar way as in the case of the D-band antenna. The cross-section dimensions at 310 GHz central frequency are $b \approx 0.26$-0.30 mm and $a \approx 0.13$-0.15 mm. As the metal waveguide dimensions are very small (0.86 x 0.43 mm^2) the accuracy and rod pointing problems are also emphasized in this frequency range.

In order to optimize the design of the antenna for the frequency band 295-325 GHz, similar simulations as those for the D-band antenna are performed. In the first stage rectangular cross-sections of different size and different taper shapes are studied. After

the best structure is chosen, the radiation characteristics of different kinds of dielectric rods are compared. As the dimensions are even more critical in this frequency range, finally the effect of the misplacement of the rod is also studied.

4.3.1 Cross-section and taper dimensions

A transition from a standard rectangular waveguide WR-3 to another one through a dielectric rod is simulated with different cross-section dimensions and tapers to find an optimal structure. Also in this case only the E-plane taper is considered as it has been found suitable already for the D-band antennas. The material of the rod is sapphire. The simulation setup is presented in Figure 4.28. The total rod length is chosen to be 10 mm including a 3-mm taper section in both ends.

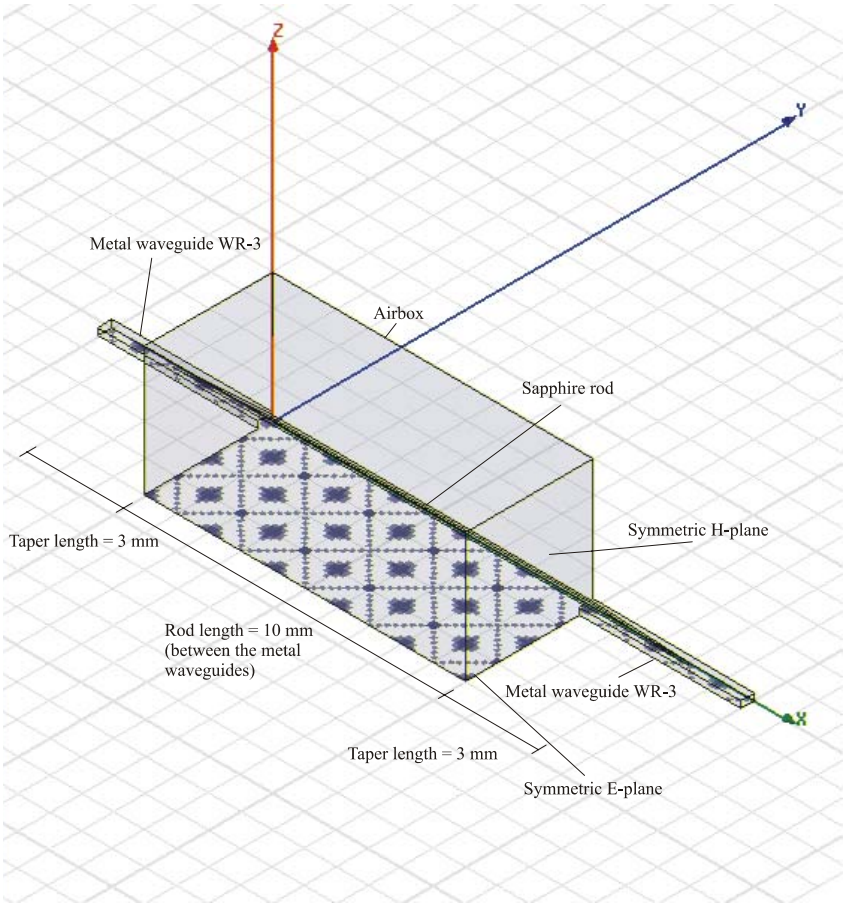

Figure 4.28. HFSS simulation setup: A quarter of the dielectric rod and the two WR-3 waveguides.

In Figures 4.29 and 4.30 the reflection (S_{11}) and transmission (S_{21}) coefficients of sapphire waveguides with five different cross-section sizes are presented.

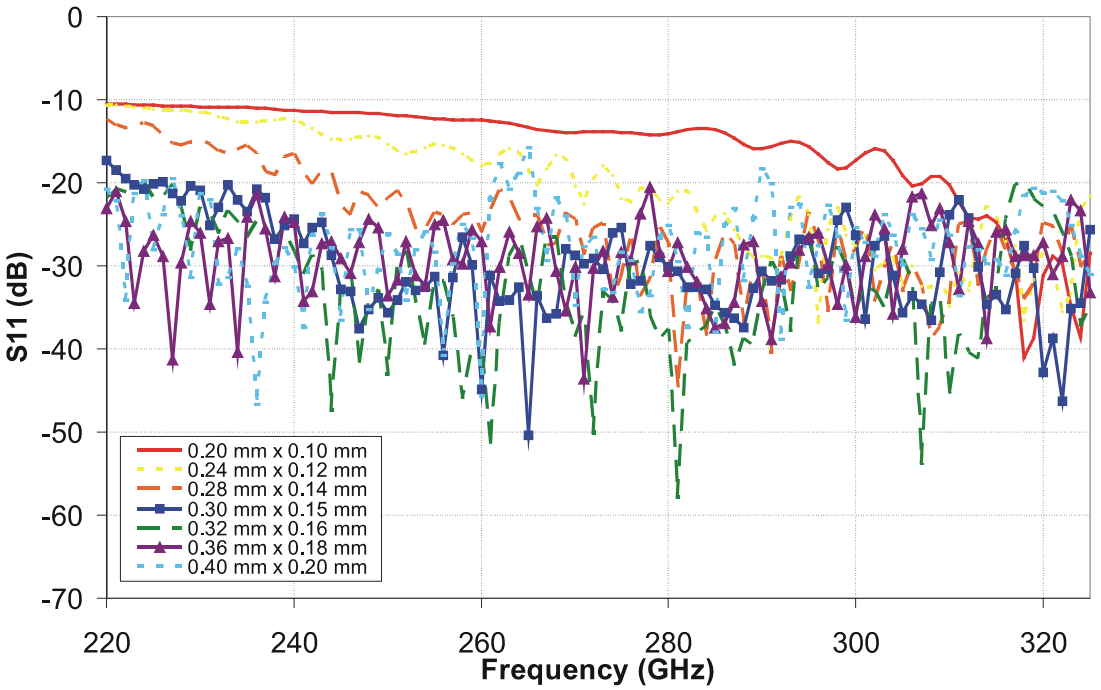

Figure 4.29. S_{11} of sapphire RW with different size cross-sections.

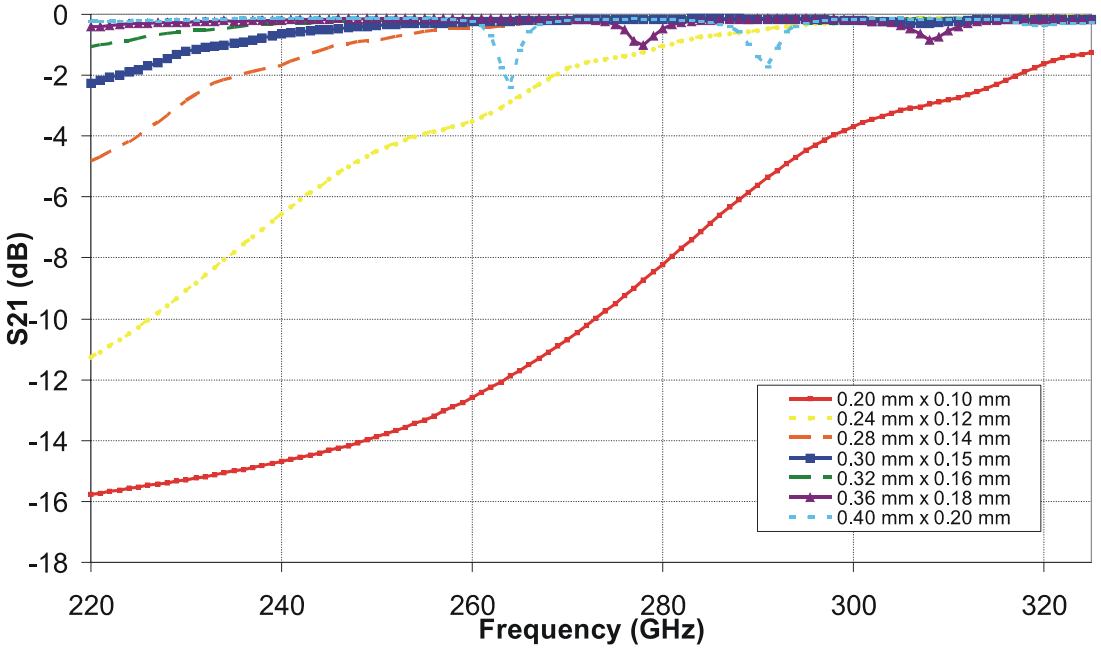

Figure 4.30. S_{21} of sapphire RW with different size cross-sections.

According to the simulation results, the reflections are significantly larger in rods having the cross-section area smaller than 0.30 x 0.15 mm^2. With larger cross-sections similar dips that were observed in D band occur, but, however, they are significantly smaller. Cross-section of 0.15 x 0.30 mm^2 seems to be a good choice for this frequency range. It also leaves some margin for manufacturing tolerances as the performance remains quite stable in little larger or smaller dimensions.

In the next stage sapphire dielectric rods with an E-plane taper section of different lengths are simulated. The simulation setup is similar to the cross-section simulations. In Figures 4.31 and 4.32 the simulation results of S_{11} and S_{21} are presented. In Figure 4.33 the results of S_{21} of sapphire RWs with tapers of length between 2 to 4.5 mm are presented in more detail.

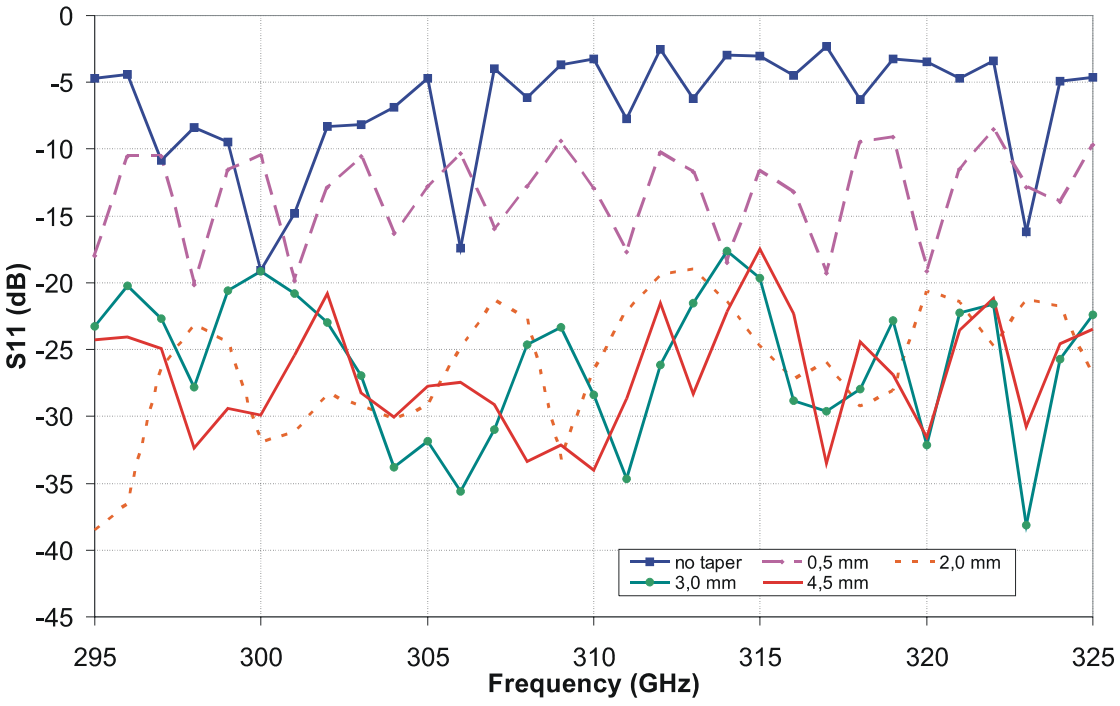

Figure 4.31. Simulated S_{11} of sapphire RWs with different taper lengths.

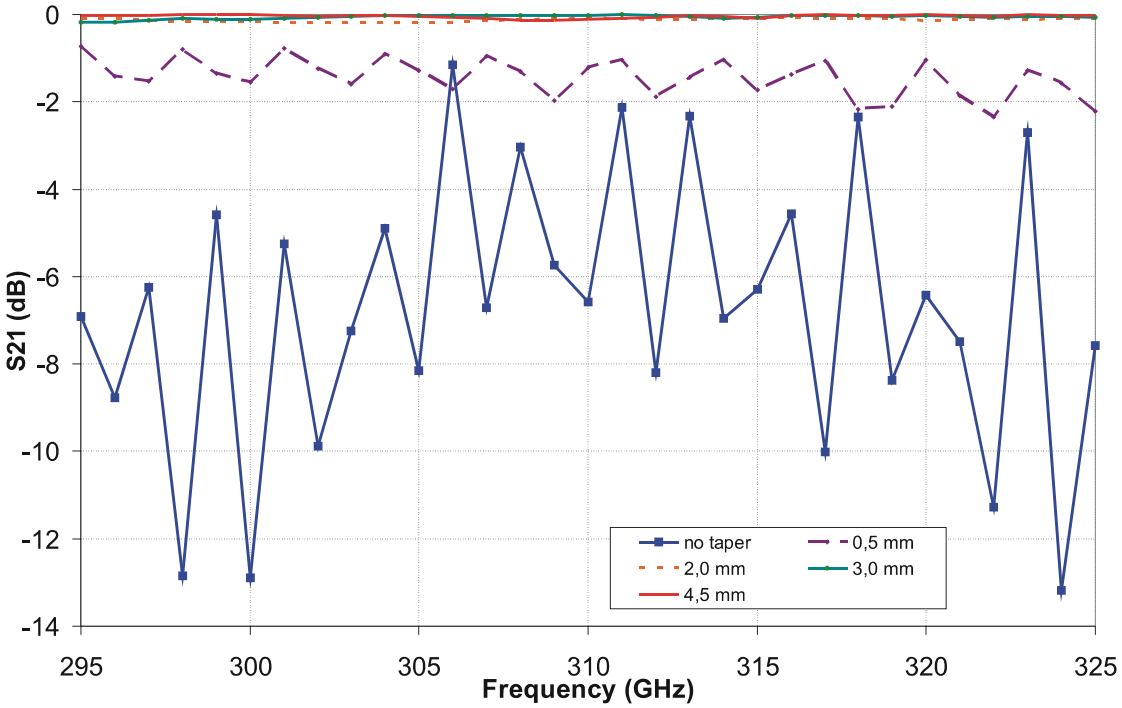

Figure 4.32. Simulated S_{21} of sapphire RWs with different taper lengths.

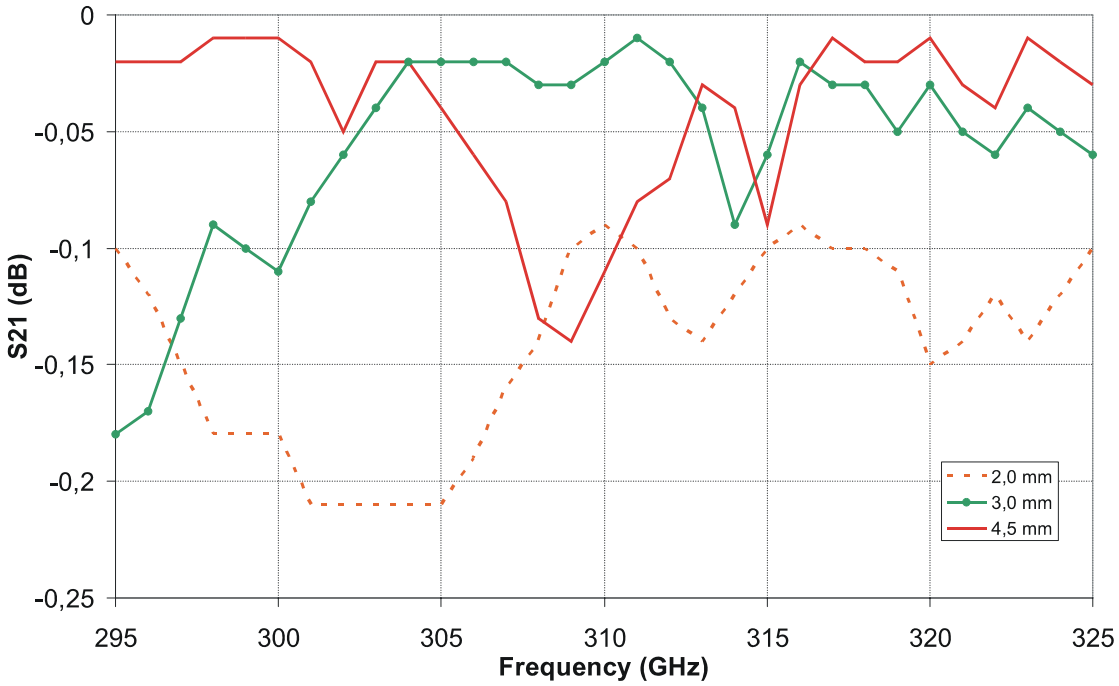

Figure 4.33. Simulated S_{21} of DRWs with different taper lengths (2.0-4.5 mm).

According to the simulated S parameters tapers longer than 2 mm do not improve the performance significantly. That is clearly visible in both S_{11} and S_{21}. Figure 4.33 shows a slight improvement in S_{21} between 2 mm and 2.5 mm, but the difference is rather marginal.

4.3.2 Radiation taper

The other end of the dielectric rod is now left free and the radiation characteristics of the sapphire antenna are evaluated. As with the D-band antenna, the radiation taper length is varied from 3 mm to 15 mm, total rod length being 26 mm and the cross-section area is 0.30 x 0.15 mm^2. Simulated S_{11} with five radiation tapers of different lengths is presented in Figure 4.34. A significant improvement in the reflection level can be seen between the taper lengths of 6 mm and 9 mm. Tapers longer than 9 mm do not improve much S_{11} anymore, but the radiated beam is more directive as can be seen from the radiation patterns. Simulated H- and E-plane (horizontal and vertical) radiation patterns at 320 GHz can be seen in Figures 4.35 and 4.36.

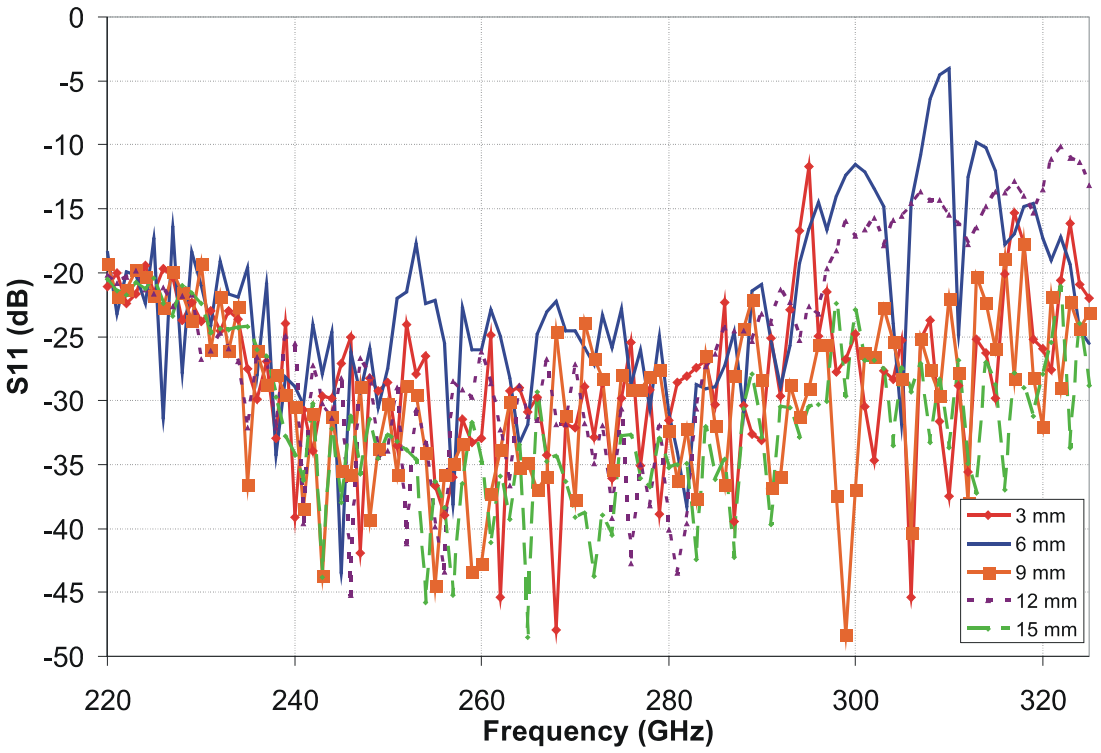

Figure 4.34. Simulated S_{11} with different radiation tapers.

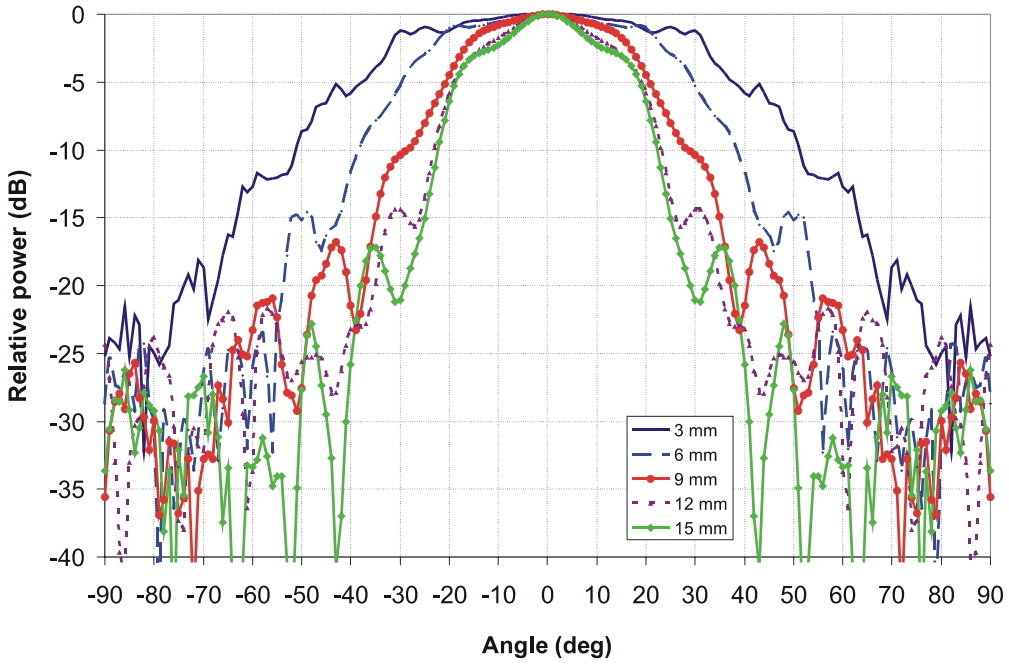

Figure 4.35. Simulated H-plane radiation patterns of DRW antennas with different radiation tapers at 320 GHz.

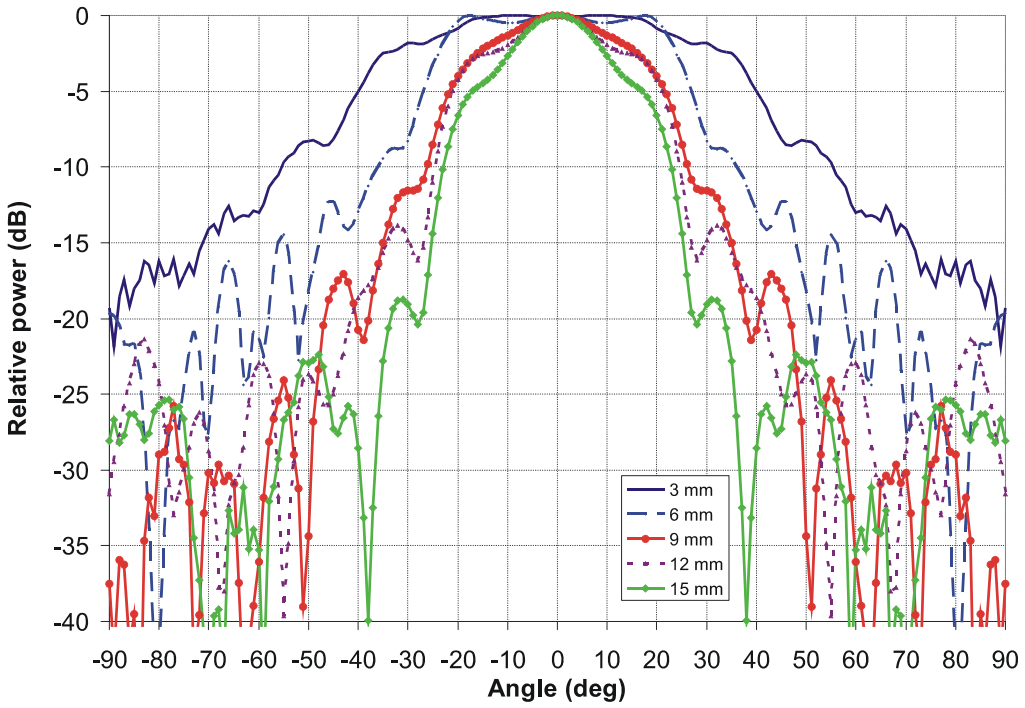

Figure 4.36. Simulated E-plane radiation patterns of DRW antennas with different radiation tapers at 320 GHz.

Beamwidths at -10-dB level are listed in Table 4.2. Compared to the D-band antenna, the beamwidths are quite much narrower. The difference is larger as the taper length is increased, almost 30˚ with 15 mm taper.

Table 4.2. Simulated beamwidths with different radiation tapers at 320 GHz.

Radiation taper length	***H-plane beamwidth (-10 dB)***	***E-plane beamwidth (-10 dB)***
3 mm	102˚	110˚
6 mm	76˚	72˚
9 mm	56˚	52˚
12 mm	46˚	50˚
15 mm	44˚	46˚

In Figure 4.37 simulated E field can be seen in the end of a 3-mm sapphire rod radiation taper. With shorter wavelengths the field propagates further inside the rod.

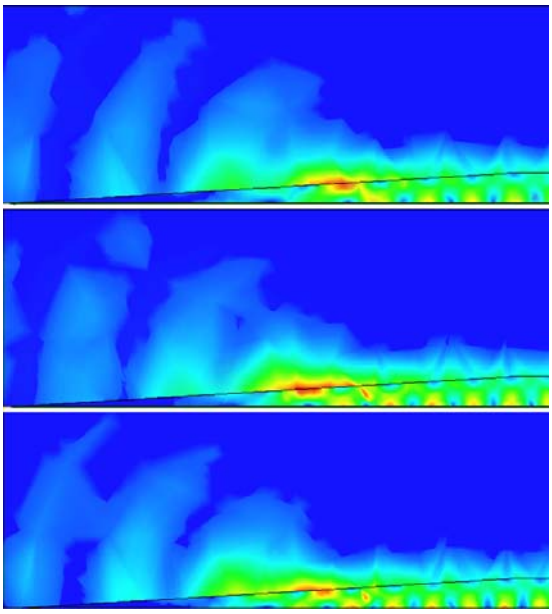

Figure 4.37. Simulated E field in a 3-mm taper at frequencies 295 GHz, 310 GHz and 325 GHz.

4.3.3 Effect of the rod length

It is interesting to know how sensitive the radiation pattern is to the rod length. It can be assumed that the EM wave radiates slightly at different phases depending on the position of the taper section. This effect of the total rod length to the radiation patterns is discussed in this section. At 320 GHz the wavelength in free space is ~0.94 mm and in sapphire waveguide ~0.31 mm ($\frac{\lambda_0}{\sqrt{\varepsilon_r}}$). This means that even a very short difference in the rod length changes the phase of the radiating wave significantly at these frequencies. Seven sapphire rods from 5 mm to 20 mm are simulated. They all have 2.5 mm feed and radiation tapers. H- and E-plane radiation patterns can be seen in Figures 4.38 and 4.39.

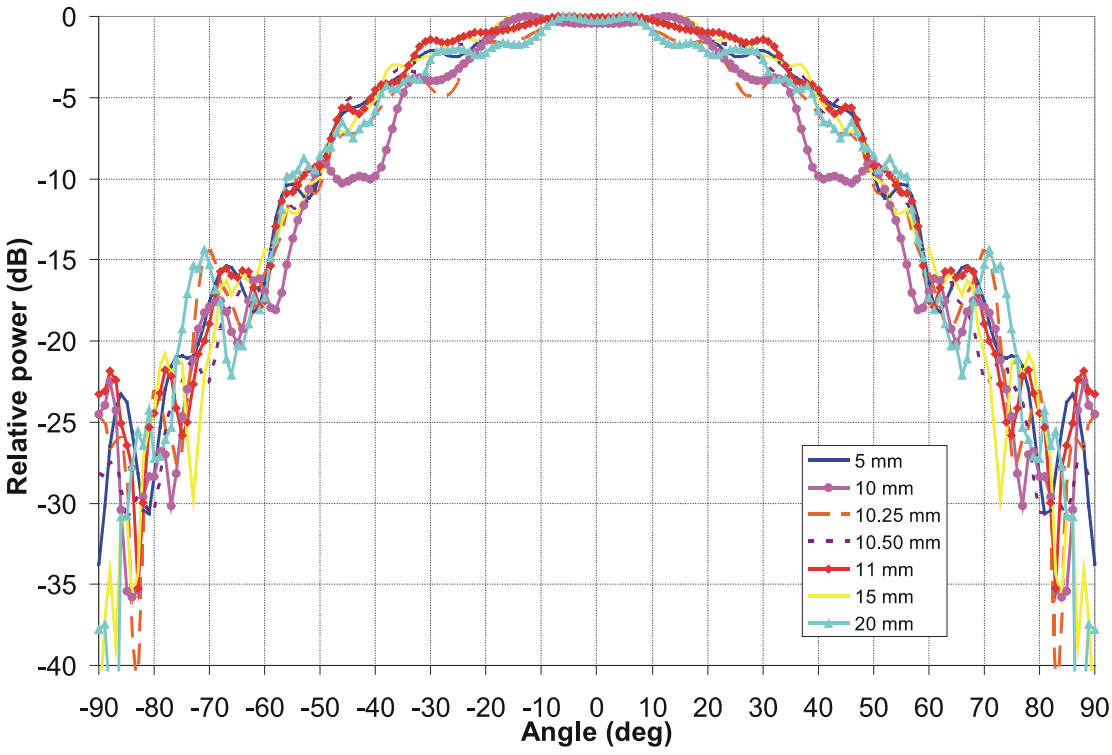

Figure 4.38. Simulated H-plane radiation pattern of DRW antenna of different lengths at 320 GHz.

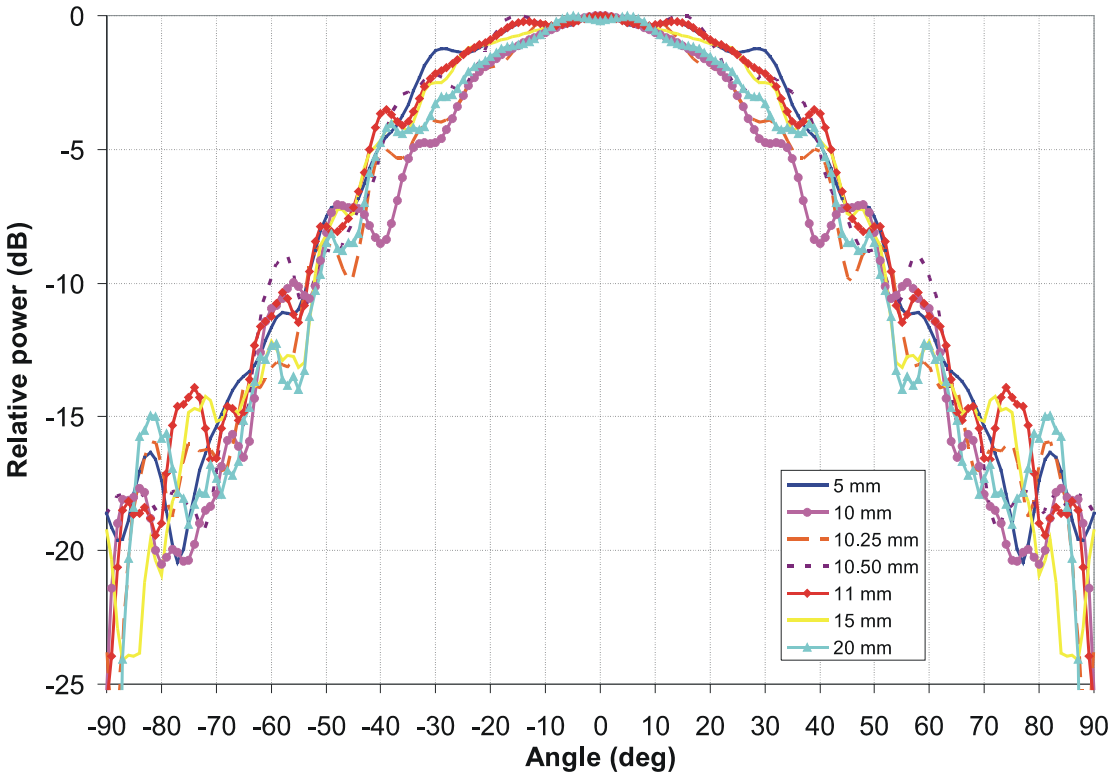

Figure 4.39. Simulated E-plane radiation pattern of DRW antenna of different lengths at 320 GHz.

The general forms of the radiation patterns are rather similar, but the differences between the rods are clearly visible. It can be concluded that a small difference in the rod length can slightly vary the radiation pattern. However, it has to be taken into account that the simulation setup does not take completely into account the parasitic radiation from the feed. The rod length has a significant effect on the phase centre, especially if the feed radiation is strong.

4.3.4 Effect of the rod misplacement

As it is very difficult to place the rod mechanically exactly in the middle of the metal waveguide, it is interesting to know the effect of the misplacement. This is studied in HFSS by placing the rod in various positions in horizontal (y-) and vertical (z-) axis. The rod used in these simulations is made of silicon and it has a 30-mm radiation taper,

so the possible differences would be more clearly visible in narrow beams. The total rod length is 38 mm. The setup is presented in Figure 4.40. This time only one symmetry plane can be used; H-plane symmetry in vertical simulations and E-plane symmetry in horizontal simulations.

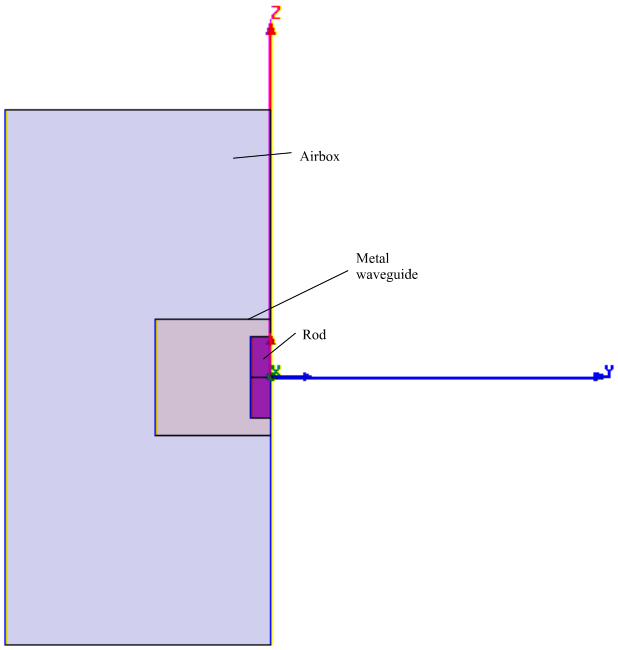

Figure 4.40. Setup for the rod misplacement simulations in z direction.

First the effect of the vertical misplacement is simulated. The rod is moved from the centre position with 0.01 mm step up to 0.06 mm, thus almost touching the upper side of the metal waveguide. Simulated S_{11} in each position over the frequency range of 295-325 GHz can be seen in Figure 4.41. At the upper end of the frequency band the matching is easily degraded due to the rod misplacement, but otherwise S_{11} does not seem to be very sensitive for misplacement in this direction.

Figure 4.42 shows the corresponding effect of the misplacement in horizontal direction to S_{11}. The effect is clear with 0.28 mm and 0.35 mm shifts as S_{11} is degraded even over 10 dB. Smaller misplacements do not seem to have very significant effect. The vertical

direction seems to be more sensitive as very small shifts in the rod's position can cause big differences in performance.

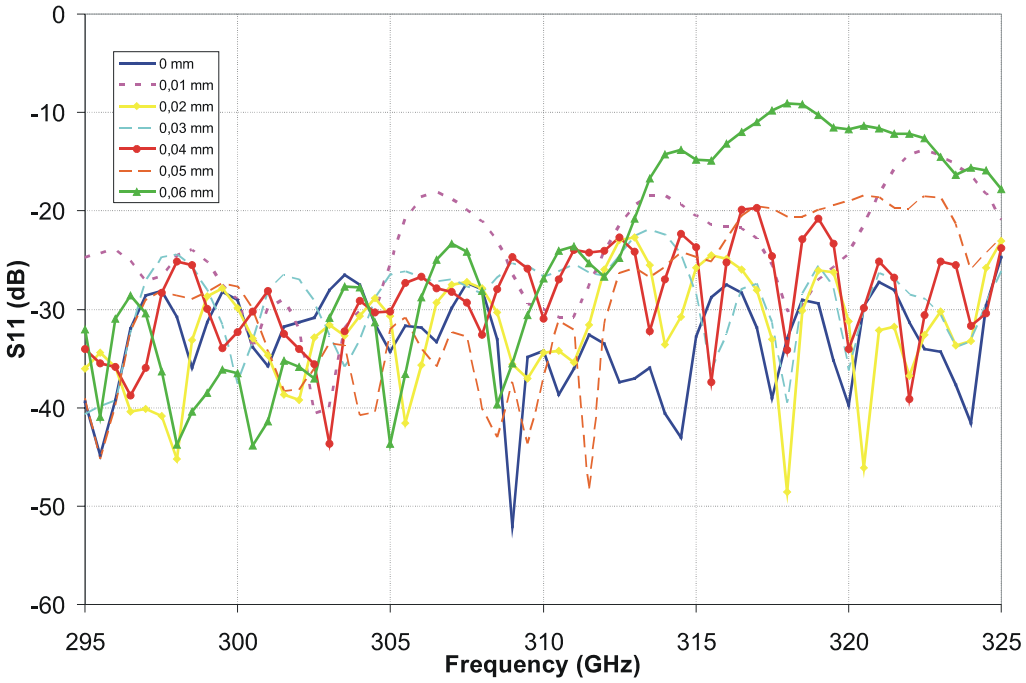

Figure 4.41. Simulated effect of the rod misplacement in z direction (S_{11}).

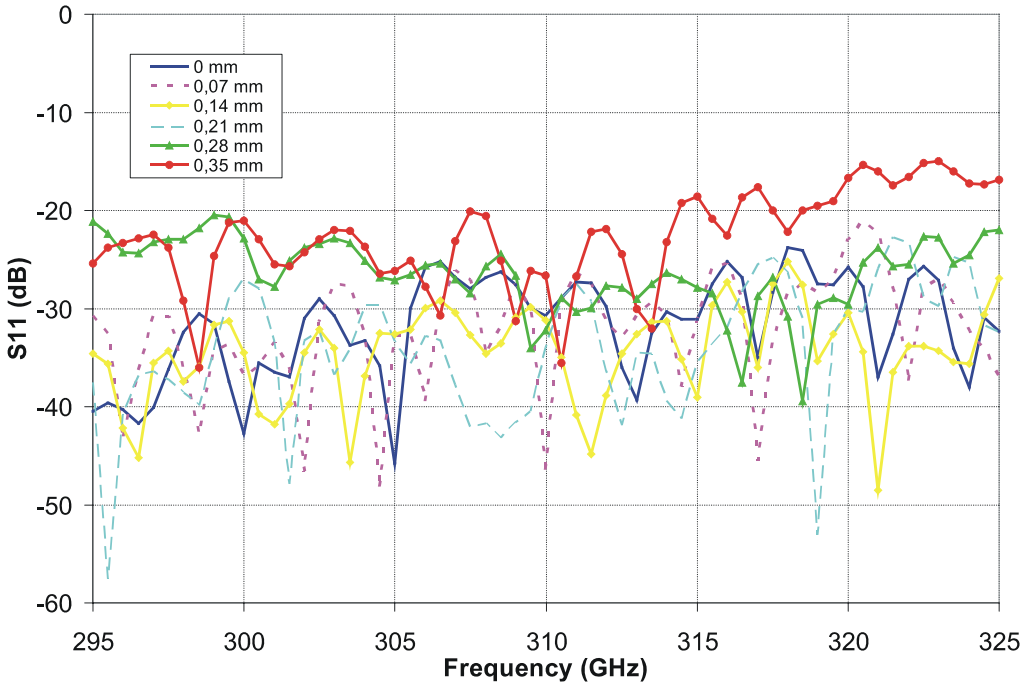

Figure 4.42. Simulated effect of the rod misplacement in y direction (S_{11}).

The misplacement effects to the radiation pattern are also studied. Figures 4.43 and 4.44 show the radiation patterns in H and E plane at each rod shift in vertical direction at 320 GHz. As it can be assumed the H-plane radiation pattern remains symmetric, but the misplacement causes the rise of the sidelobe level. With the maximum shift this rise is about 20 dB. In E plane, in addition to the rise of the sidelobe level, the radiation pattern becomes more and more unsymmetrical as the shift gets larger.

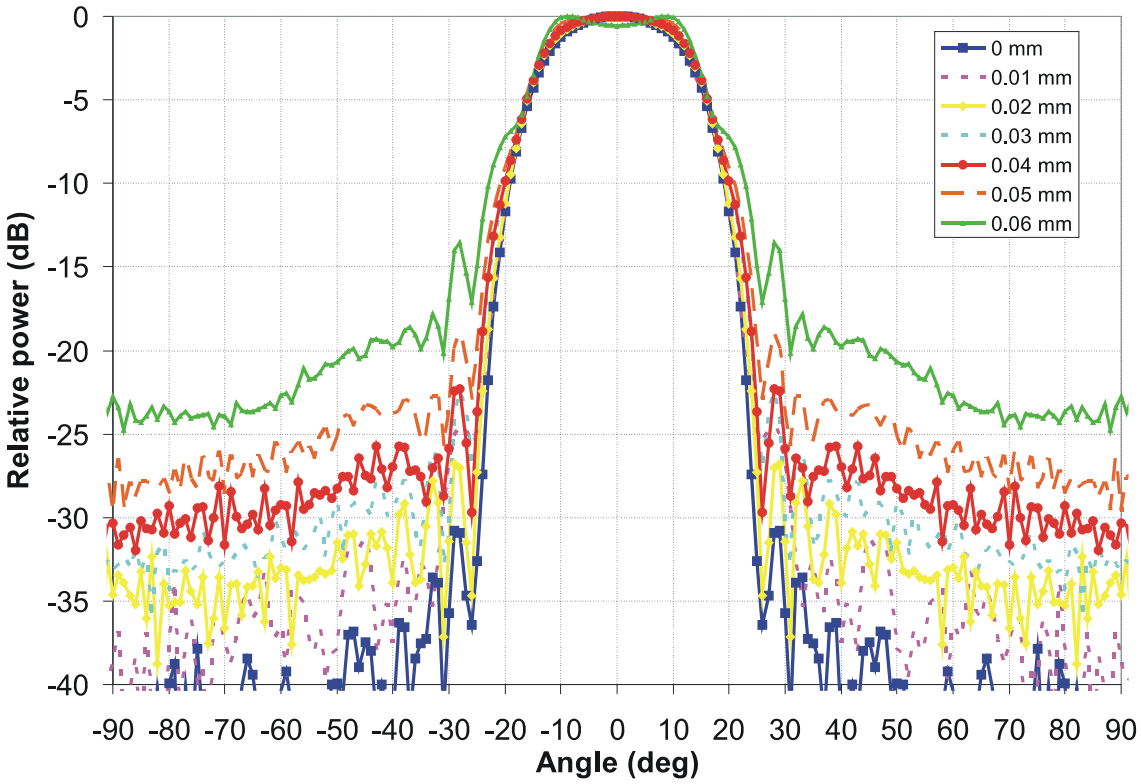

Figure 4.43. Simulated effect of the rod misplacement in z direction in H-plane radiation pattern at 320 GHz.

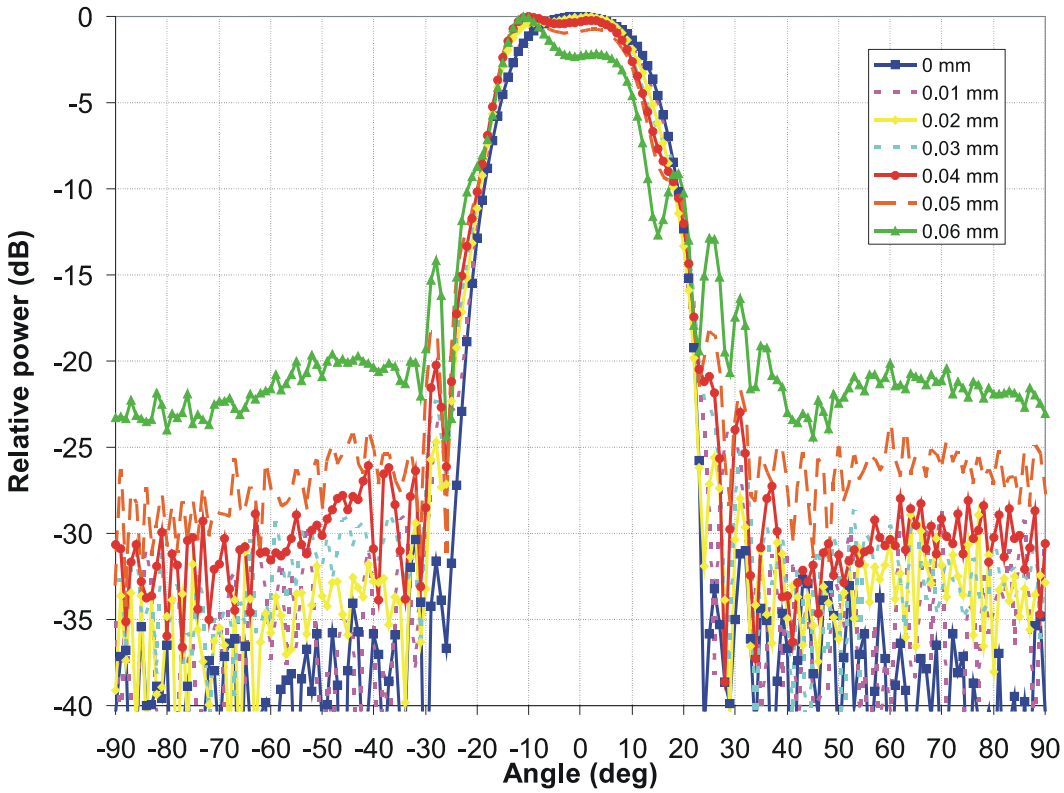

Figure 4.44. Simulated effect of the rod misplacement in z direction in E-plane radiation pattern at 320 GHz.

In the horizontal misplacement the effects are vice versa: in H plane the radiation pattern gets more and more unsymmetrical as the rod is shifted further from the centre. Figures 4.45 and 4.46 present the radiation patterns in both planes. Here the asymmetry in H plane is very clear also in sidelobe levels.

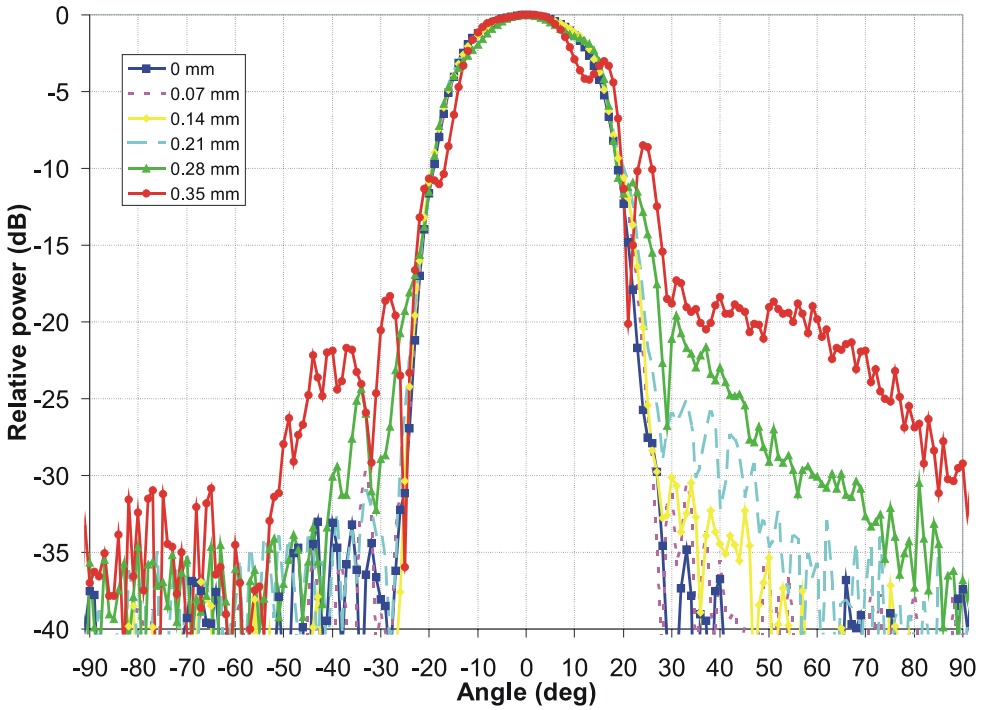

Figure 4.45. Simulated effect of the rod misplacement in y direction in H-plane radiation pattern at 320 GHz.

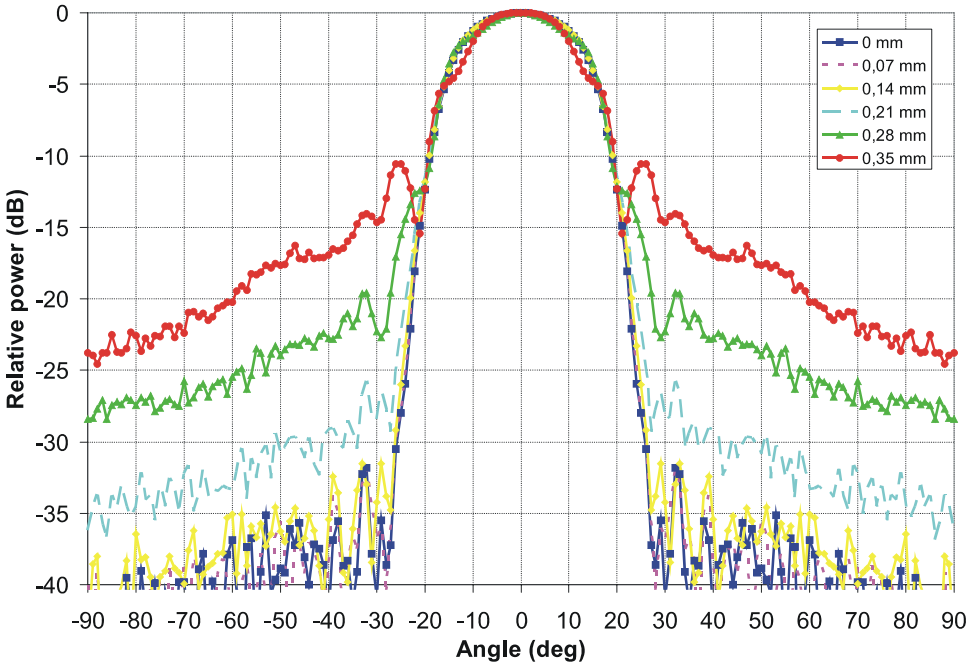

Figure 4.46. Simulated effect of the rod misplacement in y direction in E-plane radiation pattern at 320 GHz.

It can be seen in radiation patterns that the patterns degrade gradually as the misplacement increases. At other frequencies the effects to the radiation patterns can be somewhat different, but this has not been studied.

4.4 Conclusion of this chapter

In this chapter, rectangular silicon and sapphire dielectric rod waveguides and antennas are studied with HFSS simulations at 110-170 GHz and 295-325 GHz. Optimal dimensions of the DRW cross-section and taper length for wide-band operation are determined. It is found out that the DRW cross-section of 0.3 x 0.6 mm^2 offers the best compromise over the whole D band frequency range. For 295-325 GHz, the respective size is 0.15 x 0.3 mm^2. Tapers studied in this thesis are in E plane as they are the most practical in the manufacturing point of view. Of course, other types are also possible, but they are often very difficult to realize for high frequency components. For D band the optimal feed taper length is 4 mm. For 295-325 GHz range already a taper of 2 mm offers a very good performance.

One benefit of DRW antennas is that the radiation pattern can be simply modified by using different kinds of radiation tapers. For example, directivity can be easily increased by using longer tapers. The effect of the radiation taper length is studied in this chapter. For example, a 15-mm long radiation taper gives ~45˚ main beam in both E and H plane at -10-dB level. The effect of the truncation of the taper is also studied and discussed.

DRW antennas often suffer from parasitic radiation from the waveguide feed. This radiation is often strongest at the lower operating frequencies of the DRW. It can be decreased by placing an absorber or a blocking structure near the transition section. Different kinds of structures are discussed and studied in this chapter. It is important that the structure does not affect significantly the propagating wave in the DRW as it propagates partially outside the rod. However, it is very difficult to overcome this problem completely with one solution at all frequencies.

As a last point of this chapter, the effect of the rod length and misplacement effects of the DRWs have been studied. The length of the rod does affect only slightly the radiation pattern. For optimal use of DRWs it is important that the rod is inserted accurately in the middle of the metal waveguide. The misplacement effects are studied in vertical (z) and horizontal (y) directions. It can be concluded that in z direction, where the tolerances are much smaller, already a very small misplacement alters the radiation pattern. From practical point of view, however, if for example Teflon sheets are used to fix the rod with the metal waveguide, symmetric vertical position of the rod is achieved with good accuracy. In horizontal plane the misplacement errors are more difficult to avoid.

5 DRW ANTENNA MEASUREMENTS

The antenna prototypes for D band based on both silicon and sapphire rod waveguides are built. The S parameters and the radiation patterns are measured at several frequencies. Comparison with some of the simulations presented in the previous chapter is also made.

5.1 S-parameter measurements

S-parameter measurements at these frequencies are demanding and require special instrumentation. The measurements are done at the facility of Elmika Co. in Vilnius, Lithuania [53]. Dielectric rod waveguides are inserted between two metal waveguide ports (Figure 5.1) and the transmission coefficient S_{21} is measured with HP8510 VNA (Vector Network Analyzer). Small pieces of porous teflon sheets are used to hold and position DRWs in the centre of the metal waveguides.

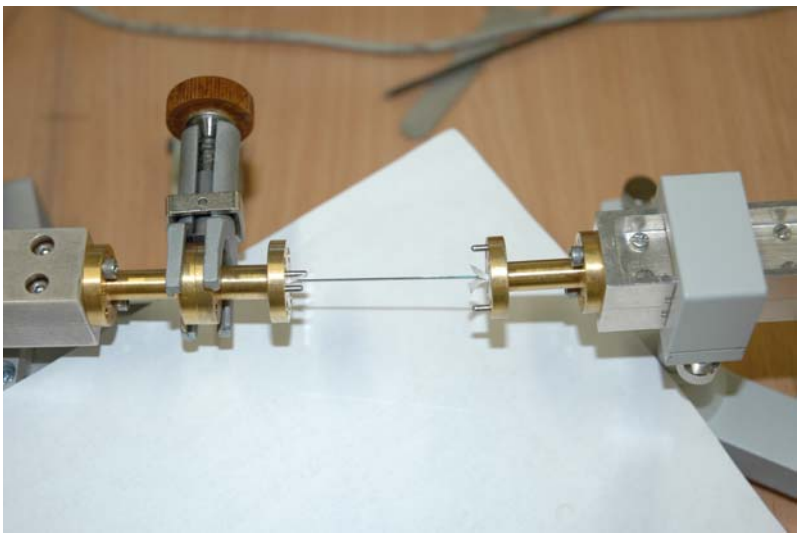

Figure 5.1. S_{21} measurement set-up.

Four different DRWs are measured:

- Silicon short: 40 mm (32 mm + 2x4 mm tapers), 0.31 x 0.61 mm^2 cross-section
- Silicon long: 58 mm (50 mm + 2x4 mm tapers), 0.31 x 0.62 mm^2 cross-section
- Sapphire short: 18 mm (10 mm + 2x4 mm tapers), 0.30 x 0.60 mm^2 cross-section
- Sapphire long: 58 mm (50 mm + 2x4 mm tapers), 0.30 x 0.60 mm^2 cross-section

Measurement results are presented in Figures 5.2 and 5.3. The black line in Figure 5.2 is the measured transmission coefficient for two metal waveguides WR-6 that are connected together. Figure 5.3 shows the S_{11} measurement results of DRWs as antennas. The black line is the return loss of an open-ended WR-6 waveguide.

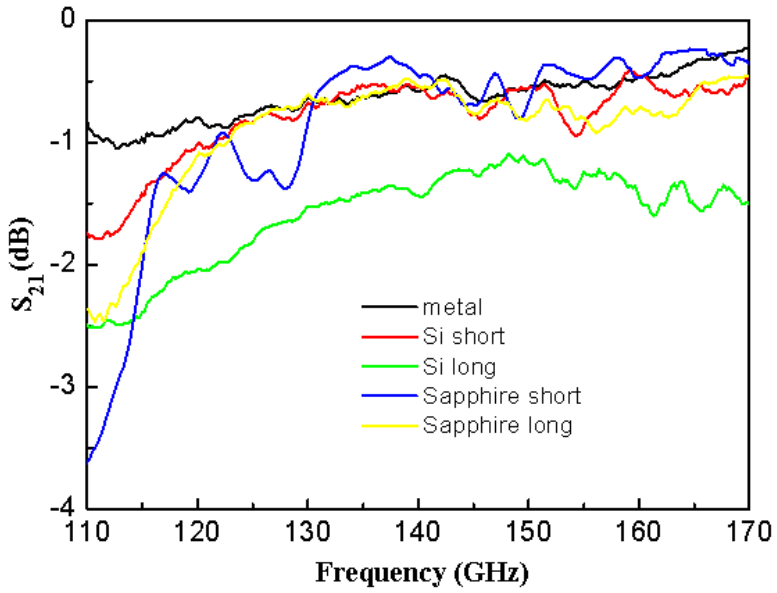

Figure 5.2. Measured S_{21} of different DRWs.

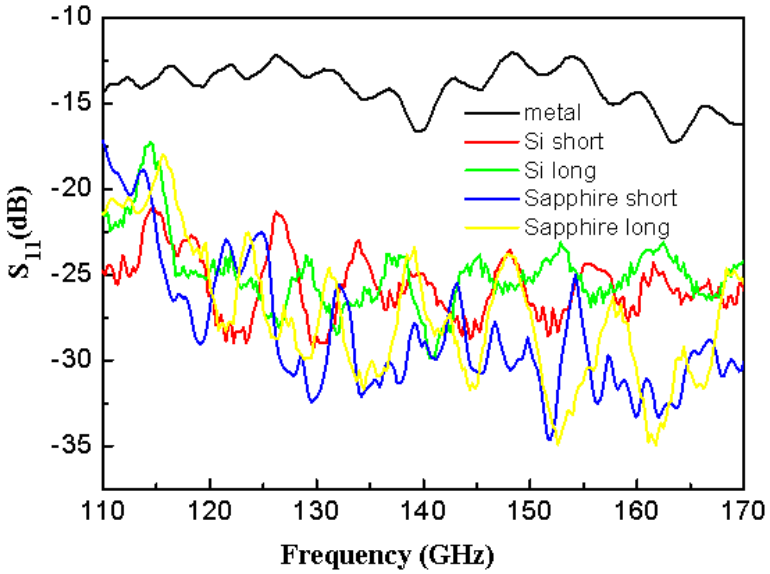

Figure 5.3. Measured S_{11} of different DRWs.

The insertion loss is about 1 dB higher for the long silicon RW over the whole frequency range. In sapphire the difference is not so clear. This result was expected due to higher loss tangent of silicon. The return loss of an open-ended WR-6 is about 10 dB higher than with any of the DRWs.

5.2 Antenna measurements in 110-150 GHz

Measuring antennas at the D band is also not so straight forward as in lower frequencies. The instrumentation of the antenna test range is complicated at the millimetre wavelengths, mostly because there is not much power available at these wavelengths and the coherent power sources are often expensive. In addition to the low power available, the atmospheric losses are high in millimetre wavelengths and thus the available dynamic range becomes often a problem.

The far-field distance can be calculated from the following equation

$$d=2D^2/\lambda, \qquad (6.1)$$

where D is the largest dimension of the antenna aperture (cross-section). In the dielectric rod waveguide antennas the antenna cross-section dimensions are often very small, thus the far field distance does not become a problem. If we consider the width of the metal waveguide including also the metal that radiates, 3.7 mm, as the largest dimension, the far field distance can be calculated to start at 10 mm from the antenna at 110 GHz and at 27 mm at 300 GHz. Normally it is good to measure the antenna even at the distance of $50D^2/\lambda$ if possible to reduce the changes in radiation pattern due to phase error [46].

The measurements are carried out with AB Millimetre millimetre-wave vector network analyzer (MVNA). Figure 5.4 presents the basic measurement setup. Different components and extensions are needed depending on the frequency range.

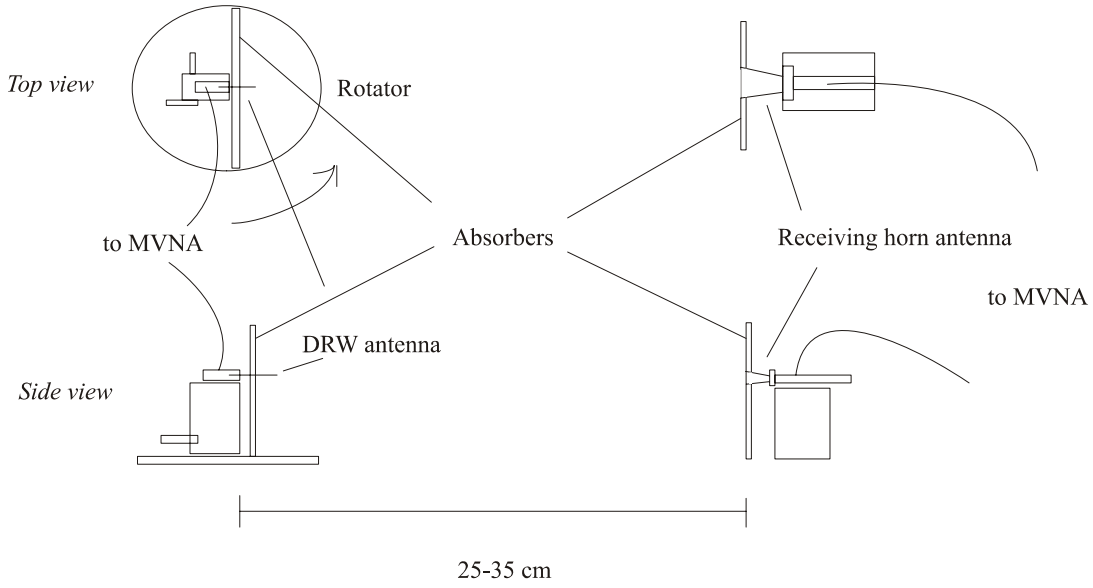

Figure 5.4. Antenna measurement setup.

A rotator with a step motor is used to rotate the DRW antenna. Support structures of the antennas are covered as well as possible with absorbers to avoid the reflections in the test range. LabView™ based program is used to control the rotator and to collect the measurement data from the MVNA.

The radiation patterns are recorded in both main axis, in H and E plane. H plane is the horizontal plane and E plane the vertical plane. Antenna and the measurement setup are presented in Figure 5.5.

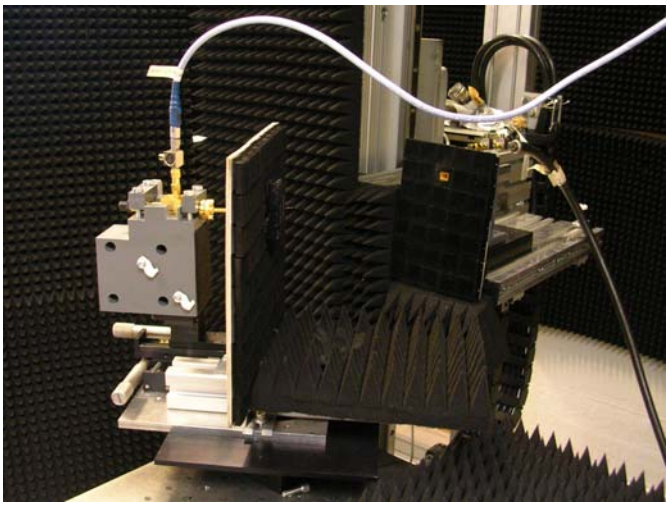

Figure 5.5. D-band antenna measurement setup.

5.2.1 Silicon rod waveguide antenna

One TK THz RAM tile is decided to be used for parasitic radiation suppression. A 4-mm hole is drilled in the middle of the tile and it is attached to a Styrofoam support. Styrofoam is practical in many electromagnetic applications as its electrical parameters are very close to those of air. Nylon screws (M2.5) are used to fix the structure with the waveguide flange. The schematic structure of the silicon rod antenna prototype is presented in Figure 5.6. Teflon films and Styrofoam holder are used to keep the rod in the middle of the metal waveguide.

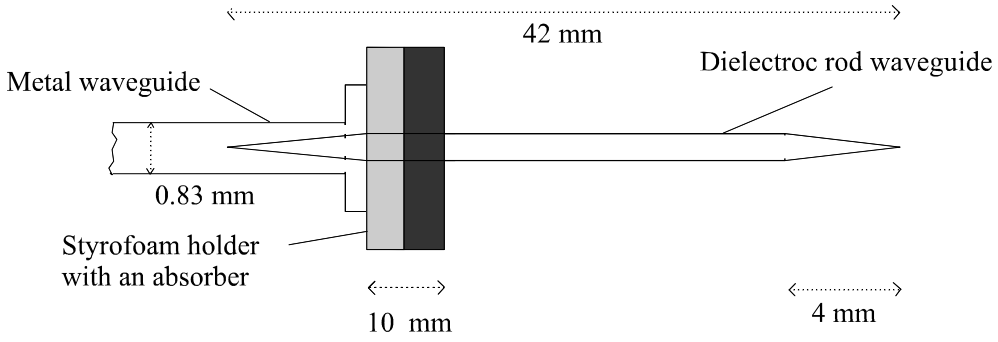

Figure 5.6. D-band sapphire DRW antenna with parasitic radiation absorber.

A silicon rod of the total length of 42 mm with 4 mm E-plane tapers in the both ends (Figure 5.7) is inserted into the standard WR-6 metal waveguide. Figures 5.8 and 5.9 present the recorded radiation patterns at the frequencies from 110 GHz to 150 GHz with 10 GHz step. Patterns are measured also at 160 GHz and 170 GHz, but the dynamic range of the MVNA is too low for good measurement results. MVNA is able for good dynamic range also at these frequencies, but it requires the use of the extension sections and also the change of the whole setup.

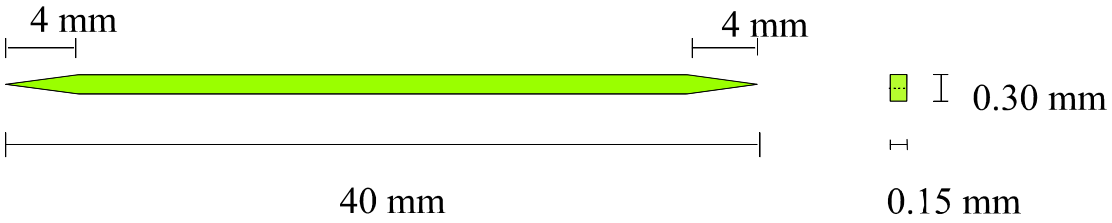

Figure 5.7. Dimensions of the measured silicon rod.

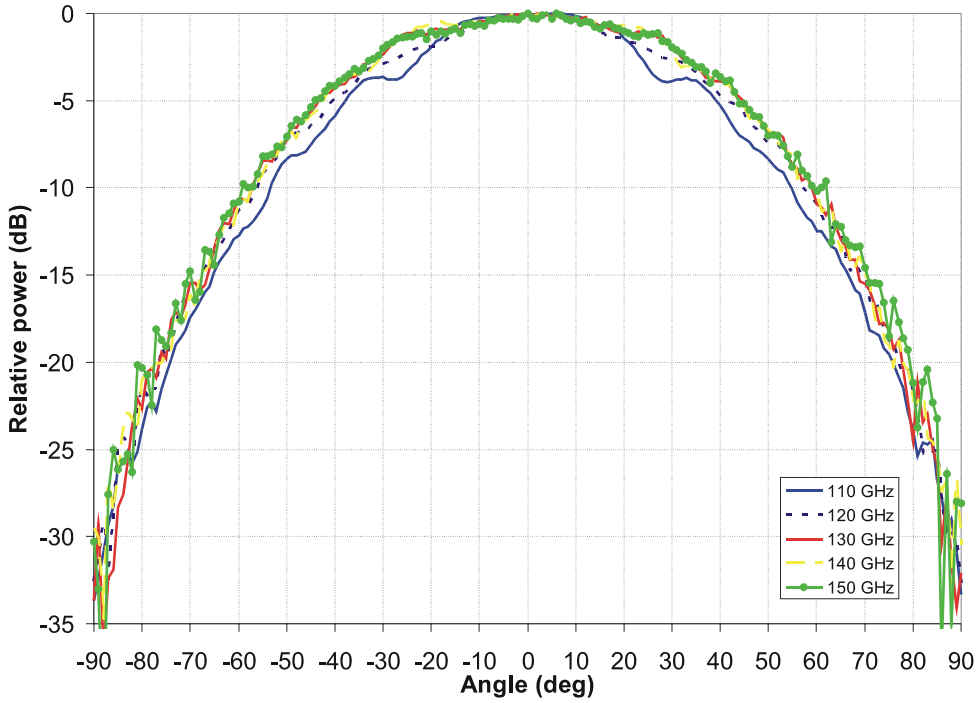

Figure 5.8. Measured H-plane radiation pattern of the silicon RW antenna at 110-150 GHz.

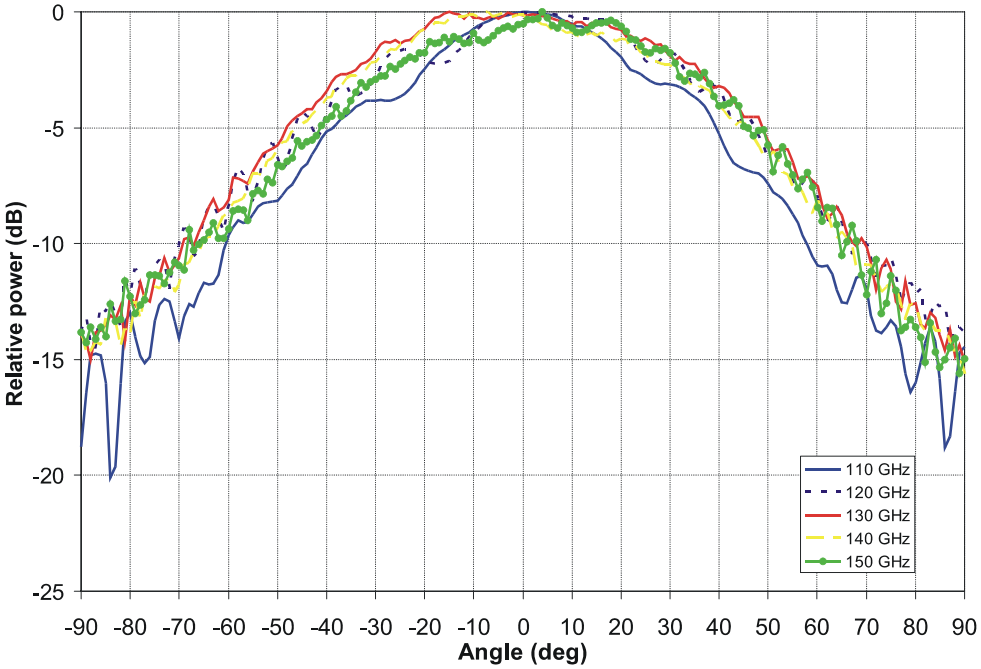

Figure 5.9. Measured E-plane radiation pattern of the silicon RW antenna at 110-150 GHz.

The radiation patterns seem to have a rather constant beamwidth over the measured frequency range. Exception is the pattern at 110 GHz that is narrower compared to the rest of the results, about 6˚ narrower than the average in H plane and 15˚ narrower in E plane. This is probably due to worse matching of the rod with this cross-section (0.60 x 0.30 mm^2) at lower frequencies that has been seen earlier both in simulations and measurements. Also the radiation from the transition is larger at lower frequencies and this produces higher sidelobes. Otherwise the absorber seems to work rather well, although in E-plane ripple can be observed especially at 120 GHz.

Table 5.1. Measured beamwidth of the silicon RW antenna in H and E plane.

Frequency	***H-plane beamwidth (-10 dB)***	***E-plane beamwidth (-10 dB)***
110 GHz	108˚	118˚
120 GHz	113˚	136˚
130 GHz	113˚	138˚
140 GHz	114˚	132˚
150 GHz	116˚	133˚

These measurement results are compared to simulations at two frequencies, 120 and 140 GHz (Figures 5.10 and 5.11). Simulated structure is similar to the structure that has been used in Section 4.2.1.

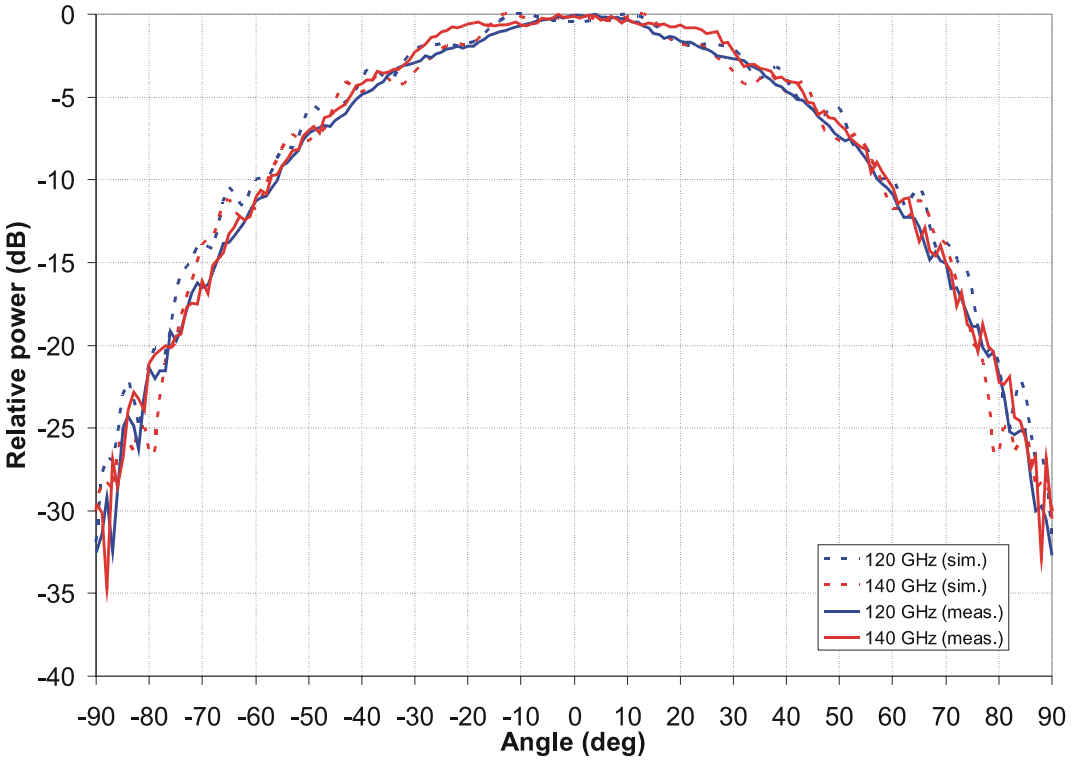

Figure 5.10. Comparison of the measured and simulated H-plane radiation patterns.

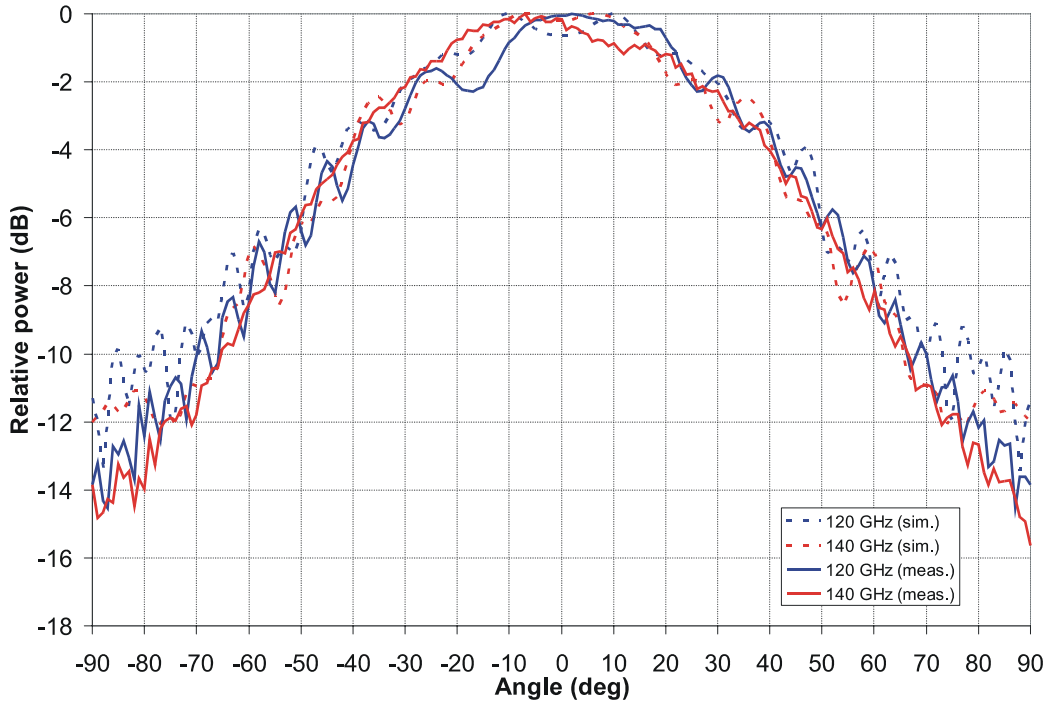

Figure 5.11. Comparison of the measured and simulated E-plane radiation patterns.

In H plane the measured and simulated patterns correspond very well. In E plane the deviation between the results is larger. One reason for that can be that DRW antennas are more sensitive to the vertical position inside the metal waveguide as it has been seen in Section 4.3.4. It seems also that the radiation taper is slightly asymmetric.

5.2.2 Sapphire rod waveguide antenna

The same measurements are performed with a 58-mm long sapphire RW antenna (Figure 5.12). An absorber tile is used around the rod.

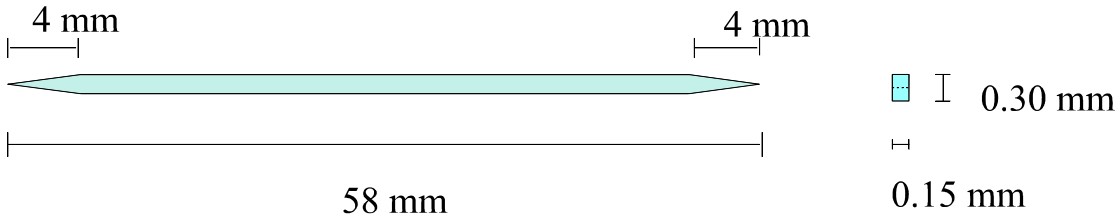

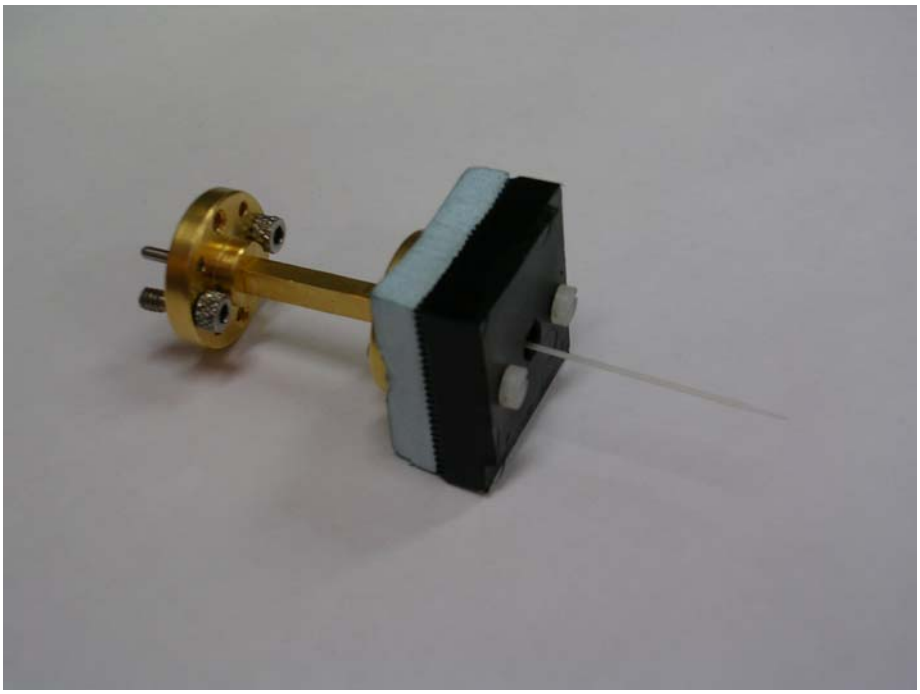

Figure 5.12. The dimensions and a photo of the measured sapphire RW.

Similar setup as that with the silicon antenna is used. The recorded radiation patterns are presented in Figures 5.13 and 5.14 and the measured beamwidths at different frequencies are listed in Table 5.2. As with silicon the pattern at 110 GHz has quite large undulation. Otherwise the beamwidth is quite constant, within 8˚ in H plane and 3˚ in E plane at -10-dB level.

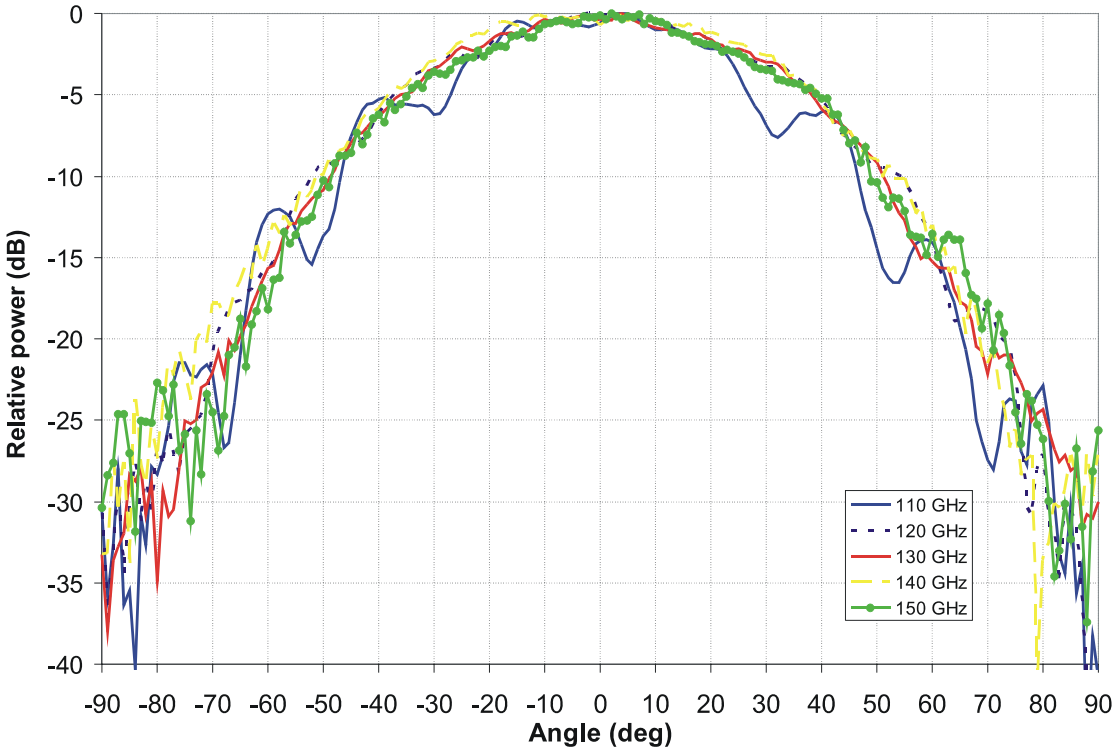

Figure 5.13. Measured H-plane radiation pattern of the sapphire RW antenna at 110-150 GHz.

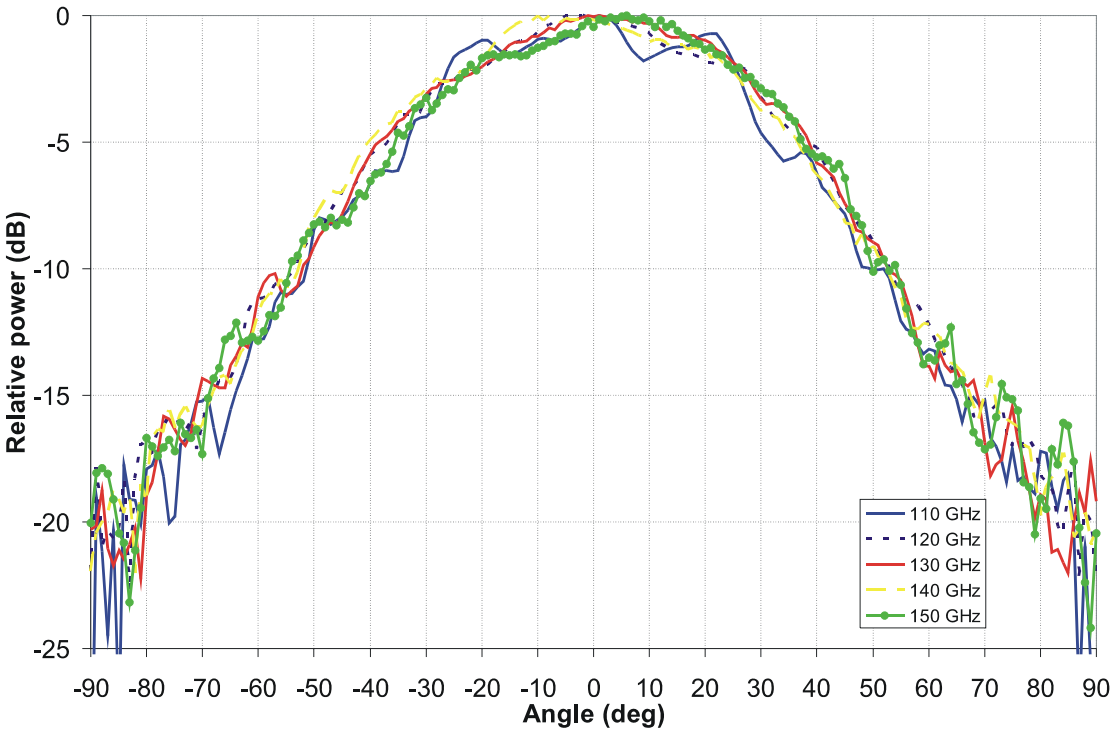

Figure 5.14. Measured E-plane radiation pattern of the sapphire RW antenna at 110-150 GHz.

Table 5.2. Measured beamwidth of the sapphire RW antenna in H and E plane.

Frequency	***H-plane beamwidth (-10 dB)***	***E-plane beamwidth (-10 dB)***
110 GHz	94˚	105˚
120 GHz	106˚	106˚
130 GHz	100˚	105˚
140 GHz	105˚	106˚
150 GHz	98˚	108˚

The measured radiation patterns are compared to simulated patterns at 120 and 140 GHz in Figures 5.15 and 5.16. In H plane the correspondence is again quite good and in E plane the results deviate more as in the case of the silicon antenna.

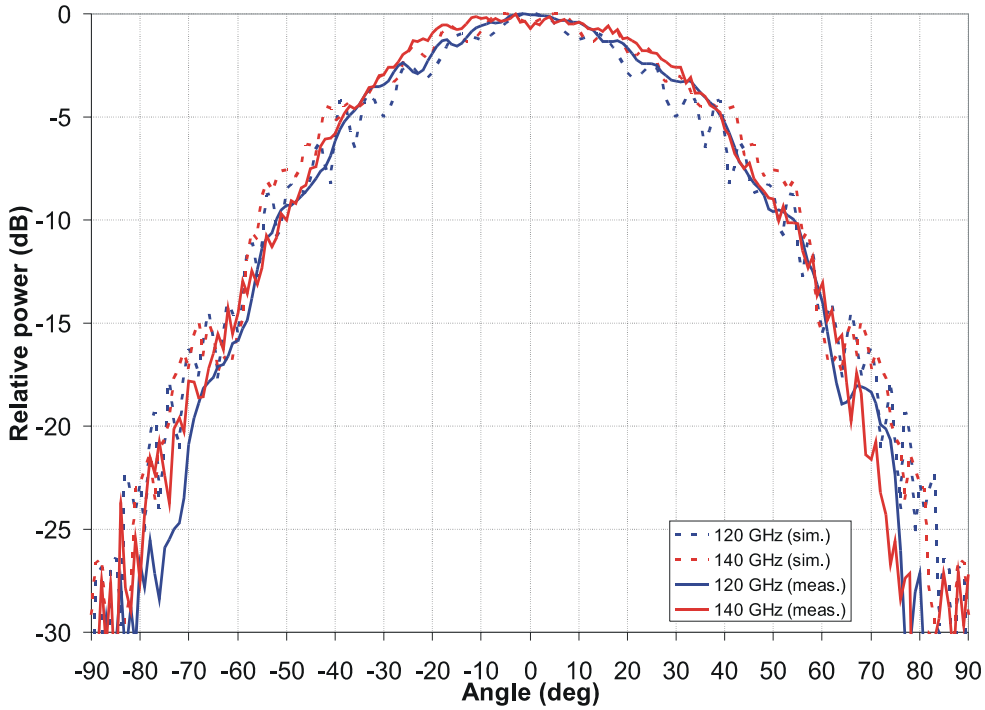

Figure 5.15. Comparison of the measured and simulated H-plane radiation patterns.

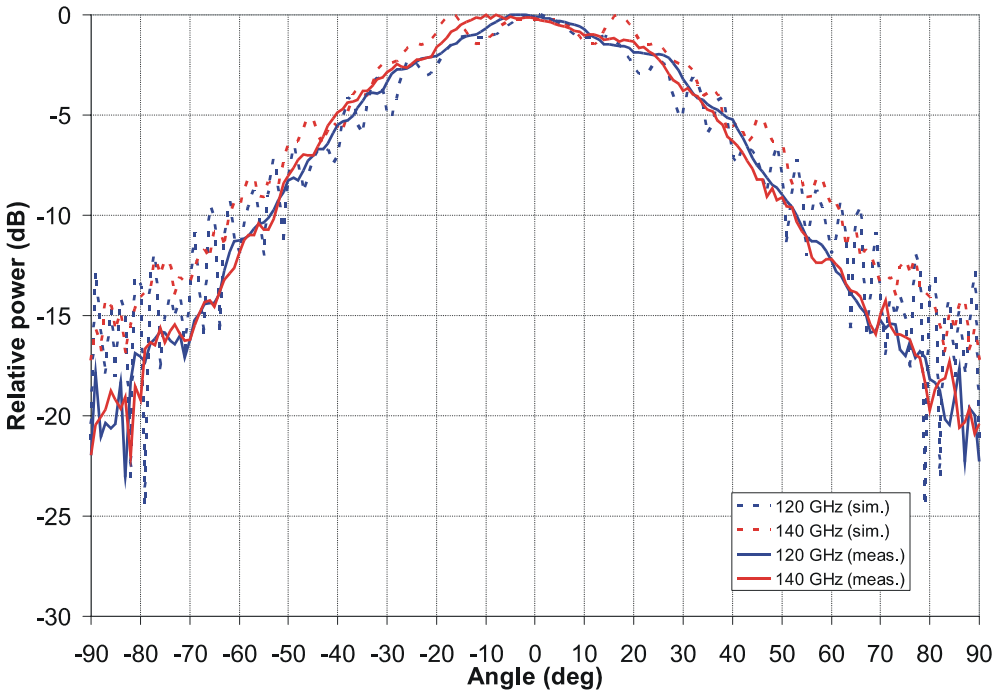

Figure 5.16. Comparison of the measured and simulated E-plane radiation patterns.

5.3 Conclusion of this chapter

In this chapter, silicon and sapphire rod waveguide antennas are measured at D band. Both antennas can be very well matched to a metal waveguide with a very simple configuration. This can be seen in S_{11} measurements that show very good results. The radiation pattern of these antennas is almost frequency independent over a wide frequency range. At lower frequencies the matching is little worse and there is also more radiation from the metal waveguide transition. This alters the radiation pattern at these frequencies.

Measurement results are compared with the simulations and some differences can be seen. As discussed in Section 4.1.1, one reason for differences is that in the simulations the metal waveguide is modeled with infinitely thin PEC boundaries that are outside of the radiation boundary. This model does not take into account the currents flowing on the waveguide external surfaces causing extra radiation. Also the tapers are not perfectly symmetric that can be seen in the measured radiation patterns.

6 DETERMINATION OF THE DRW ANTENNA PHASE CENTRE

For the correct application to millimetre-wave systems (for instance, as reflector/lens feeders), it is essential to determine not only the radiation pattern but also the phase centre position of the DRW antenna, together with the variation of its position when the operating frequency is changed. This chapter provides an approach to DRW antennas radiation pattern characterization and phase centre calculation by means of measurements carried out with a planar acquisition system at W band.

6.1 Phase centre determination

The most straightforward methods for phase centre determination are derived from rotational measurements. In these methods (e.g. [47],[48]), the phase centre can be determined experimentally by finding a spherical equi-phase surface over a range of directions. Then, the centre of this surface corresponds to the phase centre of the antenna. To obtain the phase pattern, the antenna under test is rotated in the test zone of the rotational measuring system. However, rotational measurements at mm-wave frequencies suffer from accuracy problems, yielding inaccurate results [54]. If several measurement planes are desired to be taken into account, several rotators are also needed. Rotary joints at these frequencies are one critical problem due to the ripples introduced into the amplitude and the uncertainty of the phase pattern.

Thus, in this work the main purpose is to explore the phase centre position for mm-wave DRW antennas with a planar acquisition system. Three different analysis methods for the computation of the phase centre of the DRW antennas are applied and they are briefly described in this section.

6.1.1 Least squares fit

The calculation of the phase centre with the least squares fit technique comes from the comparison between the measured phase and the theoretical phase for different distances (DRW antenna to probe distances). The distance that provokes the smallest deviation of theoretical results compared to the measured ones is the one that establishes the phase centre position. As mentioned, to minimize the deviation between the theory and the measurements, the least squares fit procedure is applied with the theoretical phase value as given in Figure 6.1 and Equation (6.1). Equation (6.2) gives the minimum phase deviation calculation for the least squares fit, for different distances from the probe. Variables x_n and y_m identify the measurement points in the *x-y* measuring grid.

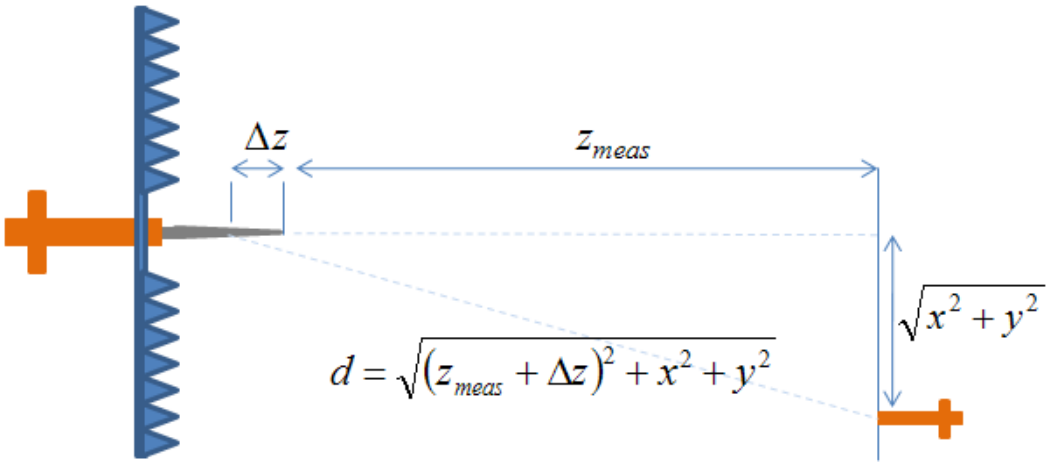

Figure 6.1. Measurement setup. The tip of the DRW antenna is located at the origin of the coordinate system. The measurement grid lays in the x-y –plane at $z = z_{meas}$. Phase centre corresponds to the distance Δz from the tip.

$$\varphi_{th}(x, y, \Delta z) = \frac{2\pi}{\lambda}\sqrt{(z_{meas} + \Delta z)^2 + x^2 + y^2} \quad (6.1)$$

$$S(\Delta z) = \min \sum_n \sum_m (\varphi_{meas}(x_n, y_m, z_{meas}) - \varphi_{th}(x_n, y_m, z_{meas} + \Delta z))^2 \quad (6.2)$$

where z_{meas} is the fixed distance from the tip of the DRW antenna (located at the origin) to the measurement grid, Δz is the distance from the tip to the phase centre, $\varphi_{meas}(x_n,y_m,z_{meas})$ and $\varphi_{th}(x_n,y_m,z_{meas}+\Delta z)$ are the measured and theoretical phase value at each point (x_n,y_m) of the grid.

6.1.2 Least squares fit with weighting coefficients

This approach should be considered as a variation of the previous one, considering coefficients for the different terms of the summation: the values corresponding to points placed far away from the boresight direction are considered with lower weight. The weighting coefficients are identified with the values of the amplitude in the radiation pattern, normalized to the highest amplitude value. Thus, the weight applied to each point of the grid is directly related to the importance of each point in the phase configuration. Equation (6.3) yields the modified computation of the phase error considering the weighting coefficients.

$$S(\Delta z) = \min \sum_n \sum_m A_{meas}(x_n, y_m, z_{meas})(\varphi_{meas}(x_n, y_m, z_{meas}) - \varphi_{th}(x_n, y_m, z_{meas} + \Delta z))^2 \quad (6.3)$$

where $A_{meas}(x_n,y_m,z_{meas})$ is the normalized measured amplitude and $\varphi_{meas}(x_n,y_m,z_{meas})$ and $\varphi_{th}(x_n,y_m,z_{meas}+\Delta z)$ are, again, the measured and theoretical phase values at each point (x_n,y_m) of the grid.

6.1.3 Plane wave spectrum analysis method

This third analysis method proposed in this work gives importance to the application of the DRW antenna as a feed of a parabolic reflector. A parabolic reflector antenna transforms a spherical wave front to a planar one, when the source of the spherical wave

front is placed in the focus of the reflector. Indeed, it would be possible to measure the position of the DRW antenna phase centre by repeated directivity measurement of a well-defined parabolic reflector antenna. The z-coordinate of the DRW antenna would be iteratively varied until its apparent phase centre and focus of the reflector coincide, indicated by the global maximum of the directivity of the antenna system.

The above-mentioned iteration for the highest directivity could be performed computationally using measured radiation pattern of the DRW antenna and by a conceptual parabolic reflector antenna. However, the proposed analysis method is based on a planar measurement at a fixed distance and, therefore, the above-mentioned iteration cannot be fully adopted here. The measurement distance defines the focal length of the conceptual parabolic reflector being $z_{meas}+\Delta z$. Figure 6.2 illustrates the iteration of the conceptual parabolic reflector. Three reflectors with different focal lengths are shown. Measured DRW source is applied to the focus of the conceptual reflector, a planar wave front emerges only when the focus coincides with the phase centre of the DRW antenna (solid line, case 3).

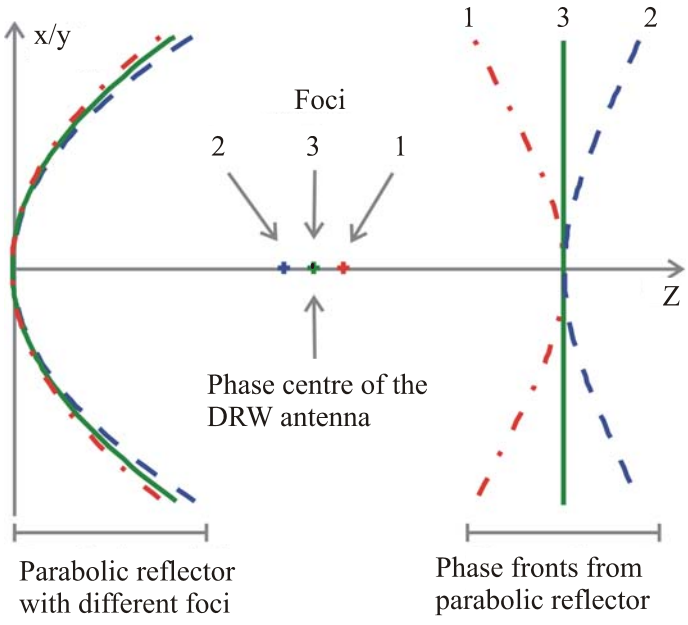

Figure 6.2. Iterative phase centre determination.

The consideration of the conceptual reflector antenna yields complex geometric calculations in terms of distances. However, the geometry of the parabolic configuration and its complexity can be significantly simplified with the calculation of the plane wave spectrum (PWS) of the equivalent array of sources, with the proper choice of the amplitude and phase value in each point of the array. DRW antenna and the conceptual parabolic reflector are replaced by the equivalent array of sources placed at the measurement plane. The size of the corresponding antenna array being the same as the measurement grid differs slightly from the size of the aperture of the conceptual parabolic reflector. However, in this case this has no effect on the results of the iteration.

The PWS of the equivalent array is as follows:

$$F(k_x,k_y,\Delta z)=\sum_m\sum_n A_{meas}(x_n,y_m,z_{meas})\exp(j\phi(x_n,y_m,z_{meas}+\Delta z)+jnk_x\Delta x+jmk_y\Delta y) \quad (6.4)$$

$$\phi(x_n,y_m,\Delta z)=\varphi_{meas}(x_n,y_m,z_{meas})-\varphi_{th}(x_n,y_m,z_{meas}+\Delta z) \quad (6.5)$$

where, again, $A_{meas}(x_n,y_m,z_{meas})$ and $\varphi_{meas}(x_n,y_m,z_{meas})$ are the measured amplitude and phase at each point (x_n,y_m) of the measuring grid, $d_{x/y}$ is the distance between points in the grid, k_x and k_y are the components of the wave vector in Cartesian coordinate system and m and n are the reference to the location of the different points in the grid. $\varphi_{th}(x_n,y_m,z_{meas}+\Delta z)$ is the expected phase value at each point of the grid, according to (6.2). In this case, the phase centre of the DRW antenna coincides with the value of $z_{meas}+\Delta z$ which provides the highest directivity estimation from the PWS, according to (6.4).

6.2 Phase centre measurements

In this section, the results obtained in the planar acquisition system are processed in order to derive the phase centre of the DRW antenna with the three analysis methods

previously mentioned. The two different DRW antennas (sapphire and silicon) are measured at four different frequencies (83.5, 93.5, 103.5, and 113.5 GHz). The cross-section of the antennas is 0.5 x 1.0 mm^2. Length of the silicon rod is 42 mm. Sapphire rod is 20 mm long. Tapering section in the antennas used in this study is 6 mm in both radiation and feed ends.

Source compensation is applied to the measured results, in order to have the correct radiation pattern of the DRW antennas. These amplitude pattern values are used in two of the three analysis methods for phase centre determination. The measurements are done with AB Millimètre MVNA-8-350 vector network analyzer. A NSI 200V–5x5 planar scanner is used in the far field. The planarity of the scanner is approximately ±5-10 μm. The measured antenna model is presented in Figure 6.3.

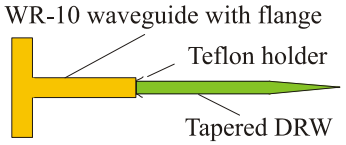

Figure 6.3. DRW antenna prototype model used in measurements.

The planar measurement setup includes an open-ended WR-10 waveguide [55], Figure 6.4, as a probe. As previously mentioned, the effects of the probe have to be eliminated from the measurements. The open-ended WR-10 waveguide is selected in order to have low influence of the probe in the pattern measurements due to its inherently wide beam.

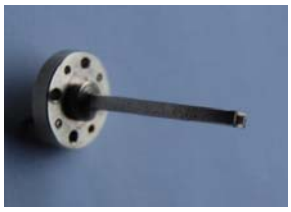

Figure 6.4. Open-ended WR-10 waveguide as a measuring probe.

The planar setup for measurements is fixed as follows (Figure 6.5):

- $A=z_{meas}$ = 204 mm and 224 mm, two distances for each antenna and frequency, in order to validate results obtained for the phase centre location.
- B = 11.5 mm for sapphire antenna, 19 mm for silicon antenna.
- C = 210 mm both in *x*- and *y*-coordinates. This dimension, together with $z_{meas.}$, results in about ±30° field of view. Please note that this is approximately the area capturing the main beam of the DRW antenna. This choice reflects potential use of the DRW antenna as a feed for a reflector.

The pattern is acquired for a rectangular grid ($\Delta x = \Delta y$ = 1.05 mm).

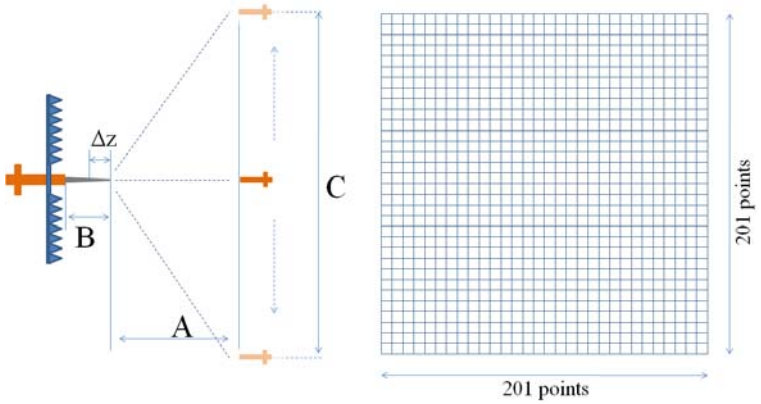

(a) (b)

Figure 6.5. Measurement setup: a) dimensions and distances, b) measuring grid. The part of the DRW antennas outside the waveguide, B, is 11.5 mm and 19 mm for sapphire and silicon antennas, respectively.

6.2.1 Probe compensation

The DRW antenna phase and amplitude patterns are corrected by means of the subtraction of the probe pattern. These patterns are measured using two identical open-ended WR-10 waveguide probes. The measured patterns contain information of both antennas working together and are corrected accordingly. The phase centre of the open-ended waveguide probe is located very accurately at the aperture [56].

6.2.2 Radiation pattern measurements

Figure 6.6 presents the measured 3D pattern of the silicon rod antenna at 83.5 GHz. Figure 6.7 presents the radiation pattern of the same antenna at four different frequencies in a traditional plot.

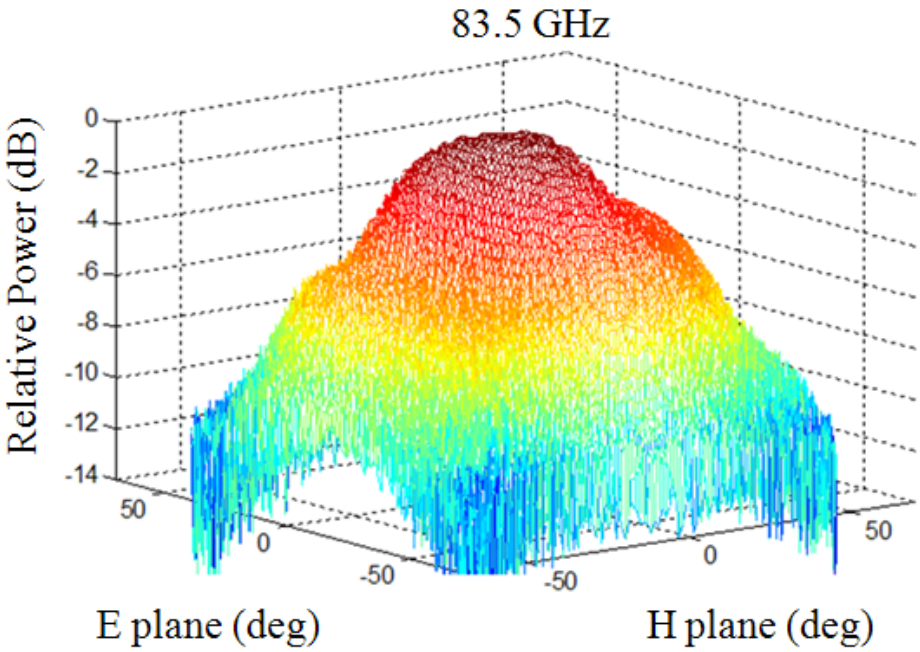

Figure 6.6. 3D radiation pattern of a silicon rod antenna at 83.5 GHz.

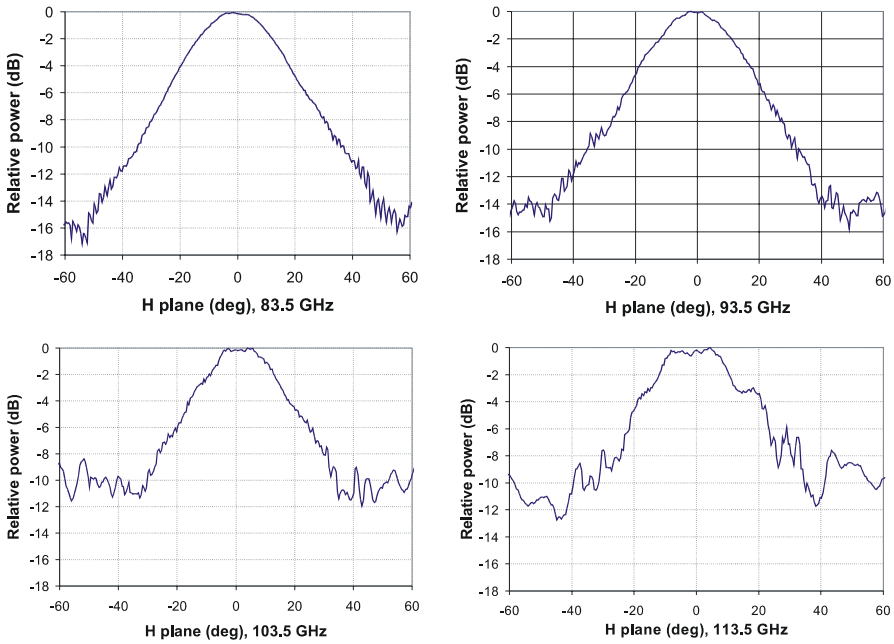

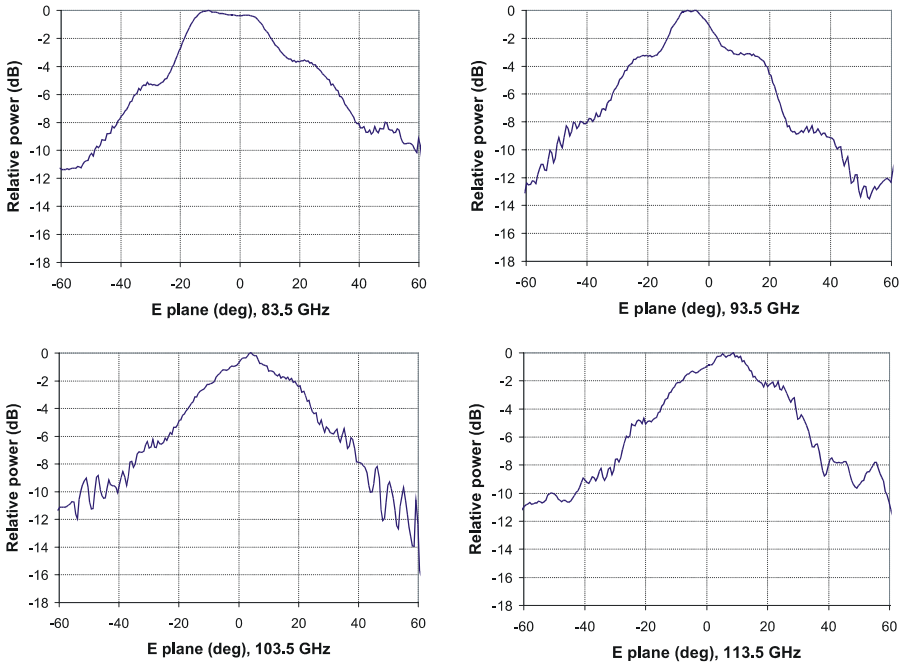

Figure 6.7. W-band radiation patterns of a silicon rod antenna measured with a planar scanner.

It can be observed from the radiation patterns that the dynamic range of the measurement system is getting lower as the frequency increases. This causes distortion to the results. It can be also seen that the E-plane patterns are slightly asymmetric. Partly this is due to the small asymmetry in the radiation taper. Another reason is that the matching from the metal waveguide to the DRW is worse at lower frequencies. This causes more additional radiation from the transition region.

6.2.3 Phase centre location results

Results obtained in the planar scanner acquisition system, with probe compensation, are processed in order to derive the phase centre position of the two different DRW antennas, with the three different approaches previously described. MATLAB™ is used for data processing and analysis.

Figures 6.9 and 6.10 offer the results for sapphire and silicon DRW antennas, respectively, for two different distances (z_{meas}) to the probe. Table 6.1 summarizes the phase centre results for both DRW antennas.

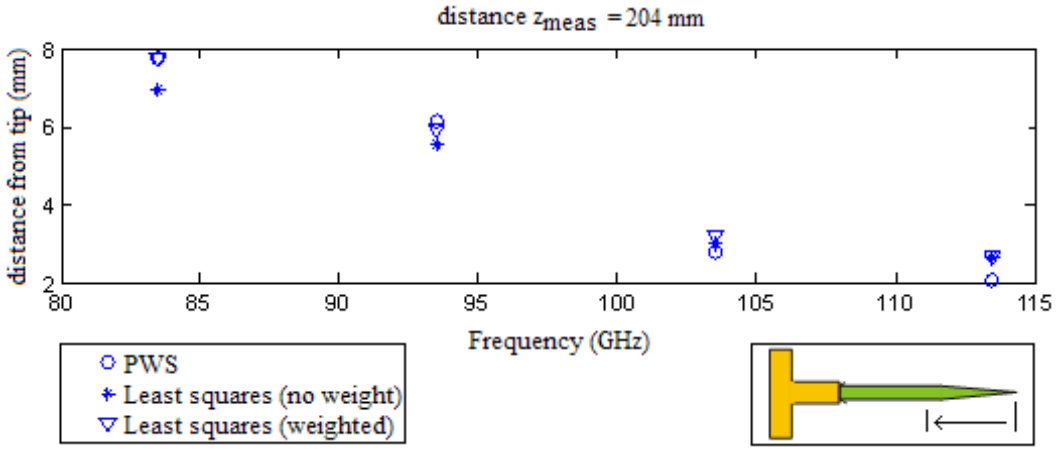

(a)

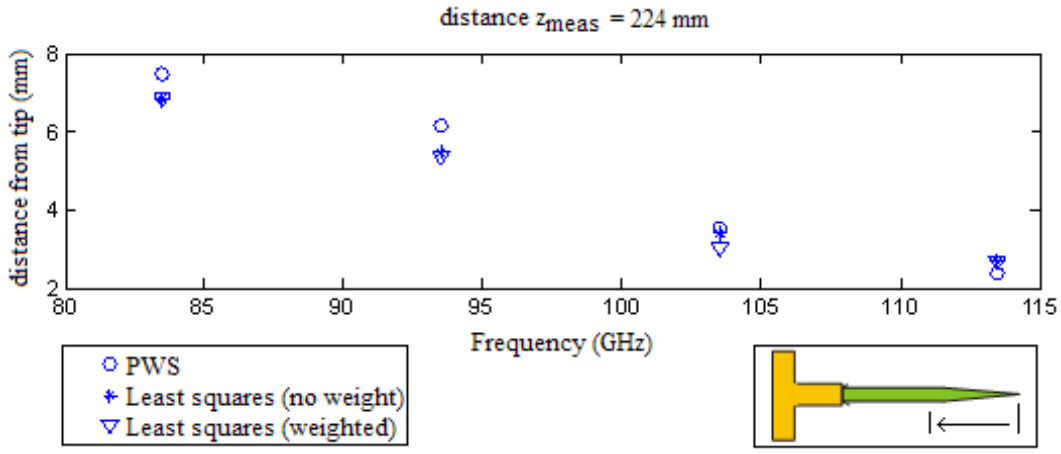

(b)

Figure 6.8. Comparison between the phase centre positions determined by the three methods at different frequencies, for sapphire RW antenna, a) 204 mm, b) 224 mm.

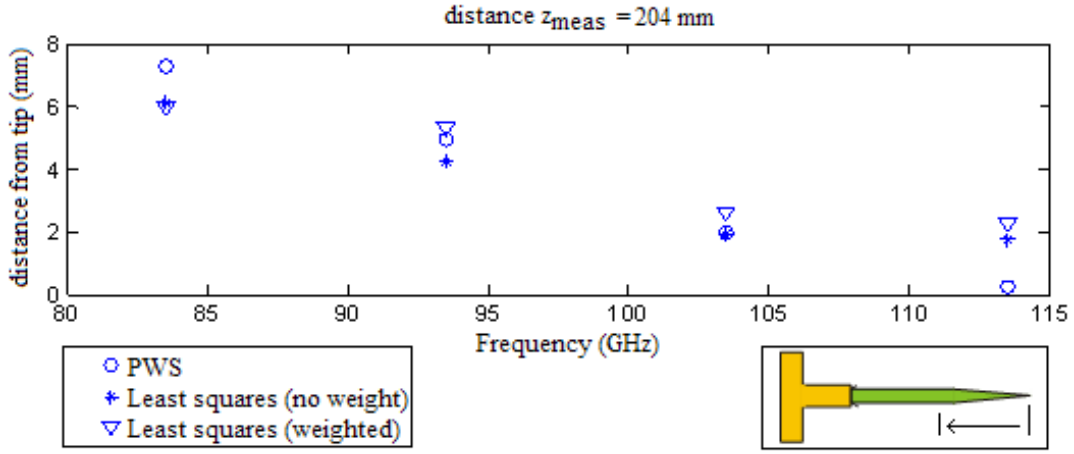

(a)

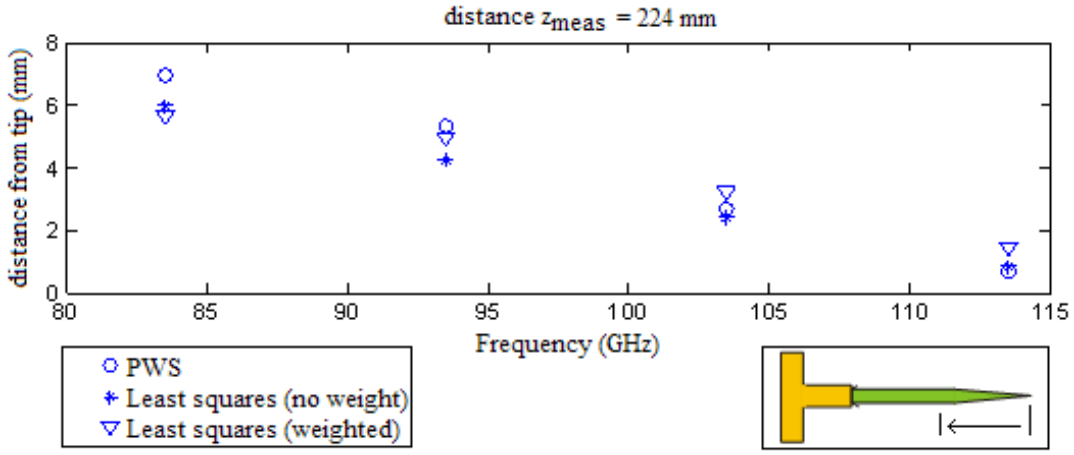

(b)

Figure 6.9. Comparison between the phase centre positions determined by the three methods at different frequencies, for silicon RW antenna, a) 204 mm, b) 224 mm.

The differences appearing in the results are not due to the measurement instrumentation. The effect of mechanical uncertainties in relation to phase centre position determination can be estimated to be in the order of 0.1 mm or less. However, uncertainty in the manually measured distance, z_{meas}, remains. The estimated uncertainty of manual measurement is ±0.5 mm. As a consequence, the vertical scale in Figures 6.9 and 6.10 is uncertain up to this value.

Table 6.1. Calculated phase centre position (from the antenna tip) for the different analysis methods, for sapphire and silicon DRW antennas.

Planar system probe to DRW antenna distance z_{meas} = 204 mm						
	Sapphire DRW antenna			Silicon DRW antenna		
Frequency (GHz)	Least sq. (no coeff.) (mm)	Least sq. (with coeff.) (mm)	PWS (mm)	Least sq. (no coeff.) (mm)	Least sq. (with coeff.) (mm)	PWS (mm)
83.5	6.9	7.7	7.7	6.1	5.9	7.2
93.5	5.5	5.9	5.9	4.2	5.3	4.9
103.5	3.4	3.2	3.0	1.9	2.6	2.0
113.5	2.6	2.6	2.6	1.7	2.1	0.2
Planar system probe to DRW antenna distance z_{meas} = 224 mm						
	Sapphire DRW antenna			Silicon DRW antenna		
Frequency (GHz)	Least sq. (no coeff.) (mm)	Least sq. (with coeff.) (mm)	PWS (mm)	Least sq. (no coeff.) (mm)	Least sq. (with coeff.) (mm)	PWS (mm)
83.5	6.8	6.8	7.4	5.9	5.6	6.9
93.5	5.4	6.1	6.1	4.2	4.9	5.3
103.5	3.4	2.8	3.5	2.4	3.2	2.7
113.5	2.6	2.0	2.3	0.8	1.4	0.6

The abovementioned results are based on the selection of the ±30° field of view. Different choice of the field of view might result in slightly different phase centre position. When the tendency of the obtained results for the phase centre position is analyzed, it can be seen that, as was expected, it is moving towards the tip of the antenna when the frequency is increased. The measured movement of the phase centre towards the tip of the DRW antenna is linked to the nearly frequency independent beamwidth that has been observed for these antennas. This is due to the fact the electromagnetic wave propagates further in the rod as the frequency increases.

Also the effect of the antenna material can be seen. Silicon has slightly higher relative permittivity compared to sapphire that makes the wavelength inside the DRW shorter. The phase centre is ~1 mm closer to the tip at all frequencies in the silicon antenna than in the sapphire antenna.

When analyzing the results further, it is seen that there is a slight difference between the PWS method and the least squares fit method (either with or without weighting coefficients). Indeed, simple analytical and numerical analyses show that these methods give slightly different results in the realistic case of non-spherical wave fronts. When applying to an ideal isotropic antenna, these methods converge to the same results. It is suggested that the PWS method is applied when designing a reflector system with highest directivity as it gives importance to the application of the DRW antenna as a feed of a parabolic reflector.

If the DRW antenna is feeding a reflector structure, in optimal case the antenna phase centre is located in the focus of the reflector. However, this is valid only for one frequency. Thus if the antenna is correctly located, for instance at 83.5 GHz, the phase centre will be slightly moved towards the tip at higher frequencies. Tables 6.2 and 6.3 present the effect to the directivity when the feed antenna phase centre is dislocated from the focus of the parabolic reflector. Results are obtained with the PWS analysis. For example, it can be seen that the directivity is diminished with 1.3 dB if the silicon antenna location optimized at 83.5 GHz is used at 113.5 GHz.

Table 6.2. Effect of the antenna location to the directivity of a reflector, sapphire antenna.

Ref. CENTRE	83.5GHz	93.5GHz	103.5GHz	113.5GHz
Centre placed at d=7.45mm	-0dB (Δd=0mm)	-0.036dB (Δd=1.3mm)	-0.39dB (Δd=3.95mm)	-0.78dB (Δd=5.1mm)
Centre placed at d=6.15mm	-0.04dB (Δd=-1.3mm)	-0dB (Δd=0mm)	-0.179dB (Δd=2.65mm)	-0.37dB (Δd=3.8mm)
Centre placed at d=3.5mm	-0.356dB (Δd=-3.95mm)	-0.146dB (Δd=-2.65mm)	-0dB (Δd=0mm)	-0.037dB (Δd=1.15mm)
Centre placed at d=2.35mm	-0.55dB (Δd=-5.1mm)	-0.515dB (Δd=-3.8mm)	-0.033dB (Δd=-1.15mm)	-0dB (Δd=0mm)

Table 6.3. Effect of the antenna location to the directivity of a reflector, silicon antenna.

Ref. CENTRE	83.5GHz	93.5GHz	103.5GHz	113.5GHz
Centre placed at d=6.95mm	-0dB (Δd=0mm)	-0.056dB (Δd=1.6mm)	-0.49dB (Δd=4.25mm)	-1.3dB (Δd=6.3mm)
Centre placed at d=5.35mm	-0.044dB (Δd=-1.6mm)	-0dB (Δd=0mm)	-0.186dB (Δd=2.65mm)	-0.71dB (Δd=4.7mm)
Centre placed at d=2.7mm	-0.31dB (Δd=-4.25mm)	-0.151dB (Δd=-2.65mm)	-0dB (Δd=0mm)	-0.13dB (Δd=2.05mm)
Centre placed at d=0.65mm	-0.64dB (Δd=-6.3mm)	-0.45dB (Δd=-4.7mm)	-0.111dB (Δd=-2.05mm)	-0dB (Δd=0mm)

6.3 Conclusion of this chapter

In this chapter, the phase centre of the silicon and sapphire rod antennas is defined experimentally with three analysis methods at four different frequencies at W band. The measurements are done with the planar scanner. The three analysis methods used are the least squares fit, the least squares fit with weighting coefficients and the plane wave spectrum (PWS) analysis method. The results with different methods contain some differences, but they correspond each others rather well. As expected, the tendency of the phase centre is to move closer to the antenna tip as the frequency increases.

7 HIGH-PERMITTIVITY DIELECTRIC ROD WAVEGUIDE AS AN ANTENNA ARRAY ELEMENT

As dielectric rod waveguides have a small cross-sectional area, and this way a high packing potential, it might be interesting to use them in antenna arrays. As it has been shown in previous sections, high-permittivity DRW antennas of rectangular cross-section have a broadband input matching and the EM field is concentrated near the rod. Horizontally tapered rods offer also a low polarization cross-coupling. This will probably provide a low mutual coupling between the elements combined with a high packing potential that is often desired in antenna arrays. In this section a two-element DRW antenna for W band is analyzed with simulations and prototype measurements. Figure 7.1 illustrates the possible use of DRWs in a 2 x 2 antenna array block.

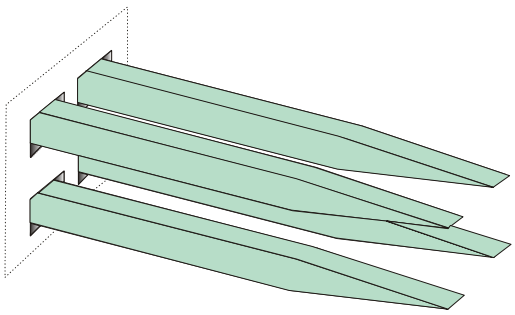

Figure 7.1. Illustration of a 2 x 2 DRW antenna array block.

7.1 DRW arrays

In general an antenna array enables a larger gain and narrower beam than a single antenna element. By changing the element spacing and increasing the number of elements a wide variety of radiation patterns can be created. However, it has to be remembered that the larger the number of elements, the more complex will be the element feeding network. Another way to create different radiation patterns is to change the phase between the antenna elements. By using electric phase shifters a very effective

beam steering can be achieved. In [57] an integral equation analysis is applied to an infinite array of dielectric waveguides including a mode transition analysis.

The radiation pattern of an antenna array is a product of the element pattern and the array factor. The element spacing larger than one wavelength leads to grating lobes. The directivity as a function of the element spacing reaches local maxima about every 0.9λ [58],[59]. Grating lobes can be suppressed for example by the use of a combination of subarrays and an array amplitude tapering as it has been done in [60].

Earlier, dielectric rod antennas have been studied as optimized feed elements for focal plane arrays [61]. Dielectric rods were made of polyethylene (ε_r = 2.3) and they were fed by slotlines as the metal waveguide feeding requires a horn structure with low permittivity rods. Similar ideas have been used in [62] for an array operating at 8 GHz. Using a horn feed would require too much space and would lead to large element spacing.

HFSS^{TM} is used to simulate a two-element DRW array with different element spacing. The difficulty in modeling the rectangular DRWs is the rapidly changing field near the waveguide corners. Earlier, it has been studied by comparing simulations with measurements, that by setting δ_s = 0.01 (parameter in HFSS referring to the absolute difference between two iterations), a very accurate approximation of electromagnetic fields in rectangular DRWs can be obtained with HFSS [25].

HFSS allows to take the radiation pattern of a single element and then calculate the pattern of an array made of similar elements. Thus the patterns obtained this way do not take into account the mutual coupling between the elements. Figure 7.2 presents the simulated radiation patterns at 90 GHz. If the spacing is $3/2\lambda$, a narrow main beam (between nulls), about 40˚ is obtained, but also high sidelobes. With spacing of one wavelength the main beam is about 60˚ and sidelobes about 6 dB lower. It is decided to manufacture a prototype array with element spacing of one wavelength.

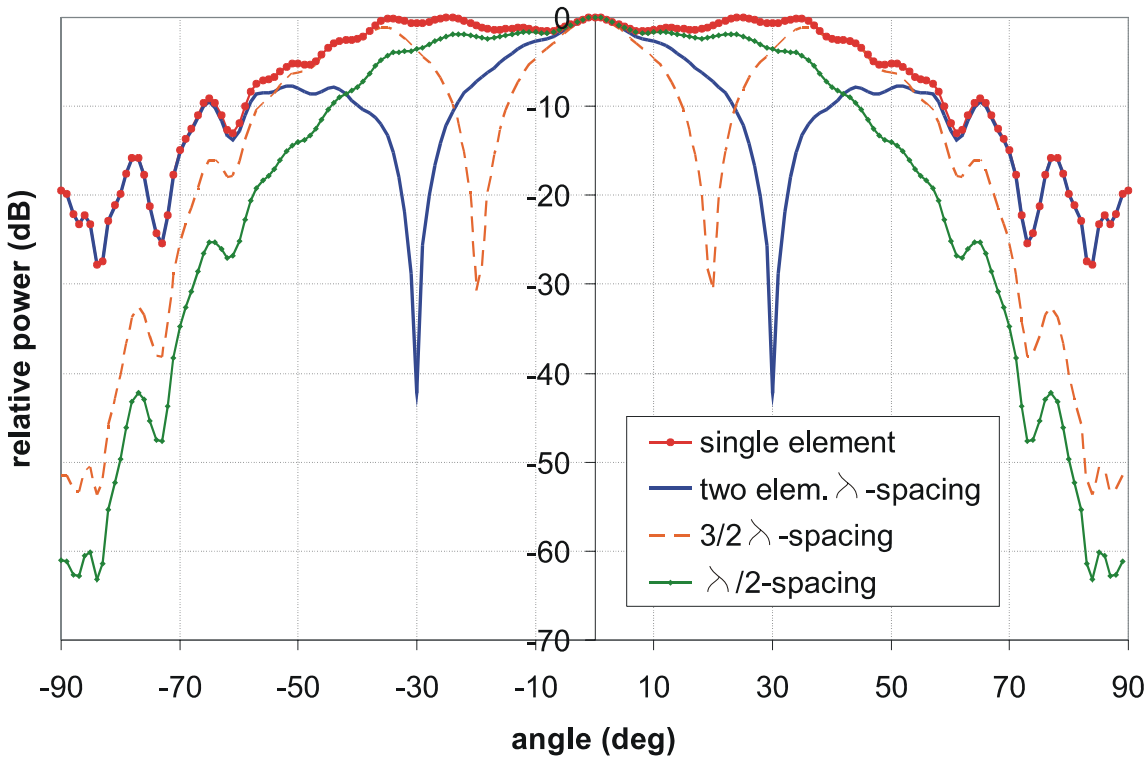

Figure 7.2. Simulated E-plane radiation pattern of a two-element DRW antenna array with λ/2-, λ- and 3/2λ-element separations at 90 GHz.

7.2 Feed system

One problem in DRW antenna arrays is the difficulty to design an efficient feed system with high packing density. In [61] a metal waveguide feed and a slotline feed were considered. In that case, the problem with the metal waveguide transition is the need of a horn as the rod has a low permittivity and thus the required space of the feed is too large. A slotline feed have been studied more in detail in [63] and also in [64],[65]. Figure 7.3 presents the optimal slotline transition designed in [63]. In the proposed transition the slotline substrate was inserted in the middle of the DRW. Insertion losses between 0.5 and 1.5 dB were reported over the frequency band of 60-90 GHz. Also the

mutual coupling between two adjacent transitions was studied. It was estimated to be less than -20…-25 dB when the distance between the lines is 10 mm.

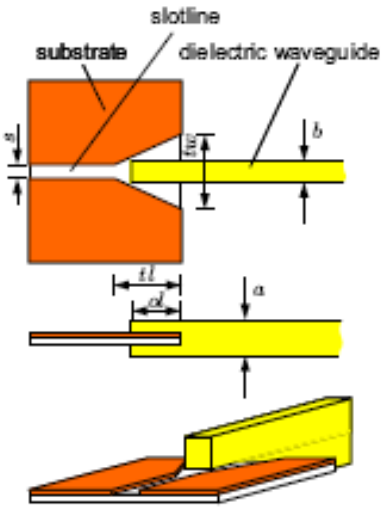

Figure 7.3. Slotline feed for mm-wave dielectric rod waveguides [63].

With high permittivity DRWs in W band the slotline feeds would be very difficult to realize mechanically. But as the high permittivity DRW can be well matched to a regular rectangular metal waveguide, also this type of DRW feed enables less than λ_0 antenna element separation. At 90 GHz $\lambda_0 = c_0 / f \approx 3.3$ mm.

As it is not wanted to study separate channels with separate antennas, the array feed can be designed as a power splitter, where the power is equally divided into two waveguides. Such a splitter is studied and optimized in detail with HFSS™.

As the distance between the middle points of the two feeding waveguides is wanted to be only 3.3 mm, the matching of the junction becomes difficult. However, it is seen in simulations that when the corners near the junction are rounded the matching is significantly improved. Further matching improvement can be done with an inductive post [66],[67]. A post causes reflections that cancel out the reflection of the junction. If the amplitude of the second reflection is equal to the reflection of the junction and with

an opposite phase, the sum reflection of the entire junction is zero. The shape of the object that causes second reflection is irrelevant, but it should have similar frequency dependence as the junction itself. Cylindrical post is often chosen as it is easy to manufacture. An optimal position and size of the post is studied with simulations. It is found out, that the radius of the post should be 0.25 mm, the height 0.2 mm and the distance from the junction wall 1.77 mm. Structure and schematic of the feed system is presented in Figures 7.4 and 7.5.

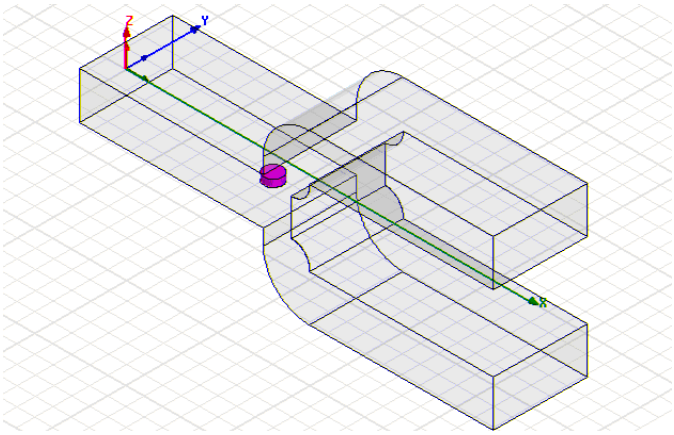

Figure 7.4. Two-element array feed designed with HFSS.

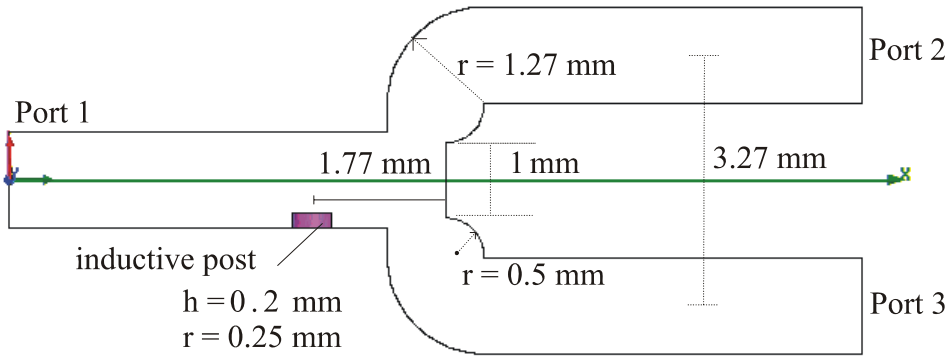

Figure 7.5. Schematic structure of the feed system.

It would be also possible to use two inductive posts to make the system symmetrical. However, it would make to manufacturing more complicated and relatively good performance is already achieved with one post. Feed system is manufactured and measured in Elmika Co., Lithuania. In Figures 7.6-7.8 the simulated and measured S parameters are compared. The port 2 is located in the upper arm of the power splitter. From the results it can be concluded that the splitter works quite well as it was designed. The resonant frequency in the prototype is slightly shifted up from the desired 90 GHz, but still the -20-dB bandwidth is about 10 GHz. The undulations in S_{11} are mostly due to difficulties to match the ports 2 and 3 as they do not have any screws in the flange. The power division is not completely equal between the ports, because of the asymmetry caused by the matching post, but near 3-dB power division is obtained. Figure 7.9 shows the simulated propagating H field in the splitter.

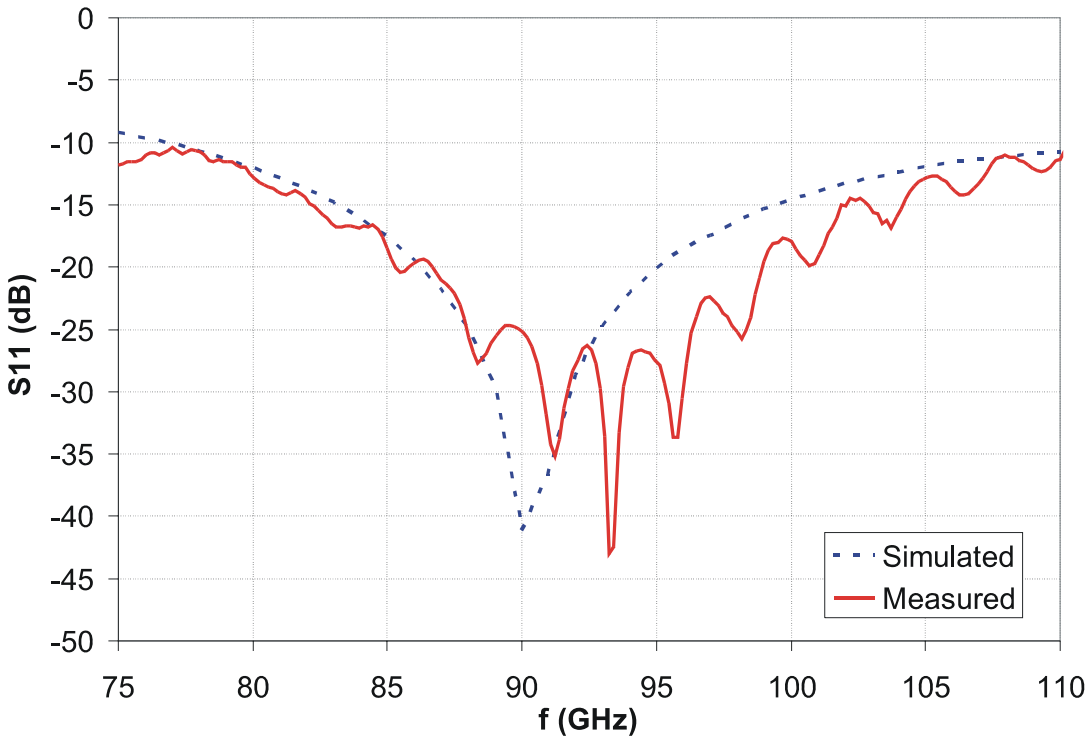

Figure 7.6. Simulated and measured S_{11} of the feed system.

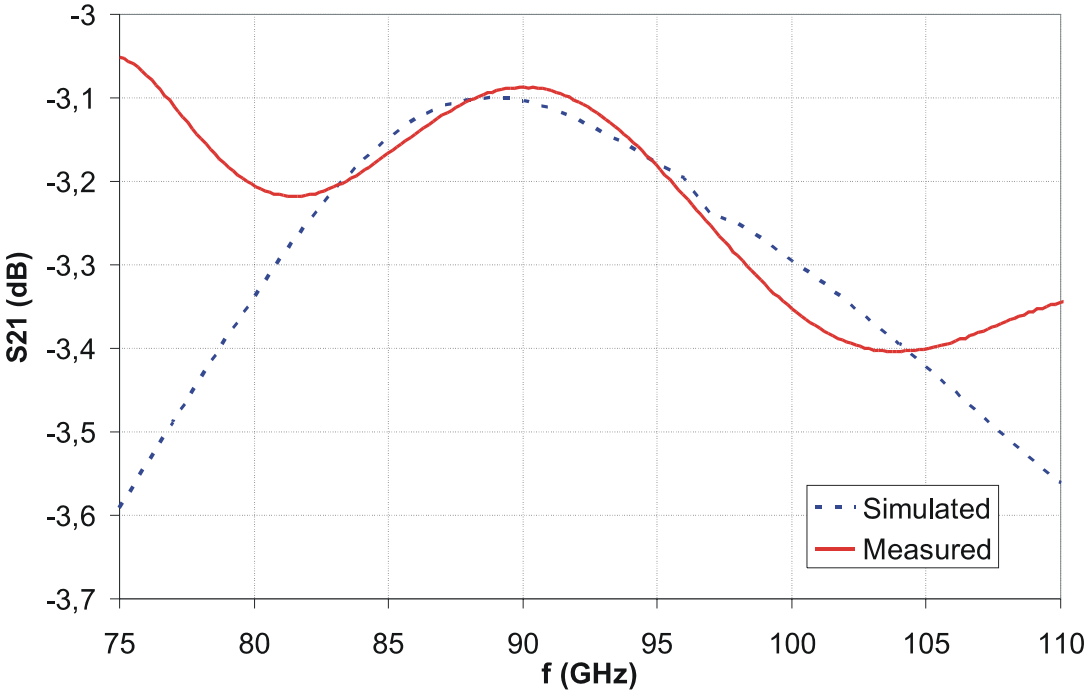

Figure 7.7. Simulated and measured S_{21} of the feed system.

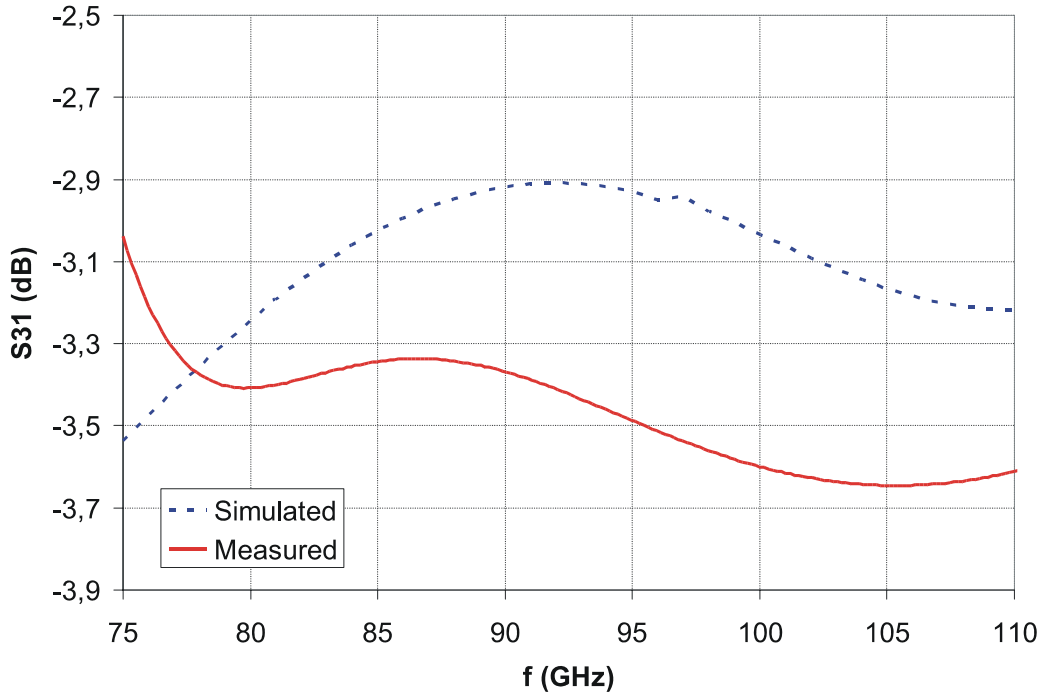

Figure 7.8. Simulated and measured S_{31} of the feed system.

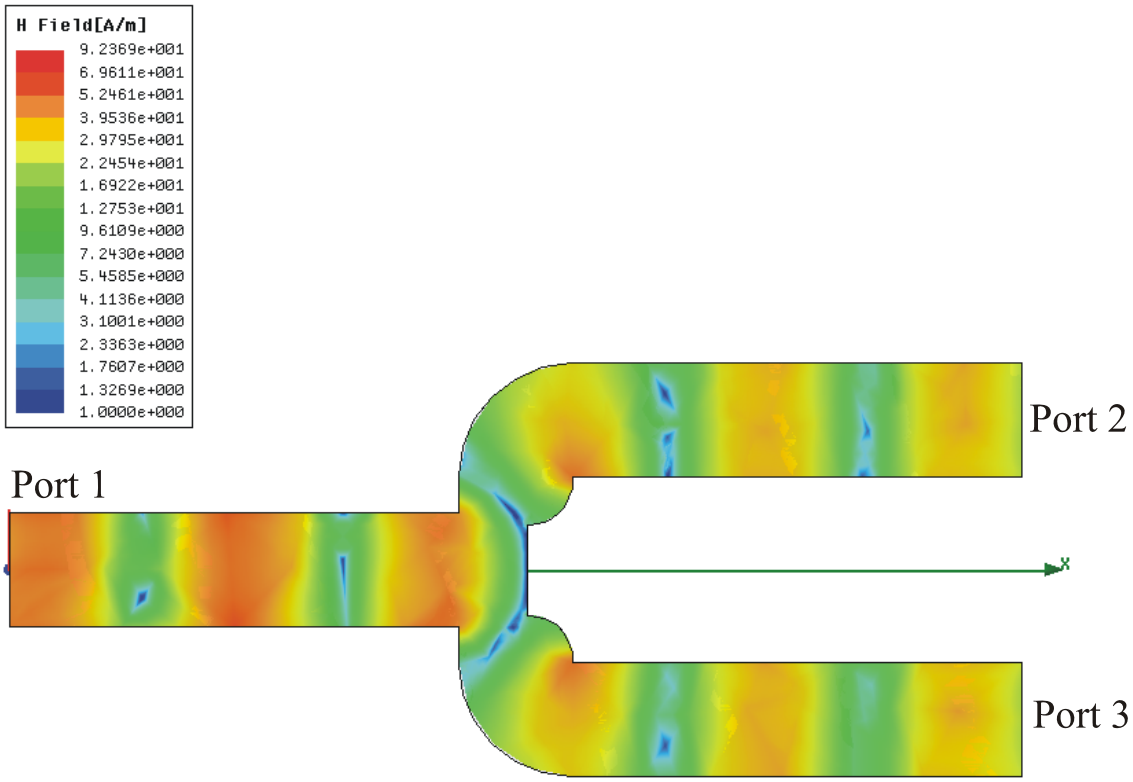

Figure 7.9. Simulated H field in the feed system.

7.3 Mutual coupling

Mutual coupling is an important parameter in antenna array design. It can distort the adjacent channels in the array and also modify the desired radiation pattern. In simulations some effects of the mutual coupling can be seen by comparing the array radiation pattern calculated from a single antenna with a simulated two element pattern. A comparison can be seen in Figure 7.10.

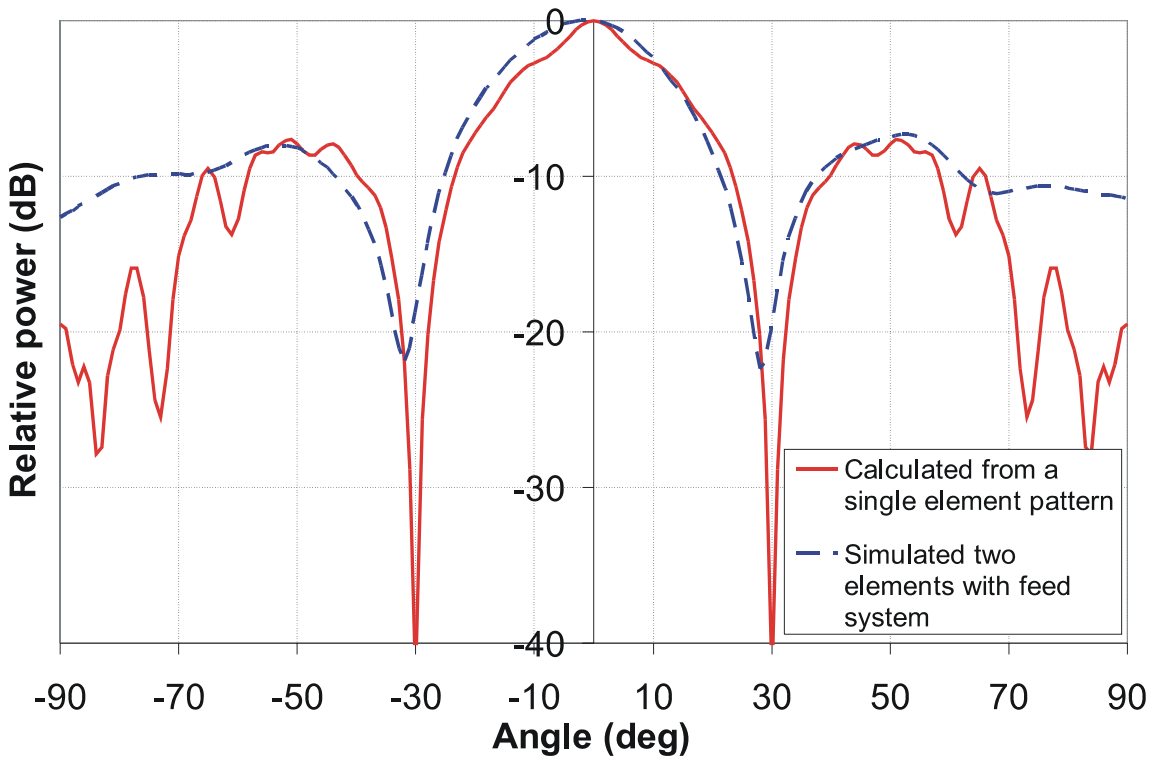

Figure 7.10. Comparison of the E-plane radiation patterns obtained by two different methods.

According to HFSS simulations, it seems that the mutual coupling is not very significant when the element separation is one wavelength. Due to a small asymmetry in the feed system the main beam is slightly squinted (2˚…3˚).

Mutual coupling is further studied by simulating two adjacent 56 mm long sapphire rods with different vertical distances between them. All the rod ends are tapered with 6 mm tapering section and matched to a metal waveguide. The simulation setup is presented in Figure 7.11. A vertical symmetry plane is used to reduce the simulation time. The lower rod is matched to ports 1 and 2 and the upper rod to ports 3 and 4. When the lower rod is fed from port 1 the power coupled to the upper rod can be seen in S_{31} and S_{41}. S_{41} is plotted in frequency range 75-110 GHz with five different distances *d* between the rods in Figure 7.12.

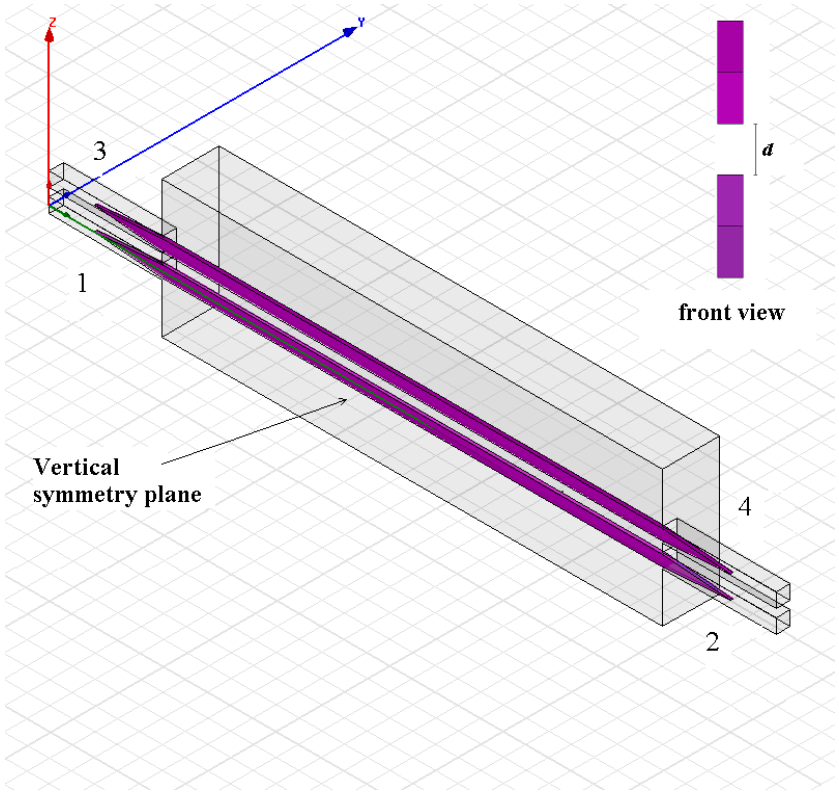

Figure 7.11. HFSS setup for mutual coupling simulations.

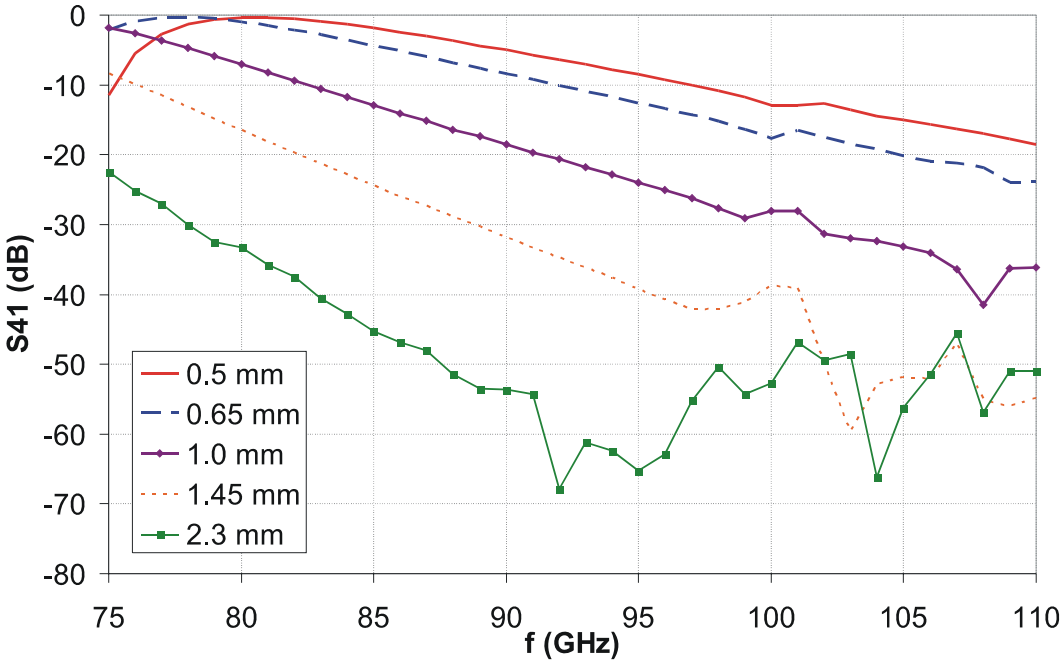

Figure 7.12. Mutual coupling between the sapphire rods with different vertical separation.

The S_{41} results are interesting and show that the coupling is very low when the distance is over 2.3 mm. With shorter distances the coupling is stronger and it seems that at some frequencies all the power is coupled to the upper rod. For example when the distance is 0.5 mm, S_{41} is -0.19 dB at 80 GHz. Simulated E-field distributions are presented in Figures 7.13 and 7.14 at 90 GHz and 80 GHz when the distance is 0.5 mm. It seems that the coupling is strongest at a rod length of 37-41λ_g. Phenomenon is similar to the cross-talk that can occur in optical fibers, where this complete power transfer is used, e.g., in directional couplers. This phenomenon will be studied in more detail in the next section.

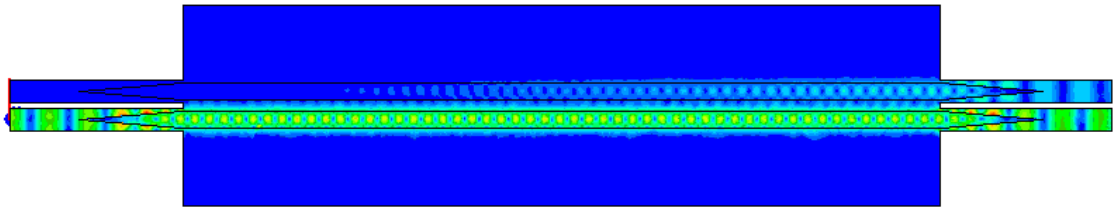

Figure 7.13. Simulated E field demonstrating coupling between the DRWs at 90 GHz, d=0.5 mm.

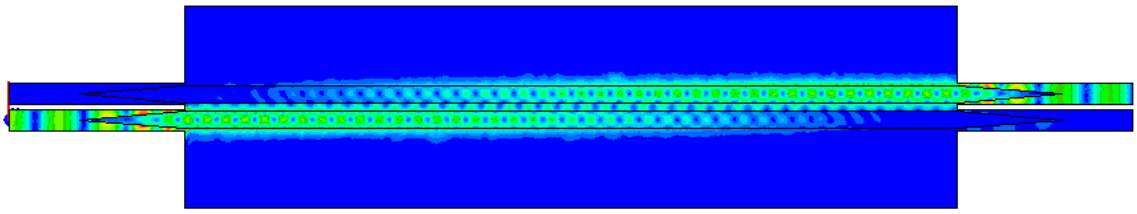

Figure 7.14. Simulated E field demonstrating coupling between the DRWs at 80 GHz, d=0.5 mm.

7.4 Measurement results

A prototype antenna is built by inserting two 20 mm long sapphire rods into the power splitter. The separation between the rod centre points is 3.3 mm. The tapering section in both ends of the rod is 6 mm. Thin porous teflon sheets are used to attach the rods in the middle of the metal waveguides. Figure 7.15 shows the antenna prototype.

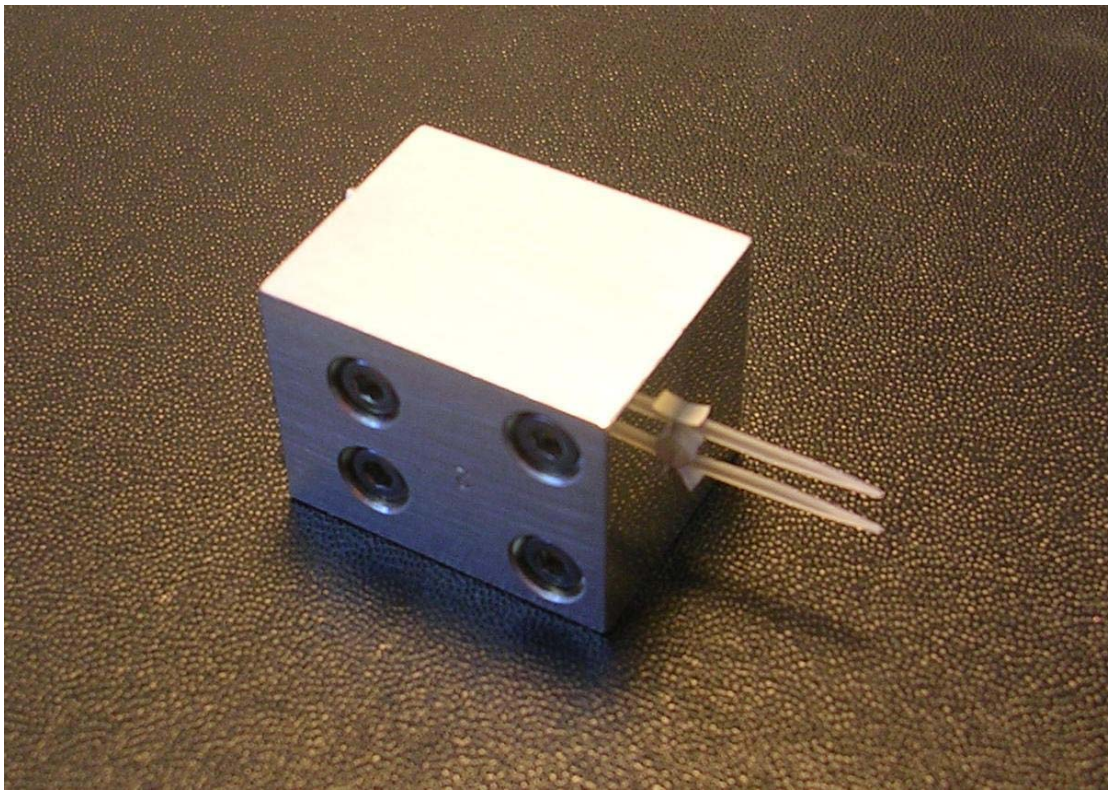

Figure 7.15. A two-element DRW antenna prototype with two 20 mm long sapphire rods.

Antenna is measured both in E and H planes. Similar measurement setup has been used as earlier with D-band antennas. It is described in Figure 5.4. Measurement results are compared with the simulations made with HFSS. Simulation setup is presented in Figure 7.16. The setup has a vertical symmetry plane (H symmetry) to reduce the calculation time. The simulated H-field distribution is presented in Figure 7.17.

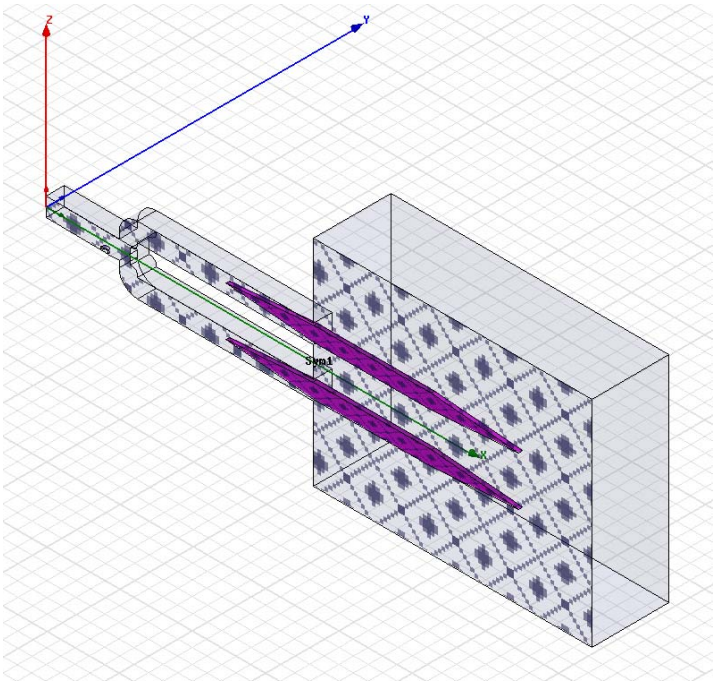

Figure 7.16. Simulation setup of two-element DRW antenna with two 20 mm long sapphire rods.

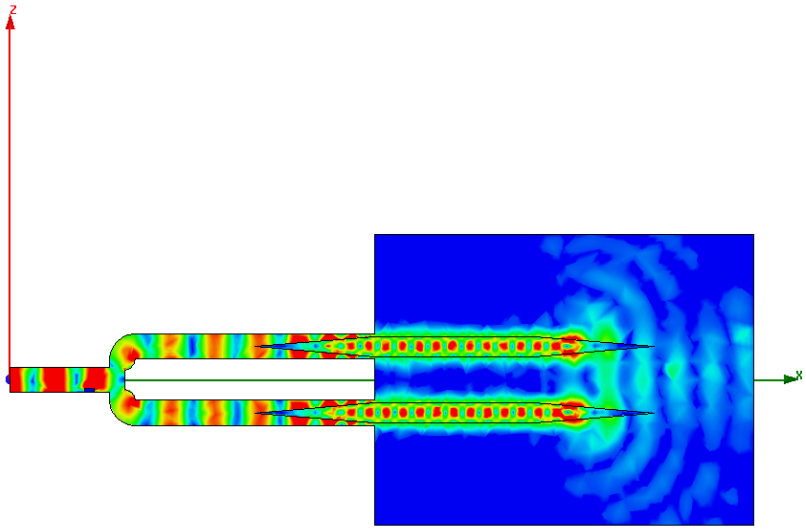

Figure 7.17. Simulated H-field distribution in the antenna.

The reflection coefficient of the antenna is measured with HP 8510 vector network analyzer. It is compared with the simulated values in Figure 7.18. The measured S_{11} is below -10 dB between 82-92.5 GHz. In general, the measured S_{11} corresponds well with the simulation results.

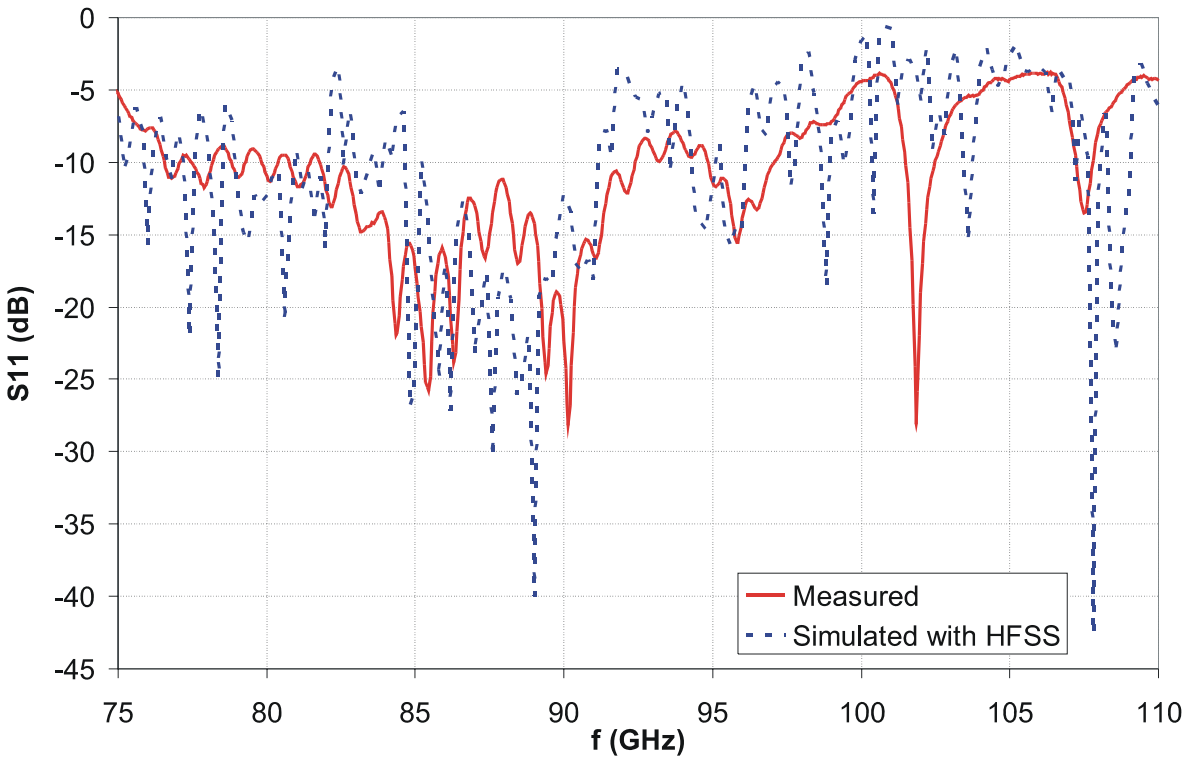

Figure 7.18. Measured and simulated S_{11} of the two element antenna.

The measured E-plane radiation pattern at 90 GHz is presented in Figure 7.19. It is compared to the simulated pattern and they seem to correspond very well. Also all the other radiation patterns are measured and simulated at this frequency. The main beam (between nulls) is about 60˚ wide. At -10-dB level the beamwidth is about 45˚. In Figure 7.20 a two-element E-plane pattern is compared with a single element pattern. As in Figure 7.2 the single element pattern should cover the two element pattern and this is shown also with the measurements. The H-plane radiation pattern is presented in Figure 7.21.

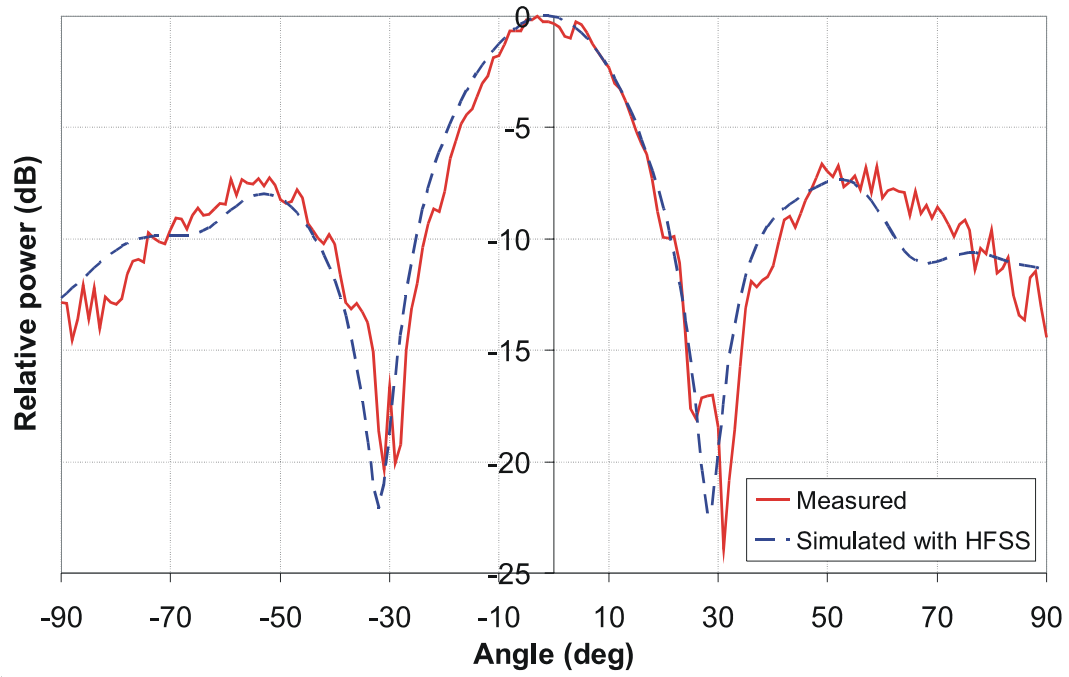

Figure 7.19. Measured and simulated E-plane radiation pattern of the two-element antenna at 90 GHz.

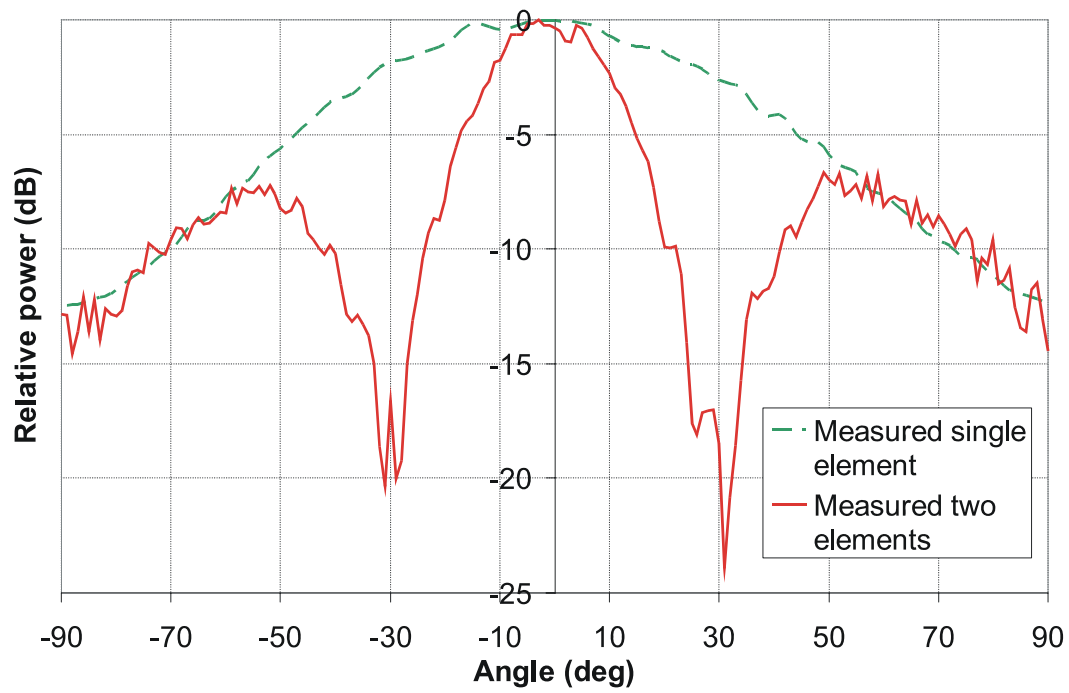

Figure 7.20. Comparison with the measured E-plane radiation pattern of a single element antenna at 90 GHz.

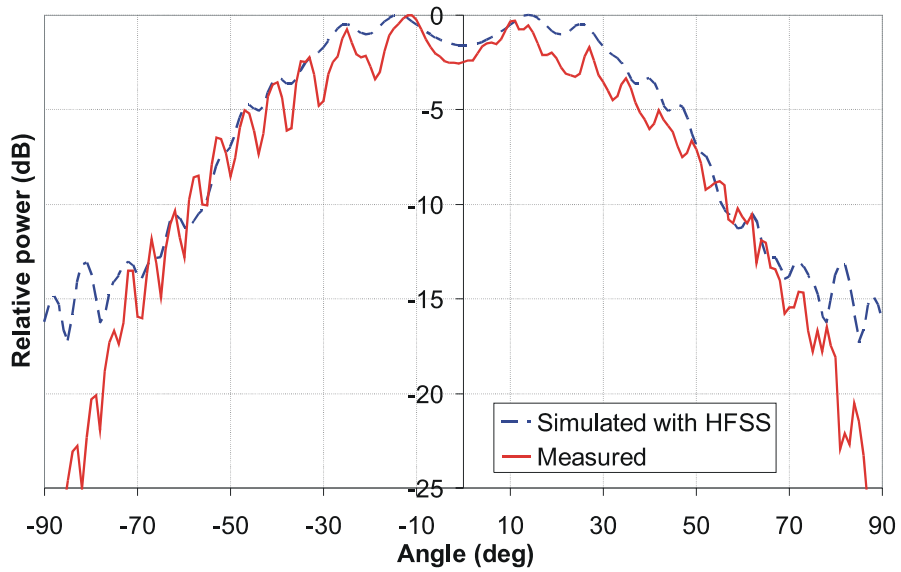

Figure 7.21. Measured and simulated H-plane radiation pattern of the two-element antenna at 90 GHz.

Finally the radiation pattern of a 2x2-sapphire rod waveguide antenna array is simulated at 90 GHz. The vertical and horizontal element separations are both 3.3 mm. The results are presented in Figure 7.22. In such an array the main beams of the H- and E-plane radiation patterns are practically identical.

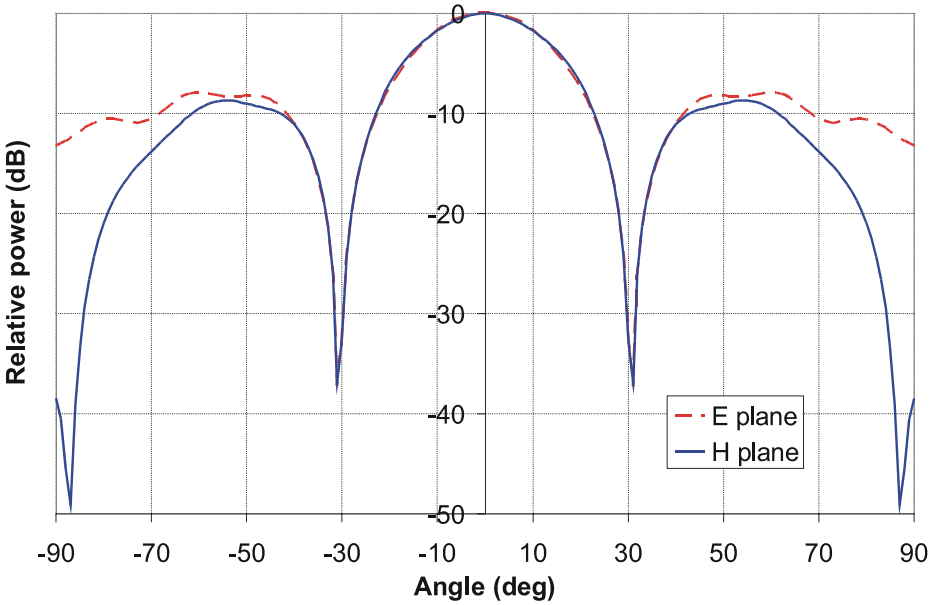

Figure 7.22. Simulated E- and H-plane radiation patterns of the 2x2 sapphire rod array at 90 GHz.

7.5 Conclusion of this chapter

In this chapter, features that should be taken into account when using DRW as an antenna array element are studied with simulations and prototype measurements. It is found out that at very short distances between the elements the mutual coupling is very strong and complete power transfer can occur (Figure 7.12). However, already at distances larger than ~λ/4 the mutual coupling is very low between vertically placed elements. In horizontal plane the mutual coupling is assumed to be stronger due to wider field distribution in this plane. This is studied in next chapter. Low mutual coupling makes DRWs an interesting alternative to be used in antenna arrays.

A two-element prototype antenna for 90 GHz is built with a metal waveguide power splitter as a feed. In general, such a splitter is not a very good solution for larger arrays. The feeding network becomes very difficult to manufacture as the number of elements increases. In many applications, like imaging, also the separation of adjacent channels is often needed. In larger DRW antenna array applications other type of feed systems should be developed. A solution based on the slotline feed could be a good candidate.

The measured antenna prototype shows good agreement with the simulations. If the number of the elements is higher the possibilities to create different radiation patterns is increased. For example an array with 2x2 elements enables a radiation pattern with almost identical main beam characteristics both in H and E plane.

8 TOTAL POWER TRANSFER BETWEEN TWO DIELECTRIC ROD WAVEGUIDES

As seen in the previous chapter, when a rectangular dielectric rod waveguide is fed with electromagnetic power and an identical DRW is placed parallel and close to the first one, a total power transfer to this second DRW can occur at certain conditions. The phenomenon is similar to cross-talk in optical fibers [68]- [72]. This phenomenon could be used for example in frequency selective couplers as it has been done in optical regime [73],[74] or, e. g., to monitor the propagating power in a DRW. Some filtering applications are also possible. However, at millimetre-wave frequencies components based on this phenomenon are very rarely used. In this chapter the total power transfer is studied in rectangular sapphire rod waveguides in W band with simulations and measurements.

8.1 Cross-talk in DRWs

As mentioned earlier, for a rectangular dielectric rod waveguide without any metal ground plane, two modes exist with zero cut-off frequencies, corresponding to two possible polarizations. These fundamental modes are often written as E_{11}^{x} and E_{11}^{y}. Letter *x* or *y* denotes the direction of the strongest electric field component. If the operating frequency is selected such that only these two fundamental modes can propagate in a single waveguide and two such waveguides are put close to each other and in parallel, the number of modes doubles [68], and one or two extra antisymmetrical modes can join to the set of propagating modes (beyond the cut-off, see Figure 2.3). It is possible because in a simpler case with infinite spacing between the waveguides, electromagnetic waves can be considered to propagate independently, in phase or in counter phase, and it can be considered as symmetrical or antisymmetrical mode in a system of two dielectric rods. These modes are also called as supermodes [73]. In this case it is assumed that only *y*-polarized waves are excited, and the power transfer from one waveguide to the other can be considered as an interference of two, namely

symmetrical and antisymmetrical, waves, propagating with slightly different propagation constants.

In this thesis the complete power transfer is studied only with simulations and measurements. Analytical calculations of the propagation constants for symmetrical and antisymmetrical waves could be derived by adapting, for example, Marcatili's method. From that, we could estimate the transfer coefficient analytically. When all the power is concentrated in one waveguide, this power is approximately proportional to $\left|E_{11}^{y+} + E_{11}^{y-}\right|^2$, while in the reverse case the proportionality can be presented as $\left|E_{11}^{y+} - E_{11}^{y-}\right|^2$. Also higher order modes are excited at the transitions, but they decay and therefore they can be omitted.

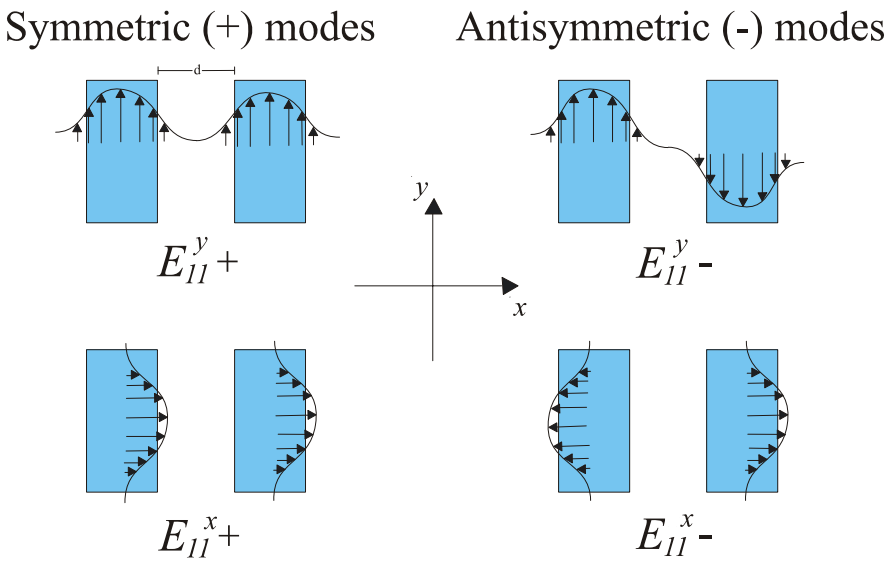

Figure 8.1. Fundamental modes in the system of two rectangular dielectric rod waveguides placed horizontally.

8.2 Simulations

Cross-talk in DRWs is simulated with Ansoft HFSS™. Figure 8.2 shows the simulated electric field in two vertically (*y* plane) placed sapphire waveguides. The waveguides are matched to the metal waveguides with a tapering. Vertical air gap between the

dielectric waveguides is varied from 0.5 to 2.3 mm. Total length of the rods is 56 mm including a 6-mm tapering section in both ends.

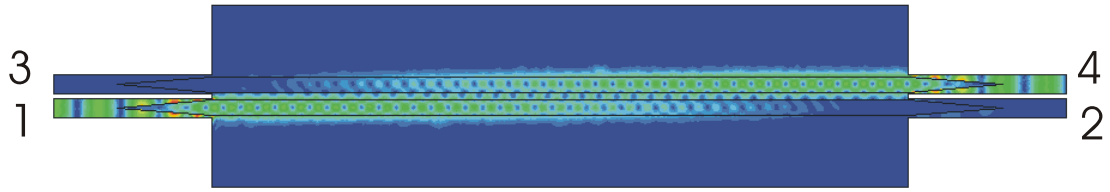

Figure 8.2. Simulated E field in sapphire waveguides at 80 GHz.

Figure 8.3 shows the mutual coupling between two vertically aligned parallel waveguides. One can observe that the cross-talk is near zero starting from 1 mm distance between the rod central axes. At shorter distances a nearly complete power transfer can occur, e.g., at 77-83 GHz with d=0.5 mm.

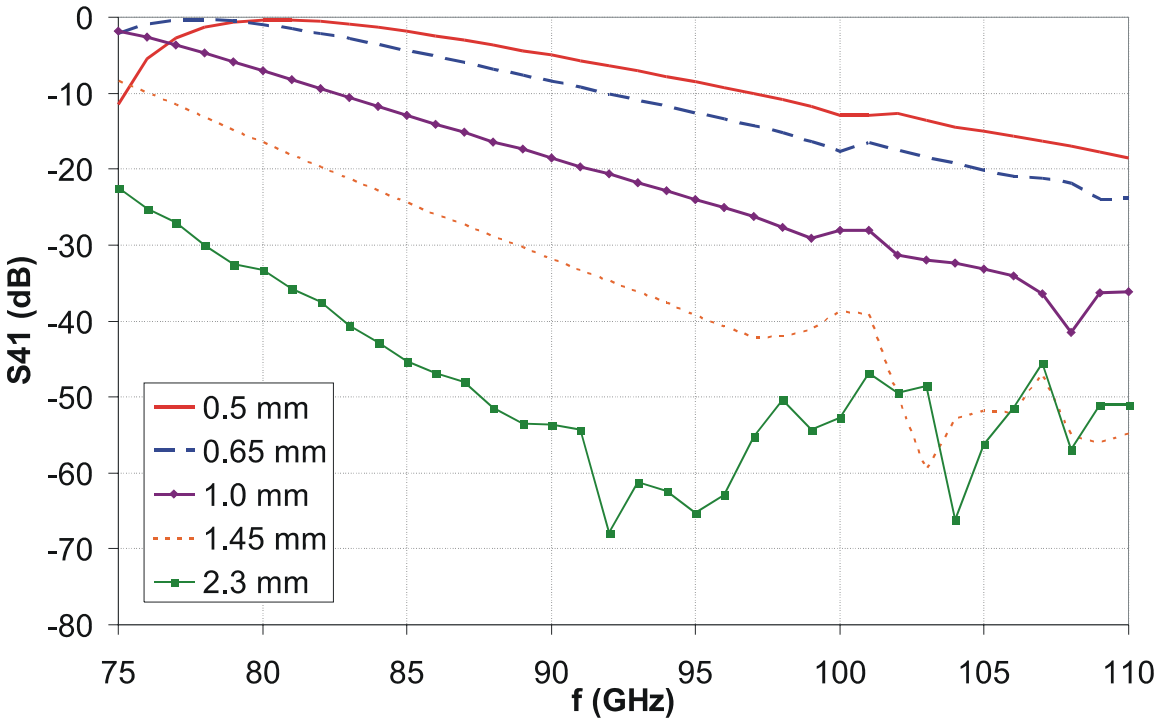

Figure 8.3. Simulated mutual coupling between two vertically parallel sapphire waveguides with different air gaps between the waveguides.

The distance along the waveguide in which there is complete transfer of power from one waveguide to the other and back again is also called as the beat length [68]. When the vertical air gap is 0.5 mm, the distance where the EM power is completely transferred to the upper waveguide (there is no field in the lower waveguide) is 37-41 λ_g.

If the rods are aligned horizontally (*x* plane), the power transfer is supposed to be even stronger due to a wider field distribution in this plane. This is also verified in the simulations. Figure 8.4 presents the simulations results with three different air gaps: 0.5 mm, 0.6 mm and 1.0 mm. It can be observed that the smaller the air gap between the rods the higher is the number of frequencies where the complete power transfer occurs.

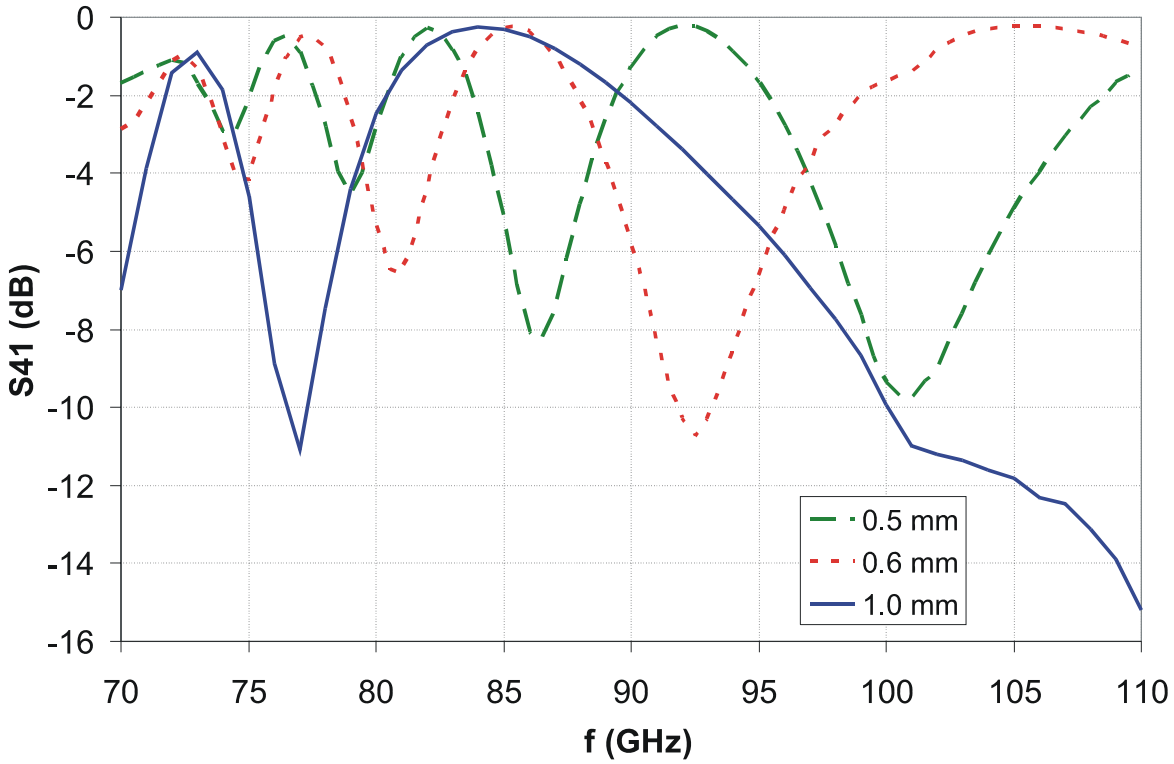

Figure 8.4. Simulated mutual coupling between two horizontally parallel sapphire waveguides with different air gaps between the waveguides.

When the distance d=0.6 mm the system has complete power transfer at 72.5 GHz, 77.5 GHz, 85 GHz and 105 GHz. The behavior of the simulated electric field at these frequencies is seen in Figure 8.5.

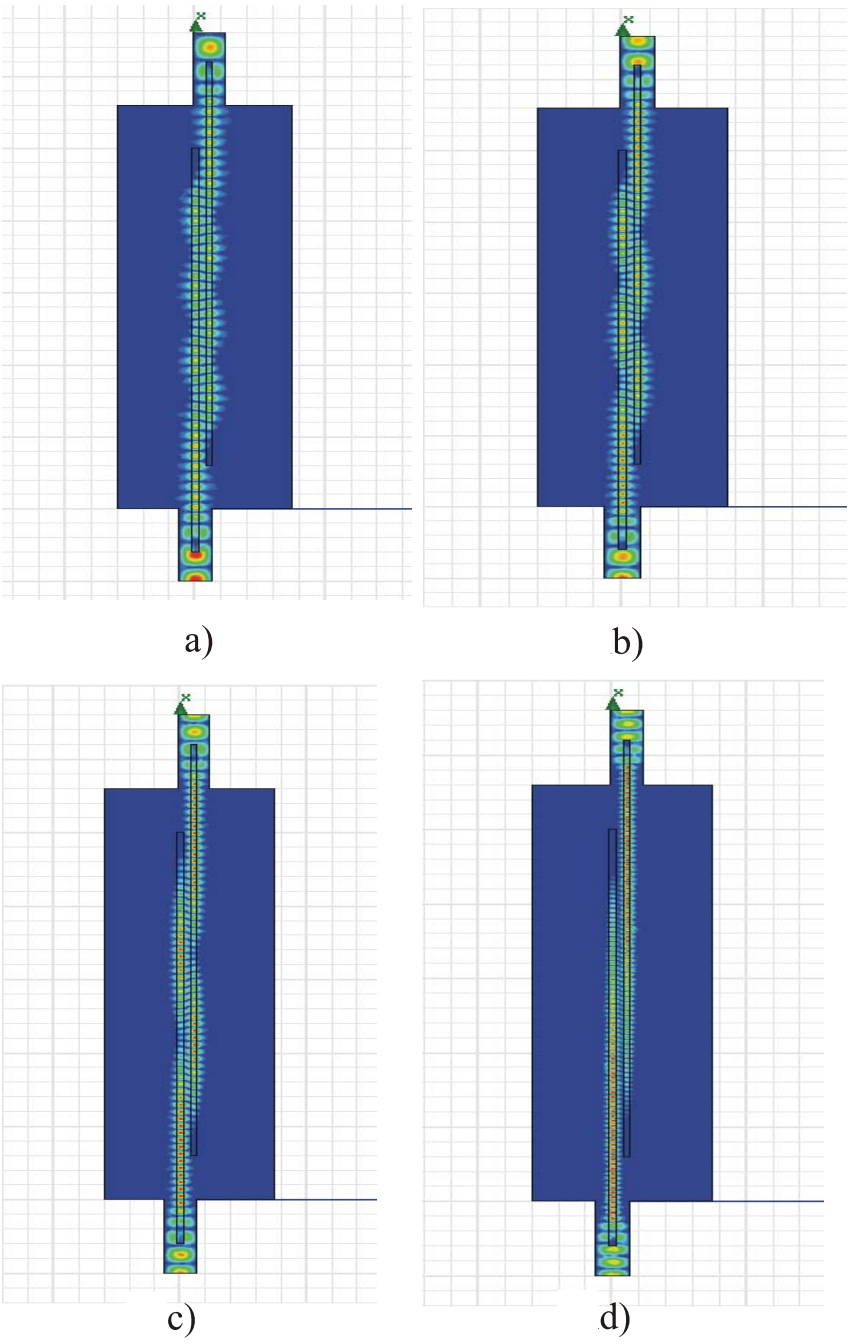

Figure 8.5. Simulated electric fields in the system of two horizontally placed DRWs at a) 72.5 GHz, b) 77.5 GHz, c) 85 GHz and d) 105 GHz.

It is clearly seen that the beat length increases with the frequency. At 72.5 GHz power is transferred seven times between the rods when at 105 GHz it transfers only once. This is due to the fact that the EM field is more concentrated to the core of the rod at higher frequencies, thus leading to smaller interaction between the waveguides.

8.3 Measurements

Complete power transfer is also verified experimentally. Measurement system is presented in Figure 8.6. Measurements are performed with HP8530A vector network analyzer. 56-mm long sapphire waveguides, similar to those in simulations, are used.

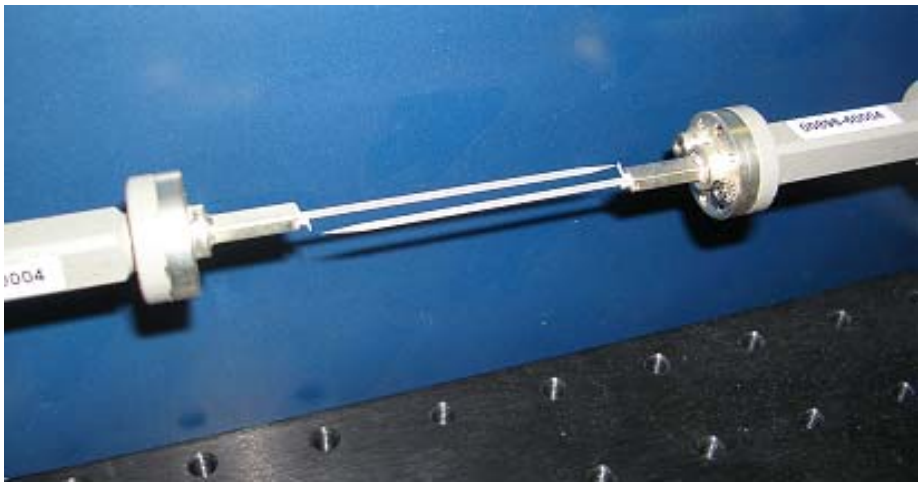

Figure 8.6. Measurement setup.

The results in both planes are presented in Figures 8.7-8.9. The agreement between the simulations and measurements is relatively good and the measurements verify the cross-talk phenomenon in these frequencies with these waveguides.

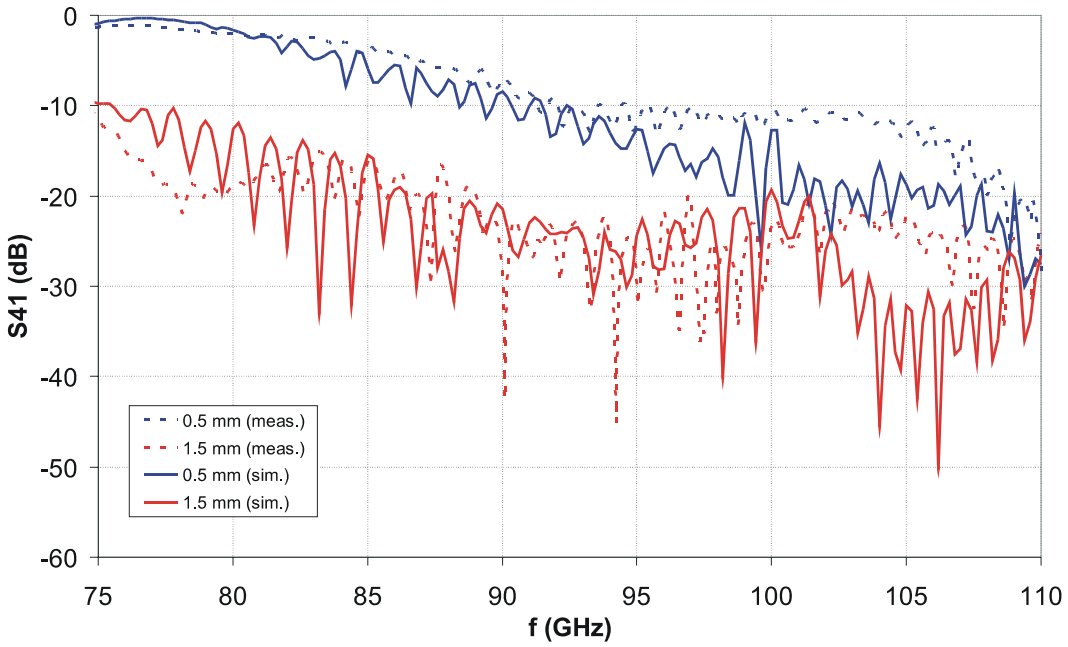

Figure 8.7. Comparison between simulated and measured mutual coupling between two vertically placed sapphire waveguides.

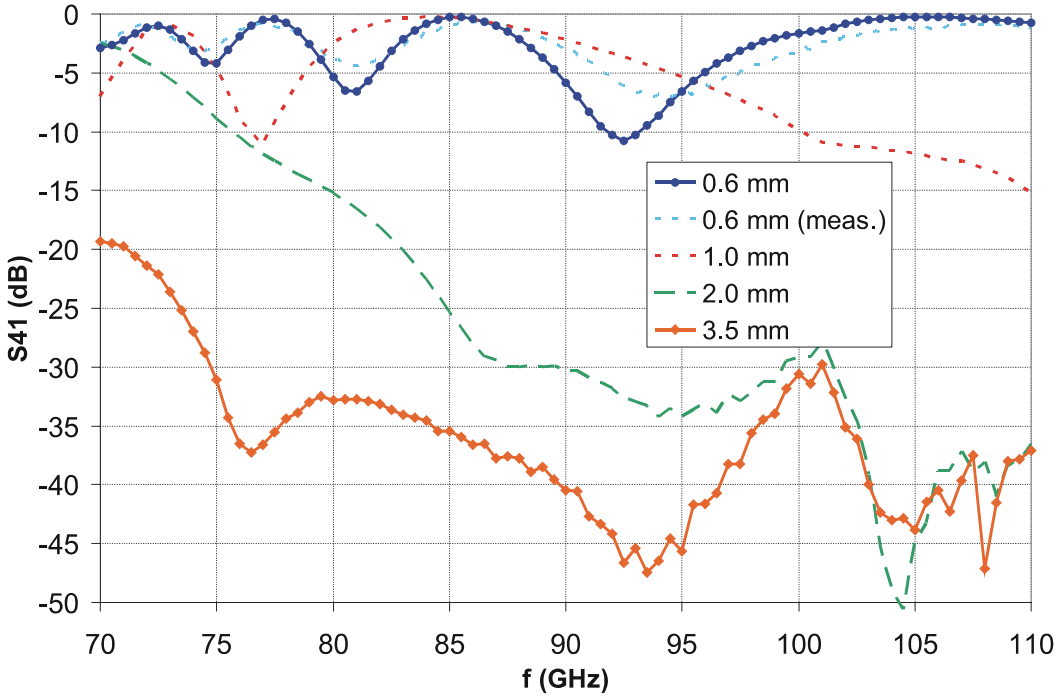

Figure 8.8. Simulated and measured mutual coupling between two horizontally placed sapphire waveguides.

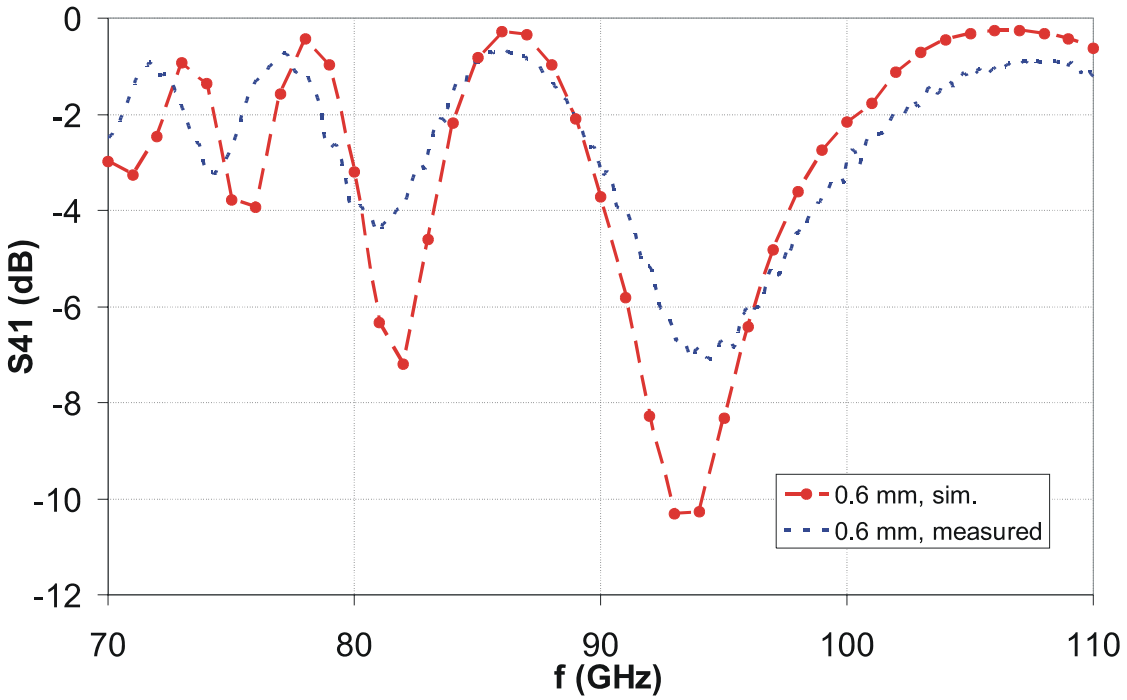

Figure 8.9. Comparison between simulated and measured mutual coupling between two horizontally placed sapphire waveguides in more detail.

When the waveguides are placed vertically the measurement results deviate more from the simulation at higher frequencies, especially with 1.5 mm separation. One reason for this is the slight tilting of the waveguides in the measurements as they are difficult to position exactly parallel.

8.4 Conclusion of this chapter

In this chapter, power transfer between two parallel rectangular DRWs is studied with simulations and measurements. The results are very promising and this phenomenon could be used, e.g., in frequency selective couplers, filtering or in monitoring the propagating power in a DRW. When the DRWs are placed horizontally, the effect is stronger due to wider field distribution than in vertical direction.

Also, these studies may be useful when designing dielectric rod antenna arrays. Two directions for the future studies can be taken: the ways to increase and utilize the cross-talk phenomenon, and the ways to suppress it, however, keeping the waveguide separation small. In the next chapter a frequency selective coupler based on power transfer between two identical waveguides is designed and built.

9 FREQUENCY SELECTIVE DIRECTIONAL COUPLER BASED ON TOTAL POWER TRANSFER

The beat length being frequency dependent is the reason for frequency selectivity of a coupler based on power transfer through cross-talk. As explained in the previous chapter, the beat length is the length in the waveguide that is required for the power to completely transfer to the second waveguide and back. However, for the prototype coupler straight dielectric rods are not practical as the ports would be too close to each other. For this reason a waveguide bend must be designed. Such bend is presented in the next section.

9.1 Dielectric rod waveguide bend

In order to be able to connect four ports to the coupler at least two turns must be added to the waveguides in the coupling region. Such turns are studied with Ansoft HFSS^{TM}. Figure 9.1 presents the simulation setup for a bend in GaAs waveguide.

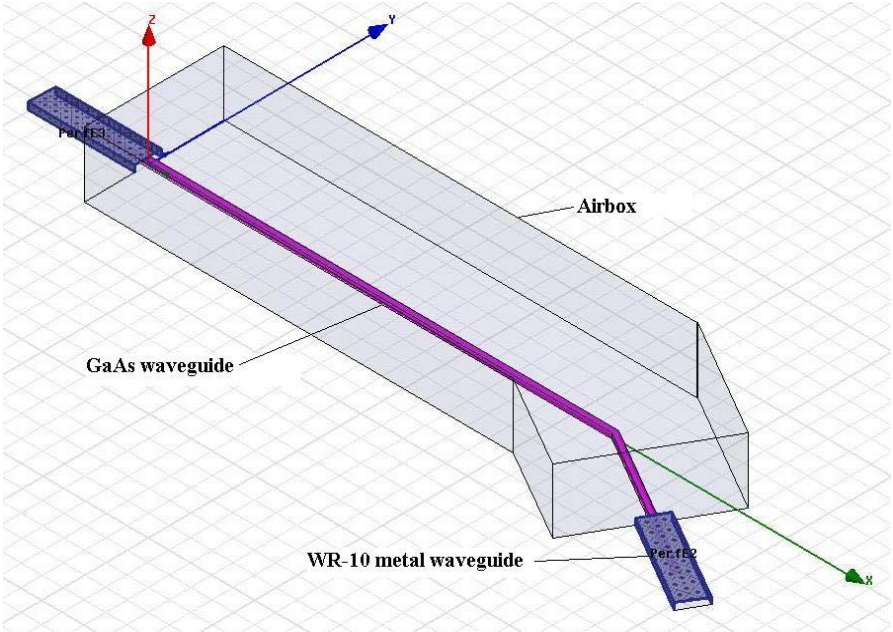

Figure 9.1. Simulation setup for the bend in GaAs waveguide.

Figure 9.2 presents the simulated transmission coefficient (S_{21}) with different bend angles. Also the S_{21} of a single straight waveguide is included. One can see that the bends up to 30˚ angle increase the losses only slightly, ~ 0.5-1 dB, compared to a straight waveguide. The losses at the 45˚ angle is already much higher, ~ 2 dB. A small rounding in the outer side of the bend decreases the losses a little, but such rounding is difficult to realize in the real prototype.

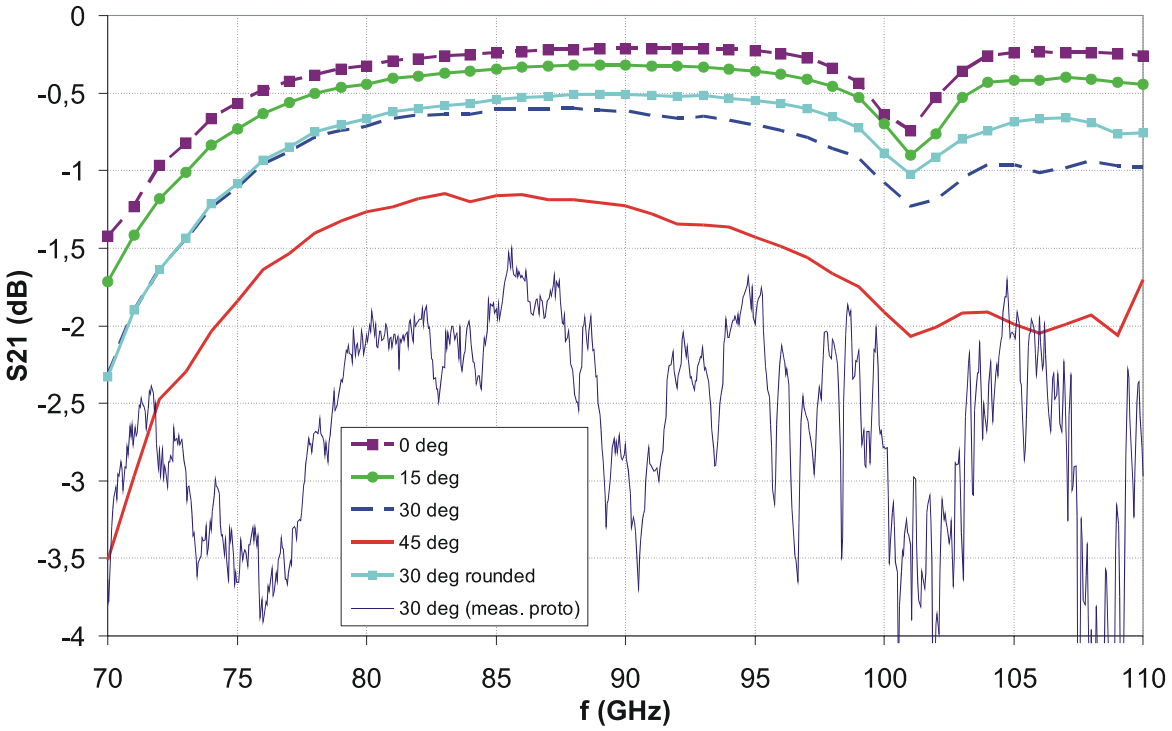

Figure 9.2. S_{21} of different types of GaAs waveguide bend.

A 30˚ bend is found to have large enough angle for the metal waveguide ports with reasonable losses and such a prototype is made. The prototype is made of two separate GaAs waveguides with 30˚ cuts in the interface. The two pieces are put together on a low loss and low permittivity holder made of Rohacell (Figure 9.3). For this reason the losses in the prototype are assumed to be larger than in the simulation. The measured S_{21} is also presented in Figure 9.2.

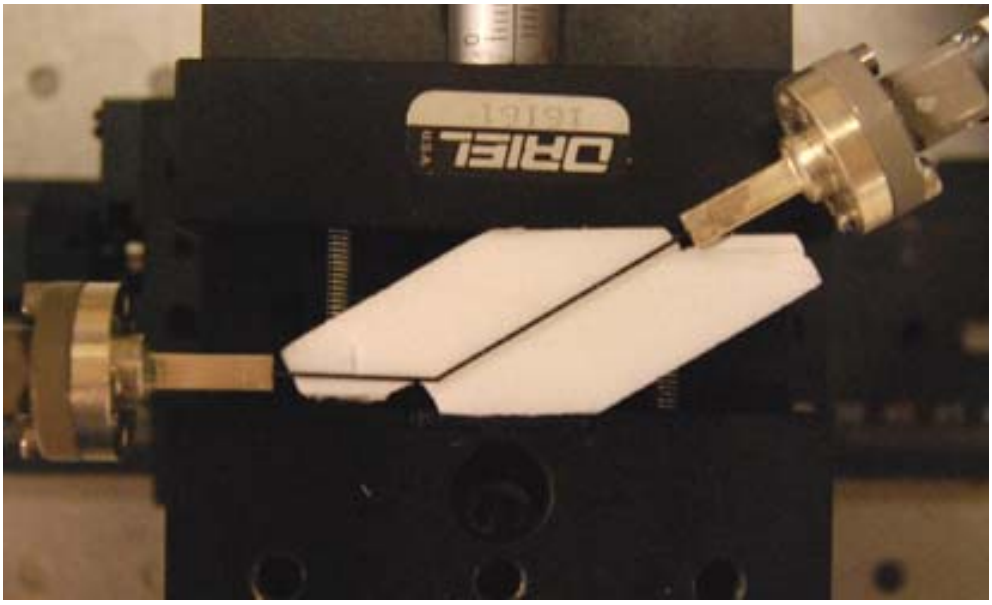

Figure 9.3. Prototype of the 30˚ bend between two GaAs waveguides.

9.2 Frequency selective coupler prototype: simulations

Figure 9.4 shows the simulation setup of a four-port prototype of the FS coupler. It includes GaAs waveguides with a 30˚ turn that allows a good separation of the ports from each other. The distance between the waveguides in the coupling region is 0.5 mm.

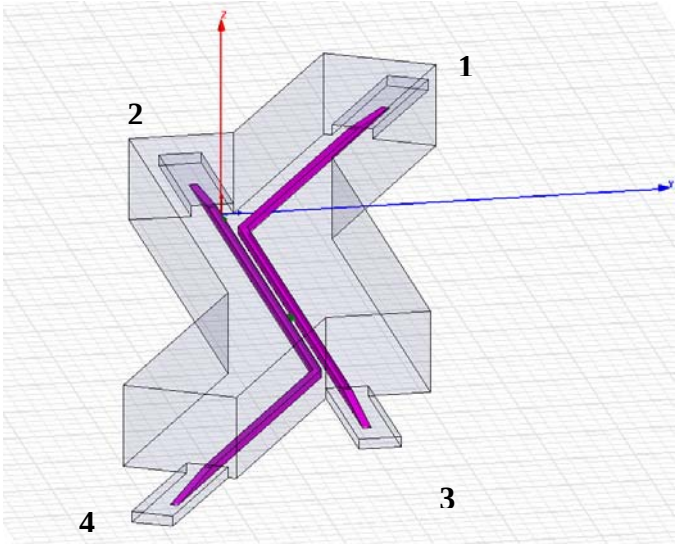

Figure 9.4. Simulation setup of the FS coupler.

Figure 9.5 presents the simulated S parameters of the coupler. It can be seen that the power fed to the ports 1 and 2 is effectively coupled either to the port 3 or 4 over the whole frequency band of 70-110 GHz. Ports 1 and 4 with the bend increase slightly losses. While S_{31} and S_{42} are nearly identical, S_{41} includes more dielectric losses and two bends compared to S_{32}. The isolation between the ports next to each other is presented in Figure 9.6. The isolation is over 30 dB over the whole frequency band except the 105-110 GHz region at which it is slightly lower. Figure 9.7 shows the simulated E field at 80 GHz, when feeding port 1.

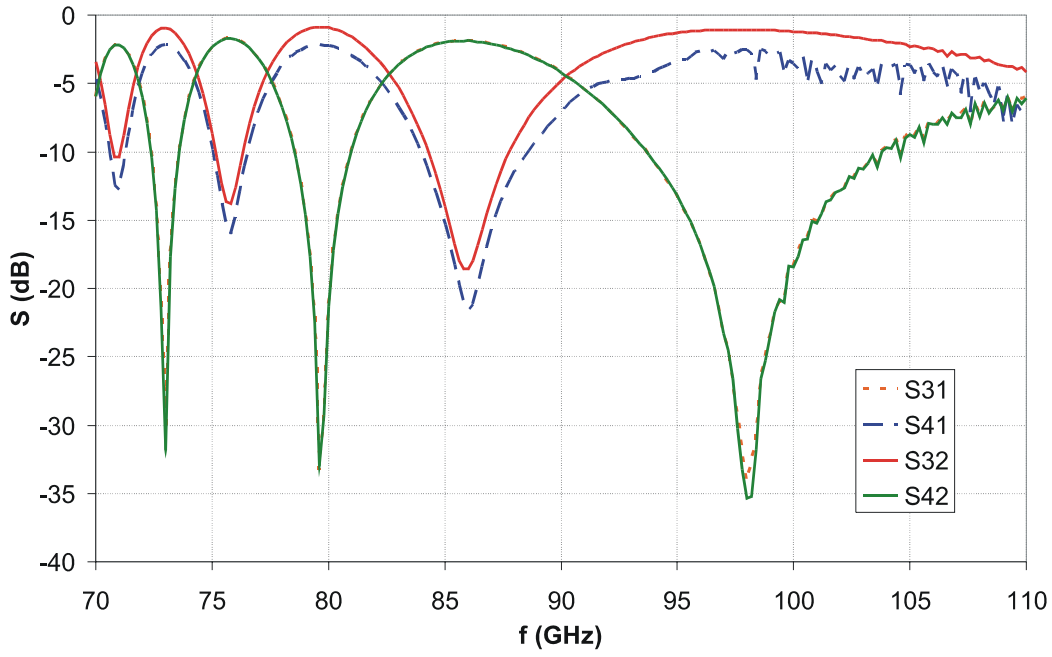

Figure 9.5. Simulated S parameters of the coupler.

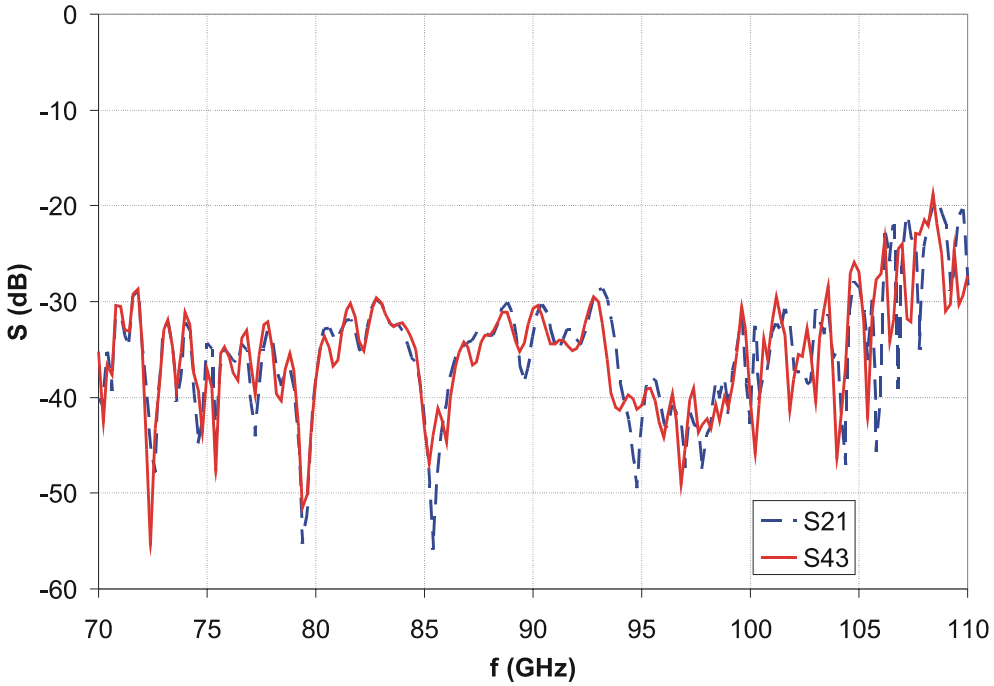

Figure 9.6. Simulated transmission coefficient between the ports (isolation) next to each other.

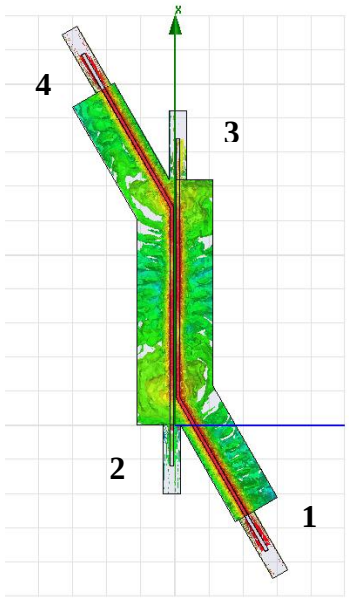

Figure 9.7. Coupling at 80 GHz.

9.3 Frequency selective coupler prototype: measurements

At the next stage a prototype is fabricated. Due to practical reasons it is made of four different pieces of GaAs. These pieces are put together on a Rohacell holder. HP 8510A vector network analyzer is used at the measurements. Unfortunately it does not support 4-port measurements and thus two ports are left freely radiating. This is, though, assumed to cause only small inaccuracies to the measurements due to small reflections of the tapered waveguide end. Figure 9.8 presents the prototype and the measurement setup when measuring S_{32}, S_{41} and S_{31} parameters.

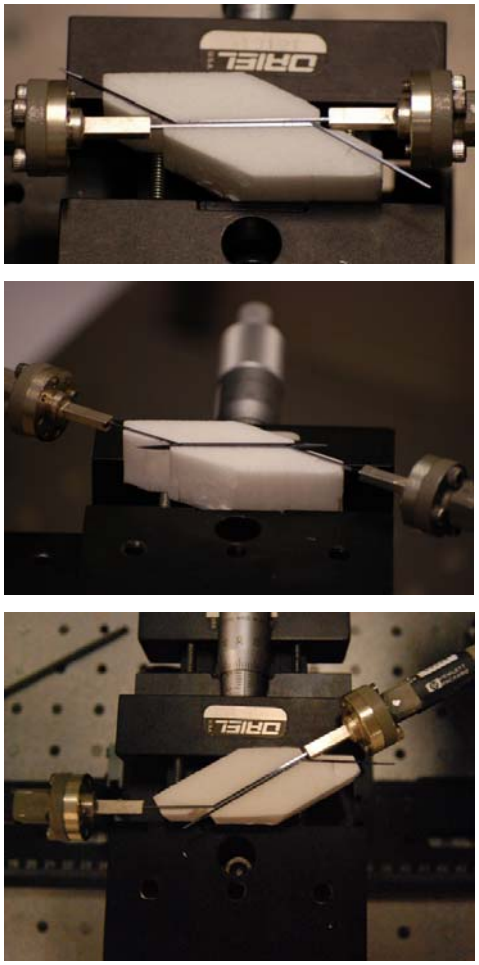

Figure 9.8. Coupler prototype and measurement setup of S_{32}, S_{41} and S_{31} parameters.

Figure 9.9 presents the measurement results. As the prototype is made of four different pieces, the prototype bends cause slightly more losses than the continuous bends in the simulations. Despite of the extra losses the measurements show good frequency selective coupling between the ports.

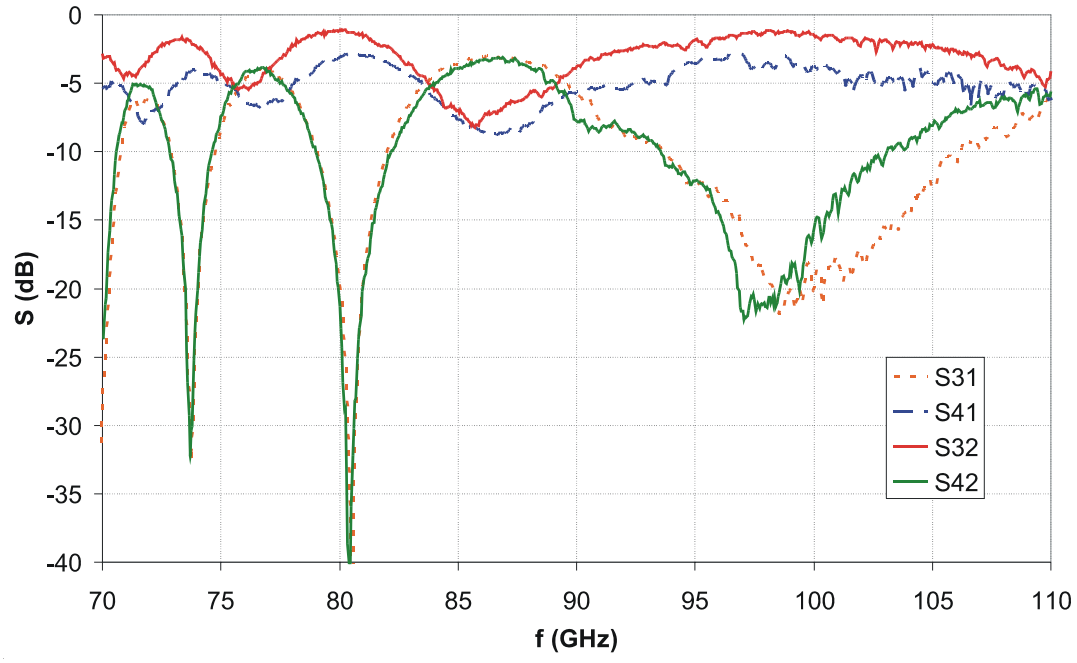

Figure 9.9. Measured S parameters.

9.4 Conclusion of this chapter

In this chapter, the design of the prototype of the frequency selective coupler for W band based on horizontally parallel rectangular DRWs is presented. Frequency selectivity is based on cross-talk between the waveguides. The prototype is fabricated and its measurements show good correspondence with the simulations. They confirm that the components, e.g. couplers and filters, based on cross-talk phenomenon are well feasible also at millimetre-wave frequencies. Waveguide bends are required for the necessary separation of the ports.

10 DRW POWER DIVIDERS

Another way to make couplers and power dividers with dielectric rod waveguides is to use different types of junctions, e.g. symmetric and asymmetric Y junctions. Dielectric waveguide junctions are important devices for example in beam splitters and recombiners. In integrated optics Y junctions are also used in active devices such as Mach-Zender interferometric modulators and switches [75],[76].

In millimetre-wave frequencies only few studies of dielectric waveguide junctions have been made. They have mainly concentrated on low permittivity dielectrics, like polypropylene (ε_r=2.25) on a ground plane, thus image waveguides [77]. Other studies on similar type of waveguides are e.g. [78],[79].

In this chapter high-permittivity dielectric waveguides are studied as different types of power dividers at W band.

10.1 Symmetric and asymmetric Y junctions in E plane

Y junctions can be symmetric or asymmetric. The symmetric junctions are practical when equal power is desired for both output ports. In asymmetric designs the splitting ratio of the output power between the ports can be controlled with the junction angle. As also the isolation between the output ports is high, such a Y junction can be used as a directional coupler [77].

At optical wavelengths small angles between the branches are often needed to avoid too large radiation losses at the junction as low permittivity waveguides are needed. In millimetre wavelengths this angle can be larger due to the possibility to use higher permittivity dielectrics. Figures 10.1 and 10.2 present the asymmetric and symmetric junctions modeled in HFSS in E plane (vertical).

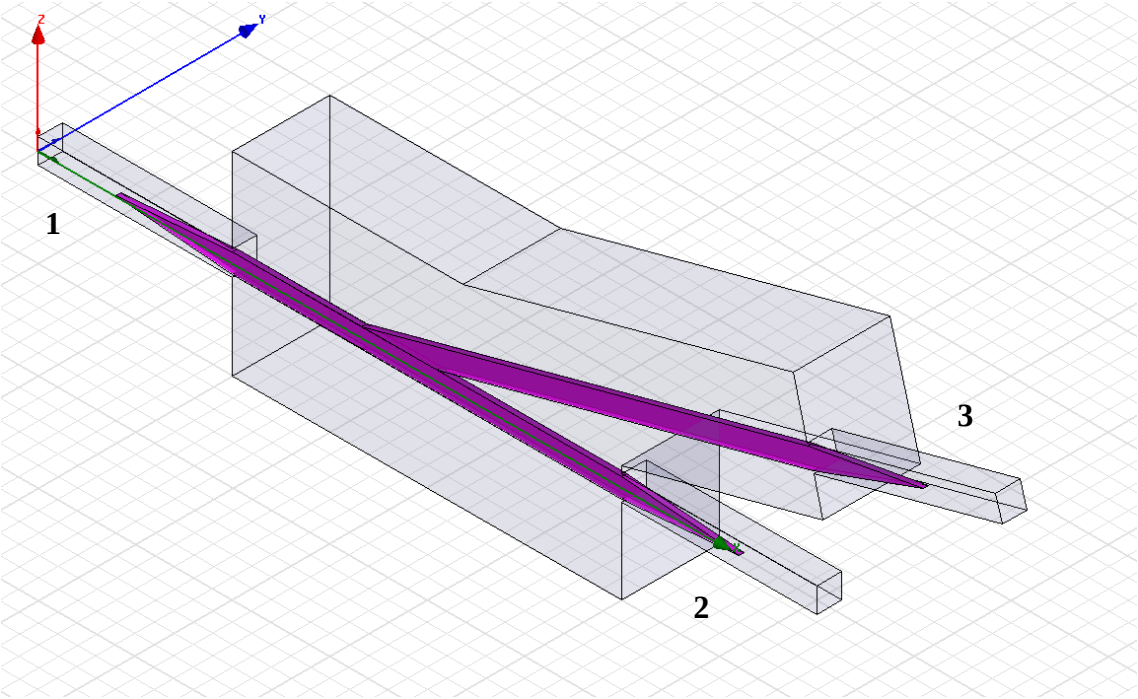

Figure 10.1. HFSS-simulation model of an asymmetric Y junction. Angle between the waveguides is 15˚.

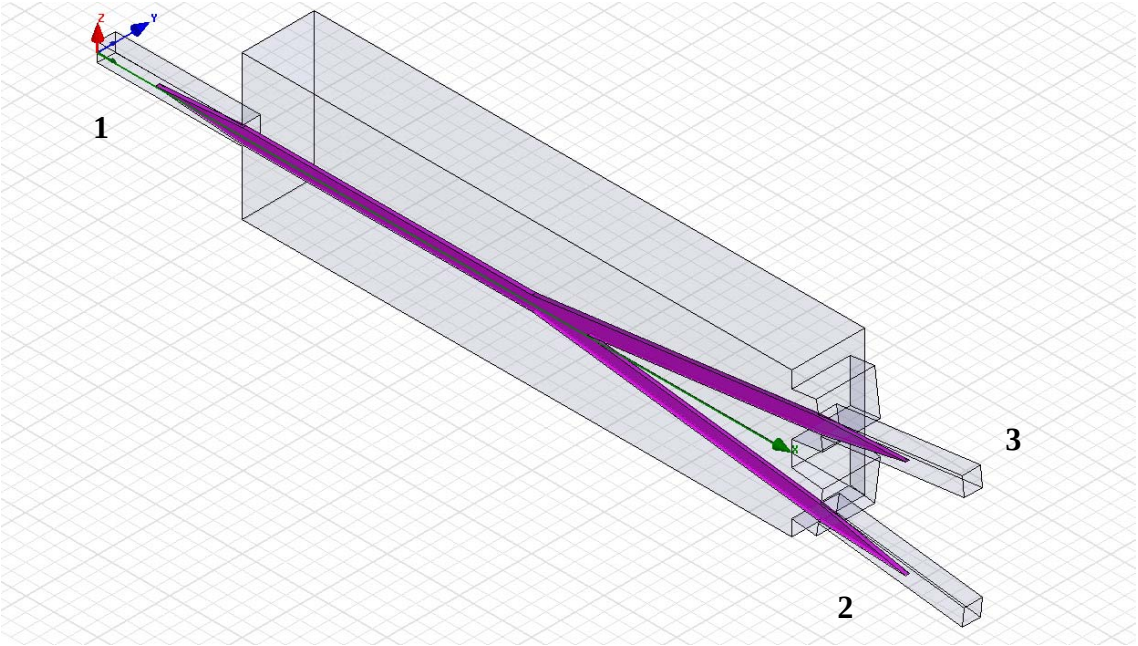

Figure 10.2. HFSS-simulation model of a symmetric Y junction. Opening angle is 15˚.

10.2 Simulations

Simulations are performed with Ansoft HFSS according to the simulation models presented in Figures 10.1 and 10.2. DRW material is silicon. In addition to Y junctions in the E plane also some H-plane (horizontal) dividers are simulated and studied.

10.2.1 Asymmetric junction in E plane

Figure 10.3 presents the simulated transmission coefficients to both ports with different divider angles (from 15˚ to 90˚). According to the results a 3-dB power division can be obtained with an angle about 20˚ (red lines for 30˚, blue lines for 15˚). At higher frequencies (>100 GHz) the power division is not stable anymore. Figure 10.4 presents the reflection coefficient of the divider. In Figure 10.5 the transmission coefficient from port 2 to port 3 is presented. The 15˚ angle gives the highest isolation in low frequencies as expected, more than 15 dB. Finally in Figure 10.6 simulated E field is plotted in a 30˚ power divider at 85 GHz.

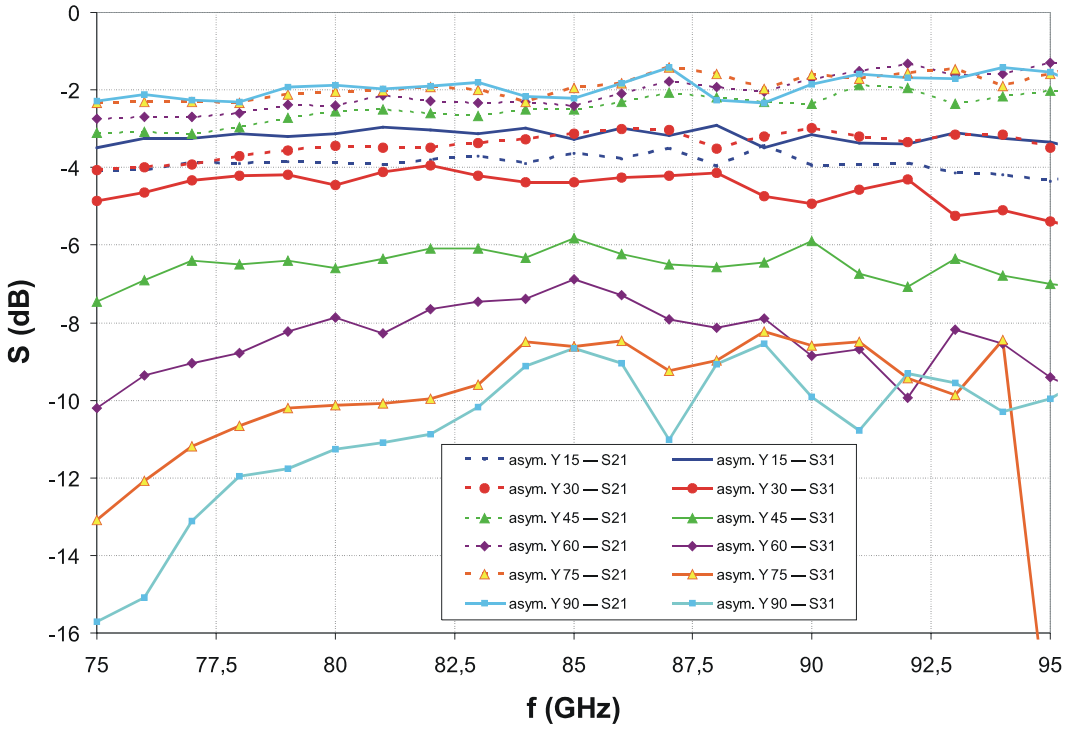

Figure 10.3. Simulated S_{21} and S_{31} of an asymmetric DRW power divider.

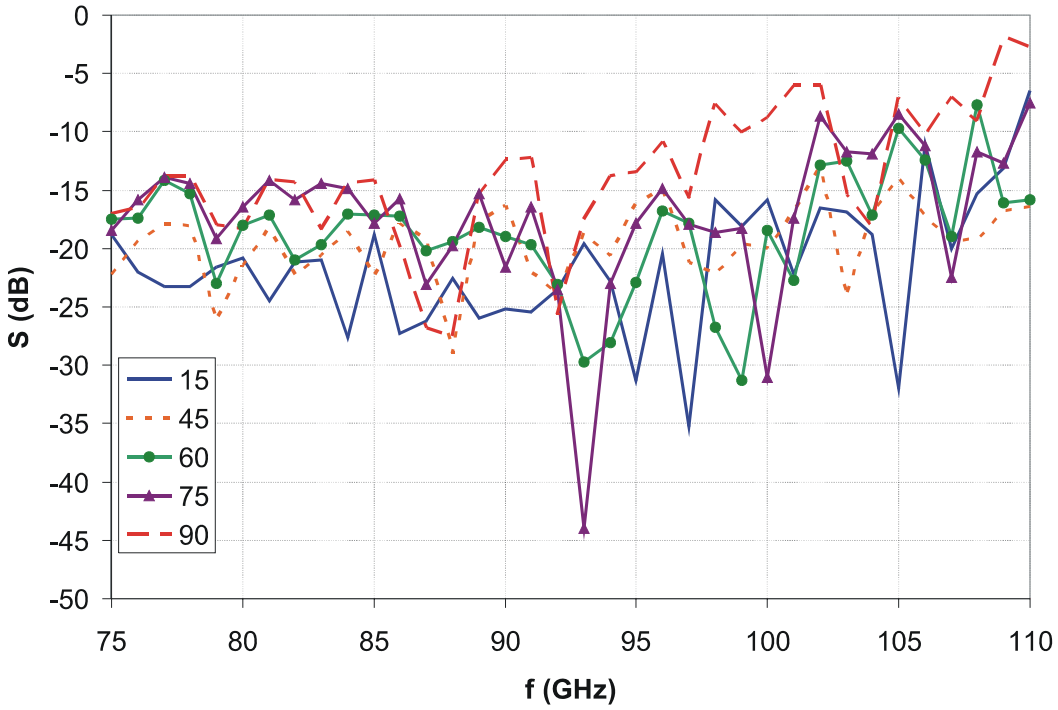

Figure 10.4. Simulated S_{11} of an asymmetric DRW power divider.

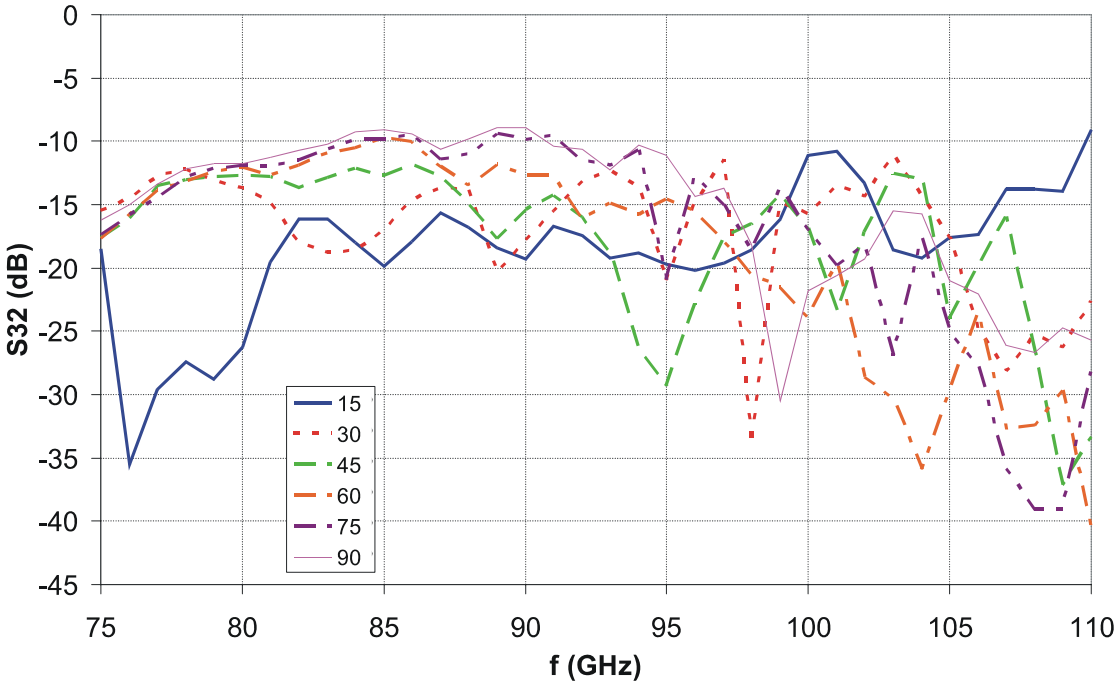

Figure 10.5. Transmission coefficient from port 2 to port 3.

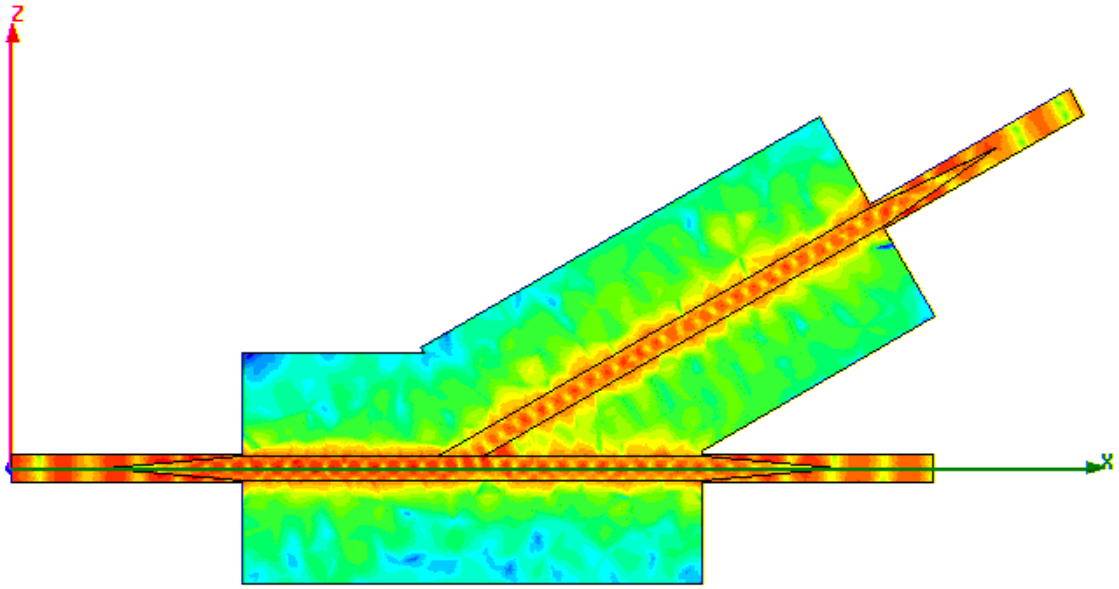

Figure 10.6. Simulated E field in a 30˚ asymmetric divider at 85 GHz.

10.2.2 Symmetric junction in E plane

In the symmetric junction the power division is always equal between the ports. The reflection from the junction increases with the angle between the ports as can be seen in Figures 10.7 and 10.8. Figure 10.9 presents the simulated E field in a 60˚ power divider.

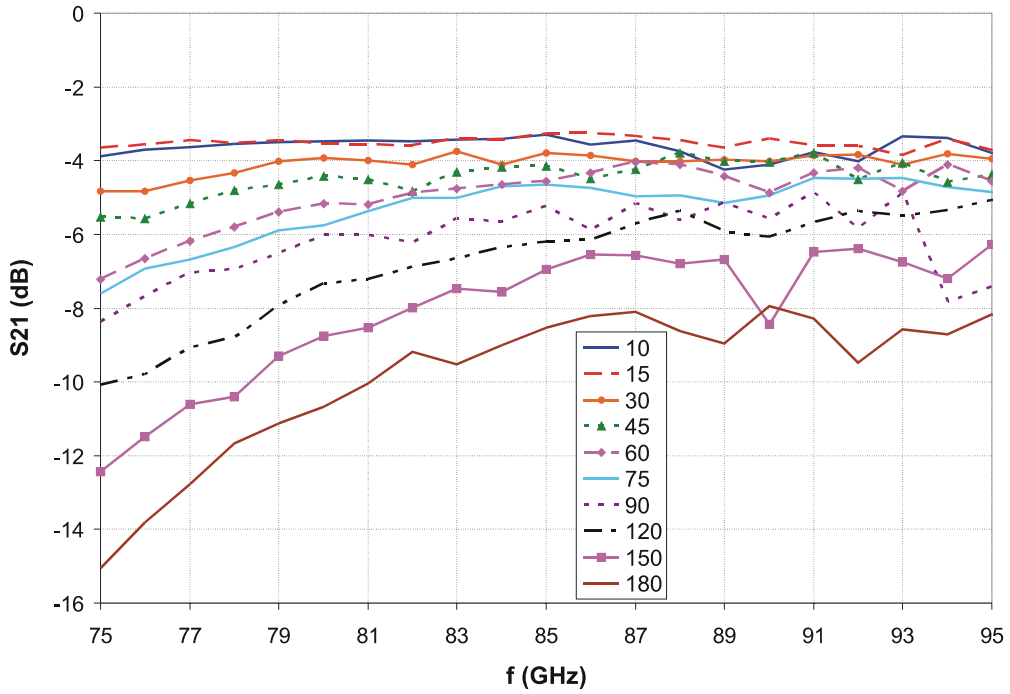

Figure 10.7. Transmission coefficient of the symmetric power divider with different port angles.

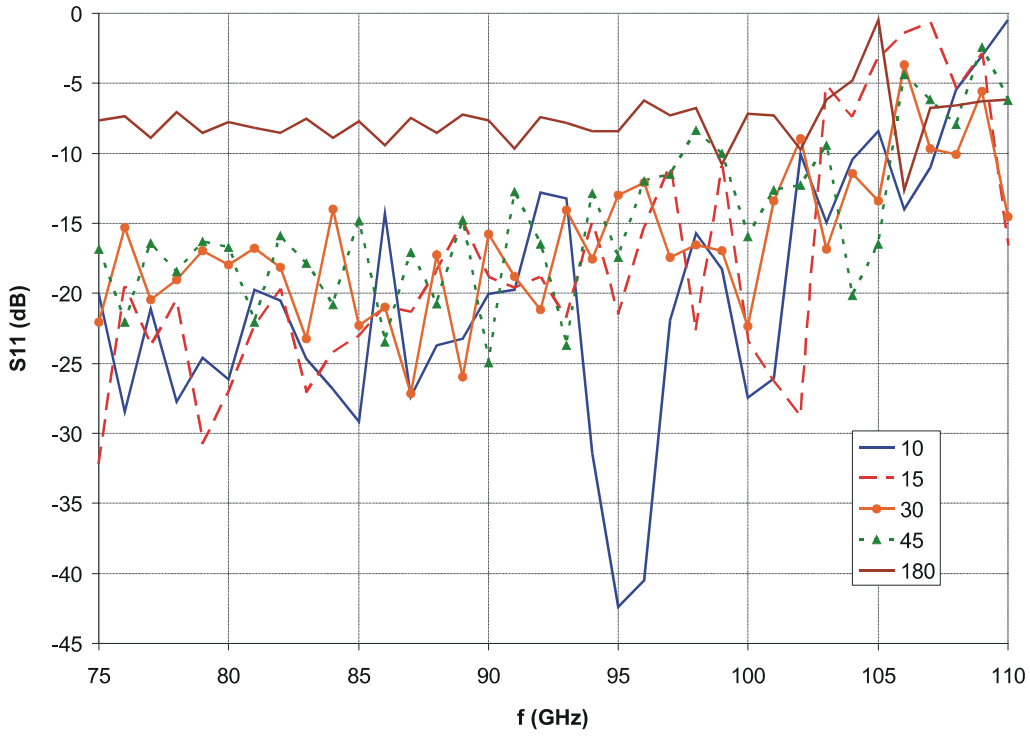

Figure 10.8. Simulated S_{11} of the symmetric DRW power divider.

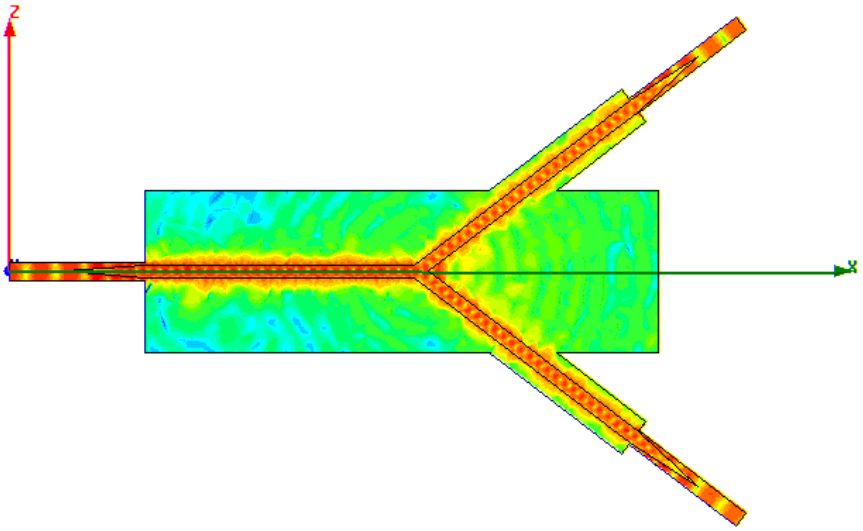

Figure 10.9. Simulated E field in a 60˚ symmetric divider at 85 GHz.

10.2.3 V-type power divider in H plane

Similar power divider types as in E plane can be realized also in H plane (horizontally), which is often also more practical. In addition, a so called V-type divider is also possible. Figure 10.10 presents the simulated E field in such a divider. Power division is realised already at the feed. The optimum angle between the rods is 9˚…10˚ and nearly 3-dB power division is obtained with low losses.

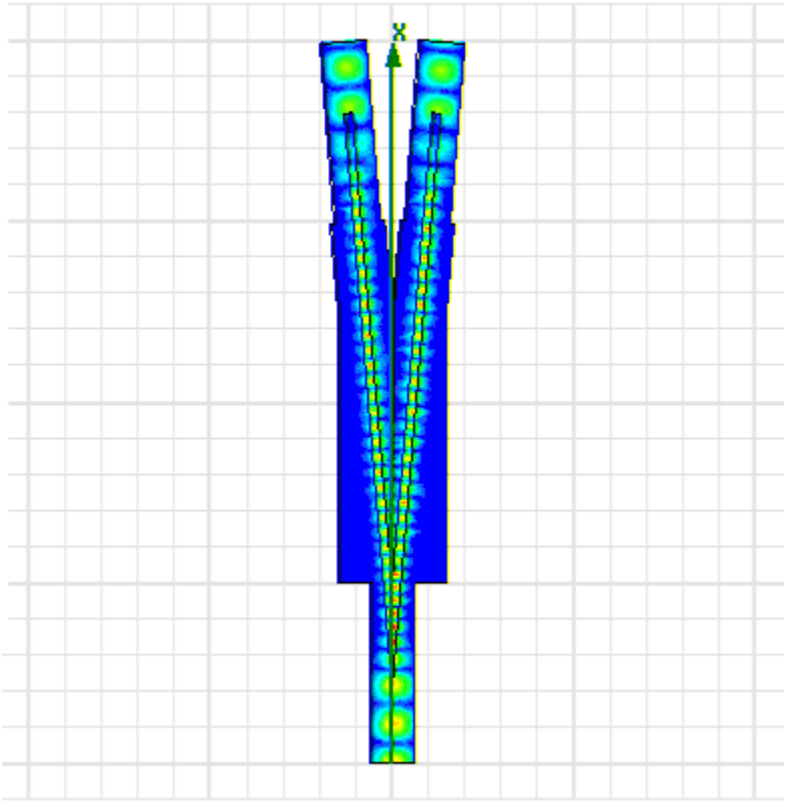

Figure 10.10. Simulated E field in a V-type symmetric power divider in H plane.

10.2.4 Y-type division in H plane

In Figure 10.12 power division between the asymmetric Y-type dividers in E and H plane are compared. The angle between the rods is 15˚ in both cases. Reflection loss is slightly smaller in the H-plane divider and near 3-dB power division is obtained. In general H-plane dividers are often easier to realize, especially in the cases where integrated circuits are required. In those cases image waveguides are often the best choice even if the losses are higher.

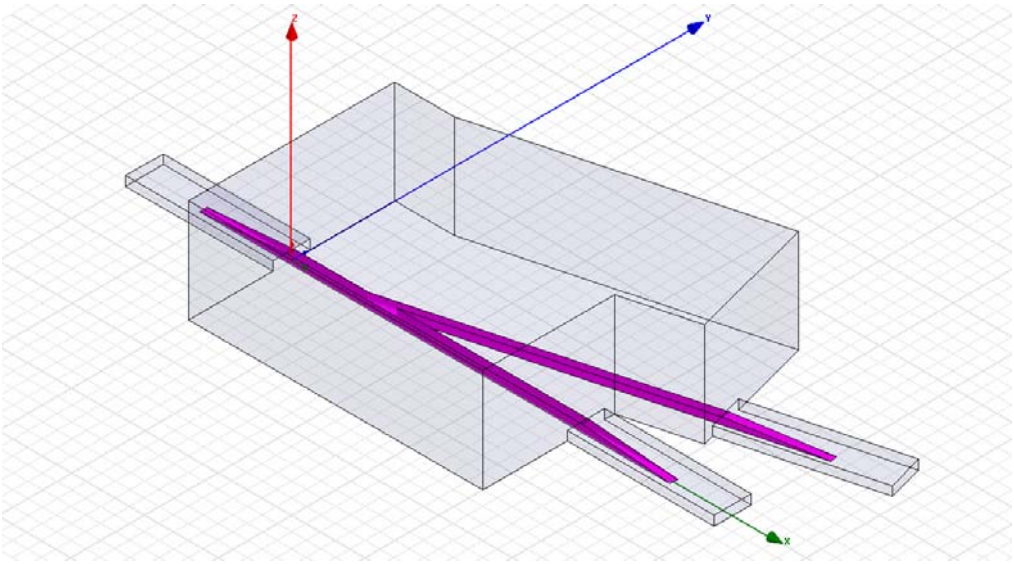

Figure 10.11. Asymmetric Y-type power divider in H plane.

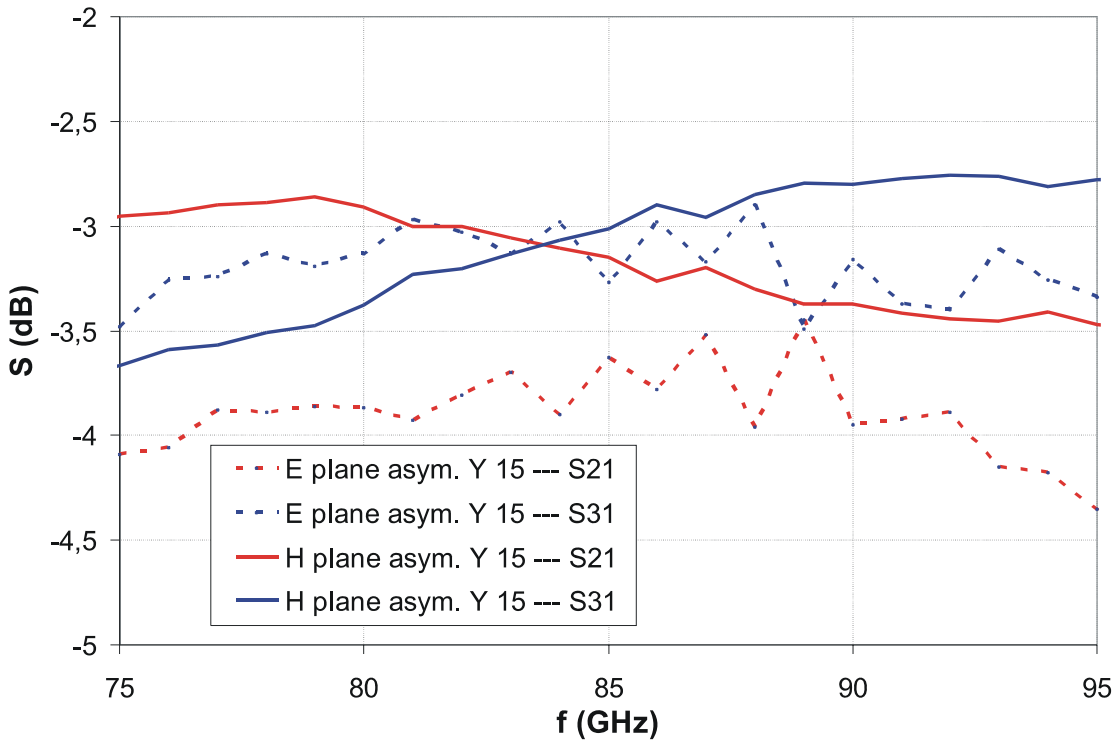

Figure 10.12. Comparison of the power division between the asymmetric Y-type dividers in E and H plane.

10.3 Conclusion of this chapter

In this chapter, different power dividers based on DRW junctions are proposed and designed for W band. These junctions can be scaled also to other frequencies. Junctions can be formed in any arbitrary planes, but vertical and horizontal planes are usually the most practical. The horizontal plane is best, if integration of other components or the use of image waveguides is needed.

Junctions can be divided in several groups; asymmetric and symmetric Y junctions and V junctions. Asymmetric Y junctions are the most practical as they are relatively easy to implement. V junctions and symmetric junctions always offer nearly 3-dB power division if low loss dielectric rods are used. In asymmetric junctions also other division ratios are possible. If a 3-dB asymmetric junction is needed for 85 GHz, in horizontal plane the angle between the rods should be 15˚. In vertical junction the respective angle is ~20˚.

11 DRW TRAVELLING-WAVE AMPLIFIER

The main problem of active millimetre-wave systems is the fundamental limitations of the conventional discrete semiconductor devices. Usually the maximum achievable output power of traditional devices is very small in millimetre wave frequencies. Thus, alternative principles, like travelling-wave amplification, are interesting.

The idea of travelling-wave amplification in the semiconductor with drifting electron flow is analogous to the principle of the vacuum travelling-wave tube [11],[80]. The electromagnetic wave amplification is based on the energy transfer from the drifting electrons. Gain occurs when the drift velocity of the electrons becomes slightly higher than the phase velocity of the electromagnetic wave component. The electron drift velocity in semiconductors is in the order of $10^6 \ldots 10^7$ cm/s, therefore the electromagnetic wave has to be decelerated in a slow-wave structure. Delay structure should provide a sufficient decrease of the phase velocity without considerable dispersion. Field of the propagating electromagnetic wave in a periodic structure can represented as a sum of plane waves according to Floquet's theorem.

In case of the electron tubes, the coupling between the current and the electromagnetic wave is often a problem as the electron beam and the slow-wave structure are difficult to put close to each other. In the semiconductor layered structure, this problem can be avoided, because the distance between the conducting layer and the periodic structure can be in the order of 10 nanometres. First semiconductor based amplifiers were built by using a helix or a metallic meander line as a slow-wave structure, but the required small periods were very difficult to accomplish. Also the coupling between the current and the electromagnetic wave was not efficient [81].

In this thesis work an attempt has been made to build a DRW travelling-wave amplifier for W band. In this chapter, first the principle of travelling-wave amplification in DRW is considered, then the properties of a semiconductor heterostructure for efficient

electron drift is discussed. A DRW travelling-wave amplifier prototype has been designed, fabricated and measured.

11.1.1 Travelling-wave amplification in DRW

In [82],[83] some traveling-wave interactions in semiconductors were considered and in [81],[84] a monolithic dielectric rod image waveguide amplifier with simple with periodic corrugations was proposed and theoretically analysed. Such a structure allows tight coupling between the carrier current and the slow electromagnetic wave component. In [85] an image waveguide amplifier was realised and a 4 dB/cm electronic gain at 75 GHz with 1200 V/cm electric field was reported. In [86] Gunn effect was utilized to amplify signal in GaAs waveguide and antenna at W band. Similar effect was used for compensating losses in GaAs waveguide up to 20 GHz [87]. In [88] the effects of thin conducting layers for active components in GaAs and silicon waveguides with were studied.

In general, when an electromagnetic wave propagates along a periodic structure, it can be represented as a series of spatial harmonics according to the Floquet's theorem. If a TM mode propagates in a periodic waveguide, the magnetic field component is given by

$$H_y(x,z) = \sum_{m=-\infty}^{\infty} a_m(x)\exp(-i\beta_m z)\,, \tag{11.1}$$

where $\beta_m = \beta_0 + 2\cdot\pi\cdot m/L$. L is the period of the perturbation and β_0 is the propagation constant.

The terms, space harmonics, in Eq. (11.1) with $m \neq 0$ can have different phase velocity according to the choice of L and m. Thus, they can be chosen to satisfy the condition for energy transfer, which occurs when the carrier velocity exceeds the phase velocity of the electromagnetic wave. For the m^{th} harmonic, the condition is

$$v_0 > (v_{ph})_m = \frac{\omega}{\beta_0 + 2 \cdot \pi \cdot m / L}, \tag{11.2}$$

where v_0 is the carrier's drift velocity and ω the wave angular frequency. When $\beta_0 << 2\pi/L$, the amplification condition can be written as $\lambda > Lc/v_0$. Nowadays, periods of about 20 nm are feasible with electron beam lithography and if $v_0 \approx 2 \cdot 10^7$ cm/s, it can be calculated the amplification should be possible at the wavelengths longer than ~30 μm.

The carrier drift velocity can be calculated from the applied electric field, E, and the electron mobility μ as follows

$$v_d = \mu E . \tag{11.3}$$

Drift velocity saturates at certain electric fields, e.g., GaAs reaches its maximum $2 \cdot 10^7$ cm/s at ≈ 3 kV/cm and starts decreasing towards the saturation level of ≈ 10^7 cm/s [89].

In Figure 11.1 the electron drift velocity is plotted at different values of electron mobility (cm^2/Vs) as a function of the applied electric field. Also the phase velocity of the electromagnetic wave is plotted as a function of the harmonic number m according to Floquet's theorem to see what kind of values of electric field and electron mobility are required to reach the amplification condition at each harmonic number m.

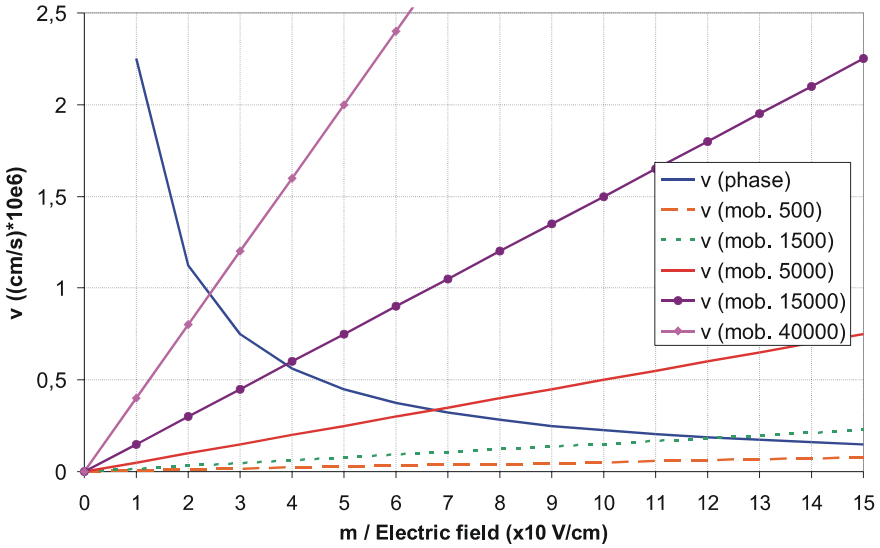

Figure 11.1. Electron drift velocity with different values of mobility and electric field. Also the phase velocity is plotted at different harmonic number m, f=75 GHz, L=0.3 µm.

As in room temperature the mobility over 10 000 cm^2/Vs is very difficult to reach with any traditional semiconductor structure, it can be concluded that the room temperature devices require high electric field to reach the first harmonic operation.

Table 11.1. The required electric field for different values of electron mobility for electron drift velocity to reach the 1st harmonic phase velocity.

Mobility (cm^2/Vs)	**500**	**1500**	**5000**	**15000**
Electric field (V/cm, for 1st harmonic phase velocity)	***4500***	***1500***	***450***	***150***

In [85] GaAs epitaxial structures were used as image-type waveguides and travelling-wave amplification was experimentally observed at 75 GHz with the electric field around 1000 V/cm. Pulsed electric field was used to prevent the excess heating of the device. Also a voltage between the terminals was detected when an electromagnetic

wave was travelling along the dielectric waveguide. This effect can be used for the electromagnetic wave power detection. However, real input-output gain was not achieved in this experiment, because of the high insertion loss of the image waveguide. Earlier, and also in this thesis, it has been shown that dielectric rod waveguides of GaAs, sapphire and silicon can impose very low propagation losses and good matching with a single mode metal waveguide in the frequency region of 75-170 GHz [27],[36]. Such waveguides offer also new opportunities for active component performance as they allow decreasing the insertion losses.

11.1.2 Heterostructures for creating an efficient electron drift

Heterostructures with two-dimensional electron gas layer seem to be prospective material structures for travelling-wave amplifiers as the mobility of electrons in the structure would be higher than in those used in earlier experiments. In general, heterostructure consists of two different semiconductor materials in junction contact, with unique electrical or electro-optical characteristics. A heterojunction is a junction in a single crystal between two dissimilar semiconductors. The most important differences between the two semiconductors are generally in the energy gap and the refractive index. In semiconductor heterostuctures, differences in energy gap permit spatial confinement of injected electrons and holes, while the differences in refractive index can be used to form optical waveguides. Semiconductor heterostuctures have been used, e.g., for diode lasers, light-emitting diodes, optical detector diodes and solar cells. Structures of current interest utilize III–V and IV–VI compounds having similar crystal structures and closely matched lattice constants. A close lattice match is necessary in heterostuctures in order to obtain high-quality crystal layers by epitaxial growth and thereby to prevent excessive carrier recombination at the heterojunction interface.

A heterostructure enables high electron mobility between a non-doped layer and highly doped n-type thin layer. These layers can be, for example, n-AlGaAs and GaAs. The electrons created in n-type AlGaAs drop completely into the next GaAs layer to form a depleted AlGaAs layer, because the heterojunction created by different band-gap

material forms a canyon in the GaAs side where the electrons can move quickly without colliding with any impurities.

Electron mobility is very much related to the temperature and electron concentration. The higher is the temperature and the electron concentration the lower is the electron mobility. Figure 11.2 presents how the electron drift velocity in AlGaAs/GaAs heterostructure depends on the electric field, temperature and electron concentration [90].

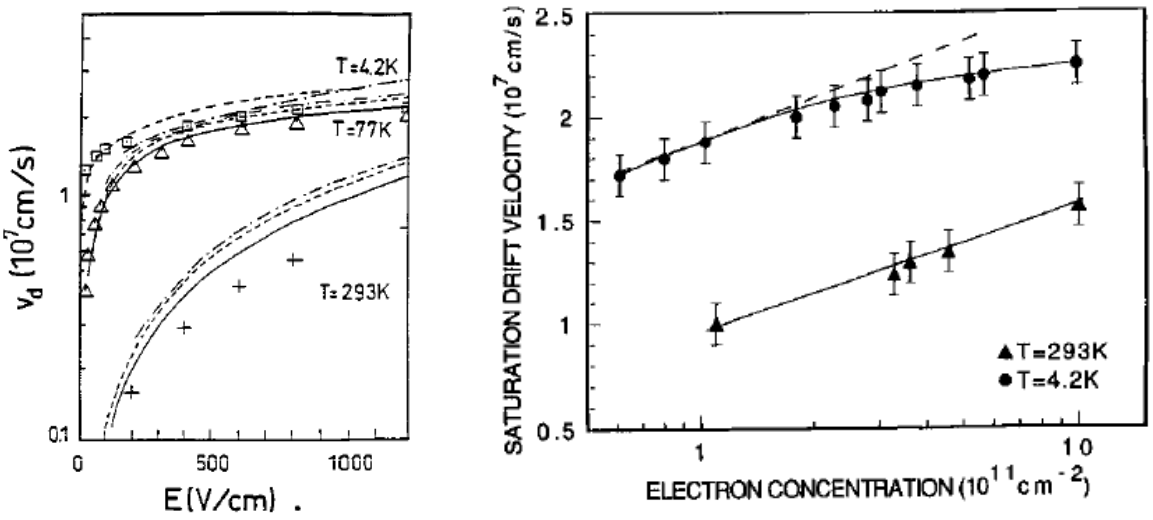

Figure 11.2. a) Electron drift velocity in AlGaAs/GaAs heterostructure in different temperatures. b) Saturation drift velocity as a function of 2-dimensional electron concentration [90].

Electron mobility of $Al_{0.3}Ga_{0.7}As$ is about 500 cm^2/Vs with electron concentration n=5·10^{18} cm^{-3} [91]. From Figure 11.2 b it can be seen that the saturation drift velocity increases significantly in 2-dimensional concentrations of 10^{11} cm^{-2}…10^{12} cm^{-2}. The mobility in AlGaAs/GaAs/AlGaAs heterostuctures with double sided doping has been measured in room temperature to be 2000-5000 cm^2/Vs depending on the thickness of

the quantum well (GaAs layer thickness). At 77 K the mobility increases up to 46 500 cm^2/Vs [92].

11.2 Structure of the device

As it is rather complicated to manufacture the slow-wave structure directly on a dielectric rod waveguide, in the first prototype stage the structure with ohmic contacts is made on a small chip that is embedded in the dielectric rod waveguide as presented in Figure 11.3.

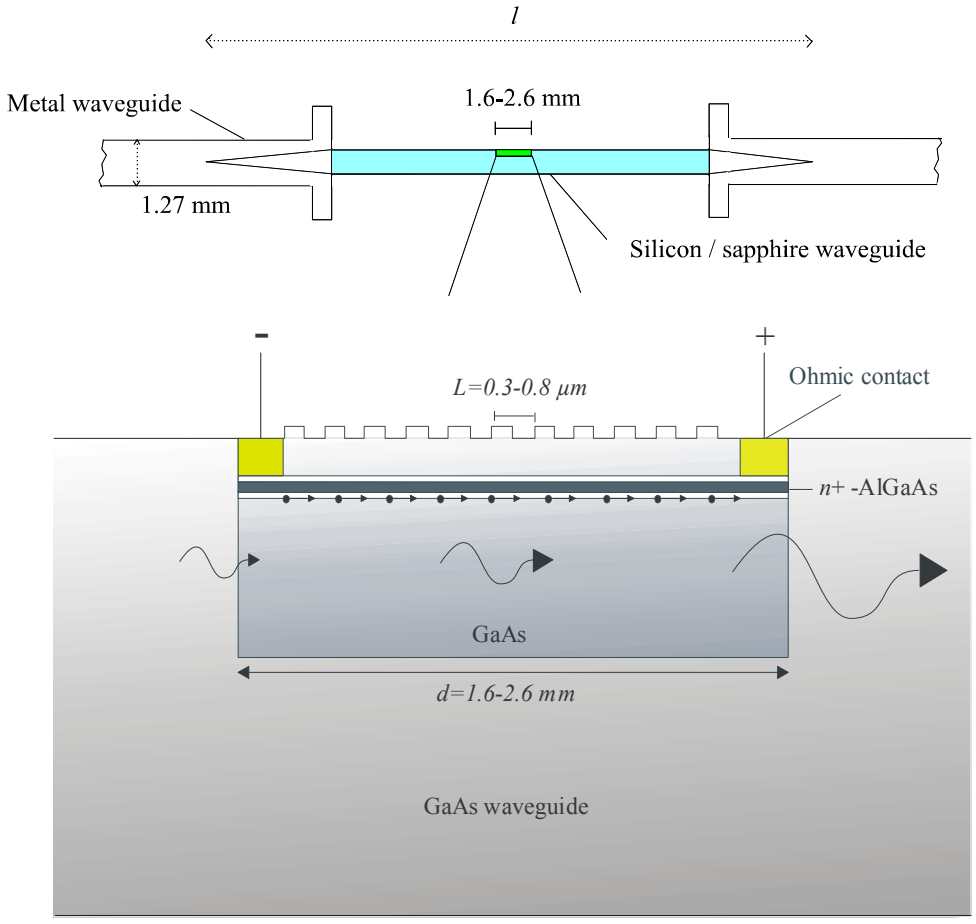

Figure 11.3. Structure of the DRW travelling-wave amplifier.

In the chip, the bottom layer of the heterostructure is GaAs and the upper highly doped layer is n^+-AlGaAs (40 nm) with the electron concentration of $5 \cdot 10^{18}$ cm^{-3}. Such structures are presented in more detail, e.g., in [93]. On top of the highly doped layer the slow-wave structure is made of GaAs. Figure 11.4 shows the layer structure after the molecular beam epitaxy (MBE). In the next section the manufacturing process steps are presented in more detail.

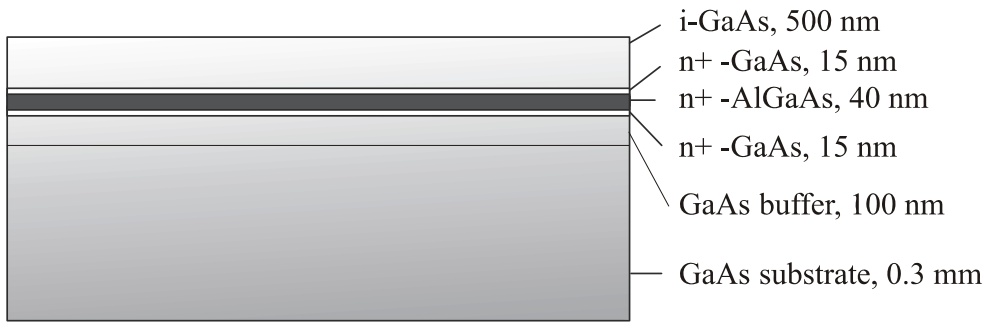

Figure 11.4. Layer structure after MBE.

11.3 Manufacturing process steps

11.3.1 MBE – Molecular Beam Epitaxy

Molecular beam epitaxy is used to grow the heterostructure described in Figure 11.4 on a 2" GaAs wafer. An important aspect of the MBE is that the deposition rate is low. This allows the films to grow epitaxially. However, this slow deposition requires a very good vacuum to achieve a good purity level. In solid state MBE the pure element sources are heated until they begin slowly to evaporate. The evaporated elements are then condensed on the wafer.

11.3.2 Ohmic contacts: photolithography for etching

A photo mask is manufactured for the ohmic contacts. As different size chips were desired, the ohmic contacts were designed so that the active region is varied between 1-2 mm. First the wafers are heated to drive off any moisture that can be present on the

surface. The wafer is covered by the photoresist by spin coating, this means spinning the wafer around rapidly to make a uniformly thick photoresist layer. In this case two layers of photoresist are required to form an undergap in etching. This undergap helps to remove the excess metal after the evaporation of ohmic contacts. This procedure is called as the lift off.

After adding the photoresist layers, the wafer is split in four pieces and placed under the mask, where the locations for the ohmic contacts are left open. The wafer is exposed with intense ultraviolet light that removes the photoresist where the mask is not present. The mask and a quarter of the wafer after light exposure are presented in Figure 11.5.

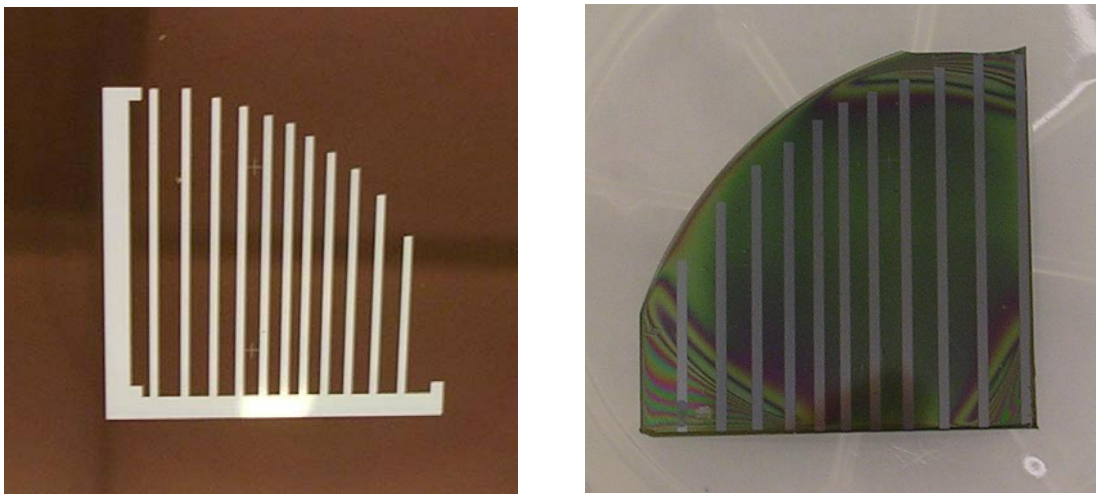

Figure 11.5. A photo mask for ohmic contacts and the processed wafer after light exposure.

11.3.3 Ohmic contacts: dry etching

In dry etching a plasma chemical agent removes the uppermost layer of the wafer in the areas that are not protected by the photoresist. In our case the top GaAs is etched with a mixture of chloride and argon gases ($2Cl_2Ar$). The etching time is defined by measuring the reflection of a laser beam from the wafer. The reflection varies with the thickness of the upper GaAs layer as can be seen in Figure 11.6.

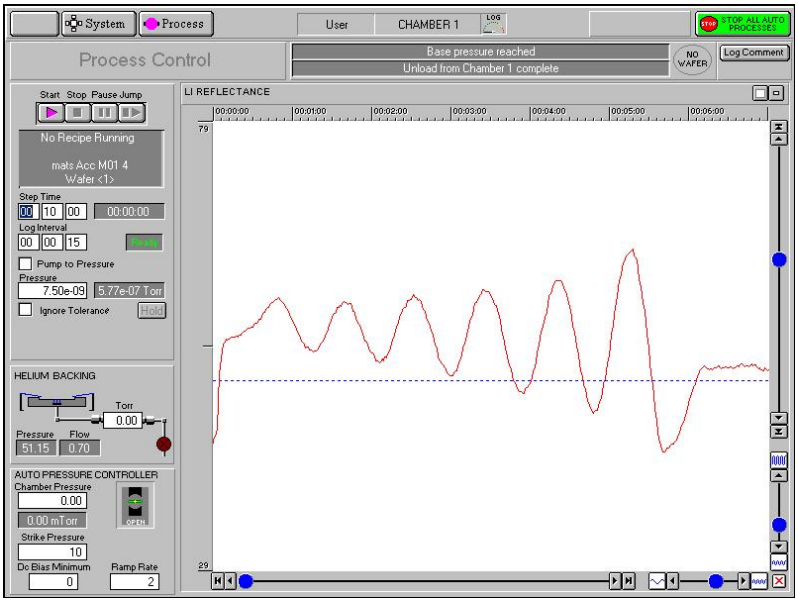

Figure 11.6. Laser reflectance from the wafer as a function of the etching time.

Cross-sectional image of the wafer after the dry etching can be seen in Figure 11.7.

Figure 11.7. Wafer after dry etching.

11.3.4 Ohmic contacts: evaporation of metal

Ohmic contacts are deposited on the etched wafer with an evaporator (Lesker Spectros, Figure 11.8). First a 20-nm layer of Ni was grown on AlGaAs to make a good contact as Au can not be deposited directly on AlGaAs. On top of the Ni layer a 520 nm, a Ge and a 2000-nm Au layer were deposited to make altogether ~300 nm ohmic contact. The wafer quarters after metal deposition are presented in Figure 11.9.

Figure 11.8. Evaporator for ohmic contact deposition.

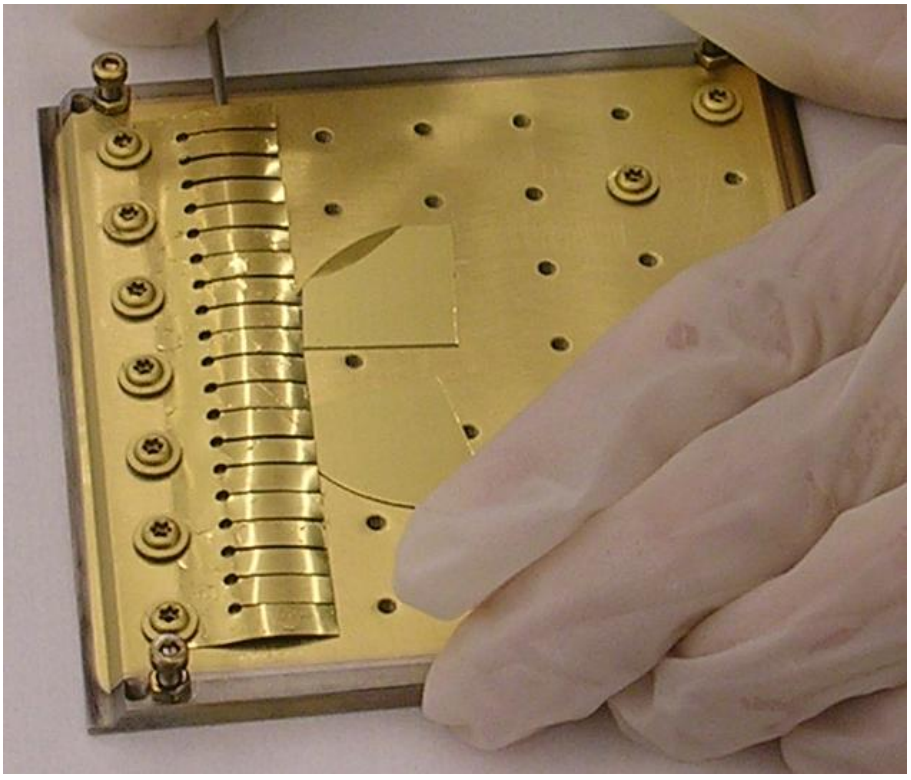

Figure 11.9. Wafer quarters after metal deposition.

11.3.5 Ohmic contacts: lift-off

In this process step the rest of the photoresist and the excess gold on top of it are removed chemically (Figure 11.10).

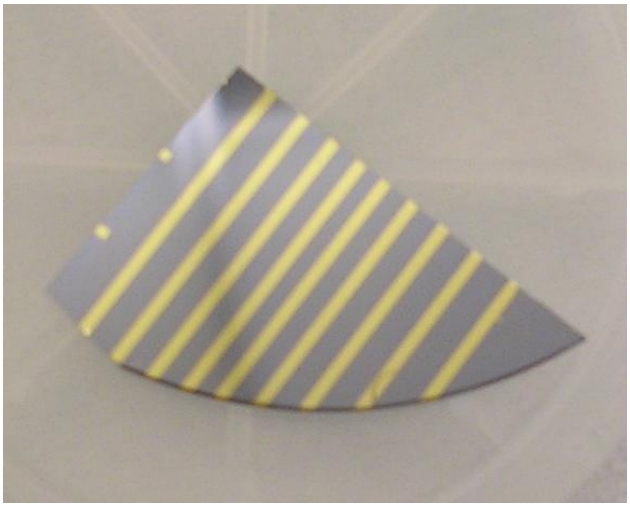

Figure 11.10. Wafer quarter after lift-off.

11.3.6 Periodic grating: electron beam lithography

This process step is used for making the grating between the ohmic contacts. Electron beam lithography can be used for making very small patterns on a resist with an electron beam without a mask. Nowadays line widths in order of 10 nm are possible. These patterns can be then used for making for example very small electronic circuits. In this case, it is desired to make several samples with different grating periods, 0.3-0.8 μm. Figure 11.11 shows the test sample for defining the correct electron dose to create good quality patterns. Correct dose is the amount that reaches the substrate through the resist without dosing too much the substrate. Six regions with different periods can be seen. Different periods of patterns reflect different colours.

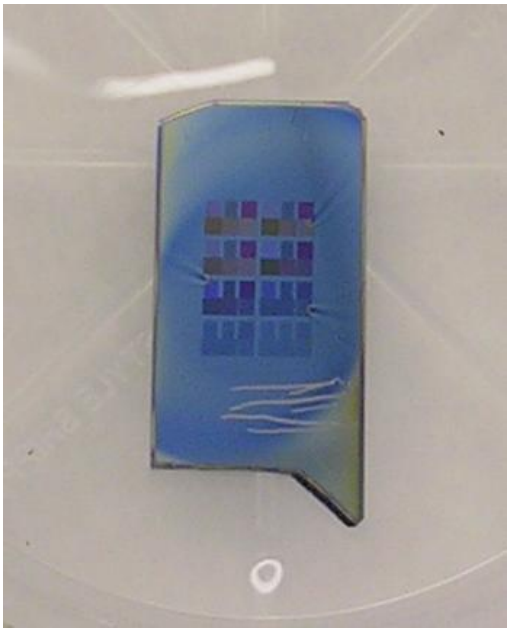

Figure 11.11. Test sample for electron beam lithography.

Scanning electron microscope (SEM) is used to compare the pattern quality between different doses. Two samples of these pictures with different magnification can be seen in Figures 11.12 and 11.13. Rectangular shapes represent areas with different grating periods.

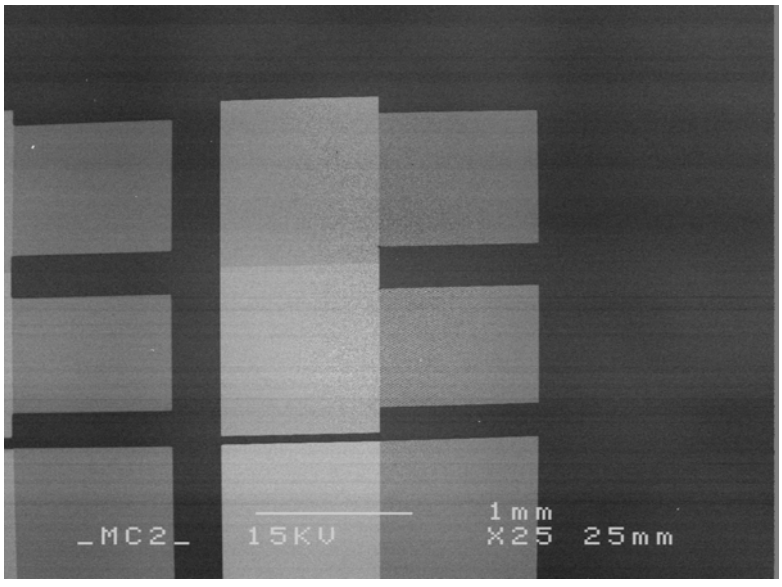

Figure 11.12. Scanning electron microscope picture of the periodic patterns with x25 magnification.

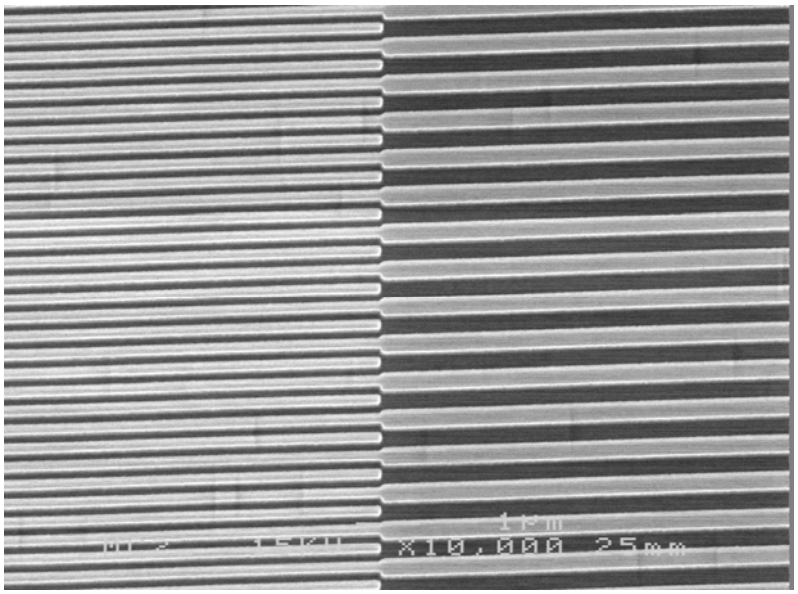

Figure 11.13. Scanning electron microscope picture of the periodic patterns with x10000 magnification (0.3 μm and 0.8 μm grating periods).

11.3.7 Periodic grating: dry etching

Electron beam lithography makes only the pattern on the resist, so the next step is to etch the wafer to get the desired depth of the grating, 100 nm. This is done in a similar way as for the ohmic contacts in Section 11.3.3. Figure 11.14 shows the wafer structure after etching. A surface profiler (Alpha-Step 500) is used to measure the etched depth and it is measured to be around 90 nm.

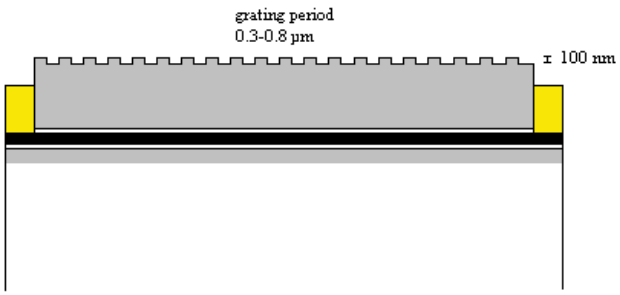

Figure 11.14. Wafer structure after dry etching the grating.

11.3.8 Alloying

To alloy the ohmic contacts, the wafers are annealed in a heat chamber at 460 ˚C for 30 s. Post-deposition annealing of contacts is also useful for relieving stress as well as for inducing any desirable reactions between the metal and the semiconductor.

11.3.9 Sawing

Finally the wafer is cut to chips with a dicing saw (Figure 11.15). Also GaAs waveguides with a small groove for the amplifier chip are cut with the dicing saw.

Figure 11.15. Dicing saw (Disco DAD3350).

11.4 Measurement results

In this section measurement results are presented. Figure 11.16 presents a microscopic photograph of three processed chips with different gratings. Different periods reflect different colours.

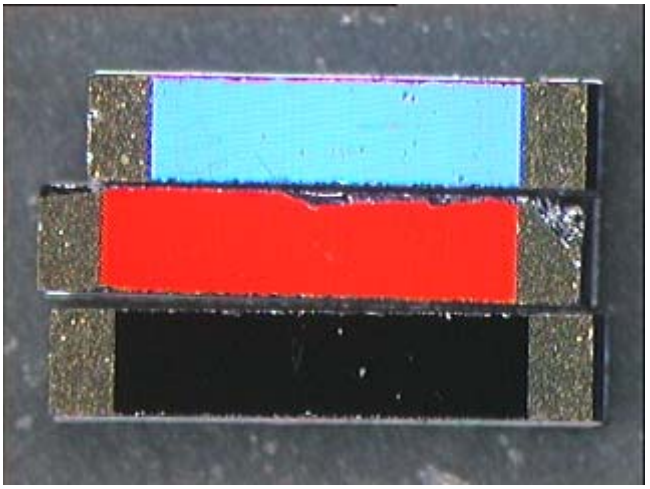

Figure 11.16. Microscopic photograph of the grated amplifier chips. Three chips with different grating periods 0.5 µm (blue), 0.7 µm (red) and 0.3 µm (black) are presented.

11.4.1 I-V characteristics

The current between the ohmic contacts is measured with different voltages to characterize the behaviour of the chip. A cryogenic cooling system using liquid helium and vacuum is used to get measurement results in different temperatures. The system is able to cool down to a temperature near 10 K. Figure 11.17 presents the measurement results of a 2.2 mm long chip at six different temperatures.

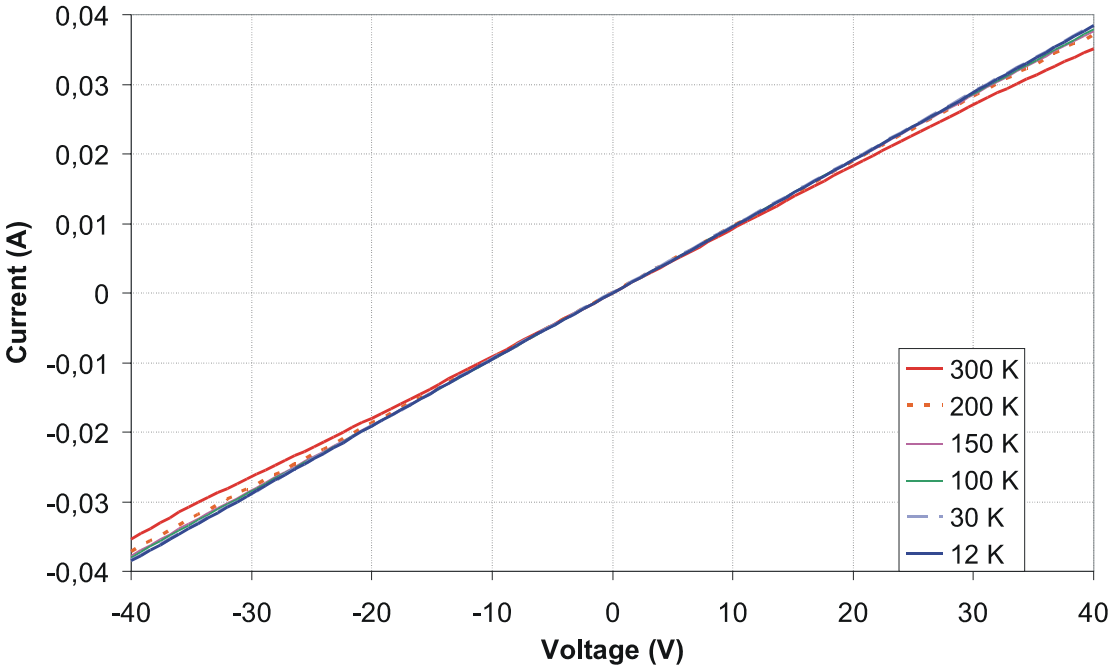

Figure 11.17. I-V characteristic of GaAs/AlGaAs chip (2.2 mm long).

According to the results the chip seems to have very linear, resistor-like, behaviour. Unfortunately the measurement system is limited in voltage, giving maximum voltage of only ± 40 V. The current slightly increases with the cooler temperatures.

Another, and more robust, setup is used to measure the current at higher voltages. It is observed that without the vacuum the room temperature measurement can not be performed at higher DC voltages than 35 V due to the heating of the chip. The temperature of the chip is cooled down by placing it on a metal holder and cooling the metal with liquid nitrogen (Figure 11.18).

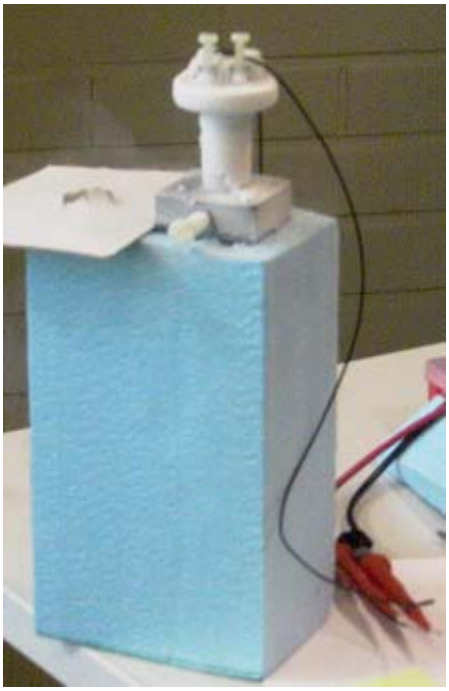

Figure 11.18. I-V characteristic measurement with liquid nitrogen cooling.

Figure 11.19 presents the measured I-V characteristics of the AlGaAs/GaAs chip. Resistance between the chips varies slightly (850 Ω… 1110 Ω). This is also the reason why electric current is slightly increased in this measurement. Temperature of the chip is measured with a thermometer probe to be ≈ -100 ˚C. Three nearly linear sections of the I-V curve can be observed (0-15 V, 15-55 V, 55-65 V). The average electron mobility of the AlGaAs/GaAs heterostructure is measured to be 1575 cm^2/Vs in room temperature. This value is slightly lower than expected.

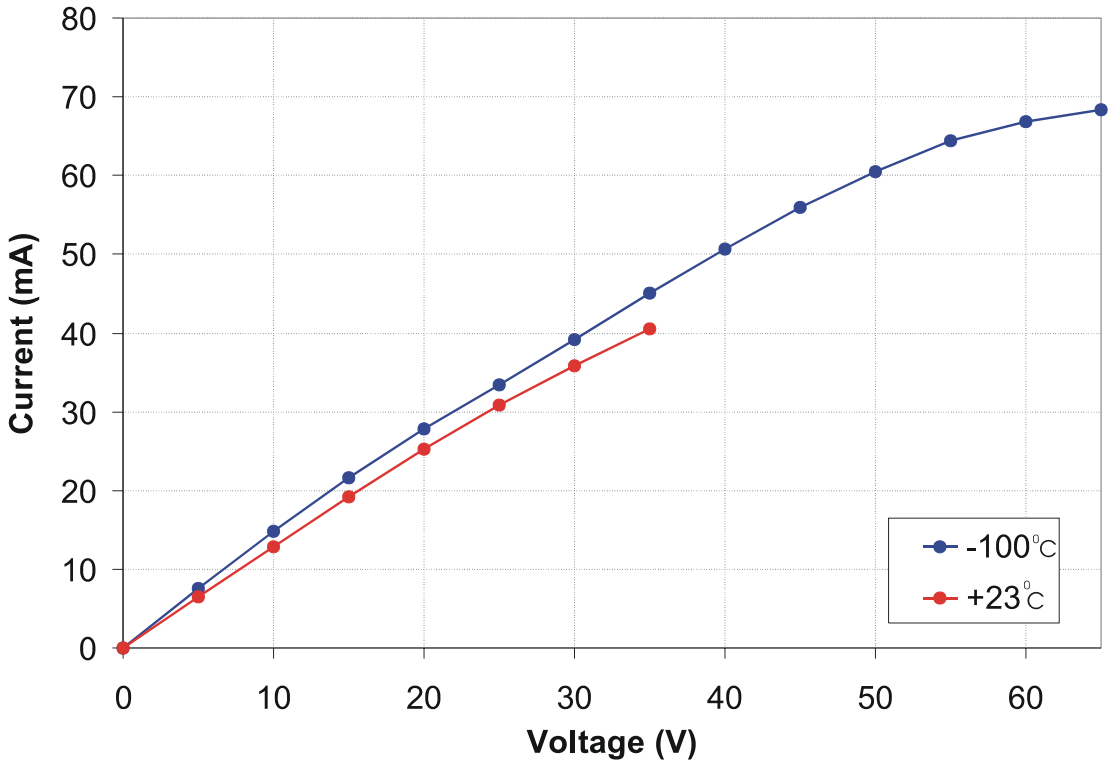

Figure 11.19. I-V measurement with liquid nitrogen based cooling.

11.4.2 Measurement of gain

DRWs are measured with HP8610 vector network analyzer (VNA). Measurement setup is presented in Figures 11.20 and 11.21. Electric field is applied to the ohmic contacts with metal pins.

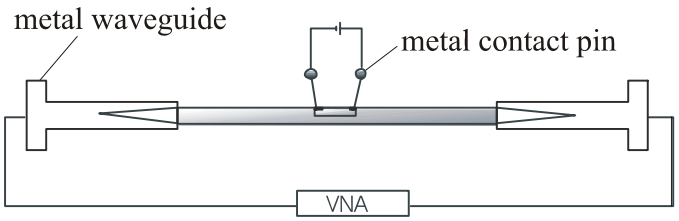

Figure 11.20. Schematic of the measurement setup.

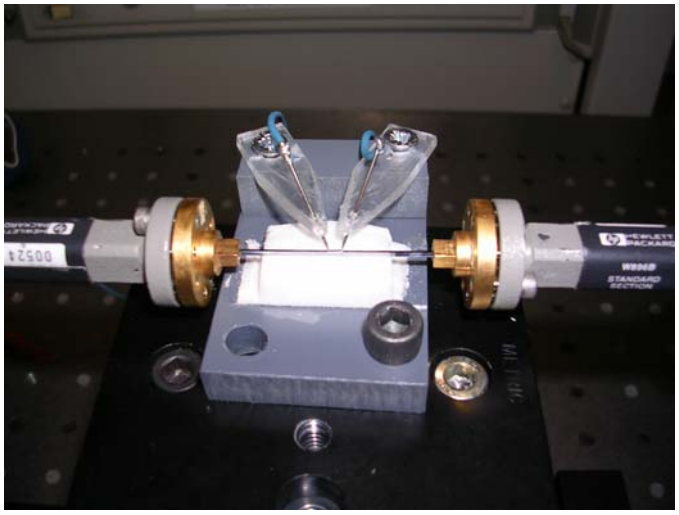

Figure 11.21. Photograph of the measurement setup.

Transmission characteristics of the GaAs waveguide are measured with and without the chip (2.2 mm). The results are presented in Figure 11.22. Measurement reveals that the groove for the chip degrades very much the transmission characteristics. If the contact pins are used, especially at low frequencies (70-80 GHz) the metal contact pins cause a lot of additional losses.

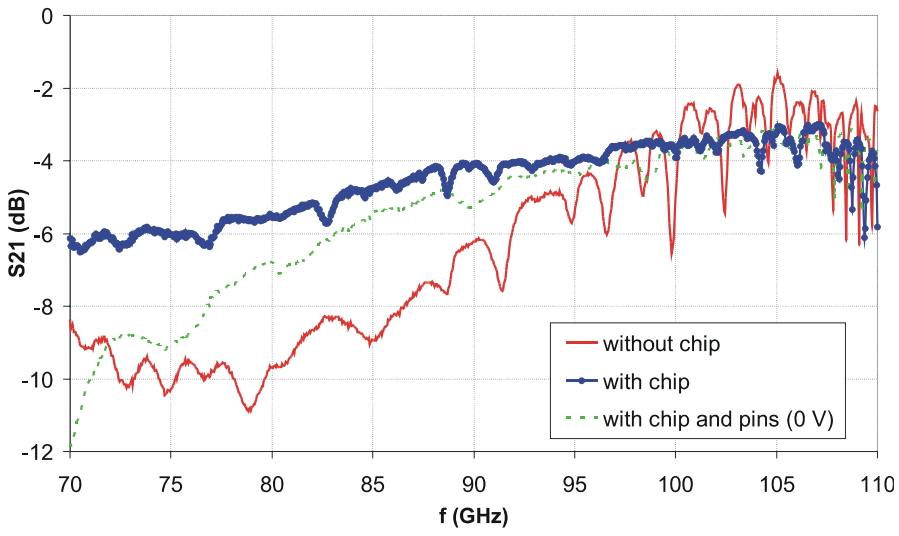

Figure 11.22. Measured S_{21} of the GaAs waveguide with and without a chip (2.2 mm) and metal contact pins.

Three sets of chips with different lengths (1.6 mm, 2.2 mm and 2.6 mm) are measured in gallium arsenide waveguide. The length of the ohmic contact is always 0.3 mm. Figure 11.23 shows the measured transmission coefficient with different applied electric fields in 2.2 mm chip, where the grating period is 0.3 µm. The improvement in S_{21} is clearly visible as the electric field is increased. As can be seen the S_{21} curves are slightly shifted as the electric field is increased. This can be interpreted as a shift in the signal phase. Length of the active region in the chip did not influence on the effective amplification.

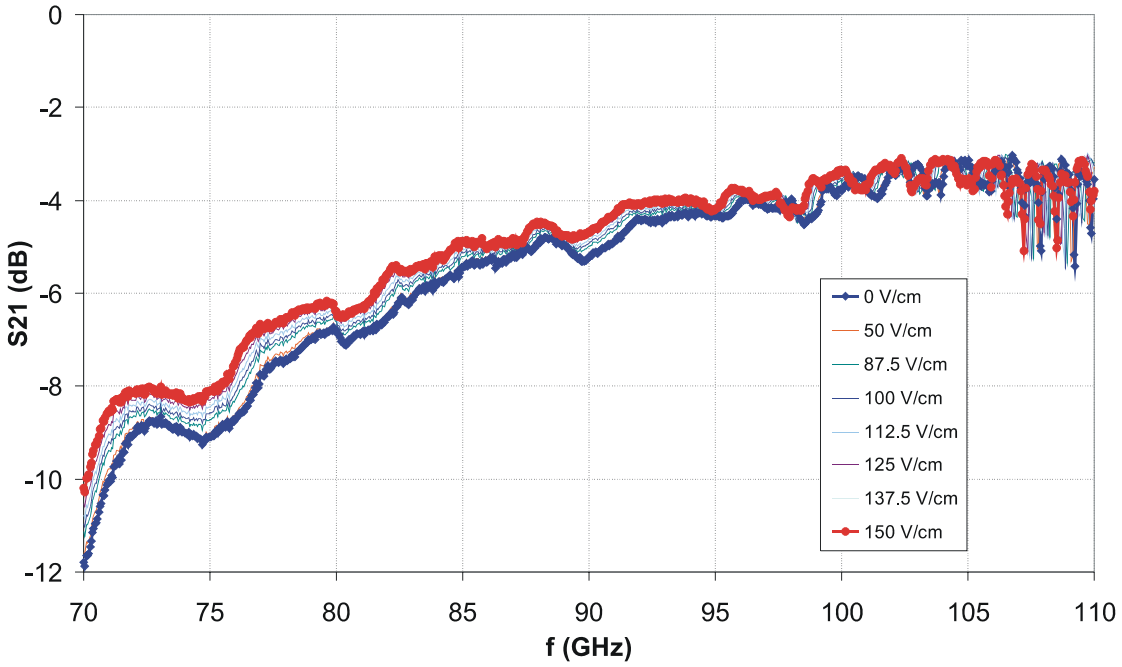

Figure 11.23. Measured S_{21} with the 2.2 mm chip (0.3 µm grating period) with different applied electric fields.

In Figure 11.24 the measured S_{11} is presented. Similar shifts as in S_{21} can be observed. Amplitude level of S_{11} remains the same between the different measurements.

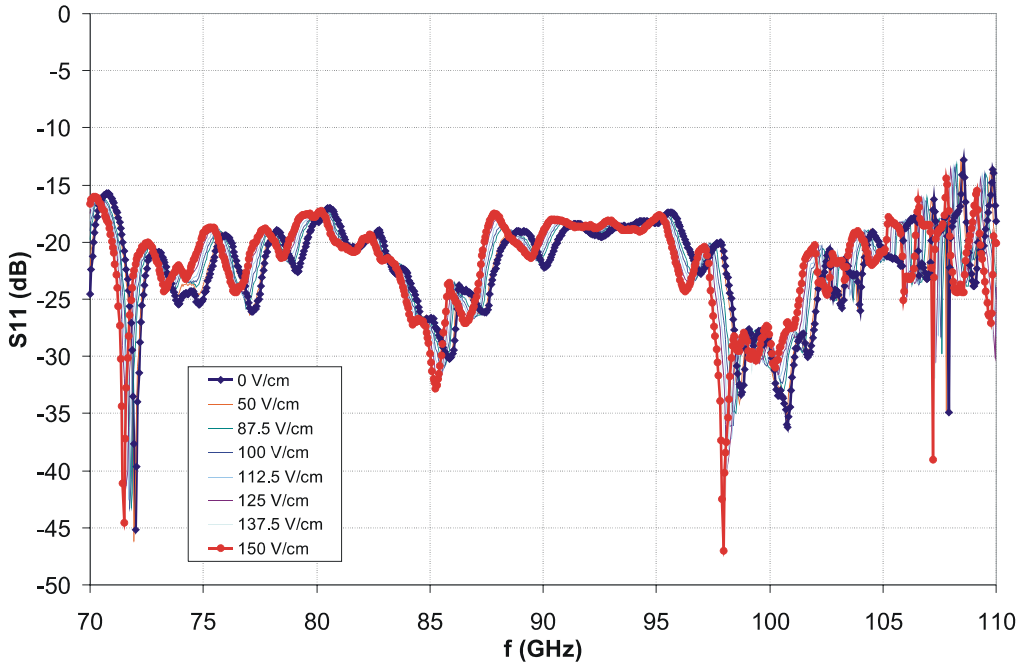

Figure 11.24. Measured S_{11} with the 2.2 mm chip.

One might think that the improvement in S_{21} is due to the improvement in matching as both curves contain similar shifts. However, this is not the case as can be seen in Figures 11.25 and 11.26, where the change in reflection and transmission coefficients is plotted at different frequencies.

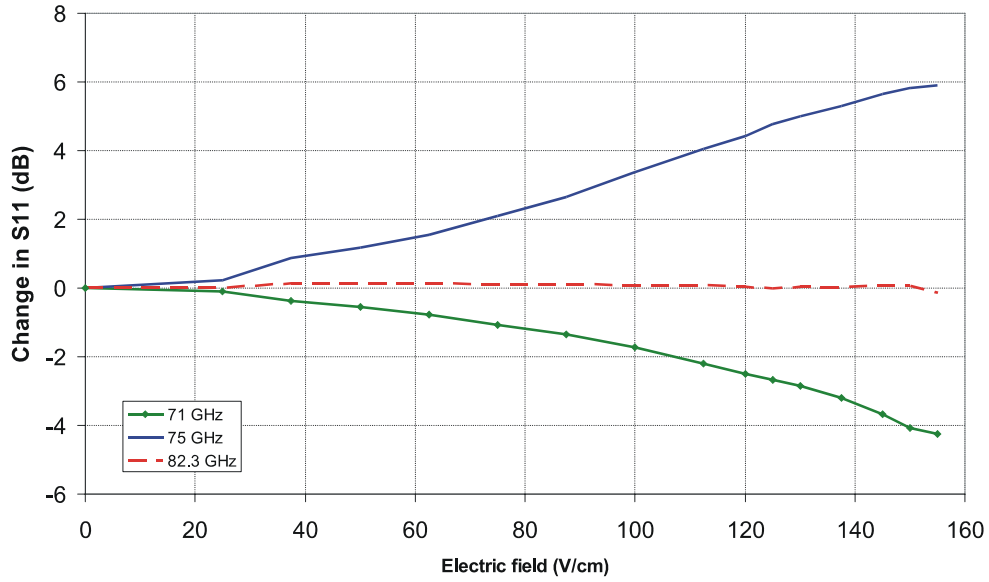

Figure 11.25. Change in S_{11} at different frequencies.

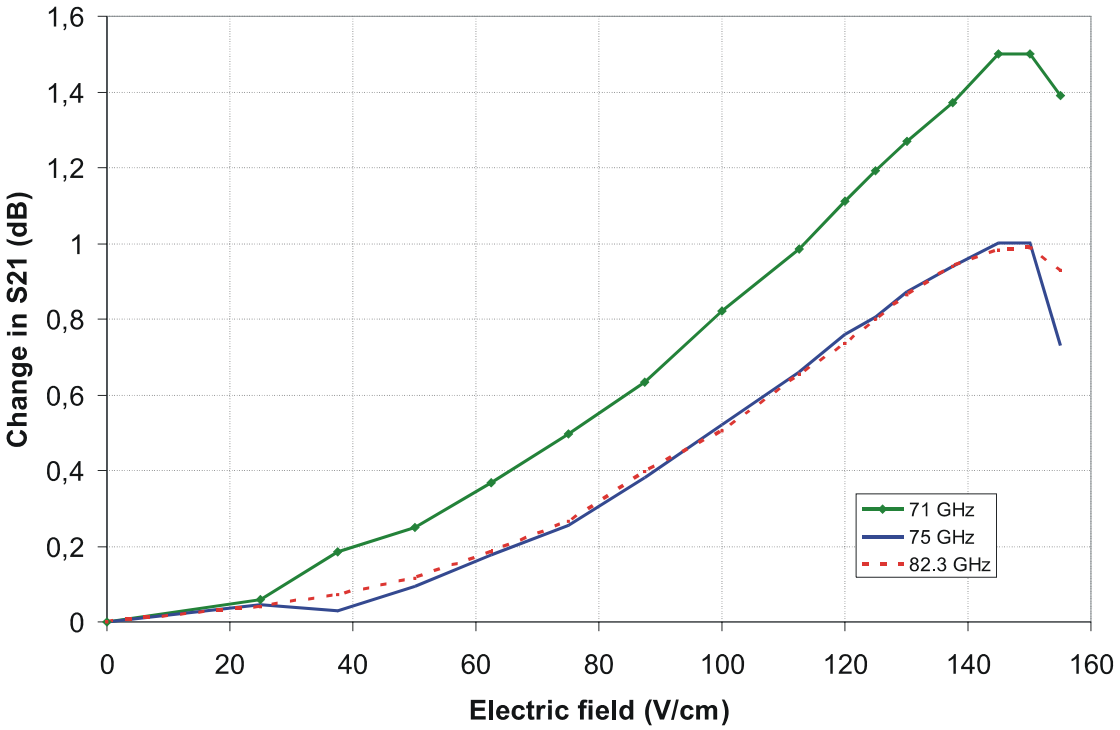

Figure 11.26. Change in S_{21} at different frequencies.

It can be noticed that at some frequencies S_{11} is improved (descending green line) with the electric field and at some frequencies S_{11} is getting worse (rising blue line). S_{21} is improving at all frequencies up to 135 V/cm. However, change in S_{11} has some effect to S_{21}. Normally the amplification effect should decrease with the frequency, but at 82.3 GHz the matching is better than at 75 GHz and the corresponding S_{21} curves are almost identical.

Measurements reveal that with current setup the maximum electric field that can be used is around 150 V/cm. Higher voltages burn the chip. To reach higher electric field values a cooling system or a pulsed electric field should be applied to the setup. According to Figure 11.1, with current setup, at maximum a 3rd-harmonic operation is reached, depending on the dispersion in electron drift. However, the amplification is effect is very clear already with this setup and also with low values of electric field. This indicates that the used heterostructure is very effective candidate for this application.

In Figure 11.27 the electronic gain calculated from the measured S_{21} is presented. S_{21} with 0 V/cm is simply reduced from S_{21} measured with different voltages. Note that the unit is now dB/cm, thus the dB values in Figure 11.23 are multiplied by 5 (10 mm/2.0 mm, the ohmic contacts are not taken into account to effective chip length). As expected the effect is strongest at lower frequencies and it decreases with the frequency. This can be explained by the fact that the longitudinal electric field component at the surface of the waveguide is larger at lower frequencies because of a lower field concentration inside the dielectric.

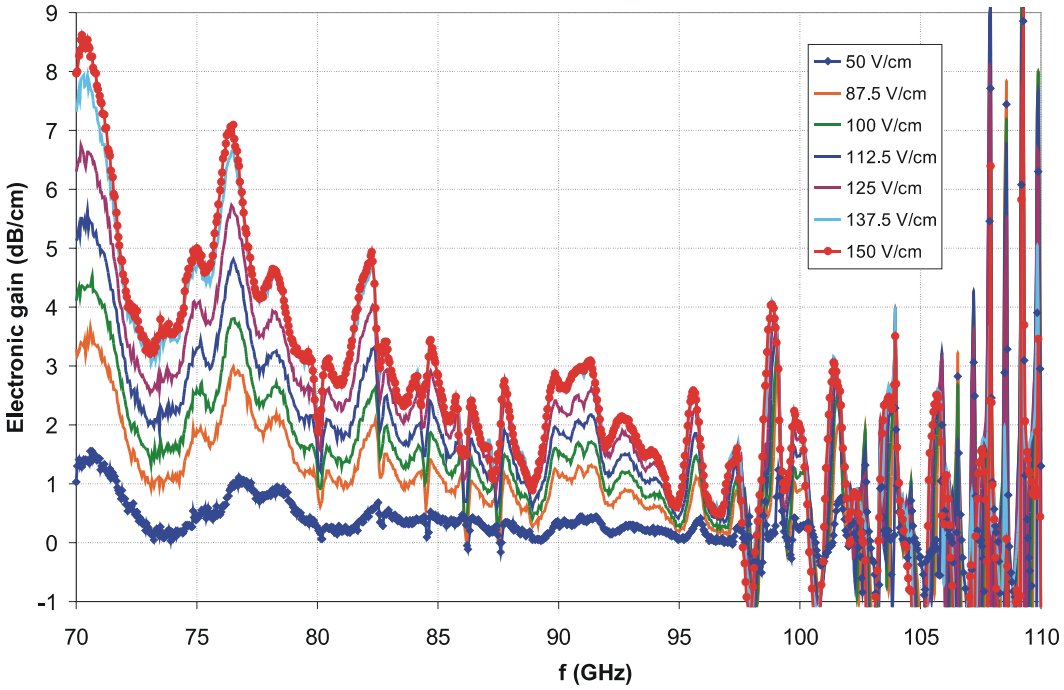

Figure 11.27. Electronic gain.

Figure 11.28 presents the gain behavior at a single frequency of 76.5 GHz. The gain starts decreasing at electric fields higher than 150 V/cm. Cooling should enable higher operating voltages. Unfortunately it can not be applied with current setup.

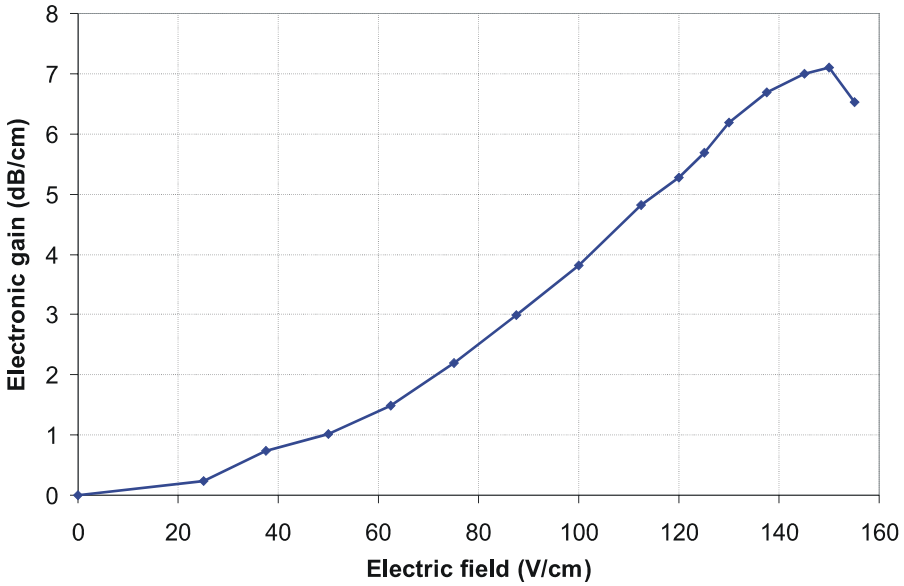

Figure 11.28. Measured electronic gain at 76.5 GHz.

The effect of the different grating periods in the chip can be seen in Figure 11.29. The highest gains are obtained with the 0.3 µm period at this frequency range.

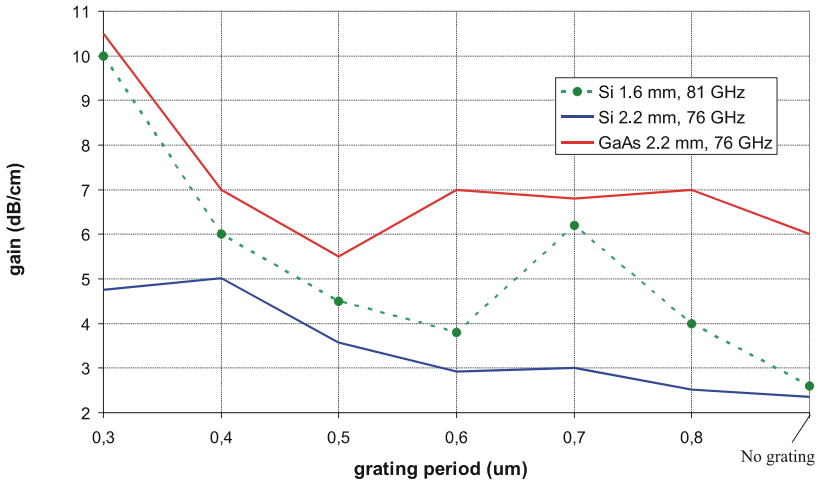

Figure 11.29. The effect of the grating period for the gain.

The phase shift observed in S_{21} during the measurements is presented in Figure 11.30. The phase shift is slightly increasing with the applied electric field and also with the frequency.

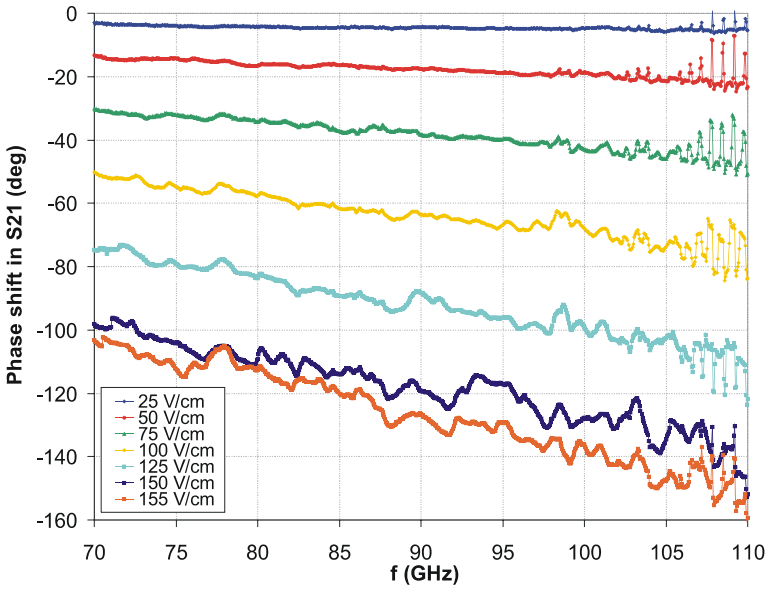

Figure 11.30. Measured phase shift in S_{21}.

11.5 Conclusion of this chapter

This chapter presents an experimental study of a DRW travelling-wave amplifier. The amplification is based on energy transfer from an electron drift to an electromagnetic wave. The electromagnetic wave propagates through a slow-wave structure where it interacts with the electron drift. The slow-wave structure is implemented with a grating on a GaAs layer on top of an AlGaAs/GaAs heterostructure. Grating period is 0.3-0.8 μm. Use of a heterostructure aims at more efficient energy transfer than that achieved in earlier experiments. Heterostructure and the grating are implemented on a small chip that is inserted in a grooved GaAs rod waveguide.

The measurement results are promising although a true insertion gain has not been achieved. The improvement in S_{21} at lower end of the measured frequency band (70-80

GHz) is observed to be ~10 dB/cm at highest with 150 V/cm electric field. The highest effect is achieved with the smallest period of grating, 0.3 μm. A phase shift due to the applied electric field is also observed in the measurements of S_{21}. However, the first harmonic operation is not achieved with this combination of the applied electric field and the electron mobility in the chip. At highest, a 3rd-harmonic operation is used depending also on the dispersion both in electron and electromagnetic propagation.

In the next development stage of this type of a travelling-wave amplifier, the goal is to manufacture a monolithic device without a separate chip. The structure with the chip has too many uncertainties that make it difficult to analyze all the phenomena included. Also the insertion losses are very high and they should be reduced. For example the DC pins cause a lot of reflections to the system and other feeding solutions should be considered. In addition to a cooling system, a pulsed operating voltage is also one way to decrease heating. Concerning the structure of the chip, thickness of the layer below the grating could be thinned for more effective interaction between the electrons and the electromagnetic field. Also smaller grating periods should be considered as the highest effect was observed with the smallest period available.

12 TUNABLE DRW PHASE SHIFTER BASED ON FERROELECTRIC VARACTORS

Phase shifters are needed in many applications, especially in phased array antennas (PAA). Earlier, in microwave regime most of these antennas were controlled by ferrite or p-i-n diode phase shifters [94]. Ferroelectric phase shifters have offered substantial cost and size reduction to array antennas [95],[96].

Different types of phase shifters are possible to implement on a dielectric rod waveguide. One recent idea has been to use high impedance surfaces with dielectric rod waveguides for phase shifting. In [97] such a surface is implemented with a metal waveguide to operate together as a phase shifter. In this chapter a novel millimetre-wave phase shifter targeted on thin ferroelectric film technology is presented. Earlier dielectric rod waveguides have been loaded with metal strips and p-i-n diodes to operate as a leaky wave antenna with a controllable beam direction at 3.5 GHz [98]. In this case the DC bias to diodes has been realized with thin magnet wires loaded with ferrite-bead chokes.

The architecture of the proposed phase shifter includes a dielectric rod waveguide with a periodic printed array of electrically small dipoles loaded with ferroelectric varactors (also e.g. p-i-n diodes or Schottky diodes could be used) to control the phase of the propagating wave (Figure 12.1). Such voltage tunable varactors have been used earlier in a silicon coplanar waveguide phase shifter [99]. The varactors are deposited on a BCB (benzocyclobutene) layer. At this stage the proposed architecture of the phase shifter is verified by simulating and measuring two prototypes, where the ferroelectric varactors are replaced by non-tunable capacitors with 10 fF and 15 fF capacitance.

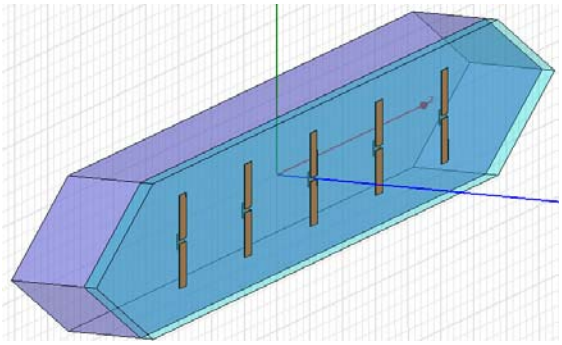

Figure 12.1. DRW phase shifter prototype with loaded metal dipoles.

12.1 Phase shifter prototypes

The DRWs are fabricated from Si wafer with 3 kOhm/cm resistivity. To simulate the performance of the phase shifter using a ferroelectric varactor, two waveguide samples are fabricated using fixed capacitive loading of the dipoles. The dipoles are made of Au on a thin 0.5 µm BCB layer. The thickness of the gold strip is also 0.5 µm. The value of the capacitance for each sample waveguide is set by the gap corresponding to 10 fF and 15 fF respectively. Total length of the both dipoles is 800 µm. The period of dipoles is calculated for the operational frequency of 80-90 GHz, thus for this case the total amount of 40 dipoles is chosen on the waveguide length of 20 mm, Δz= 500 µm (Figure 12.2). The other dimensions of the dipoles are presented in more detail in Figure 12.3. Two types of waveguides with different cross-section dimension (0.5 x 1.0 mm^2 and 0.5 x 0.8 mm^2) are fabricated as in simulations thinner waveguide has performed better in terms of losses at higher frequencies [100]. Total length of the waveguide is 30 mm including tapering sections. In order to estimate the contribution of the electrodes to the loss, a third waveguide with the identical length is cut from the same wafer prior to deposition of the dipoles.

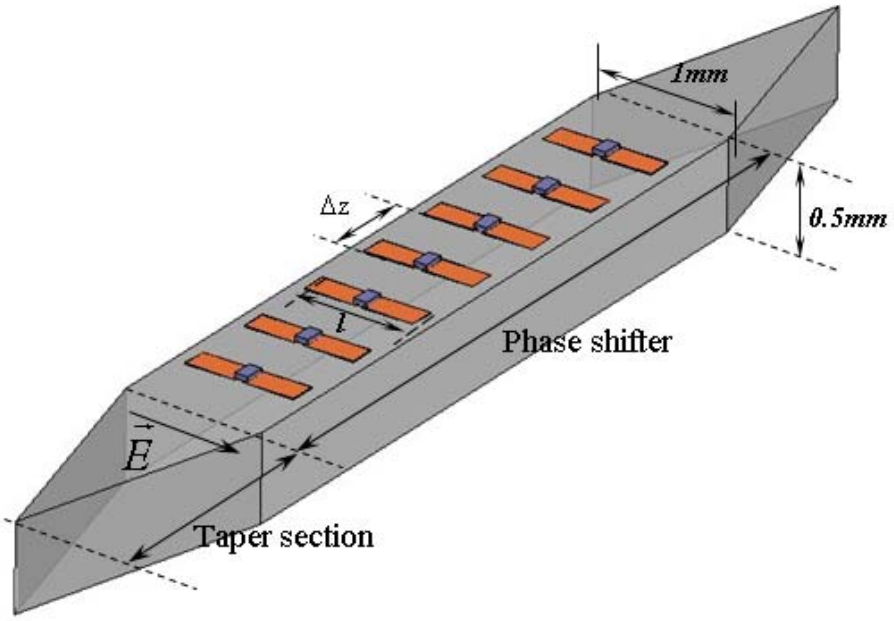

Figure 12.2. DRW phase shifter prototype with dimensions. Varactors are not included in the manufactured prototype.

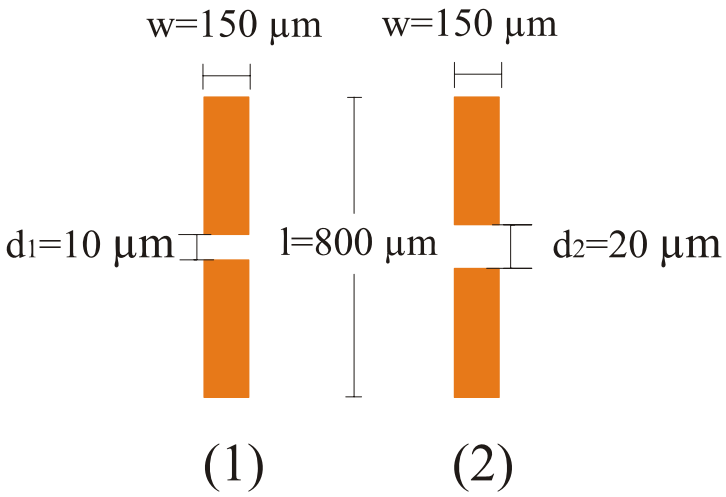

Figure 12.3. Two capacitances (C_1=15 fF, C_2=10 fF) implemented with Au strips.

12.2 Measurements

S parameters are measured with HP 8610 VNA. The measurement results of the phase shifter prototypes are shown in Figures 12.4 and 12.5. The averaged transmission loss is about 3…4 dB for both printed capacitance structures at 75-90 GHz. Thinner waveguide has larger losses at low frequencies. The measurements of the DRWs without the printed structure are also shown. According to measurements the printed structures radiate strongly at frequencies over 100 GHz.

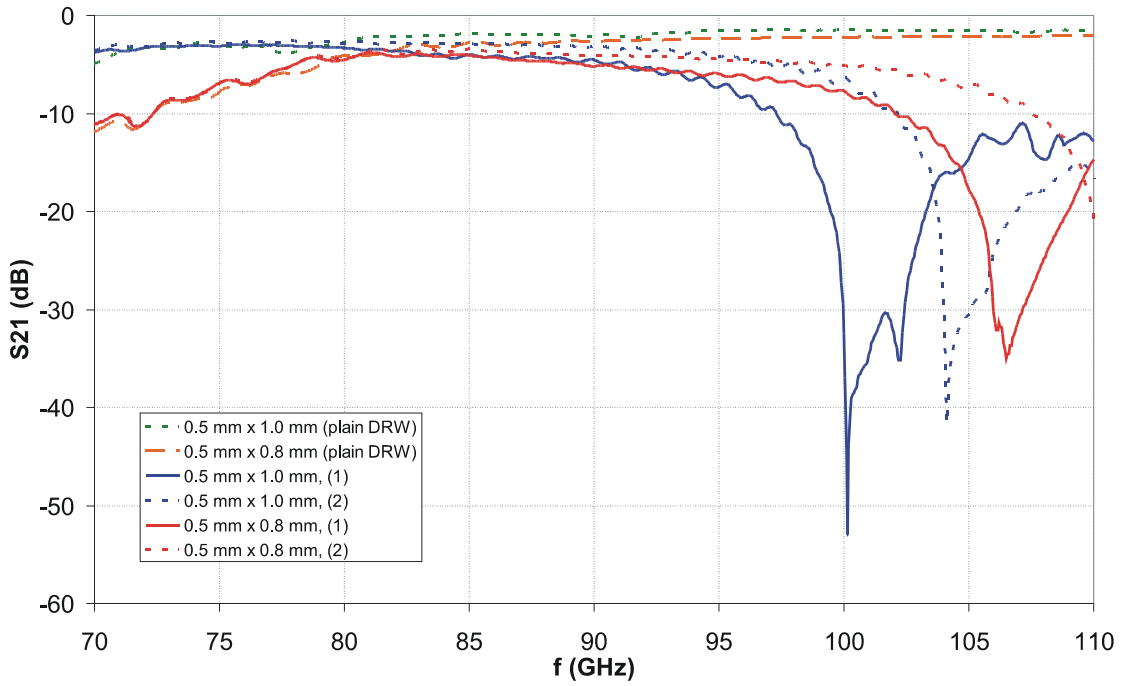

Figure 12.4. Measured S_{21} for different phase shifter prototypes.

The measurement of the blank DRW reveals approximately 2 dB of insertion loss at 75-90 GHz, Figure 12.6, implying that two major factors are the dielectric and coupling loss. S_{11} at the same frequency band is shown in Figure 12.7. The contribution of the dielectric loss can be decreased by a dielectric substrate with a lower loss tangent. For instance, DRW made of sapphire has about 1 dB/m insertion loss [36]. Thus, by using Si substrate with higher resistivity the insertion loss can be decreased by at least 1 dB.

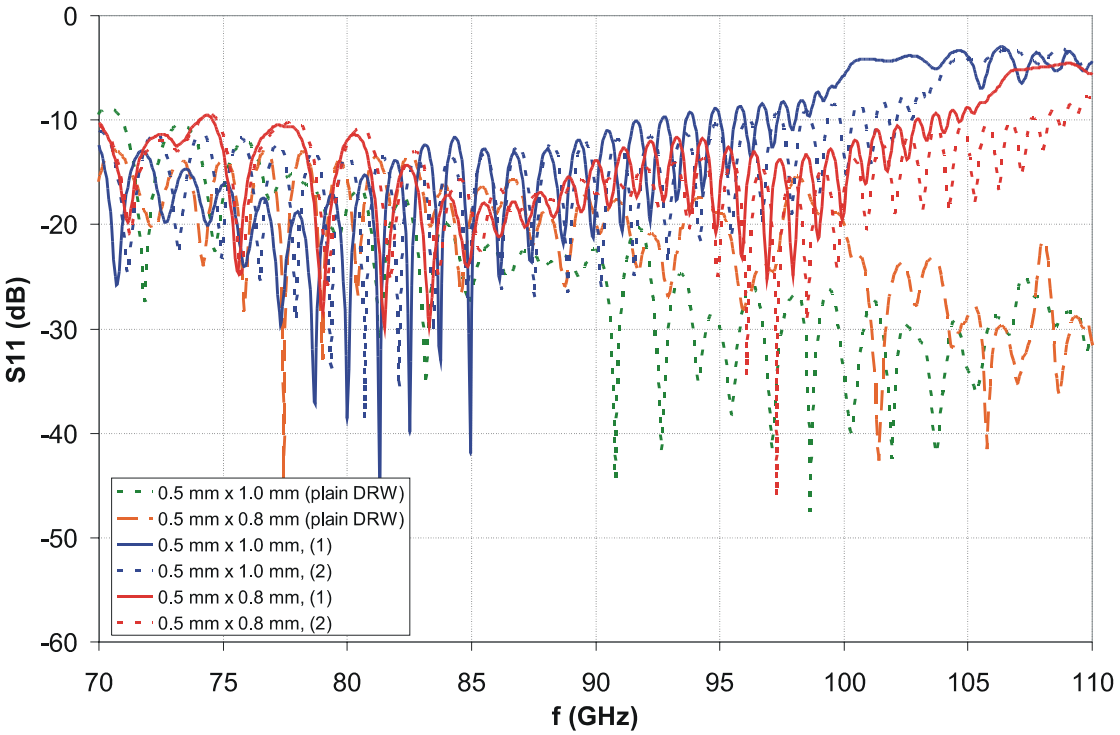

Figure 12.5. Measured S_{11} for different phase shifter prototypes.

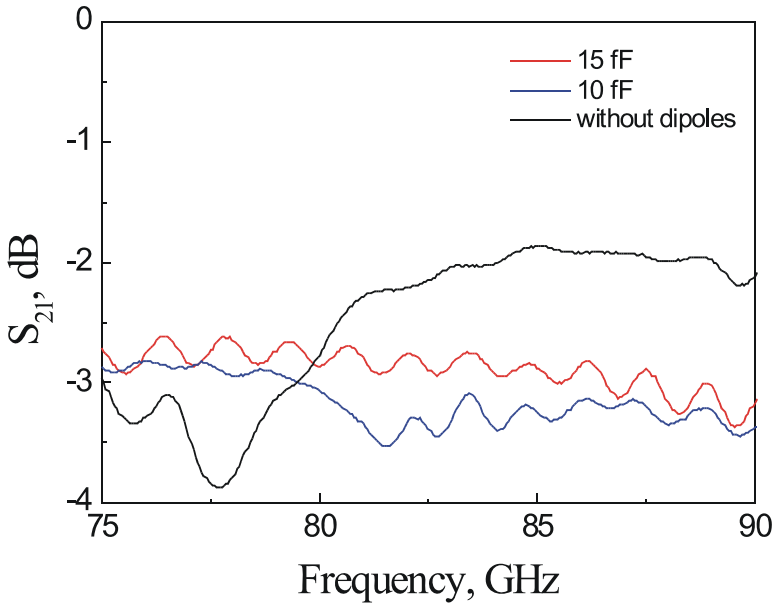

Figure 12.6. S_{21} comparison of the waveguides of 0.5 x 1.0 mm^2 cross-section with and without the printed capacitances.

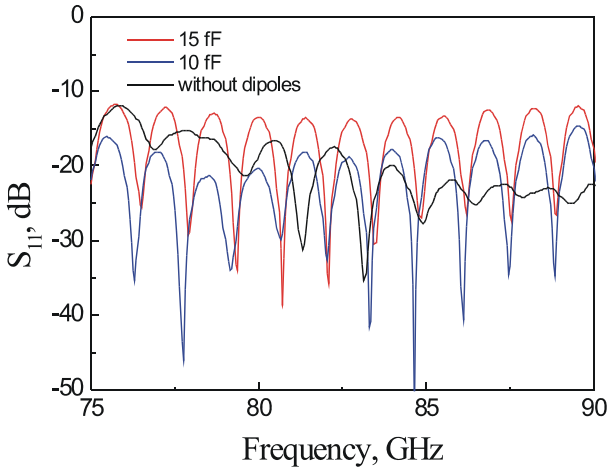

Figure 12.7. S_{11} comparison of the waveguides of 0.5 x 1.0 mm^2 cross-section with and without the printed structure.

The measured transmission phase is shown in Figure 12.8 for the three structures investigated with cross-section of 0.5 x 1.0 mm^2. The smaller waveguides are omitted at this stage. Figure 12.9 presents the differential phase between the structures with 10 fF and 15 fF loadings. In the middle of the considered bandwidth (85 GHz) this is 120 deg.

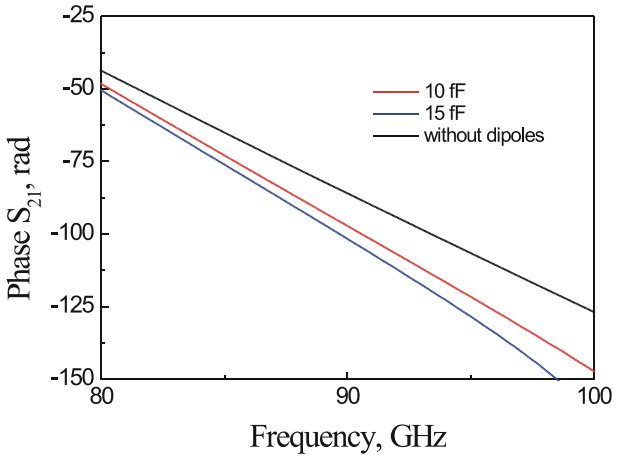

Figure 12.8. Measured phase characteristics of the 0.5 x 1.0 mm^2 waveguides with and without the printed structure.

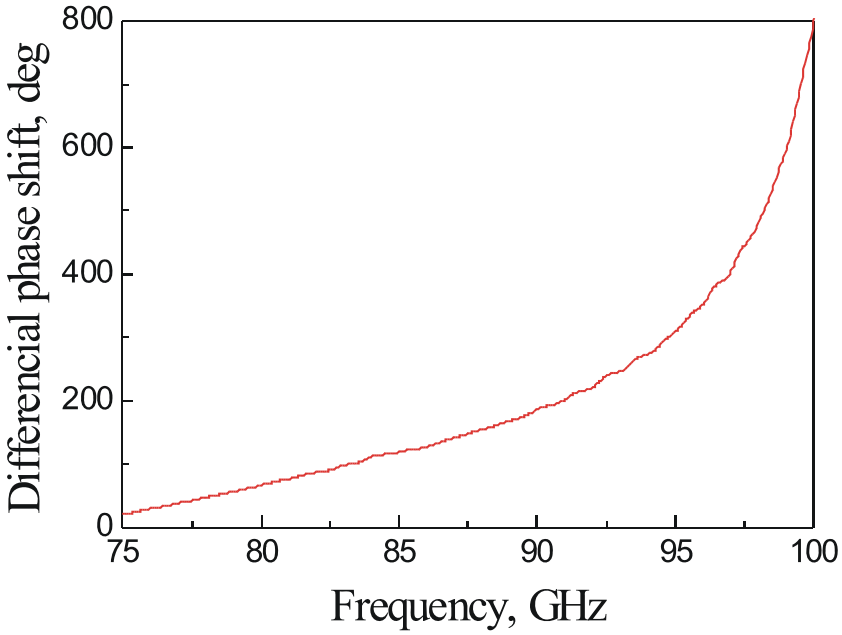

Figure 12.9. Differential phase between the waveguides of different printed structures.

12.3 Conclusion of this chapter

In this chapter, a concept for a phase shifter based on a DRW and ferroelectric varactors for W band is presented. The architecture of the proposed phase shifter includes a DRW with a periodic printed array of electrically small dipoles loaded with ferroelectric varactors. Varactors are implemented on the side of the DRW. They can be controlled electronically to vary the phase of the signal. At this stage the proposed architecture of the phase shifter is verified by simulating and measuring two prototypes, where the ferroelectric varactors are replaced by non-tunable capacitors with 10 fF and 15 fF capacitance. Capacitors are implemented by two different gaps in the metal dipoles.

Measurements results show that the architecture has a good potential to be operated at 70-95 GHz. At higher frequencies the dipoles radiate strongly. The radiation at selected frequencies could be avoided by using different dimensions and separations of the metal

dipoles. Measured insertion loss of the DRW was ~3 dB with the dipoles and ~2 dB without. This value could be decreased by ~1 dB by using the Si substrate with higher resistivity. In that case the insertion loss of the loaded DRW should approach 2 dB, which corresponds to ~60 deg/dB FOM (figure of merit) for the phase shifter. This limiting value can be obtained for a lossless varactor with n=1.5 tunability. In practice, however, all tunable elements are associated with additional loss that degrades the above estimation. In the future, this concept is considered to be used with thin film ferroelectric varactors developed at Chalmers [101]. However, these varactors are not applicable at frequencies above W band. For higher frequencies other solutions, e.g. Schottky varactor diodes, can be considered.

13 CONCLUSION

In this thesis, several active and passive dielectric rod waveguide components are proposed, studied and developed for millimetre wavelengths. The major problem in millimetre-wave and terahertz technology is that the fundamental hardware for many applications is very expensive or does not exist at all today. Components based on dielectric rod waveguides are an interesting field of research that could partly answer to some of the open questions. They often offer cost effective and low loss solutions.

The first component under study is a dielectric rod waveguide antenna made of relatively high permittivity materials, silicon and sapphire. Antennas has been studied with HFSS simulations up to 325 GHz. A prototype for D band (110-170 GHz) has been fabricated and measured.

Dielectric rod waveguide antennas are travelling-wave antennas with a wide operating frequency band. The benefits of the high permittivity DRWs are the reduced size without losing the waveguide properties and a good matching with a standard metal waveguide. Also antenna radiation efficiency is normally very good, even over 90% in some applications. Such designs do not need any launching horns that are needed in the case of low permittivity materials. These antennas are also lightweight and simple to construct. Today the modern semiconductor fabrication technology has enabled to manufacture these high permittivity rods that often require high precision as the required dimensions are so small at high frequencies. Both simulations and the measurements show very wide band radiation characteristics with an almost frequency independent radiation pattern. Therefore these antennas could be an attractive alternative to be used for example as a feed in wideband reflector type antennas or in high capacity short range WLANs.

The location of the phase centre of an antenna is an important parameter in many applications, especially when the antenna is used as a feed for a reflector. This location

for the DRW antenna is studied with three different analysis methods from the data obtained with planar scanner measurements at W band. If many planes of the radiation pattern are desired to be analyzed, the rotational systems would require several rotational joints that can be avoided with planar measurements. As expected, it is found out that the phase centre is moving towards the antenna tip as the frequency increases.

A high-permittivity DRW antenna is an interesting candidate for an antenna array element due to its high packing potential. According to W-band simulations and measurements the mutual coupling between the elements is relatively low even with the vertical distance of ~λ/4 as the element spacing. In horizontal plane mutual coupling is somewhat stronger and respective distance is ~λ/2. Low mutual coupling makes DRWs an appealing alternative as an element for densely packed arrays. A very challenging task is to design the antenna feeding network.

However, mutual coupling studies for antenna arrays revealed a very strong coupling phenomenon when the distance between the elements is smaller than mentioned above. At some points of the waveguides the power is transferred completely to the other waveguide. This phenomenon is similar to the cross-talk in optical fibres. In that regime the cross-talk has been utilised in many applications, e.g. in directional couplers. In this thesis a frequency selective coupler based on that strong coupling has been developed for W band. Frequency selectivity is based on the fact, that the waveguide length required for complete power transfer depends on the frequency. The length that is required for the power to transfer to the other waveguide and back is also called as a beat length. A prototype coupler has been simulated, manufactured and measured. The results are very promising for this type of components made of DRWs for millimetre wavelengths.

Different types of DRW junctions for power division have been also studied. Such junctions can be used also, e.g., for power combining or monitoring the propagating power in a DRW. Junctions can be designed for both E and H planes depending on the

application. Symmetric and asymmetric Y-type junctions were designed and studied with HFSS in both planes at W band.

Active components studied in this thesis include a travelling-wave amplifier based on GaAs/AlGaAs heterostructure and a DRW phase shifter designed with ferroelectric varactors fed with Au strips, both for W band. Phase shifter is active in that sense, that it is designed to be electronically tunable. The DRW travelling-wave amplifier is based on the interaction between an electron drift and an electromagnetic wave travelling in a periodic structure. It is also called as a slow-wave structure. The fabricated prototype has a small amplifier chip, 1.6-2.6 mm, inserted in the GaAs waveguide. On the top of the chip there is a grating with a period of 0.3-0.8 μm. DC voltage is fed to the ohmic contacts of the chip to create the electron drift. The first measurement results are promising. At highest ~10 dB/cm electronic gain is obtained at 70-80 GHz with 150 V/cm electric field. However the insertion loss in the system is relatively high, mostly due to the feeding pins. Also the separate chip in the grooved rod increases the reflections. In the next stage, other current feeding solutions should be considered. A completely monolithic DRW amplifier would simplify also the analysis.

The proposed novel prototype of millimetre-wave phase shifter includes a dielectric rod waveguide with a periodic printed array of electrically small dipoles loaded with ferroelectric varactors. In this stage, the phase shifter is studied only with Au strips that are designed for two different capacitances, 10 fF and 15 fF, simulating the tuning range of the varactors. Measurement results of the non-tunable phase shifter prototype showed that optimally the phase shift of ~60 deg/dB could be obtained. Introducing a ferroelectric or Schottky varactor between the dipoles makes it possible to obtain a low loss tunable millimetre-wave phase shifter.

In summary, the main new scientific results of this thesis are:

1) Further development and analysis of dielectric rod waveguide antennas with rectangular cross-section for 110-170 GHz and 220-325 GHz

frequency ranges have been made. Prototype silicon and sapphire antennas for 110-170 GHz have been fabricated and measured. A study of the phase centre position in such an antenna with different analysis methods based on planar scanner measurements at W band has been performed.

2) A study of the suitability of the DRWs to be used as an antenna array element has been carried out. Results showing low mutual coupling between the elements with separation over ~λ/2 have been obtained. A metal waveguide power splitter for the feed of the antenna elements at 90 GHz has been developed, fabricated and tested. A two-element prototype antenna has been fabricated and measured.

3) Power dividers based on DRW junctions have been developed. Different types of junctions have been proposed for W band.

4) Cross-talk phenomenon in rectangular DRWs at millimetre-wave frequencies has been studied. A frequency selective directional coupler for W band based on cross-talk between two identical DRWs has been developed. A prototype has been fabricated and successfully tested.

5) Experimental study of the travelling-wave amplifier principle to be used in DRWs by using an AlGaAs/GaAs heterostructure has been carried out. A prototype amplifier has been developed with promising results of ~10 dB/cm electronic gain with 150 V/cm electric field at 70-80 GHz. However, true insertion gain has not yet been achieved.

6) A tunable DRW phase shifter concept for W band based on ferroelectric varactors has been developed. Measurement results of the non-tunable phase shifter prototype have shown that optimally a phase shift of ~60 deg/dB can be obtained.

REFERENCES

[1] J. P. Pousi, D. V. Lioubtchenko, S. N. Dudorov, J. A. Mallat, and A. V. Räisänen, ”High permittivity dielectric rod waveguide antenna for 110-150 GHz,” in *Proc. of the First European Conference of Antennas and Propagation (EuCAP06)*, Nice, France, 6-10 November, 2006, CD-ROM SP-262, paper 347786.

[2] P. Padilla, P. Pousi, A. Tamminen, J. Mallat, J. Ala-Laurinaho, M. Sierra-Castañer, and A. Räisänen, ”Mm-wave DRW antenna phase centre determination,” in *Proc. of the 4thEuropean Conference of Antennas and Propagation (EuCAP10)*, Barcelona, Spain, 11-16 April, 2010, paper 1843763.

[3] P. Padilla, P. Pousi, A. Tamminen, J. Mallat, J. Ala-Laurinaho, M. Sierra-Castañer, and A. Räisänen, ”Mm-wave DRW antenna phase centre determination: comparison of different experimental methods,” submitted to *IEEE Trans. on Antennas and Propagation*.

[4] J. P. Pousi, D. V. Lioubtchenko, S. N. Dudorov, and A. V. Räisänen, ”High permittivity dielectric rod waveguide as an antenna array element for millimeter waves,” *IEEE Transactions on Antennas and Propagation*, vol. 58, March 2010, pp. 714-719.

[5] J. P. Pousi, D. V. Lioubtchenko, S. N. Dudorov, and A. V. Räisänen, ”Dielectric rod waveguide antenna array element for millimeter waves,” in *Proc. of the 31st National URSI Convention on Radio Science*, Espoo, Finland, 28 October 2008, pp. 15-16.

[6] J. P. Pousi, S. N. Dudorov, D. V. Lioubtchenko, and A. V. Räisänen, ”Complete power transfer between two dielectric rod waveguides,” in *Proc. of the 3rd European Conference of Antennas and Propagation (EuCAP 2009)*, Berlin, Germany, March 2009, pp. 1651-1654.

[7] J. P. Pousi, S. N. Dudorov, D. V. Lioubtchenko, and A. V. Räisänen, ”Frequency selective coupler for W band based on power transfer in dielectric rod waveguides,” in *Proc. of the 4th European Conference of Antennas and Propagation (EuCAP10)*, Barcelona, Spain, 11-16 April, 2010, paper 1840244.

[8] P. Pousi, D. Lioubtchenko, S. Dudorov, and A. V. Räisänen, ”Dielectric rod waveguide travelling-wave amplifier based on AlGaAs/GaAs heterostructure,” in *Proc. of the 38th European Microwave Conference*, Amsterdam, Netherlands, 28-31 October, 2008, pp. 1082-1085.

[9] D. V. Lioubtchenko, V. E. Lyubchenko, P. Pousi, S. N. Dudorov, and A. V. Räisänen, ”Dielectric rod waveguide traveling wave amplifier,” in *Proc. of the 32nd Workshop on Compound Semiconductor Devices and Integrated Circuits*, Leuven, Belgium, 18-21 May 2008, pp. 159-160.

[10] D. V. Lioubtchenko, P. Pousi, S. N. Dudorov, and A. V. Räisänen, ”Millimetre-wave phase shifter based on dielectric rod waveguide,” in *Proc. of the 38th European Microwave Conference*, Amsterdam, Netherlands, 28-31 October, 2008, pp. 1204-1206.

[11] A. Lehto and A. Räisänen, *Millimetriaaltotekniikka*, Espoo: Otatieto 1997.

[12] T. Yoneyama and S. Ishida, ”Nonradiative dielectirc waveguide for millimeter-wave integrated circuits,” *IEEE Transactions on Microwave Theory and Techniques*, vol. 29, no. 11, November 1981, pp. 1188-1192.

[13] A. V. Räisänen and A. Lehto, *Radio Engineering for Wireless Communication and Sensor Applications*, Boston: Artech House, 2003.

[14] P. Helistö, A. Luukanen, L. Grönberg, J. Penttilä, H. Seppä, H. Sipola, C. Dietlein, and E. Grossman, ”Antenna coupled microbolometers for passive THz direct detection imaging arrays,” in *Proc. of the 1st European Microwave Integrated Circuits Conference*, Manchester, U.K., 10-13 September, 2006, pp 35-38.

[15] G. Rebeiz, ”Millimeter-wave and terahertz integrated circuit antennas,” *Proc. of the IEEE*, Vol. 80, no. 11, pp. 1748-1770, 1992.

[16] N. Lombart and G. Chattopadhyay, “Extended hemispherical silicon lens excited by a leaky wave waveguide feed,” in *Proc. of the 4thEuropean Conference of Antennas and Propagation (EuCAP10)*, Barcelona, Spain, 11-16 April, 2010.

[17] S. A. Long, M. McAllister, and L. C. Shen, ”The resonant cylindrical dielectric cavity antenna,” *IEEE Trans. on Antennas and Propagation*, vol. 31, pp. 406-412, May 1983.

[18] A. W. Glisson, D. Kajfez, and J. James, ”Evaluation of modes in dielectric resonators using a surface integral equation formulation,” *IEEE Trans. on Microwave Theory and Techniques*, vol. 31, pp. 1023-1029, Dec. 1983.

[19] A. Rashidian and D. Klymyshyn, ”Very low permittivity slot-fed dielectric resonator antennas with improved bandwidth for millimeter-wave applications,” in *Proc. of the 3rd EuCAP*, Berlin 23-27 March 2009, pp. 3554-3557.

[20] F.J. Zucker, ”Surface and leaky-wave antennas,” ch. 16 in *Antenna Engineering Handbook*, ed. H. Jasik, New York: McGraw-Hill, 1961.

[21] C. Chen, ”Novel wide bandwidth dielectric rod antenna for detecting antipersonnel mines,” in *Proc. of Geoscience and Remote Sensing Symposium*, Honolulu, U.S.A, July 2000, pp. 2356-2358.

[22] S. Kobayashi, R. Lampe, N. Deo, and R. Mittra, ”Dielectric antennas for millimeter-wave applications,” in *IEEE MTT-S International Microwave Symposium Digest*, 1979, pp. 566-568.

[23] S. Kobayashi, R. Mittra, and R. Lampe, ”Dielectric rod antennas of rectangular cross section,” in *IEEE Antennas and Propagation Society International Symposium*, Jun. 1980, pp. 27-30.

[24] D. V. Lioubtchenko, S. N. Dudorov, J. A. Mallat, and A. V. Räisänen, ”Dielectric rod waveguide antenna for W band with good input match,” *IEEE Microwave and Wireless Components Letters,* vol. 15, no. 1, pp. 4-6, Jan. 2005.

[25] S. Dudorov, *Rectangular Dielectric Waveguide and Its Optimal Transition to a Metal Waveguide*, Doctoral Thesis, Helsinki University of Technology, Radio Laboratory, Otamedia 2002.

[26] S. M. Hanham, T. S. Bird, B. F. Johnston, A. D. Hellicar, and R. A. Minasian, ”A 600 GHz dielectric rod antenna,” in *Proc. of the 3rd European Conference of Antennas and Propagation (EuCAP 2009)*, Berlin, Germany, March 2009, pp. 1645-1647.

[27] D. Lioubtchenko, S. Tretyakov, and S. Dudorov, *Millimeter-Wave Waveguides*, Netherlands: Kluwer Academic Publishers, 2003.

[28] A. S. SudhØ, ”Why are accurate computations of mode fields in rectangular dielectric waveguides difficult?,” *Journal of Lightwave Technology*, vol. 10, no. 4, pp. 418-419, April 1992.

[29] E. A. J. Marcatili, ”Dielectric rectangular waveguide and directional coupler for integral optics,” *Bell System Technical J.*, vol. 48, pp. 2071-2102, 1969.

[30] J. E. Goell, ”A circular-harmonic computer analysis of rectangular dielectric waveguides,” *Bell System Technical J.*, pp. 2133-2160, Sep. 1969.

[31] S. N. Dudorov, D.V. Lioubtchenko, and A.V. Räisänen, ”Modification of Marcatili’s method for the calculation of anisotropic rectangular dielectric waveguides,” *IEEE Trans. on Microwave Theory and Techniques*, vol. 50, pp. 1640-1642, Jun. 2002.

[32] A. C. Studd, ”Towards a better dielectric antenna,” In *Proc. of the 7th International Conference on Antennas and Propagation*, York, U.K., April 1991, pp. 117-120.

[33] J. Weinzierl, J. Richter, G. Rehm, and H. Brand, ”Simulation and measurement of dielectric antennas at 150 GHz,” in *Proc. of the 29th Eur. Microwave Conf.*, Munich, Germany, 1999, pp. 185-188.

[34] S. Kobayashi, R. Mittra, and R. Lampe, ”Dielectric tapered rod antennas for millimeter-wave applications,” *IEEE Trans. on Antennas and Propagation*, vol. 30, pp. 54-58, Jan. 1982.

[35] D. V. Lioubtchenko, S. Dudorov, and A. V. Räisänen, ”Development of rectangular open dielectric waveguide sections for the frequency range of 75-110 GHz,” in *Proc. 31st Eur. Microwave Conf.*, London, U.K., 2001, pp. 201-204.

[36] D. V. Lioubtchenko, S. Dudorov, J. Mallat, J. Tuovinen, and A. V. Räisänen, ”Low loss sapphire waveguides for 75-110 GHz frequency range,” *IEEE Microwave Wireless Components Letters*, vol. 11, no. 6, pp. 252-254, June 2001.

[37] T. Ando, I. Ohba, S. Numata, J. Yamauchi, and H. Nakano, ”Linearly and curvilinearly tapered cylindrical-dielectric-rod antennas,” *IEEE Trans. Antennas and Propagation*, vol. 53, no. 9, pp. 2827-2833, Sep. 2005.

[38] G. L. Yip, ”Launching efficiency of the HE_{11} surface wave mode on a dielectric rod,” *IEEE Trans. on Microwave Theory and Techniques*, vol 18, no. 12, pp. 1033-1041, Dec. 1970.

[39] J. Duncan and R. DuHamel, ”Launching efficiency of wires and slots for a dielectric rod waveguide,” *IEEE Trans. on Microwave Theory and Techniques*, vol. 6, no. 3, pp. 277-284, Jul. 1958.

[40] C. Angulo and W. Chang, “The excitation of a dielectric rod by a cylindrical waveguide,” *IEEE Trans. on Microwave Theory and Techniques*, vol. 6, no. 4, pp. 389-393, Oct. 1958.

[41] M. Cohn and M. King, ”Selected surface wave excitation studies,” Electronic Communications Inc., 1962, Tech. Rep. No. 3, Contract: AF 19.

[42] S. M. Hanham and T. S. Bird, ”High efficiency excitation of dielectric rods using a magnetic ring current,” *IEEE Trans. on Antennas and Propagation*, vol. 56, no. 6, pp. 1805-1808, June 2008.

[43] M. N. Afsar, H. Chi, and X. Li, “Millimeter wave complex refractive index, complex dielectric permittivity and loss tangent of high purity and compensated silicon,” in *Proc. of Conference on Precision Electromagnetic Measurements*, Ottawa, Canada, June 1990, pp. 238-239.

[44] S. Biber, J, Schür, A. Hofmann, and L.-P. Schmidt, ”Design of new passive THz devices based on micromachining techniques,” in *Proc. of Symposium of Physics and Engineering of Microwaves, Millimeter and Submillimetre Waves*, Kharkov, Ukraine, June 21-26, 2004, pp. 26-31.

[45] J. Weinzierl, C. Fluhrer, and H. Brand, ”Dielectric waveguides at submillimetre wavelengths,” in *Proc. of 6th Int. Conf. on THz Electronics*, Leeds, U.K., 1998, pp. 166-169.

[46] A. Lehto, and A. Räisänen, *Mikroaaltomittaustekniikka*, Espoo: Otatieto 1999.

[47] J. Richter, M. Müller, and L.-P. Schmidt, ”Measurement of phase centers of rectangular dielectric rod antennas,” in *Proc. of IEEE Antennas and Propagation Society Symposium*, Monterey, California, U.S.A., 20-25 June, 2004, pp. 743-746.

[48] J. Richter, J.-U. Garbas, and L.-P. Schmidt, ”Mean and differential phase centers of rectangular dielectric rod antennas,” in *Proc. of the 34th European Microwave Conference*, Amsterdam, Netherlands, 11-15 October, 2004, pp. 1193-1196.

[49] V. V. Meriakri and M. P. Parkhomenko, ”Millimeter wave phase shifters based on ferrite dielectric waveguides,” in *Proc. 12th Int. Conf. Microwaves Radar (MIKON’98)*, vol. 2, Krakow, Poland, 1998, pp. 514-517.

[50] Website of Thomas Keating Ltd., http://www.terahertz.co.uk/TKI/tkins.html.

[51] J. Säily and A. Räisänen, *Studies on Specular and Non-specular Reflectivities of Radar Absorbing Materials (RAM) at Submillimetre Wavelengths*, Report S 258, Helsinki University of Technology, Otamedia 2003.

[52] B. Riddle, J. Baker-Jarvis, and J. Krupta, ”Complex permittivity measurements of common plastics over variable temperatures,” *IEEE Trans. on Microwave Theory and Techniques*, vol. 51, no. 3, pp. 727-733, March 2003.

[53] Measurements done by Dr. Dmitri Lioubtchenko in April 2005.

[54] J. Mallat, A. Lehto, and J. Tuovinen, “Antenna phase pattern measurements at millimeter wave frequencies using the differential phase method with only one power meter,” *International Journal of Infrared and Millimeter Waves,* vol. 15, no. 9, pp. 1497-1506, 1994.

[55] J. Wang, ”An examination of the theory and practices of planar near-field measurements,” *IEEE Trans. on Antennas and Propagation*, vol. 36, no. 6, pp. 746-753, Jan. 1988.

[56] I. Lindell and K. Nikoskinen, *Antenniteoria*, Otatieto 1995.

[57] H.-Y. Yang, J. A. Castaneda, and N. G. Alexopoulos, ”An integral equation analysis of an infinite array of rectangular dielectric waveguides,” *IEEE Trans. on Microwave Theory and Techniques*, vol. 38, no. 7, pp. 873-880, July 1990.

[58] C. A. Balanis, *Antenna Theory: Analysis and Design*, New York: Harper Row, 1982.

[59] W. L. Stutzmann and G. A. Thiele, *Antenna Theory and Design*, London, U.K.: Peter Peregrius, 1984.

[60] T. Sehm, A. Lehto, and A. V. Räisänen, ”A high-gain 58-GHz box-horn array antenna with suppressed grating lobes,” *IEEE Transactions on Antennas and Propagation*, Vol. 47, No. 7, pp. 1125-1130, July 1999.

[61] J. Richter and L.-P. Schmidt, ”Dielectric rod antennas as optimized feed elements for focal plane arrays,” in *Proc. of Antennas and Propagation Society International Symposium*, 3-8 July, 2000, Salt Lake City, U.S.A., pp. 667-670.

[62] S. Lin, S. Yang, A. Elsherbini, and A. E. Fathy. ”Dielectric rod antennas array feed using substrate integrated waveguides,” in *Proc. of Antennas and Propagation Society International Symposium*, 5-11 July 2008, San Diego, U.S.A, pp. 1-4.

[63] J. Richter, Y. Yazici, C. Ziegler, and L.-P. Schmidt, “A broadband transition between dielectric and planar waveguides at millimeter-wave frequencies,” in *Proc. of the 33rd European Microwave Conference,* Munich, Sep. 2003, vol. 3/3, 2003, pp. 947-950.

[64] H. Tehrani, M.-Y. Li, and K. Chang, ”Broadband microstrip to dielectric image line transitions,” *IEEE Microwave and Guided Wave Letters*, vol. 10, no. 10, pp. 409-411, Oct. 2000.

[65] J. Tang and K. Wu, ”Co-layered integration and interconnect of planar circuits and nonradiative dielectric (NRD) waveguide,” *IEEE Trans. on Microwave Theory and Techniques*, vol. 48, no. 4, pp. 519-524, April 2000.

[66] T. Sehm, A. Lehto, and A. V. Räisänen, ”Matching of a rectangular waveguide T junction with unequal power division,” *Microwave and Optical Technology Letters*, vol. 14, no. 3, pp. 141-143, Feb. 1997.

[67] J. Hirokawa, K. Sakurai, M. Ando, and N. Goto, ”An analysis of a waveguide T junction with an inductive post,” *IEEE Trans. on Microwave Theory and Techniques*, vol. 39, pp. 563-566, March 1991.

[68] A. W. Snyder and J. D. Love, *Optical Waveguide Theory*, London: Chapman and Hall, 1983.

[69] D. Marcuse, *Theory of Dielectric Optical Waveguides*, New York: Academic Press, 1974.

[70] S. E. Miller, ”Coupled wave theory and waveguide applications,” *Bell System Technical J.*, vol. 33, no. 3, pp. 661-720, 1969.

[71] D. Marcuse, *Light Transmission Optics*, Van Nostrand Reinhold, 1972.

[72] T. Tamir, *Guided-Wave Optoelectronics*, Springe, 1990.

[73] S. Boscolo, M. Midrio, and C. G. Someda, ”Coupling and decoupling of electromagnetic waves in parallel 2-D photonic crystal waveguides,” *IEEE Journal of Quantum Electronics*, vol. 38, no. 1, pp. 47-53, 2002.

[74] H. C. Cheng and R. V. Ramaswamy, ”Determination of the coupling length in directional coupler from spectral response,” *IEEE Photonics Technology Letters*, vol. 2, no. 11, pp. 823-825, 1990.

[75] W. E. Martin, ”A new waveguide switch/modulator for integrated optics,” *Appl. Phys. Letters*, vol. 26, pp. 562-564, May 1975.

[76] H. Saaki and R. M. De la Rue, ”Electro-optic Y-junction modulator/switch,” *Electron. Letters*, vol. 12, pp. 459-460, Sept. 1976.

[77] K. Ogusu, ”Experimental study of dielectric waveguide Y-junctions for millimeter-wave integrated circuits,” *IEEE Trans. on Microwave Theory and Techniques*, vol. 33, no. 6, pp. 506-509, June 1985.

[78] K. Ogusu, “Dielectric waveguide corner and power divider with a metallic reflector,” *IEEE Trans. on Microwave Theory and Techniques*, vol. 32, pp. 113-116, Jan. 1984.

[79] A. Axelrod and M. Kisliuk, ”Experimental study of the W-band dielectric guide Y-branch interferometer,” *IEEE Trans. on Microwave Theory and Techniques*, vol. 32, pp. 46-50, Jan. 1984.

[80] L.-P. Schmidt, S. Biber, G. Rehm, and K. Huber, ”THz measurement technologies and applications,” in *Proc. of the 14th Int. Conference on Microwaves, Radar and Wireless Communications*, Gdansk, Poland, May 20-22, pp. 581-587.

[81] A. Gover and A. Yariv, ”Monolithic solid-state traveling-wave amplifier,” *Journal of Applied Physics*, vol. 45, pp. 2596-2600, 1976.

[82] L. Solymar and E. A. Ash, ”Some travelling-wave interactions in semiconductors, theory and design considerations,” *International Journal of Electronics*, vol. 20, no. 2, pp. 127-148, 1966.

[83] M. Meyer and T. van Duzer, ”Traveling-wave amplification and power flow in conducting solids,” *IEEE Trans. on Electron Devices*, vol. 17, no. 3, pp.193-199, 1970.

[84] A. Gover, K. H. Burrell, and A. Yariv, ”Solid-state travelling-wave amplification in the collisionless regime,” *Journal of Applied Physics*, vol. 45, pp. 4847-4851, 1974.

[85] V.E. Lyubchenko and V.A. Martyakhin, ”Traveling wave amplification in GaAs image waveguide at V-band,” *Electronic Letters*, vol. 30, no. 11, pp. 869-870, 1994.

[86] M. Pokorný and Z. Raida, ”Active semiconductor waveguides and antennas,” in *Proc.of the 4th Workshop on Antenna Systems and Sensors for Information Society Technologies*, Dublin, Ireland, 2008, pp. 132-137.

[87] M. Pokorný and Z. Raida, ”Active transmission line on GaAs substrate,” in *Proc.of Loughborough Antennas and Propagation Conference*, Loughborough, U.K., 2009, pp. 477-480.

[88] V. E. Lyubchenko, T. A. Briantseva, S. N. Dudorov, D. V. Lioubtchenko, I. A. Markov, R. I. Markov, and A. V. Räisänen, “Millimeter wave propagation in GaAs and Si two-layer dielectric rod waveguides,” in *Proc.*

on International Conference of Microwaves, Radar and Wireless Communications, Krakow, Poland, 2006, pp. 897-900.

[89] M. Levinshtein, S. Rumiantsev, and M. Shur, *Handbook on Semiconductor Parameters*, vol. 1, London: World Scientific, 1996.

[90] G. Zandler, C. Kiener, W. Boxleitner, E. Vass, C. Wirner, E. Gornik, and G. Weimann, "Experimental and theoretical investigation of the drift velocity and velocity distribution functions in GaAs/AlGaAs heterostructures," *Journal of Applied Physics*, vol. 70, 1991, pp. 6842-6846.

[91] NSM Archive, Aluminiun Gallium Arsenide (AlGaAs): http://www.ioffe.ru/SVA/NSM/Semicond/AlGaAs/Figs/b13_04.gif

[92] V. G. Mokerov, G. B. Galiev, J. Pozela, K. Pozela, and V. Juciene, "Electron mobility in a AlGaAs/GaAs/AlGaAs quantum well," *Semiconductors*, vol. 36, no. 6, pp. 674-678, 2002.

[93] G. Weimann, "Transport properties of semiconductor heterostructures," *Advances in Solid State Physics*, vol. 26, pp. 231-250, 1986.

[94] S. K. Koul and B. Bhat, *Microwave and Millimeter Wave Phase Shifters*, London: Artech House, 1991.

[95] F. de Flaviis, N. G. Alexopoulos, and O. M. Stafsudd, "Planar microwave integrated phase-shifter design with high-purity ferroelectric material," *IEEE Trans. on Microwave Theory and Techniques*, vol. 45, pp. 963-969, June 1991.

[96] E. Carlsson, P. Petrov, R. Chakalov, P. Larsson, Z. Ivanov, and S. Gevorgian, ”Experimental study of thin film HTS/ferroelectric CPW phase shifter for microwave applications,” *Inst. Conf. Phys. Ser.*, no. 158, pp. 339-342, 1997.

[97] D. Chicherin, S. Dudorov, D. Lioubtchenko, V. Ovchinnikov, and A. V. Räisänen, ”Millimetre wave phase shifters based on a metal waveguide with a MEMS-based high-impedance surface,” in *Proc. of 36th European Microwave Conference*, 10-15 September, 2006, Manchester, U.K., pp. 372-375.

[98] L. Huang, J.-C. Chiao, and M. P. de Lisio, ”An electronically switchable leaky wave antenna,” *IEEE Trans. on Antennas and Propagation*, vol. 48, no. 11, pp. 1769-1772, 2000.

[99] A. Deleniv, S. Abadei, and S. Gevorgian, ”Tunable ferroelectric filter-phase shifter,” in *IEEE MTT-S International Microwave Symposium Digest*, vol. 2, 2003, pp. 1267 –1270.

[100] Simulations done by Anatoli Deleniv from Physical Electronics Laboratory, Department of Microtechnology and Nanoscience, MC2, Chalmers University of Technology.

[101] A. Vorobiev, P. Rundqvist, K. Khamchane, and S. Gevorgian, ”Silicon substrate integrated high-Q factor parallel-plate ferroelectric varactors for microwave/millimeterwave applications,” *Appl. Phys. Lett.*, vol. 83, pp. 3144–3146, 2003.

5. J. Praks, A. Sihvola, editors: URSI XXXI Finnish convention on Radio Science and Electromagnetics 2008 meeting, Book of Abstracts, October 2008.

6. T. Hovatta: Radio variability of active galactic nuclei: analysis of long-term multifrequency data, March 2009.

7. S. Ranvier: Radiowave propagation and antennas for high data rate mobile communications in the 60 GHz band, March 2009.

8. P. Alitalo: Microwave transmission-line networks for backward-wave media and reduction of scattering, July 2009.

9. S. Ilvonen: Models and methods for computational electromagnetic dosimetry, July 2009.

10. A. Sihvola, S. Lindberg: TKK Department of Radio Science and Engineering Research and Education 2008, September 2009.

11. O. Luukkonen: Artificial impedance surfaces, November 2009.

12. V-M. Kolmonen: Propagation channel measurement system development and channel characterization at 5.3 GHz, March 2010.

13. J. Praks, E. Koskinen, M. Karjalainen, A. Leskinen, K. Luojus, E. Parmes, Y. Sucksdorff, M. Takala, M. Törmä: Nordic remote sensing days 2009. Book of abstracts. March 2010.

14. M. Pitkonen: Exact solutions to some spherical electrostatic scattering problems, May 2010.

15. E. Nieppola: Synchrotron emission from blazar jets – energy distributions and radio variability, May 2010.

16. A. Sihvola, S. Lindberg, editors: Aalto University of Science and Technology Department of Radio Science and Engineering Research and Education 2009, June 2010.

17. J. Toivanen: Measurement methods for mobile terminal antenna performance, September 2010.

18. P. Pousi: Active and passive dielectric rod waveguide components for millimetre wavelengths, November 2010.

ISBN 978-952-60-3462-1 (paper)

ISBN 978-952-60-3463-8 (electronic)

ISSN 1797-4364 (paper)

ISSN 1797-8467 (electronic)